UNIVERSIDADE FEDERAL DE SANTA CATARINA
CENTRO DE CIÊNCIAS FÍSICAS E MATEMÁTICAS
PROGRAMA DE PÓS-GRADUAÇÃO EM QUÍMICA

HERCULYS BERNARDI JORGE

INNOVATIVE METAL CARBONYL COMPOUNDS AND CARBON QUANTUM **DOTS:** Breakthroughs in Therapeutic and Photocatalytic Applications

FLORIANÓPOLIS
2024

Herculys Bernardi Jorge

INNOVATIVE METAL CARBONYL COMPOUNDS AND CARBON QUANTUM **DOTS:** Breakthroughs in Therapeutic and Photocatalytic Applications

Thesis submitted to the Chemistry Postgraduate Program, Department of Chemistry, School of Physical and Mathematical Sciences, Federal University of Santa Catarina, as a partial requirement for obtaining the Doctor degree in Chemistry.

Supervisor: Prof Rosely Aparecida Peralta, Dr.
Co-supervisor: Prof. Enrique Rodríguez Castellón, Dr.

FLORIANÓPOLIS

2024

Bernardi Jorge, Herculys
INNOVATIVE METAL CARBONYL COMPOUNDS AND CARBON QUANTUM DOTS : Breakthroughs in Therapeutic and Photocatalytic Applications / Herculys Bernardi Jorge ; orientador, Rosely Aparecida Peralta, coorientador, Enrique Rodríguez Castellón, 2024.
200 p.

Tese (doutorado) - Universidade Federal de Santa Catarina, Centro de Ciências Físicas e Matemáticas, Programa de Pós-Graduação em Química, Florianópolis, 2024.

Inclui referências.

1. Química. 2. Organometálicos. 3. Valorização de biomassa. 5. Pontos quânticos de carbono. I. Peralta, Rosely Aparecida. II. Castellón, Enrique Rodríguez . III. Universidade Federal de Santa Catarina. Programa de Pós-Graduação em Química. IV. Título.

Herculys Bernardi Jorge

INNOVATIVE METAL CARBONYL COMPOUNDS AND CARBON QUANTUM DOTS: Breakthroughs in Therapeutic and Photocatalytic Applications

The present Doctorate level work has been reviewed and approved, at 05 of august of 2024, by the examination board comprised of the following members:

Prof. Maria Helena Araújo, Dr.
Institution: Universidade Federal de Minas Gerais

Prof. Sofia Nikolaou, Dr
Institution: Universidade de São Paulo, Ribeirão Preto

Prof.Daniela Zambelli Mezalira, Dr.
Institution: Universidade Federal de Santa Catarina

We certify that this is the original and final version of the final work examined and judged in favor for the Doctor degree in Chemistry

Documento assinado digitalmente
Daniel Lazaro Gallindo Borges
Data: 02/09/2024 20:06:45-0300
CPF: ***.794.969-**
Verifique as assinaturas em https://v.ufsc.br

Head of Chemistry Postgraduate Program

Documento assinado digitalmente
Rosely Aparecida Peralta
Data: 02/09/2024 17:43:41-0300
CPF: ***.719.349-**
Verifique as assinaturas em https://v.ufsc.br

Prof Rosely Aparecida Peralta, Dr.
Supervisor

FLORIANÓPOLIS, 2024.

Work dedicated to all the silent victories, even when they felt like losses.

ACKNOWLEDGEMENTS

By standard I'd like to thank the Department of Chemistry and the Chemistry Postgraduate Program and thank the universities that made this project possible UFSC, Málaga University, and funding agencies that financed this research CNPq, INCT-Catálise, in particular CNPq for the scholarship and sandwich doctorate through the CAPES-PRInt program. The financial support of projects PID2021-126235OB-C32 and TED2021-130756B-C31 of Ministerio de Ciencia e Innovación of Spain and FEDER funds is also acknowledge.

I would also like to thank all the professors I had throughout my journey, who made this experience possible. Special thanks go to those who directly contributed to this work: Prof. Enrique Rodríguez-Castellón, for welcoming me with open arms into his group, providing networking opportunities, and guiding me during my internship in Málaga, Spain, as well as being my Co-Supervisor; Prof. Manuel Algarra, for his guidance and help in project development; Prof. Juan Manuel Lázaro, for his expertise in NMR analysis and his friendship; Prof. Regina de Fátima Peralta Muniz Moreira, for her insights and analyses; and last but not least, Prof. Rosely Aparecida Peralta, my Supervisor, for providing the space, support, and patience that allowed me to develop and complete this thesis.

I extend my gratitude to all the technicians at the Central de Análises, CEBIME, and SCAI for their care with my samples and the conversations during the waiting times, especially those at SCAI.

I would also like to thank my colleagues from LABINC and other labs, particularly André, Bruna, Carina, Daniel, Daniele, Débora, Josi, Marcielli, Suelly, and Vinicius, for their help, time, conversations, and for sharing our daily routines and frustrations. Special thanks to Prof. Suélen for her guidance and support. To everyone else who passed through the lab during my doctorate, thank you for your presence and for bringing life to the space.

To my friends from Málaga—Abraham, Adri, Ale, Álvaro, Antônio, Benjamin, Cinthya, Fran, Fernando, Gaby, Imane, Inés, Javi, Kiara, Marilia, and Marco—you have no idea how much you helped me through everything. Thank you for all the laughs, tears, game nights, and parties that made me feel seen, cared for, and loved, turning Málaga into my second home. You all will always be in my heart and mind. Vos echo de menos <3.

To my core family—Rita, Ernesto, and Érika—thank you for your unwavering support and love, even when the distance felt overwhelming. You always remained present, whether through video calls, in person, or in thoughts.

To my new and old friends—Alexandre, Angel, Barbara, Bianca, Dimas, Eliseu, Jéssica, Leonardo, Malu, Mich, Rafa, and Thuanne—thank you for helping me stay centered and decompress after all the stressful situations in and out of the lab. Sharing all the dramas, drinks, and stories with you has been invaluable.

To all my friends from the gym, especially my yoga teachers, thank you for helping me maintain my physical and mental well-being. And to everyone else but they know who contributed in any way to the making of this work, my deepest gratitude.

RESUMO

Neste trabalho, relatamos três novos compostos carbonílicos Mn(I), com calcogênio nos ligantes, com propriedades de liberação de CO, ativadas em comprimentos de onda de luz visível. Os compostos [(L1)$Mn(CO)_3Br$] (**1**, onde L1 = 2-piridil-N-(2′-metiltiofenil)metilenoimina), [(L2)$Mn(CO)_3Br$] (**2**, L2 = 2-piridil -N-(2'-metiltiofenil)-metilenoamina), [(L3)$Mn(CO)_3Br$] (**3**, onde L3 = 2-piridil-N-(2-(metiltio)etil)amina e [(L4)$Mn(CO)_3Br$] (**4**, onde L4 = 2-piridil-N-(2-tiofenilmetil)amina), foram sintetizados sob condições de baixa incidência de luz e caracterizados pelas espectroscopias de UV-Vis, FTIR, RMN de ^1H e de ^{13}C e ESI-MS, assim como raio-x, voltametria e CHN. Os resultados indicam que a transferência de carga metal-ligante (MLCT) de Mn-CO em direção aos orbitais ligante-π enfraquece o retroligação Mn-CO π*, levando à eliminação de CO da esfera de coordenação quando os compostos são irradiados por radiação UV-Vis de comprimento de onda de 450nm e 395nm. O grau de liberdade da porção calcogênica dos compostos projetados influenciou sua capacidade de liberar o CO da esfera de coordenação, sendo que para ligantes com maior mobilidade provocou deslocamento hipsocrômico na região de ativação UV-Vis, resultando em taxas de liberação aparentes de CO mais lentas e menores rendimentos quânticos, sendo assim passiveis de atuarem como fotoCORMS. Em paralelo, foi elaborado uma rota sintética verde e simples para a síntese de nanopontos de carbono (CDs) de baixa toxicidade através do aproveitamento de resíduos de papel industrial. A metodologia se mostrou eficiente tanto para produção de CDs, como também CDs dopados com N e S. Os compostos sintetizados se mostraram eficientes para degradações fotocatalíticas de p-nitrofenol assim como para reações de geração de hidrogênio. Frente ao N-CDs, as FotoCORMS apresentaram uma fotoliberação mais lenta de CO, porém ativando as mesmas fora da sua área analítica para os compostos **1** e **2**, indicando uma ação sinergética dos CDs no qual absorve a irradiação da fonte e ajudando na ativação dos compostos para liberar CO.

Palavras-chave: Organometálicos, Valorização de biomassa, Pontos quânticos de carbono.

ABSTRACT

Herein, we report three new Mn(I)-based metal carbonyl with activated CO-release properties at visible light wavelengths with non-bonding chalcogen moieties. Compounds [(L1)Mn(CO)$_3$Br] (**1**, where L1 = 2-pyridyl-N-(2′-methylthiophenyl)methyleneimine), [(L2)Mn(CO)$_3$Br] (**2**, L2 = 2-pyridyl-N-(2'-methylthiophenyl)-methyleneamine), [(L3)Mn(CO)$_3$Br] (**3**, where L3 = 2-pyridyl-N-(2-(methylthio)ethyl)amine and [(L4)Mn(CO)$_3$Br] (**4**, where L4 = 2-pyridyl-N-(2-thiophenylmethyl)amine). All complexes were synthesized under low light conditions and characterized by UV-Vis, FTIR, ^{1}H and ^{13}C NMR and ESI-MS spectroscopy, as well as x-ray, voltammetry and CHN. The results indicate that the metal-ligand charge transfer (MLCT) of Mn-CO toward the π-ligand orbitals weakens the Mn-CO π* backbond, leading to the elimination of CO from the coordination sphere when the compounds are irradiated by radiation. UV-Vis wavelengths of 450nm and 395nm. The degree of freedom of the chalcogenic portion of the designed compounds influenced their ability to release CO from the coordination sphere, and for ligands with greater mobility it caused a hypsochromic shift in the UV-Vis activation region, resulting in slower apparent CO release rates. and lower quantum yields acting like photoCORMS. In parallel, a green and simple synthetic route was developed for the synthesis of low-toxicity carbon nanodots (CDs) through the use of industrial paper waste. The methodology proved to be efficient both for the production of CDs, as well as CDs doped with N and S. The synthesized compounds proved to be efficient for photocatalytic degradation of p-nitrophenol as well as for hydrogen generation reactions. Compared to N-CDs, FotoCORMS showed a slower photorelease of CO, however activating them outside their analytical area for compounds 1 and 2, indicating a synergistic action of CDs in which it absorbs the irradiation from the source and helping to activate the compounds to release CO.

Keywords: Organometallics, Biomass valorization; Carbon dots.

RESUMO EXPANDIDO

INTRODUÇÃO

O CO, um gás comum, é frequentemente tido como tóxico, mas estudos em biologia celular revelam sua produção endógena e com participação em vários processos de sinalização celular. Esses processos regulam neurotransmissores e influenciam sistemas como o imunológico, o respiratório, o reprodutivo e o gastrointestinal. Essas descobertas indicam a possível utilização, dessas propriedades benéficas, do CO no desenvolvimento de fármacos para diversas doenças. Com compostos carbonílicos metálicos (MCC), é possível modular a liberação do CO e assim utilizá-las para fins terapêuticos. As moléculas capazes de liberar CO que são ativadas por estímulos luminosos, são denominadas fotoCORMs, oferecem uma aplicação fitoterápica eficaz e menos invasivo [1],[2].

A incorporação de elementos como o enxofre nesses compostos pode melhorar suas propriedades eletrônicas, contribuindo para sua eficácia em aplicações fototerapêuticas [3]. Assim como o uso de transportadores nanoparticulados, como pontos de carbono (CDs). Os CDs, são uma nova classe emergente de nanomateriais a base de carbono, que oferecem propriedades ópticas, térmicas e eletrônicas únicas, juntamente com uma biocompatibilidade favorável entre diversos organismos biológicos [4]. Esta diversidade na aplicação sublinha o potencial dos CDs em vários empreendimentos nanotecnológicos, tais como catalisadores, geração de energia, sensores, bioimagem e distribuição de medicamentos. Sua utilização como carreadores e ativadores de fotoCORMs ainda não foi relatada na literatura. Ao incorporar CDs no design de fotoCORMs, pode ser possível melhorar seu desempenho e funcionalidade, expandindo ainda mais sua aplicabilidade em fototerapia e outras aplicações biomédicas [5].

OBJETIVOS

Planejar, sintetizar e caracterizar novos compostos de coordenação mononucleares de manganês(I), assim como sintetizar pontos de carbono a partir de biomassa, avaliando suas propriedades físico-químicas e sua potencial aplicação como agente terapêutico.

METODOLOGIA

SÍNTESE DOS LIGANTES

O ligante 2-piridil-*N*-(2'-metiltiofenil)-metilenoimina (L1) foi sintetizado conforme relatado anteriormente na literatura [6]. O ligante 2-piridil-*N*-(2'-metiltiofenil)-metilenoamina (L2) foi obtido através da redução catalítica de L1. O ligante 2-piridil-*N*-(2-(metiltio)etil)amina (L3) foi sintetizado através de um procedimento modificado baseado na substituição nucleofílica de 2-cloroetilmetilsulfeto por 2-(aminometil)piridina [7]. O ligante 2-piridil-N-(2-tiofenilmetil)amina (L4) foi sintetizado condensando 2-formiltiofeno com 2-(aminometil)piridina, seguindo os procedimentos da literatura [8]. Todos os produtos foram purificados por cromatografia em coluna de sílica, resultando em rendimentos acima de 70%, exceto para L3 (25,5%). Todos os ligantes foram caracterizados por FTIR, UV-Vis e RMN de ^{1}H e de ^{13}C.

SÍNTESE DOS COMPOSTOS CARBONÍLICOS DE Mn(I)

Os MCCs foram sintetizados dissolvendo os ligantes de interesse em solução seca de THF e fazendo-os reagir com o precursor $[MnBr(CO)_5]$ em refluxo por 12h, seguindo procedimentos da literatura [3]. Os compostos **1-4** resultantes foram recristalizados, secos e armazenados na ausência de luz.

SÍNTESE DOS PONTOS QUÂNTICOS DE CARBONO (CDs)

Para obter nanopartículas de carbono, 2,5 g da biomassa foram transferidos para um reator de aço inoxidável revestido de Teflon contendo 50 cm^3 de H_2SO_4 (solução a 2,5% v/v). A mistura foi aquecida a 200 °C por 5,5 h. Para N-CDs e S-CDs, ureia e L-Cisteína foram usadas, respectivamente, como fontes de N e S, adicionando uma proporção de 10:1 de biomassa/agente dopante (m/m). Após a reação hidrotermal, a mistura foi centrifugada, filtrada, dialisada e a solução resultante foi liofilizada, obtendo-se finos pós de CDs, N-CDs e S-CDs.

RESULTADOS E DISCUSSÕES

Os espectros de FTIR dos compostos **1-4**, obtidos em pastilhas de KBr, exibem duas bandas proeminentes em aproximadamente 2030 e 1930 cm^{-1}, que podem ser atribuídas às vibrações de estiramento dos grupos CO, **Figura 1a**. O padrão espectral observado é indicativo de uma geometria facial dos grupos carbonila, exibindo uma simetria pseudo-C_{3v}. As análises espectroscópicas de RMN e DRX comprovam as estruturas previstas pelos espectros de FTIR e descrevem os compostos **1-4** em um modo de coordenação pseudo-octaédrica, em que os três ligantes CO estão dispostos num modo de coordenação facial, com ligantes coordenados de forma bidentada [9], **Figura 1b**. O deslocamento do brometo, que

está presente no material de partida, ocorre apenas no composto **3** devido ao alto grau de mobilidade da fração com o enxofre, comprovada por DRX [10].

Figura 1. Comparação dos espectros a) da região FTIR e b) HPDec do ^{13}C no estado sólido para os complexos **1-4**

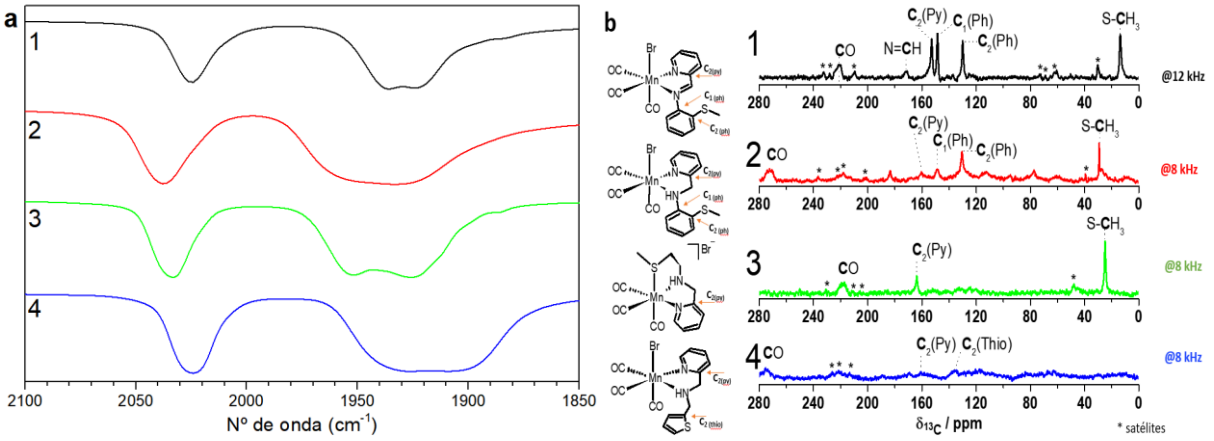

A atuação dos MCCs como fotoCORMs foi estudada através de análises da variação das bandas de estiramento do CO conforme a solução é irradiada. Os fotoprodutos apareceram por volta de 1855 cm^{-1} para os MCCs **1** a **3**, provavelmente indicando um intermediário do complexo biscarbonil. O Composto **4** não apresentou nenhuma nova banda, sugerindo degradação imediata sem formação intermediária. Além disso, uma banda em torno de 2135 cm^{-1} formou-se progressivamente durante a fotoirradiação, indicando a liberação de CO livre no meio, **Figura 2** [11].

Figura 2. Variação dos espectros FITR em CH_2Cl_2 ao longo do período de irradiação com luz azul (450±15 nm) para os compostos **1** e **2** e luz violeta (395±5 nm) para os compostos **3** e **4**.

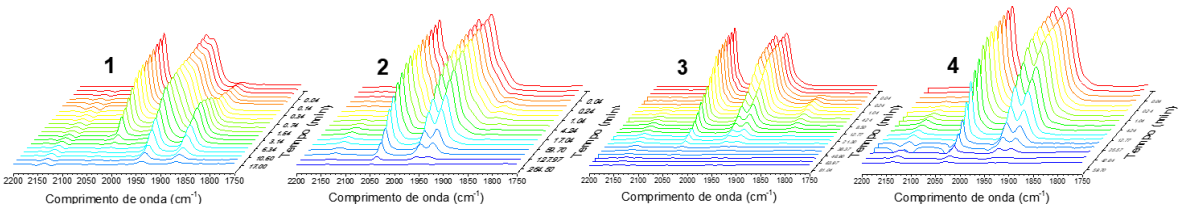

Uma vez que agem como fotoCORMs, a liberação de CO sob condições fisiológicas foi avaliada via carboxilação da mioglobina (Mb). A desoximioglobina exibe um pico de absorção em torno de 560 nm (banda Q). Os dados mostram que cada mol de Mb captura aproximadamente 2 mols de CO para o composto **3**, enquanto os demais apresentam ~2,5 mols por Mb. Os tempos de meia-vida (**t½**) observados de liberação de CO variam de 21 a 155 minutos, sendo **3** com maior **t½** e **2** o menor.

As nanopartículas de carbono também foram caracterizadas e sua morfologia analisada por HR-TEM. As imagens revelam CDs brutos quase esféricos com tamanho médio de 4,4 nm (**Figura 3a**) e um intervalo inter planar de 0,2 nm, consistente com a distância inter planar padrão. N-CDs e S-CDs exibiram tamanhos médios de 6,8 nm (**Figura 3b**) e 5,4 nm (**Figura 3c**), respectivamente. A variação no tamanho sugere mudanças na natureza do grupo de superfície devido à alteração do agente dopante, afetando as interações entre os grupos das nanopartículas [12].

Figura 3. Imagens TEM para a) CDs, inserção distancia Inter planar núcleo grafítico, b) N-CDs e c) S-CDs.

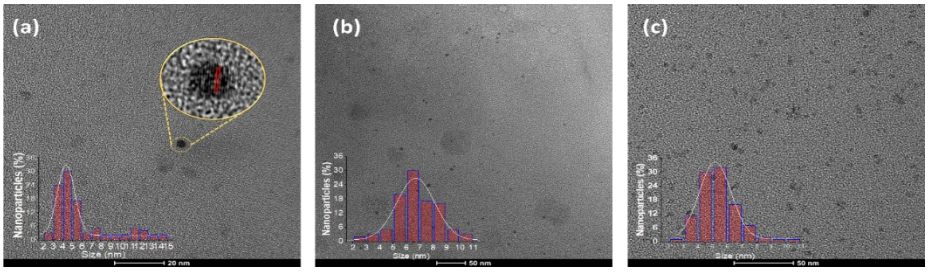

Os espectros XPS de CDs, N-CDs e S-CDs revelaram picos para a energia do núcleo C 1*s*, O 1*s*, N 1*s* e S 2*p*. **Tabela 2**. O teor de carbono foi, em média, em torno de 4×C%, indicando um material rico em carbono. N-CDs exibem maior percentual de grupos amida/aminas. Os S-CDs mostraram uma maior densidade de grupos contendo S, indicando inserção do hetero átomo bem-sucedida [13].

Tabela 2. Distribuição dos elementos na superfície (em % concentração atômica da análise XPS HRS).

	C(%)	**O(%)**	**S(%)**	**N(%)**
CDs	47,0	41,0	5,6	2,7
N-CDs	51,4	30,3	3,9	13,6
S-CDs	43,0	30,6	21,8	4,6

Os CDs e N-CDS foram avaliados em diversas aplicações, como catalisar a fotodegradação do *p*-nitrofenol (4-NP) [14], gerar energia por meio da evolução do hidrogênio na eletrólise da água [15] e interagir com as fotoCORMs. No entanto, o baixo rendimento do S-CDS impossibilitou sua aplicação nessas áreas, porém mais material está sendo sintetizado para futuras investigações.

Testes como catalisador para o poluente 4-NP revelaram ausência de adsorção do mesmo na superfície dos CDs, e após 90 minutos de reação fotolítica, 71% do

contaminante ainda permaneceu na solução. A irradiação com luz de 365 nm na presença dos pontos de carbono reduziu a concentração de 4-NP para aproximadamente 38% para os CDs e 23% para N-CDs. Na geração de hidrogênio, ambos apresentaram resultados superiores ao catalisador comercial Pt, com sobrepotencial de 78 mV, enquanto os CDs obtiveram 581 mV e os N-CDs 451 mV. Na análise da interação com os fotoCORMs, a adição de N-CDs mostrou maior controle na dissociação do CO para compostos. Para os compostos **1** e **2**, houve uma diminuição na constante de velocidade, enquanto para **3** e **4** houve um aumento, indicando a capacidade dos N-CDs de interagir com os fotoCORMs. A adiçã0 de N-CDs ajudou a liberaç4ao de CO mesmo fora do pico analítico para **1'** e **2'**. Embora este seja um estudo introdutório, mais análises e estudos são necessários para investigar os mecanismos desses processos.

CONSIDERAÇÕES FINAIS

A síntese e caracterização dos compostos $[(L_x)Mn(CO)_3]$, onde x=1-4, demonstraram a liberação de CO após exposição à luz visível, podendo assim atuar como fotoCORMs. A estrutura dos ligantes contendo enxofre mostram uma menor influência na liberação frente a coordenação do enxofre e do efeito de ressonância.

Já referente as nanopartículas de carbono, a produção dos mesmos a partir do aproveitamento da celulose proveniente de resíduos da indústria papeleira, se mostrou eficaz a partir da rota sintética elaborada neste trabalho. Além disso, os CDs dopados com nitrogênio ampliaram a janela de ativação, permitindo a liberação de CO mesmo em comprimentos de onda subótimos. Em um estudo separado, os CDs e N-CDs tiveram um desempenho catalítico aprimorado e potencial como eletrocatalisadores para reações de evolução de hidrogênio e de fotocatálise do *p*-nitrofenol.

Palavras-chave: fotoCORMs; Carbon dots; dopagem com N e S, compostos organometálicos.

REFERÊNCIAS

[1] R. Motterlini, J. E. Clark, R. Foresti, P. Sarathchandra, B. E. Mann, and C. J. Green, "Carbon Monoxide-Releasing Molecules," Circ. Res., vol. 90, no. 2, 2002, doi: 10.1161/hh0202.104530.

[2] M. N. Pinto and P. K. Mascharak, "Journal of Photochemistry and Photobiology C : Photochemistry Reviews Light-assisted and remote delivery of carbon monoxide to malignant cells and tissues : Photochemotherapy in the spotlight," "Journal Photochem. Photobiol. C Photochem. Rev., vol. 42, p. 100341, 2020, doi: 10.1016/j.jphotochemrev.2020.100341.

[3] A. L. Amorim et al., “Synthesis, characterization and biological evaluation of new manganese metal carbonyl compounds that contain sulfur and selenium ligands as a promising new class of CORMs,” Dalt. Trans., vol. 48, no. 17, pp. 5574–5584, 2019, doi: 10.1039/c9dt00616h.

[4] S. Wang et al., “Application of nanotechnology in improving bioavailability and bioactivity of diet-derived phytochemicals,” J. Nutr. Biochem., vol. 25, no. 4, pp. 363–376, 2014, doi: 10.1016/j.jnutbio.2013.10.002.

[5] D. Ozyurt, M. Al Kobaisi, R. K. Hocking, and B. Fox, “Properties, synthesis, and applications of carbon dots: A review,” Carbon Trends, vol. 12, no. June, p. 100276, 2023, doi: 10.1016/j.cartre.2023.100276.

[6] C. Bosset et al., “Iron-Catalyzed Synthesis of Sulfur-Containing Heterocycles,” J. Org. Chem., vol. 82, no. 8, pp. 4020–4036, Apr. 2017, doi: 10.1021/acs.joc.6b01827.

[7] D. C. Bebout, W. Lai, S. M. Stamps, S. M. Berry, and R. J. Butcher, “Zinc triad metal ion complexes of NN′S ligand N-(2-pyridylmethyl)-N-(2-(methylthio)ethyl)amine,” Main Gr. Chem., vol. 6, no. 3–4, pp. 155–168, Sep. 2007, doi: 10.1080/10241220802144552.

[8] I. A. Koval et al., “Dinuclear CuII complexes with a new phenol-based ligand bearing pyridine and thiophene substituents: Synthesis, characterization and interaction with catechol substrates,” Eur. J. Inorg. Chem., no. 20, pp. 4036–4045, Oct. 2004, doi: 10.1002/ejic.200400092.

[9] A. L. Amorim et al., “Synthesis, characterization and photoinduced CO-release by manganese(i) complexes,” New J. Chem., vol. 44, no. 26, pp. 10892–10901, Jul. 2020, doi: 10.1039/d0nj02260h.

[10] K. Das, A. Mondal, and D. Srimani, “Selective Synthesis of 2-Substituted and 1,2-Disubstituted Benzimidazoles Directly from Aromatic Diamines and Alcohols Catalyzed by Molecularly Defined Nonphosphine Manganese(I) Complex,” J. Org. Chem., vol. 83, no. 16, pp. 9553–9560, 2018, doi: 10.1021/acs.joc.8b01316.

[11] S. Pordel and J. K. White, “Impact of Mn(I) photoCORM ligand set on photochemical intermediate formation during visible light-activated CO release,” Inorganica Chim. Acta, vol. 500, Jan. 2020, doi: 10.1016/j.ica.2019.119206.

[12] B. Cojocaru, D. Avram, V. Kessler, V. Parvulescu, G. Seisenbaeva, and C. Tiseanu, “Nanoscale insights into doping behavior, particle size and surface effects in trivalent metal doped,” Sci. Rep., vol. 7, no. 1, pp. 4–12, 2017, doi: 10.1038/s41598-017-09026-2.

[13] K. D. B. J.F. Moulder, W.F. Stickle, P.E. Sobol, “Handbook of X-ray electron spectroscopy,” Perkin-Elmer Corporation. p. 192, 1992.

[14] S. González–Morán et al., “Application of birnessite–type solids prepared by sol–gel and oxidation methods in photocatalytic degradation of 4–nitrophenol,” Environ. Technol. (United Kingdom), vol. 0, no. 0, pp. 1–16, 2020, doi: 10.1080/09593330.2020.1791968.

[15] N. Prabu, R. S. A. Saravanan, T. Kesavan, G. Maduraiveeran, and M. Sasidharan, “An efficient palm waste derived hierarchical porous carbon towards electrocatalytic hydrogen evolution reaction,” Carbon N. Y., vol. 152, pp. 188–197, 2019, doi: 10.1016/j.carbon.2019.06.016.

INTRODUCTION

Carbon monoxide (CO), traditionally regarded as a poison due to its toxicological effects, is also produced endogenously in mammalian tissues through heme degradation catalyzed by heme oxygenase. Despite its negative connotations, CO plays crucial roles as a signaling molecule in various physiological processes, including neuronal signaling, regulation of neurotransmitters, and vasorelaxation. Its vasorelaxant and cardiac protective effects underscore its significance in multiple bodily systems, including the immune, respiratory, reproductive, gastrointestinal, kidney, and liver systems[1].

The beneficial properties of CO have been gaining interest in developing therapeutic approaches for conditions such as cancer, cardiovascular diseases, and organ transplant recovery. Advancement in the metallic carbonyl compounds (MCCs) synthesis offers means to modulate metal-CO interactions, enabling precise control over CO release through triggers, such as electromagnetic radiation. Phototherapy, with its non-invasive nature and rapid CO release control, presents a promising path for therapeutic use. Additionally, the strategic development of photo-sensitive metal-based CO-releasing molecules (photoCORMs) that can be activated in the red region of the electromagnetic spectrum, leveraging longer wavelengths for deeper tissue penetration, has considerable potential. The Incorporation of elements like sulfur into these compounds can enhance their electronic properties, contributing to their efficacy in phototherapeutic applications.

The use of nanoparticulate carriers, such as carbon dots (CDs), also presents a promising avenue for enhancing biological compatibility and solubility owing to their large and functionalizable surface areas. CDs, an emerging novel class of carbon-based nanomaterials, offer unique optical, spectroscopic, and electronic properties, along with favorable biocompatibility among a diverse biological organisms. This diversity in applications underscores the potential of CDs in various nanotechnological endeavors, such as catalysts, energy generation, sensing, bioimaging and drug delivery. Their utilization as carriers and activator of photoCORMs has not been reported in the literature. By incorporating CDs into the design of photoCORMs, it may be possible to enhance their performance and functionality, further expanding their applicability in phototherapy and other biomedical applications.

This work is structured into two chapters.

Chapter one deals with the investigation of the chemistry of four synthesized manganese(I) carbonyl compounds and their application as photoCORMs. Compound **1**, which is already reported in the literature, serves as a reference point for comparison with the other three compounds. Compounds **2** and **3** are novel MCCs and will undergo analysis to assess their potential as photoactive carbon monoxide-releasing molecules, while compound **4**, although previously reported, has not been explored for its potential as a photoCORM. The four MCCs studied in this work incorporate a sulfur-containing ligand within their coordination spheres, although with different modes of bonding within the ligand (degrees of freedom and density availability of the sulfur atom) and metal (direct or pendent bond). All MCCs synthesized underwent full characterization using a wide range of analytical techniques to study their chemical properties, such as elemental analysis, infrared spectroscopy, nuclear magnetic resonance, X-ray diffractometry, ultraviolet spectroscopy, cyclic voltammetry, and electron spray ionization couples with mass spectroscopy, and were subjected to theoretical calculations. Furthermore, they were all tested for their photo-release capacities. The influence of these ligands on the photo-release capacity of gaseous CO is a main focus of the investigation.

Chapter two of this thesis is dedicated to the synthesis, characterization, and application of a novel class of carbon dots derived from biomass. A novel, greener, and simpler synthesis route is presented, leveraging cellulose from waste paper in the paper industry, along with basic organic molecules such as urea and L-cysteine, to produce nitrogen and sulfur doped CDs. The synthesized CDs undergo wide-ranging characterization using various analytical techniques including infrared spectroscopy, ultraviolet spectroscopy, X-ray diffractometry powder, X-ray photoelectron spectroscopy, transmission electron microscopy, and high-performance liquid

Furthermore, the potential applications of these N and S doped CDs are explored. Their performance as catalysts for the hydrogen evolution reaction, their efficacy as photocatalysts for the degradation of the 4-nitrophenol pollutant, and their utility as support materials in activating photoactive carbon monoxide-releasing molecules are evaluated, thus contributing to the advancement of sustainable and eco-friendly materials.

FIGURE LIST

TABLE LIST

ABBREVIATIONS AND ACRONYMS LIST

4-NP	4-Nitrophenol
4-AP	4-Aminophenol
ACh	acetylcholine
ACN	acetonitrile
ADHD	Attention-deficit hyperactivity disorder
CEBIME	From Portuguese, Centro de Biologia Molecular Estrutural
CD	Carbon dots
cGMP	Cyclic guanosine monophosphate
CORM	CO Release Molecule
CPCM	Polarizable continuum model
CPMAS	Cross-Polarization Magic Angle Spinning
CPPI	Cross-polarization with polarization inversion
CV	Cyclic voltammetry
DCM	Dichloromethane
DFT	Density functional theory
DDGS	Dried distillers grains soluble
DTG	Derivative thermogravimetry
ECSA	Active surface area
EDA	Energy decomposition analysis
EIS	Electrochemical impedance spectroscopy
ESI-MS	Electrospray ionization mass spectroscopy
ET-CORM	Enzyme Triggered CO Release Molecule
FTIR	Fourier-transform infrared spectroscopy
GABA	4-Aminobutanoic acid
GCE	Glassy carbon electrode
Hb	Hemoglobin
HER	Hydrogen reaction evolution
HO	Heme oxygenase
HOMO	Highest Occupied Molecular Orbital
HPDec	High power proton decoupling
HR-TEM	High resolution transmission electron microscopy
LED	Light emitting diode

LSV	Linear sweep voltammetry
LUMO	Lowest Unoccupied Molecular Orbital
MAPK p38	Mitogen-Activated Protein Kinase p38
MAS	Magical angle spinning
Mb	Myoglobin
MbCO	Carboxy-Myoglobin
MCC	Metal carbonyl compound
MDMA	Methylenedioxy-methamphetamine
MLCT	Metal-to-Ligand Charge Transfer
MO	Molecular Orbital
NMR	Nuclear magnetic resonance
NOCV	Natural orbitals for chemical valence
NP	Nanoparticles
NTO	Natural Transition Orbitals
NIR	Near Infra-Red
ORTEP	Oak Ridge Thermal-Ellipsoid Plot Program
photoCORM	Photodissiciation CO Release Molecule
QCE	Quantum confinement effect l
QD	Quantum dots
RT	Room temperature
PD	Parkinson’s disease
PL	Photoluminescence
QY	Quantum yield
ROS	Reactive oxygen species
SCAI	From spanish “Servicios Centrales de Apoyo a la Investigación”
sGC	Soluble guanylyl cyclase
SMD	Solution Model based on density
STM	Scanning tunneling microscopy
TD-DFT	Time dependent density functional theory
TGA	Thermogravimectric analisys
TGS	Triglycine sulfate
THC	Tetrahydrocannabinol
TMS	Tetramethylsilane
UMA	From spanish “Universidad de Málaga”

UV-Vis	Ultraviolet-Visible spectroscopy
XPS	X-ray photoelectron spectroscopy
XRD	X-ray diffraction

SYMBOL LIST

Å	Angstrom
δ	Chemical displacement (NMR) or angular deformation (FTIR)
φ	Quantum yield
ϕ	Photons flux
ε	Molar absorption coefficient (L mol^{-1} cm^{-1})
λ	Wavelength (nm)
λ_{max}	Analytical Wavelength (nm)
v	Bond stretch (FTIR)
J	Coupling constant
r_{co}	CO release rate

SUMMARY

CHAPTER 1

SULFUR-CONTAINING METAL CARBONYL COMPOUNDS: Potential Therapeutic Applications

1.1 LITERATURE REVIEW

1.1.1 CHEMISTRY INTO LIFE

The understanding that chemistry is present in all aspects of human life took a long time. Starting with the alchemist's curiosity from material transformation to the development of systemic methodology and knowledge organization. From empirical observations to well detailed experimentation and reasoning, chemists came to the need to note and classify all elements and their compounds. Organic matter was not just carbon-based molecules produced by the body and inorganic salts and metals were not just there for tools-making elements.

Not long after, scientists started to realize that every process and all elements were connected in some way and intrinsically related to human life and health. Studies on how to prevent and cure diseases soon became the main interest of researchers as new developments and understanding of chemistry came to light. More and more biology and chemistry compounds and elements were studied, and relationships were established about their mechanism, benefits were discovered and solved.

From the late 19th to the mid-20th century there was a golden age of discoveries and science progresses. The Chemistry studied by Paul Ehrlich brought new ways of thinking, meshing biology, medical and chemistry all together with his work on dyes and the malaria treatment [2]. Erlich along with Bertheim synthesized the first organometallic with medicinal use, Arsphenamine also known as Salvarsan, **Figure 1a**, with better results than the organic medicines used at the time. Salvarsan was difficult to store, manage and deliver, which led to chemistry studies on its structure to improve their physicochemical properties without losing its medical potential. Then came Neosalvarsan, **Figure 1b**, with some modification at the imine part with sulfate salt, improving their solubility and stability [3].

Figure 1. Chemical structure of a) Salvarsan and b) Neosalvarsan.

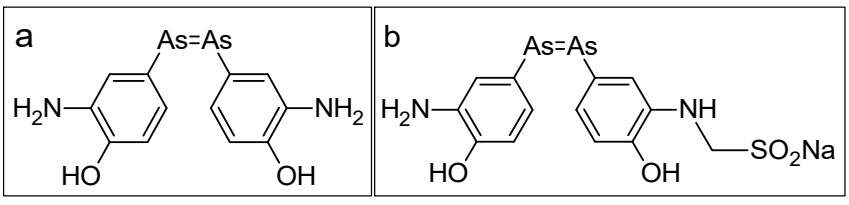

The success of Neosalvarsan settled bioinorganic as a scientific field, mixing metals, organic compounds and biology. The thought that chemical elements could improve human life, treat and prevent illness illuminate a path towards future development in the field which would come to be called bioinorganic, paving the way for future scientists to develop new compounds and methodologies to discover their structures and functionalities.

For example, Barnett Rosenberg, when working on the effects of magnetic field on bacterial cells, observed that bacterial cells were unable to grow in numbers [4]. Later, Rosenberg realized that he accidentally created Peyrone's salt, diamminedichloroplatinum(II), while applying the electrical field with platinum electrodes under an ammonium solution [5]. Further studies showed that *cis*-diamminedichloroplatinum(II), cisplatin, **Figure 2**, prevented cell growths and when tested against diseases, showed a virtually 100% reduction in cancer rats cells [6]. The great effectiveness of cisplatin against cancerous diseases led to a revolution in the chemotherapy pharmaceutical industry, thus concretizing studies of coordination compounds in modern medicinal chemistry [7].

Figure 2. Chemical structure of *cis*-diamminedichloroplatinum(II), Cisplatin.

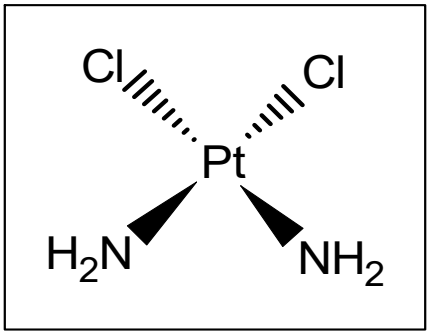

Simultaneously, technological advancements and improved methods across all areas of studies provided new insights and discoveries in human physiological and biological functionality. For instance, chemist James B. Summer set a method for crystallizing enzymes and making it possible to visualize their structures, leading to the understanding that all enzymes are proteins [8]. Having that knowledge made it possible for chemist Dorothy Hodgkin to apply X-Rays to study protein and enzymatic crystal's structure. Being the pioneer of the protein crystallography elucidation, Hodgkin was able to solve the vitamin B_{12} structure, **Figure 3**, one of the most complex and important compound present in the human body [9]. At that time, it was

believed that all human-related compounds were organics but when Hodgkin unveils proteins and vitamins structures, it became clear that proteins were also an inorganic compound constituted of coordination compounds of porphyrin derivative ring with cobalt at its center. Setting unprecedent knowledge that the human body is not only made up of carbon-based organic compounds but also has several inorganic structures with important roles for humans' health and functionalities.

Figure 3. Chemical structure vitamin B_{12}.

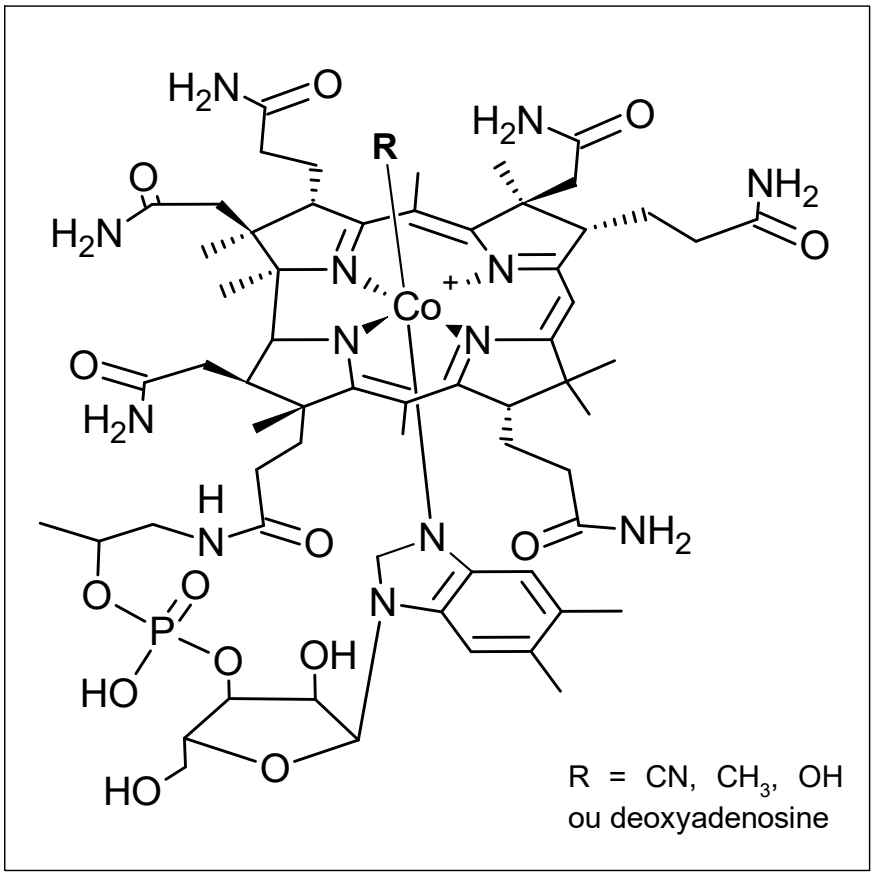

Vitamin B_{12} is one essential vitamin for humans, being part of several mechanisms such as the DNA production and assists the red blood cells maturation. Blood has long been known to be the carrier and sustainable of life, but its parts were only decomposed in the mid-20th century. Max Perutz, also using X-ray, was able to describe the hemoglobin (Hb) structure [10]. Hemoglobin was already well known and its ability to carry oxygen throughout the body was discovered by Hunefel, a century before Perutz solved the hemoglobin complex structure. Within the Hb protein, there were hemes, **Figure 4**, which has a simpler porphyrin derivative than Vitamin B_{12} and with iron in its center.

Figure 4. Chemical structure heme group of hemoglobin.

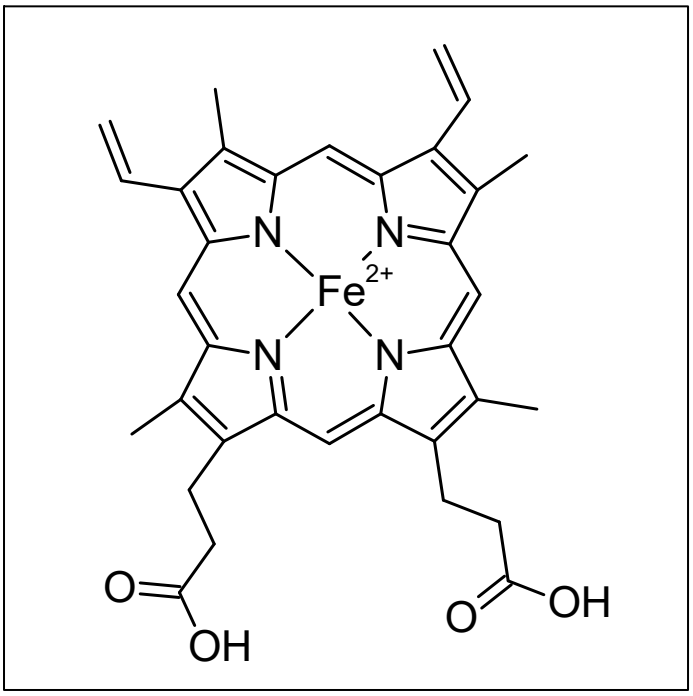

1.1.2 SIGNALING AGENTS

As knowledge about the composition of biological structures grew, scientists could focus on their functions. Understanding these processes could explain the development of certain diseases. Therefore, understanding how the different components from an organism communicate , from a single ion/compound to protein and cells, prevents or even cures an organism facing an upcoming illness or diseases[11].

The human body is a delicate and complex machine. Any change in temperature, pH, ionic concentrations or even atmospheric pressure can cause a different biological pathway, since these alterations within the organism make cell communication to occur and the machine to flow. All components work together to have the needed task to occur towards an intended response [12].

One the two most common methods of cell signaling is electric, where cell membrane potential shifts transferring ions in and out of the cell. Aforementioned communication happens when rapid responses are needed, such as muscular contraction and synapses. The second method is the most used throughout the organisms, that is chemical signaling. This process involves the exchange of small chemical compounds released in the media to be used locally or carried around to be

used elsewhere in the organism. Being directly responsible for actions such, ionic exchanges, metabolism, cell growth and genetic expressions [13].

Proteins, such as hormones, are complex signaling chemical agents that can carry information, navigating through hundreds of channels and veins within the body to pass information from one cell to another. Smaller chemical compounds, such as vitamins, organic and inorganic compounds, are also able to pass information to surrounding cells and within the cell membrane [14].

Neurotransmitters are one of the most important classes of cells signaling, due to their regulatory functions in the human body [15]. Neurotransmitters act on the brain and can modulate human functions including human humor, sleep, sex drive, appetite, growth and defenses responses. There are more than 180 known molecules that are subdivided into categories such as: amino acids, biogenic amines and gasotransmitters [16].

Among the amino acids, there is the gamma-aminobutyric acid (GABA), **Figure 5a**, a neurotransmitter mainly known for reducing neuronal activity. Thus, being responsible for controlling anxiety, stress level and flee or flight instinct. The dysregulation of GABA in the organism is associated with anxiety disorders, autism, schizophrenia and depression [17]. Drugs like benzodiazepines **Figure 5b**, and zolpidem **Figure 5c**, are compounds able to regulate and increase GABA reception, used on treatment of illness by the dysregulation of such amino acids. Reports also indicate ethanol acting as an agonist of GABA [18].

Figure 5. Chemical structures of a) GABA, b) benzodiazepines class and c) Zolpidem.

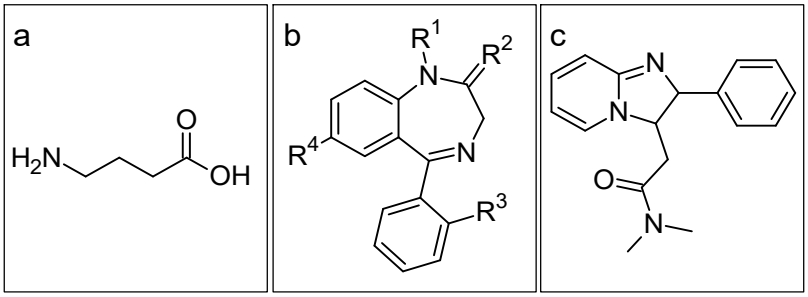

Serotonin, **Figure 6a**, and dopamine are the most popular examples of biogenic amines. Several functions are related to serotonin, such as sleep cycles, anxiety,

humor, appetite and motor development [19]. Popularly known as the happiness molecule, thus being linked to the depression illness. Drugs like 3,4-Methyl-enedioxy-methamphetamine (MDMA), **Figure 6b**, can act as agonist in post-traumatic stress disorder and Ondansetron, **Figure 6c**, to control nausea in patients undergoing chemotherapy, acting as an antagonist of serotonin. Dopamine, **Figure 6d**, is commonly known as the desire molecule, responsible for regulation of human's motivations, cognitive functions and pleasure [20]. Dopamine dysregulation is related to Parkinson's diseases (PD), addictive behaviors, and attention-deficit hyperactivity disorder (ADHD). Pramipexole, **Figure 6e**, is an agonist of dopamine and the drug is used to treat PD but has side effects by inducing addictive behaviors such as gambling and hypersexuality. Methylphenidate, **Figure 6f**, is another drug that prevents the reuptake of dopamine used as treatment of persons with ADHD.

Figure 6. Chemical structures of a) Serotonin, b) MDMA, c) Ondansetron, d) Dopamine, e) Pramipexole and f) Methylphenidate.

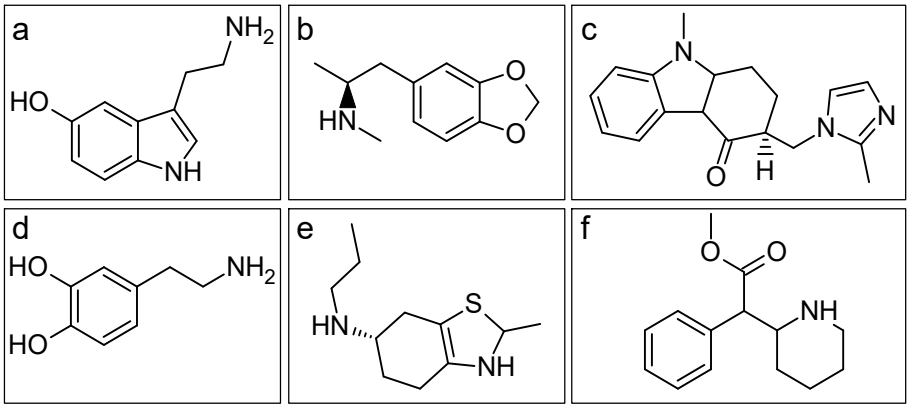

Within the realm of peptide neurotransmitters, anandamide, a fatty acid from the omega-6 family, **Figure 7a**, is noteworthy. The human body synthesizes this peptide in heightened quantities during physical exercise, and its presence is associated with an amelioration of mood and overall well-being. Molecules, including tetrahydrocannabinol (THC), **Figure 7b**, exert agonistic effects, leading to heightened appetite and inducing sedative and anesthetic sensations. The pharmaceutical agent rimonabant, **Figure 7c**, functions as an antagonist to anandamide and has been utilized in weight loss treatments. However, the commercial distribution of this drug was suspended due to its psychoactive side effects, which were implicated in the onset or exacerbation of severe depression and schizophrenia [21].

Figure 7. Chemical structures of a) Anandamide, b) THC and c) Rimonabant.

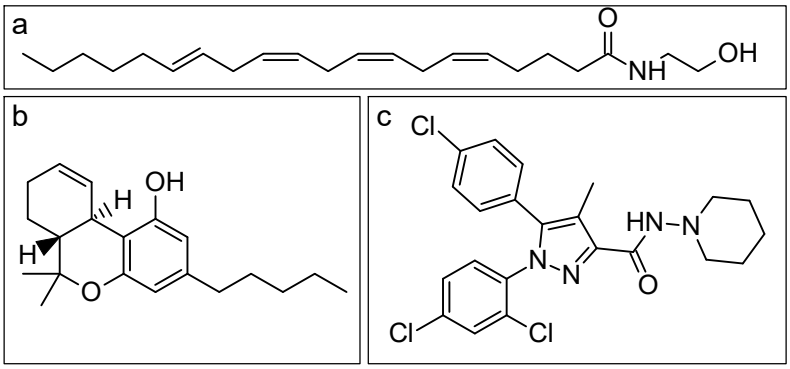

Acetylcholine (ACh), **Figure 8a**, the first neurochemical identified, assumes a pivotal role as the principal neurotransmitter implicated in processes of learning and storage of memory. Within the biological environment, this molecule also orchestrates vital functions for muscle contraction, equilibrium, and perception of wakefulness. Deficiencies in ACh production have been correlated with memory impairments characteristic of Alzheimer's disease. Certain chemical entities can modulate the activity of the same nerve terminals associated with ACh. Nicotine, **Figure 8b**, for instance, functions as an agonist for ACh, potentiating the effects of this neurotransmitter and thereby amplifying its influence. Conversely, botulinum toxin, **Figure 8c**, colloquially recognized as Botox, manifests antagonistic effects on ACh. This protein inhibits muscle contraction and impedes the synthesis of acetylcholine itself. [22].

Figure 8. Chemical structures of a) ACh, b) Nicotine and c) Botox.

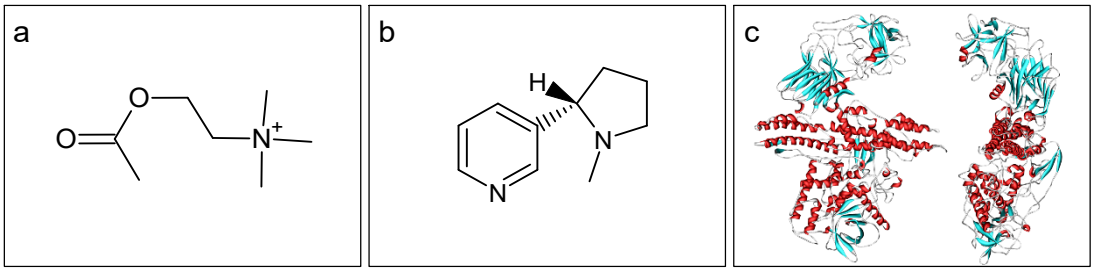

Gasotransmitters, due to their diminutive and uncomplicated molecular structures, readily diffuse throughout the body, swiftly engaging in biological processes and instigate prompt action and reaction responses highlight a pivotal role in physiological processes and their potential applications in therapeutic interventions. Nitric oxide (NO), hydrogen sulfide (H_2S), and carbon monoxide (CO) constitute prominent members within this class [23].

For instance, hydrogen sulfide is endogenously produced by selected cells in the body through the metabolic degradation of the amino acid cysteine, **Figure 9a**. Its active involvement in the memory formation process underscores its significance in cognitive functions. Notably, H_2S serves as a protective agent for cardiovascular tissue and is currently undergoing testing for potential applications in treatments involving suspended animation [24], [25].

Nitric oxide, classified as a free radical, plays a diverse role in various biological processes. Produced endogenously by the nitric oxide synthase enzyme family, NO catalyzes the oxidation process of the guanidine group of the amino acid L-arginine, **Figure 9b**. NO actively participates in muscle relaxation processes, vasodilation functions, and immunological responses [26].

Carbon monoxide, another gasotransmitter, functions as a biological signaling mediator and is produced endogenously. Recent discoveries have identified its therapeutic potential for neural and vascular systems due to its protective effects, akin to heme oxygenase-1 (HO-1), **Figure 9c**. [27].

Figure 9. Chemical structures of a) L-Cysteine, b) L-arginine and c) HO-1.

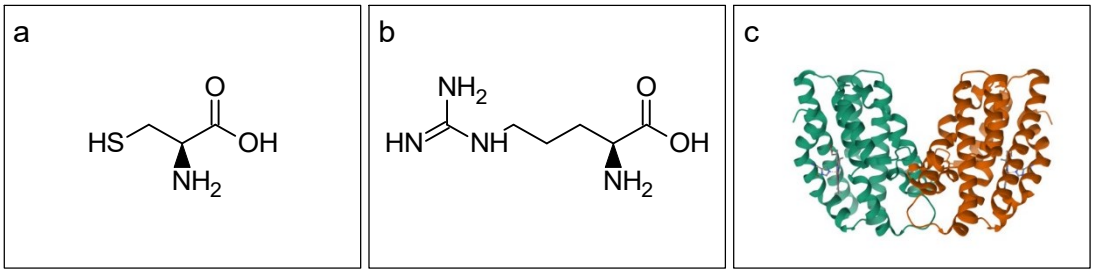

Source: HO-1 structure from https://www.rcsb.org/structure/1twn.

1.1.3 CARBON MONOXIDE

Annually, there are documented cases of accidental deaths attributed to carbon monoxide poisoning, a consequence of its odorless and colorless nature. Prolonged exposure to elevated concentrations of CO can lead to suffocation, emphasizing the toxic nature of carbon monoxide to humans. The absence of distinctive sensory cues makes CO poisoning particularly insidious, underscoring the importance of awareness and proper safety measures [28].

The toxicity of CO arises from its competitive binding with oxygen in hemoglobin. It exhibits a 200-fold higher affinity for hemoglobin compared to oxygen [29]. By binding with hemoglobin, CO prevents the binding of oxygen to the iron present in the protein and, as a result, oxygen cannot be transferred to all the body parts. This disruption leads to insufficient oxygenation, resulting in death.

However, with the discovery of endogenous production in the mid-20th century, researchers have begun to perceive carbon monoxide in a more nuanced light, recognizing its physiological roles beyond its toxic effects.

In 1949, researcher Torgni Sjöstrand conducted an innovative study on the endogenous production of carbon monoxide, revealing that organisms themselves can produce significant amounts, reaching up to 20 µmol *per* hour [30], [31]. Subsequently, Ajay Verma and collaborators elucidated the mechanism behind CO production, **Figure 10**, attributing it to the enzymatic degradation of the Heme group [32]. The enzyme HO-1 facilitates reduction of the HEME group, resulting in the cleavage of the meso bond of the porphyrin ring. This enzymatic process generates a carbon monoxide molecule, the Fe^{3+} ion, and biliverdin. The discovery of endogenous CO production in low quantities prompted extensive research into the potential functions and applications of carbon monoxide within the organism [33], [34].

Figure 10. Endogenous CO production by enzymatic oxidation.

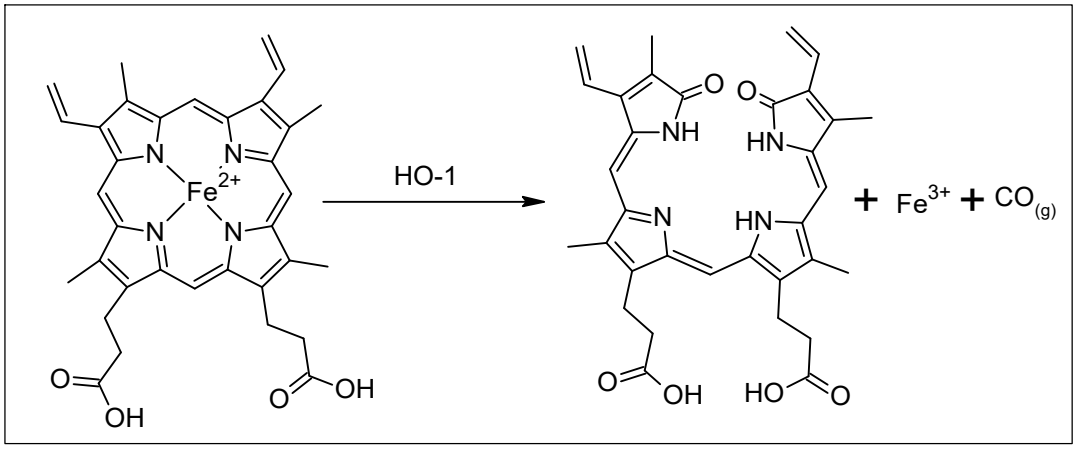

Research on the biological functions of carbon monoxide yielded significant results, **Figure 11**. Carbon monoxide associates axially with the soluble guanylyl cyclase (sGC) protein fraction containing the Heme group, forming a pentadentate organometallic compound with a central metallic Fe^{2+}. Upon establishment of this

bond, the protein is activated, initiating the production of cyclic guanosine monophosphate (cGMP). Cyclic guanosine monophosphate serves as a crucial molecule in regulating ion channels, glycogenolysis processes, and cell apoptosis. The identification of these intricate molecular interactions highlights the multifaceted roles of carbon monoxide in orchestrating various physiological functions within the organism [35].

Figure 11. Simplified CO biological pathway and effects.

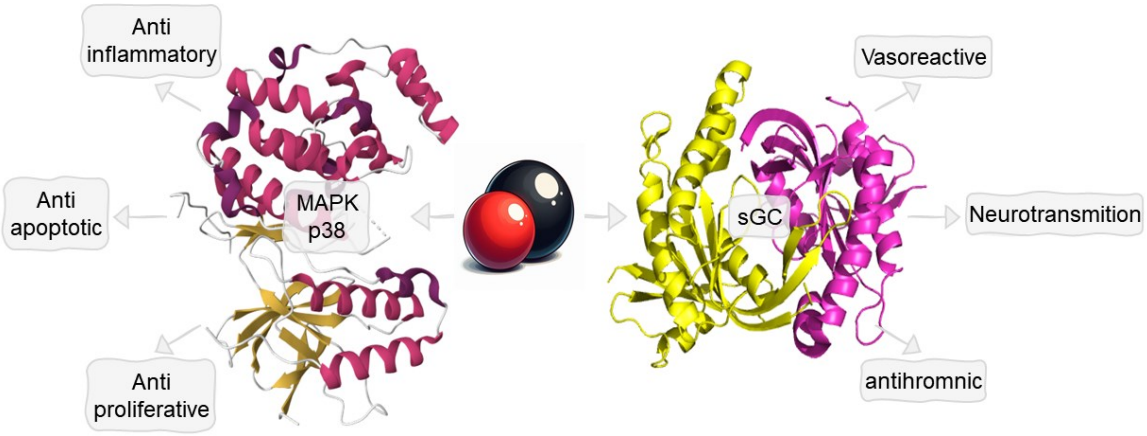

Carbon monoxide also plays a crucial role in the functioning processes of other hemoproteins, such as those within the cytochrome P450 family. This family is responsible for hormone production and in the inhibition of hydroxyeicosatetraenoic acid [36], a compound implicated in blood vessel constriction [37]. Interestingly, the activation of both soluble sGC and the cytochrome P450 family was conventionally associated with nitric oxide. However, CO presents distinct advantages, being more readily available and cost-effective [38].

The MAPK p38 (Mitogen-Activated Protein Kinase p38) was also found to respond to CO. Such organelle acts in response to diverse extracellular stimuli, such as pro-inflammatory cytokines, environmental stresses, and growth factors. Thus, when suppressed by gaseous CO, it promotes an attenuated anti-inflammatory response, enhanced cell survival under stress conditions, and modulates cell proliferation and differentiation [39], [40].

In the brain, CO, generated by enzyme HO-1, contributes to the production of cortisol, a hormone governing the circadian cycle and stress levels [32]. Furthermore, CO has been linked to neurodegenerative diseases such as Alzheimer's and

Parkinson's, showcasing protective actions on neuronal tissues [27]. At concentrations of up to 500 ppm, CO can stimulate the production of cytokines, molecules essential for the anti-inflammatory response [41]. Additionally, it aids in cell protection against apoptosis thereby reducing the likelihood of organ rejection in transplant cases. However, at higher concentrations, CO may induce apoptosis, making it a potential agent for combatting tumor or unhealthy cells [42].

The elucidation of these functions of CO has opened a vast array of possibilities for pharmacological applications, challenging the traditional perception of carbon monoxide as a lethal substance. Due to its participation in various biological functions, carbon monoxide is now being considered for pharmaceutical purposes. Some advantages are that CO can be employed in quantities up to 1000 ppm, compared to the limited 65 ppm for NO. Moreover, CO is more stable and reacts selectively with transition metals in low oxidation states, such as iron(II) [43]. These distinctive features enhance the therapeutic potential of carbon monoxide in comparison to other signaling molecules.

1.1.4 CO MOLECULE RELEASE

In the early stages of clinical trials involving CO gas, the primary method employed was inhalation. Patients would wear a mask, inhaling a mixture of oxygen and carbon monoxide to elevate blood concentrations of CO, thereby producing the desired therapeutic functions, typically anti-inflammatory and anti-apoptotic effects [44]. However, this method lacks precision in controlling the specific locations in the body where CO will exert its actions, posing the risk of unintended high doses that may lead to side effects such as dizziness, nausea, and shortness of breath [45]. Recognizing these limitations, the need emerged to develop a more targeted and controlled delivery method for carbon monoxide.

Motterlini and coworkers [46] were among the pioneering research groups that addressed this challenge. They synthesized and investigated the therapeutic capabilities of carbon monoxide-releasing molecules (CORMs), introducing the term and a novel approach to CO delivery. The advent of CORMs provided a more sophisticated means of administering CO, allowing for greater precision in targeting specific tissues or organs, thus minimizing the risk of adverse effects associated with systemic inhalation. This breakthrough marked a significant advance in the field of

carbon monoxide-based therapy, fostering safer and more effective clinical applications. Thus, to be considered suitable for future pharmacological applications, CORMs need to meet some requirements, such as having good solubility in water, biological compatibility and stability, rapid CO releasing and efficient degradation and excretion by the body after the CO release.

The CORM class does not have to be exclusively an organometallic compound; certain purely organic classes also exhibit CO-releasing properties. Notable examples include silanecarboxylic acids, boranecarboxylates, and cyclopropenones, **Figure 12**. Among silanecarboxylates, $MePh_2SiCO_2H$, **Figure 12a**, serves as an illustrative instance, releasing CO at elevated temperatures, in organic solvents, and under the influence of strong bases like BuO^- and F^-. However, it demonstrates a low CO release rate in water, liberating only 0.4 mol of the CO gas in 20 hours [47].

Figure 12. Examples of organic CORMs.

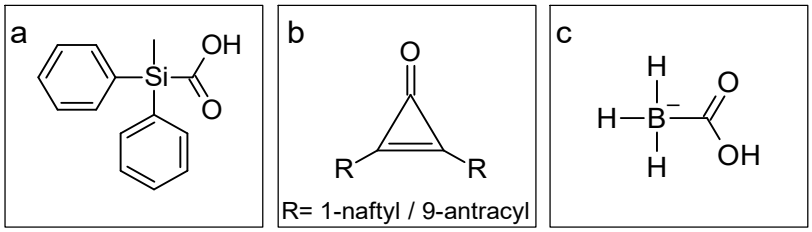

In the cyclopropenones class, compounds such as deltic acid, **Figure 12b**, and its derivatives release CO upon ring cleavage through photoexcitation in the ultraviolet region. Similar to silanecarboxylates, its solubility is favorable only in organic solvents [48]. The boranecarboxylates class exhibits promising biological affinity due to structural similarity to amino acids. An example is $Na_2[H_3BCO_2H]$, **Figure 12c**, known as CORM-A1, releasing CO in biological environments with trigger control through pH adjustments [49]. However, this class faces limitations in pharmacological applications due to the challenge of incorporating side groups for property enhancement.

Organometallic compounds, offering solutions to the issues encountered by organic CORMs, are attracting interest as carriers of CO. With a metallic center, they can interact simultaneously with diverse molecules, binding not only to CO but also to biocompatible organic compounds within their coordination sphere. The use of inorganic CORMs facilitates strategic planning of the bond strength between metal and ligands using organic compounds. The metal→carbonyl bond, of particular interest,

can be labilized to chemically modify organic ligands, enabling the enhancement and modulation of physicochemical characteristics. By introducing ligands with bioactive properties, tailored CORMs can be designed to exert action under specific biological conditions and locations, adjusting solubility in different media, modulating CO release triggers, and controlling the flow of CO for utilization.

The components constituting CORMs exhibit intricate interactions influencing their physicochemical characteristics. Thus, a comprehensive understanding of ligand-metal center interactions is crucial, particularly for comprehending electronic effects within the chemical microenvironment of the coordination sphere. This understanding is crucial for elucidating changes in the bond of interest, the M→CO, before delving into the discussion of coordination compounds releasing carbon monoxide.

Carbon monoxide exhibits a molecular electronic distribution of $1\sigma^2 2\sigma^2 1\pi^4 3\sigma^2 2\pi^* 4\sigma^{2*}$ with HOMO $3\sigma^2$ and LUMO, $2\pi^*$, **Figure 13**. Notably, carbon significantly contributes to the formation of frontier orbitals, showcasing its role as a proficient σ-donor ligand for HOMO and a π-acceptor for LUMO. The symmetry and energy equivalence of CO's molecular orbitals with the metal's *d* orbitals enable the establishment of a characteristic interaction termed backbonding. This interaction results in a robust M→CO interaction, elucidating the coordination of CO to metals with low oxidation states and the formation of stable coordination compounds. The characteristics of backbonding render these organometallic compounds ideal for precise planning to act in specific ways, given the synergistic nature of the metal→carbonyl bond [50].

By examining the CO molecular orbital diagram, it can be inferred that metals with higher positive local charge densities lower the energy of orbitals participating in backbonding. This weakens the M→CO interaction, facilitating the CO release upon a specific trigger. Modulating electron density and bond strength through electron-donor or electron-acceptor ligands allows the fine-tuning of CORMs for CO release in predetermined environments, providing control over CO release triggers. Coordination spheres can be strategically designed for M→CO bond dissociation using various strategies, such as pH changes, oxidation of the metal center, interactions with enzymes, ligand exchange for solvation, and photodissociation [51]. This precision

allows this class of drugs to serve as precise carriers for controlled CO release and targeted activation.

Figure 13. Molecular orbital for carbon monoxide.

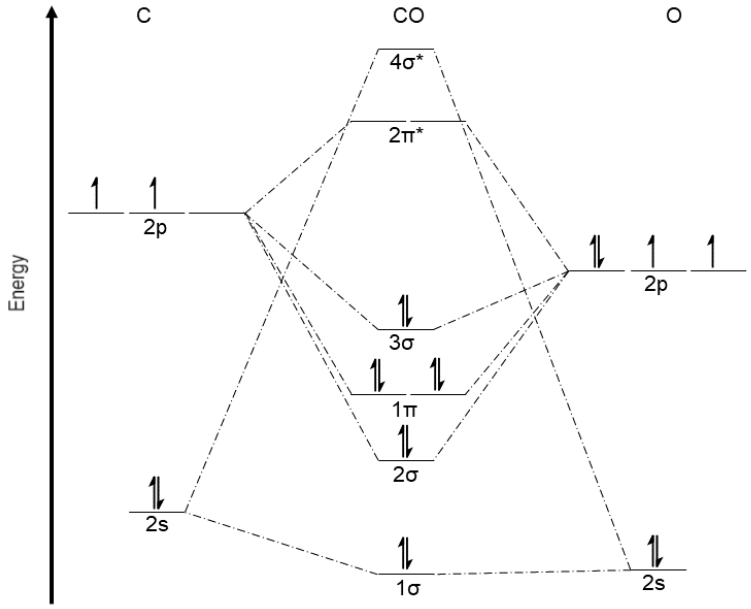

Source: Adapted from Amorim, A. L,2020[52].

Among the extensively studied CORMs, tricarbonylchloroglycinatoruthenium(II), known as CORM-3, stands out. Its structure, **Figure 14**, known and emulated in subsequent CORMs, comprises a ligand with biological activity (Glycine), a carbonyl moiety for dissociation (containing three CO molecules), and an electro-donor ligand (chlorine) to facilitate CO release. Given the myriad possibilities for combining organic compounds with the coordination sphere, numerous CORMs can be designed to function in diverse media, particularly blood media.

Figure 14. Chemical structure of CORM-3.

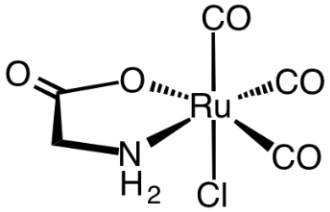

For effective utilization of CO-carrying compounds as drugs, they must circulate through the biological environment without degradation and, upon reaching the desired

tissue, undergo activation by a specific trigger. The secondary products resulting from the post-release of CO should exhibit low toxicity or be non-toxic. Therefore, the design of a CO-releasing molecule necessitates a comprehensive understanding of the mechanisms leading to CO release.

Common triggers for CO release from the coordination sphere include oxidation of the metal center and enzymatic processes, both culminating in complex decomposition. Additionally, kinetic processes involving dissociation and association, induced by changes in temperature or pH, lead to the exchange of carbonyl for a solvent molecule. Photodissociation processes, energetically driven by light, promote electron destabilization of the metal→carbonyl bond.

The early synthesized CORMs followed the dissociative/associative method, halting the CO release. In the dissociative process, exemplified by Hewison et al. [53] with $[Fe(CO)_3Br(S_2CNEt_2)]$, whereas CO is removed , creating a vacancy in the coordination sphere that facilitates solvent coordination, **Figure 15a**. In the associative process, a new ligand enters in the coordination sphere, forming a compound with seven ligands. During the rearrangement in the coordination sphere, one CO molecule is removed, restoring the octahedral geometry, **Figure 15b**.

Figure 15. Representative CO release scheme for a) dissociative and b) associative processes.

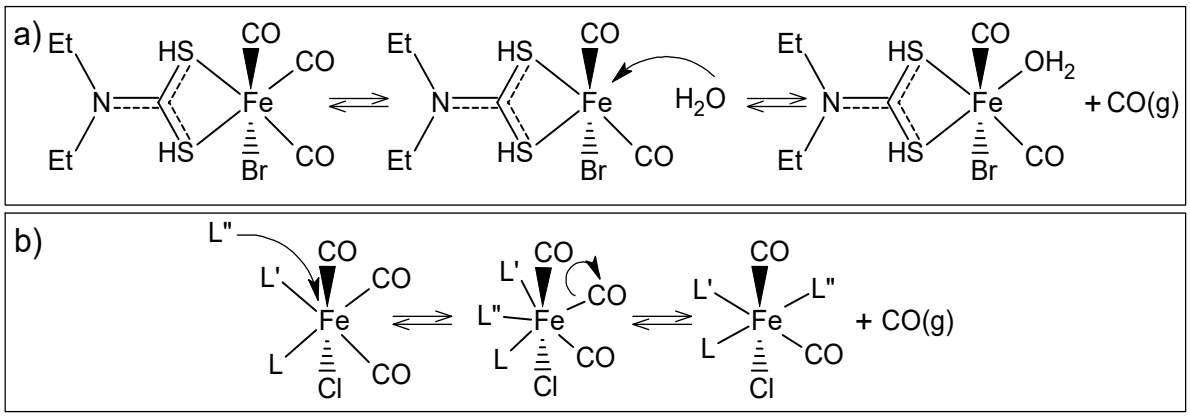

Source: Adapted from Hewison et al. [53].

In a dissociative process initiated by a thermal stimulus, the bond between the metal and carbon monoxide is broken with increasing temperature, favoring both enthalpy and entropy. Thermal dissociation is applicable to purely carbonyl compounds like $Fe(CO)_5$, $Mo(CO)_6$ and $Mn(CO)_5Cl$. However, using heat as a trigger for CO

release presents challenges in biological applications due to difficulties in administration [54].

Carbon monoxide release processes with associative and dissociative triggers impose challenges in control, often being spontaneous reactions that lack significant interest for pharmacological applications. Thus, there is a critical need for the development of new triggers and CORMs that response to other chemical changes, exemplified by CORM $[Et_4N]_2[ReBr_4(CO)_2]$, synthesized by Zobi et al. [55], **Figure 16**. In aqueous solution, this compound undergoes a redox process triggered by the ligand exchange with water molecules, resulting in the oxidation of the metallic center. At around pH= 6, all bonds are broken, leading to the release of CO and the formation of the ReO_4^- ion with bromide as reducing agent.

Figure 16. Representative scheme for oxidation process.

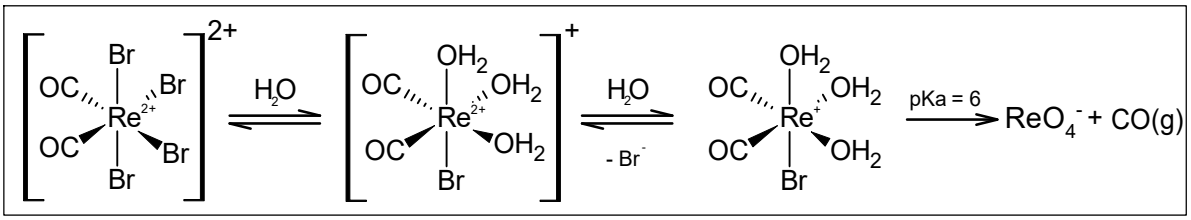

Source: Adapted from Zobi et al [55].

Researchers, including Romanski et al. [56], have synthesized compounds with specific ligands designed to interact and activate the release of CO by enzymes, creating a new class of compounds known as enzyme-triggered CO-releasing molecules, ET-CORMs. An example is the organometallic compound acyloxydiene-$Fe(CO)_3$, which interacts exclusively with the esterase enzyme class. The esterase hydrolyzes the ester function of the acyloxydiene ligand, leading to the oxidation of the compound and the subsequent release of three CO molecules, **Figure 17**. A limitation of using ET-CORMs is their applicability to a limited number of enzymes.

Figure 17. Representative scheme for enzyme assisted CO release process.

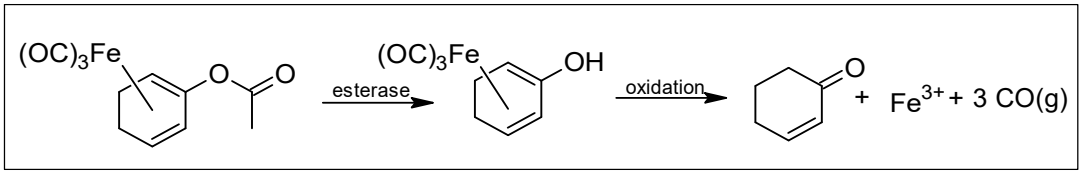

Source: Adapted from Romanski et al. [56].

PhotoCORMs represent another class for delivering carbon monoxide molecules, releasing CO upon excitation by electromagnetic radiation. The use of light as an activation method allows the use of portable equipment, facilitating easy handling and precise control of the application site. Additionally, the intensity of the electromagnetic excitation can be adjusted, enhancing the attractiveness of synthesizing compounds of this class for pharmaceutical applications [57].

1.1.5 METAL CARBONYL COMPOUNDS

The existence of a therapeutic window, discussed in the Bonnet's work [58] underscores the importance of moving towards the red and infrared regions for better penetration of electromagnetic radiation into human tissues, emphasizing the need for strategic planning in the photoCORM development. While initial photoCORMs like $Mn_2(CO)_{10}$ (CORM-1), **Figure 18a**, and $Ru_2Cl_4(CO)_6$ (CORM-2), **Figure 18b**, were activated by light, their activation under white light, poor solubility in water and other limitations led to their dismissal as potential drugs. Hence, structural planning and consideration of physicochemical characteristics become paramount in the designing of effective photoCORMs.

Figure 18. Chemical structure for a) CORM-1 and b) CORM-2.

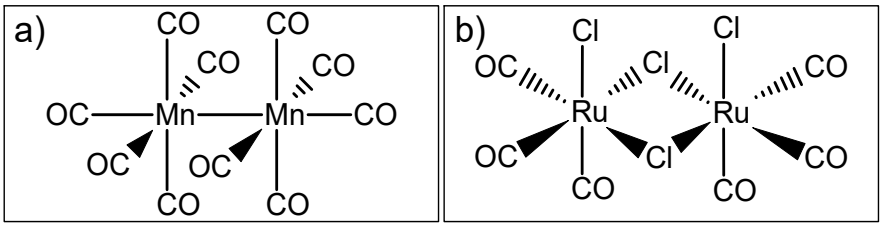

Subsequent attempts to synthesize photoCORMs faced challenges such as low solubility in aqueous solutions and activation at low wavelengths, resulting in limited skin penetration and low quantum yield for medicinal performance. Researchers like Chakraborty et al. [59] highlighted the charge transitions between the metal and the ligand in the CO photorelease process, elucidating the synergistic interaction between the metal center and ligands in photodissociation. Addressing these challenges, research groups explored the use of nanoparticles as supports, enhancing the electromagnetic radiation absorption in the NIR region. For instance, Pierri et al. [60] used gadolinium nanoparticles doped with ytterbium and thulium to activate photoCORMs. Another approach involved He et al. [61], who utilized nanostructured

sheets of graphene oxide to trap and activate photoCORMs using infrared radiation via up-conversion of electrons.

Romão's research group [51] proposed a model for photoCORMs, **Figure 19**, enabling control of the excitation range and physicochemical characteristics without relying on support materials. The model comprises a coordination sphere with octahedral geometry, in which at least one coordination point is occupied by a carbon monoxide molecule. The remaining points are filled by the organic ligand, determining physicochemical characteristics, modulating biological interactions and contributing to the electronic stability in the excited state for the photodissociation of CO.

The selection of organic ligands plays a crucial role in the design of effective photoCORMs, prioritizing the strength of the M→CO bond, influencing the CO release rate and considering the thermodynamics of the organometallic compound. Chelate ligands are frequently encountered in the literature, with tridentate ligands like tri(1H-imidazol-1-yl)methane, **Figure 19a**, and bidentate ligands such as phenanthroline, **Figure 19b**.

Additionally, monodentate ligands like alanine and imidazole, **Figure 19d-e** respectively, can enhance biological interactions, and the latter also contributes to the conjugation effect. Ligands such as bromine and adamantane derivatives induce delocalization of the electron cloud, acting as electron donors, **Figure 19f-g** respectively. Given the myriad possible combinations for forming a coordination compound, intelligent design, particularly in planning the ligand interaction with the metal center, becomes of fundamental importance for the compound's effectiveness as a drug.

The choice of metallic center is equally important in an effective photoCORM design, as it serves as an agent connecting and transporting pharmacological compounds throughout the biological system. The chosen metal should have an affinity to the biological environment and must be non-toxic to the body. Metals already present in regulatory functions of enzymes, proteins, and organelles are commonly used, highlighting iron, manganese, molybdenum, and chromium in terms of biological importance. Metals like ruthenium and rhenium, while lacking biological functions,

demonstrate good affinity with the environment due to their similarities to biologically relevant metals.

Figure 19. Proposed a model for photoCORMs by Ramão et al. and ligands examples.

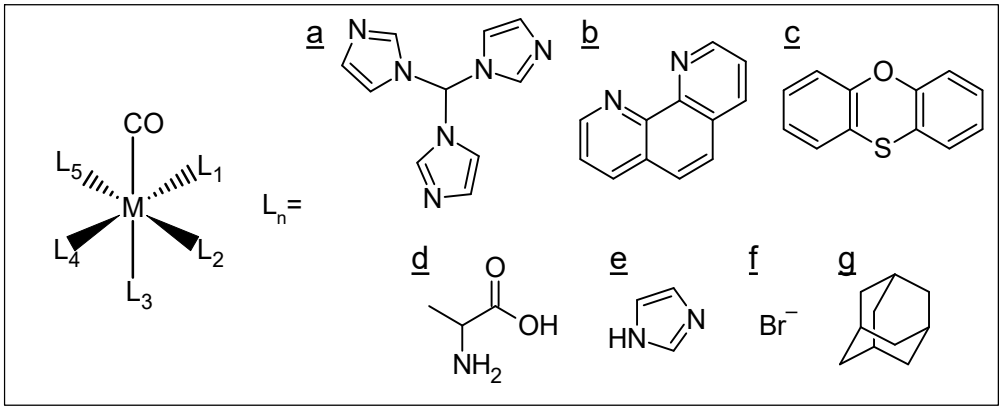

PhotoCORMs incorporating molybdenum and chromium, despite their limited regulatory functions in the human biological system, possess fluorescent capabilities, exemplified by compounds like [$Mo(C_2H_5NO_2)(CO)_5$], **Figure 20a**, [62] and the compound [$Cr(CO)_5$(=CPh(OMe))], **Figure 20b** [63].Their rapid absorption by the body, coupled with the ability to monitor their movements using fluorescent markers, allows activation only upon reaching specific desirable locations. However, it's important to note that these metals can be relatively more toxic than iron and manganese.

Figure 20. Different metals photoCORMs examples, whereas a) [$Mo(C_2H_5NO_2)(CO)_5$], b) [$Cr(CO)_5$(=CPh(Ome))]; c)[$(SBPy_3)Fe(CO)]^{2+}$; d)CORM-S1; e) [$Re(CO)_3(NC)Br$; and f) [$MnBr(CO)_3$(MIAN)].

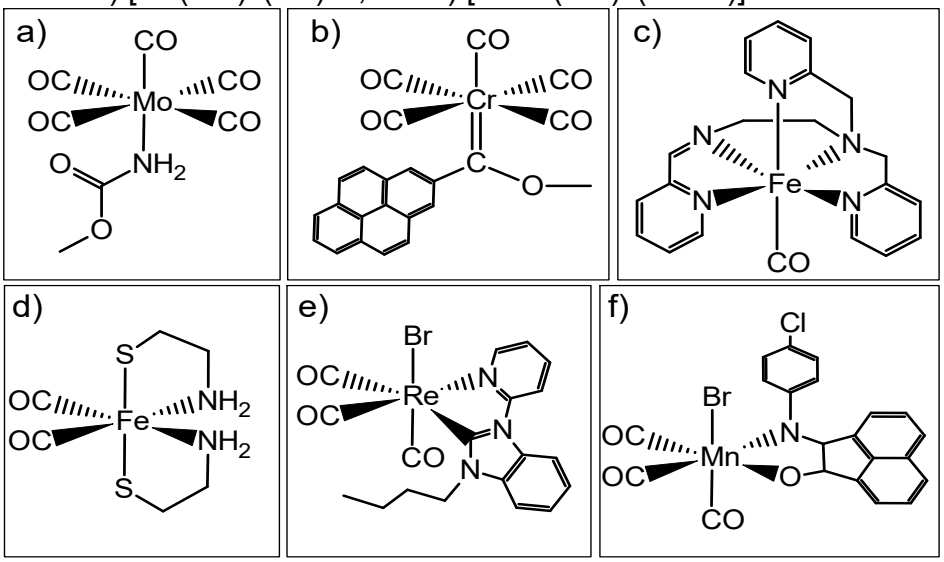

Ruthenium-based photoactive carbonyl compounds, exemplified by CORM-3, **Figure 14**, are extensively studied due to their similarity to iron, enabling their participation in biological processes and offering greater stability in the excited state compared to their iron analogues [64]. Although iron-based CORMs are an obvious choice due to the prevalence of the Fe→CO bond in hemoglobin, organometallic iron compounds are prone to oxidation, leading to their decomposition. To address this challenge, the selection of organic ligands becomes crucial to stabilize iron photoCORMs, enhancing their resistance to the oxygen-rich environment in the body. Examples include $[(SBPy_3)Fe(CO)]^{2+}$, **Figure 20c**, [65] and CORM-S1 , **Figure 20d** [66].

PhotoCORMs featuring a rhenium(I) metal center pose challenges for photoactivation due to their d^6 electronic configuration. This electronic distribution strengthens the Re→CO bond, requiring higher energy and shorter wavelengths, limiting their therapeutic window and hindering CO dissociation, diminishing their potential as drugs. An example of a photoCORM with rhenium is the compound $[Re(CO)_3(N\text{^}C)Br]$, **Figure 20e**, [67]. Manganese, which is actively participating in human enzyme function, is commonly utilized to produce photoCORMs. An example is the compound $[MnBr(CO)_3(MIAN)]$, where the MIAN ligand is 2-[(4-chlorophenyl)imino]acenaphthylen-1-one, **Figure 20f**, known for its rapid CO release [68].

Beyond planning metal-ligand bonding, excited state interactions must be taken into account during dissociation by electromagnetic radiation. Using Molecular Orbital theory for a coordination compound like $Mn(CO)_6$, **Figure 21**, the promotion of electrons from Highest Occupied Molecular Orbital (t_{2g}) to Lowest Unoccupied Molecular Orbital (e_g^*) orbitals weakens the interaction by backbonding, leading to CO lability [50]. The photodissociation process, in this case, is associated with Metal-to-Ligand Charge Transfer (MLCT) [69].

Ligands with a high degree of conjugation enhance the stability of the compound in excited states for effective electronic shifting. The conjugated π bonds in these ligands shift the wavelength to Near-Infrared (NIR) regions, favoring applications in phototherapy. For this purpose, ligands with conjugated rings are usually used, such as those derived from the MIAN ligand [68].

Figure 21. Simplified molecular orbital for $[Mn(CO)_6]$.

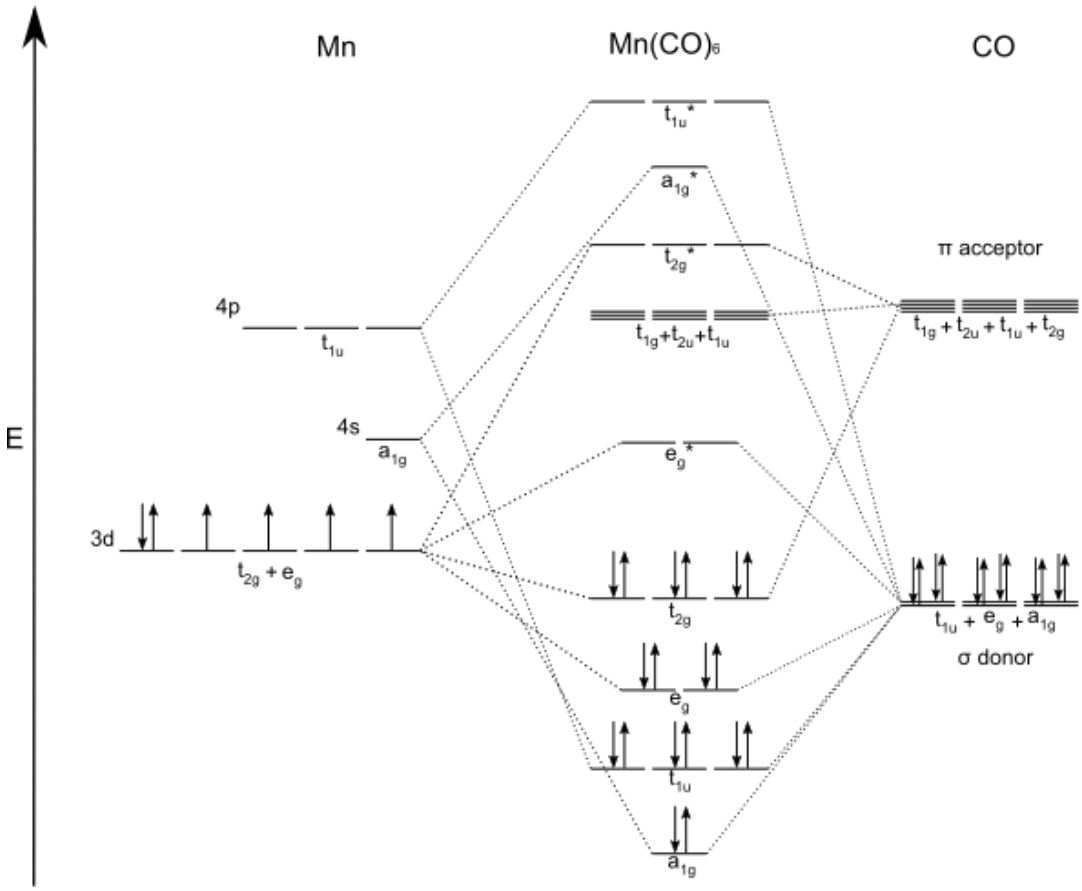

1.1.5.1 Manganese(I) PhotoCORMs

Manganese holds a ubiquitous presence in every human cell and contributes to essential processes such as energy generation, synthesis of DNA and RNA, and the functionality of more than 300 human enzymes. Its vital role extends to plants, where it actively participates in photosynthesis, a fundamental process in plant nutrition. Given its universal occurrence in plant and animal cells, its inclusion in the human diet, its association with photochemical processes, its abundance, and its relative cost-effectiveness compared to other metal centers used in pharmaceuticals, manganese emerges as a compelling choice for compounds with pharmacological activity.

Among various photoCORMs with different metal centers and oxidation states, those containing manganese stand out. The d^6 electronic configuration and the atomic radius of Mn(I) enable the formation of stable bonds with bidentate or tridentate chelating ligands, preserving its photoactive capacity [65]. The stability of these bonds allows structural modifications in the organic part of manganese(I) coordination

compounds, influencing the properties of CO photodissociation without causing structural damage. This characteristic enhances their resilience in solutions. Employing rigid ligands with conjugation effects and electron-donating characteristics generates a synergistic molecular effect, altering the absorbance range and making the compound more amenable for use in photodynamic therapy [68].

Research conducted by Mascharak and collaborators [59] on manganese(I) compounds with conjugated ligands revealed a bathochromic shift compared to similar compounds with low conjugation, **Figure 22a-c**. Berends et al. [70] explored the effects of ligands with varying electron density, both donating and withdrawing, on the capacity to photorelease carbonyl groups. Their findings concluded that electron-withdrawing ligands decrease the electron density of the metal center, weakening the Mn→CO bond and requiring less energy for CO release, while electron-donating ligands exhibit the opposite effect, **Figure 22d**. Amorim et al. [69] synthesized Mn(I) photoCORMs with ligands containing chalcogen atoms such as sulfur and selenium, both in conjugated and aliphatic forms, releasing CO at wavelengths close to 380 nm, **Figure 22e**.

Figure 22. Different manganese photoCORMs examples.

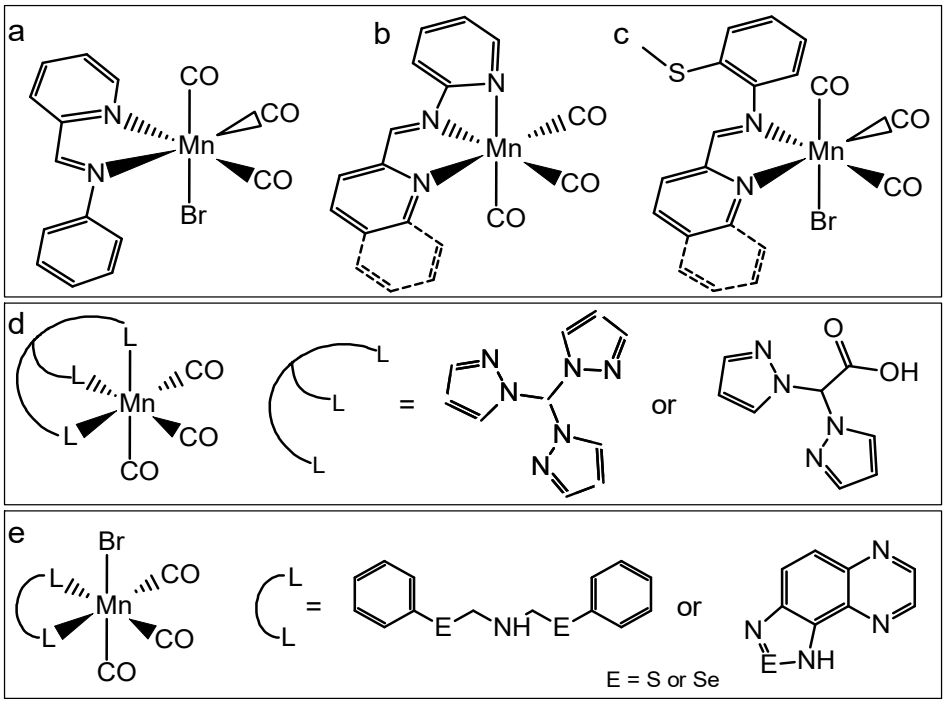

Kurz's research group [70] proposed studies on the photoactivation and labilization of manganese(I) compounds with local C_{3v} symmetry, indicating a three-stage process for the photodissociation of carbon monoxide, **Figure 23**.

Figure 23. CO release mechanism proposed by Kurz et al [70].

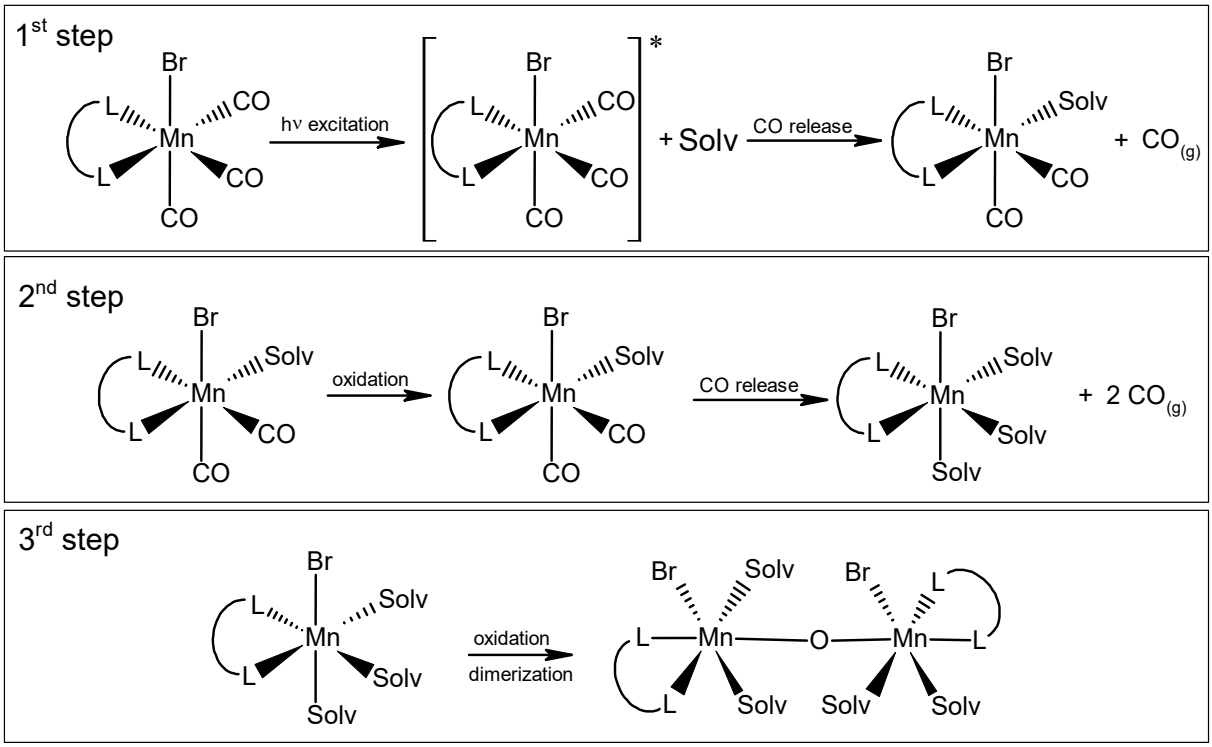

The first stage involves electromagnetic excitation followed by the rapid release of CO and the creation of a vacancy in the coordination sphere, quickly occupied by a solvent molecule. In the second stage, the slow oxidation of the metal center from Mn(I) to Mn(II) and the release of the two remaining CO molecules. The third stage includes further oxidation of the metal center and the formation of a dimer linked by a μ-oxide bridge.

1.2 AIMS AND OBJECTIVES

1.2.1 AIMS

The comprehensive objectives of Chapter 1 of this thesis investigation are divided into two distinct but interrelated parts. In this first part the aims are to synthesize and systematically characterize Mn(I) mononuclear organometallic compounds and conduct a comprehensive evaluation of their physicochemical characteristics. Special attention is directed towards an in-depth analysis of how their ligands intricately

influence their chemical behavior. Additionally, the exploration extends to probing the potential application of these compounds as photoCORMs, providing insights into their viability for advanced functionalities.

1.2.2 OBJECTIVES

- Synthesis and characterization of four ligands containing sulfur in their structure;
- Synthesis of four distinct Mn(I) and study their physicochemical properties through spectroscopic, electrochemical;
- Analyze how different ligands can affect metal carbonyl compounds Photorelease properties.

1.3 METHODOLOGY AND EXPERIMENTAL DATA

1.3.1 MATERIALS AND REAGENTS

All reagents were purchased from commercial sources and used without prior purification. The solvents used in the synthesis of the coordination compounds were dried before their use, using 4 Å molecular sieves.

Solvents: Dichloromethane, Ethanol 97%, Ethyl acetate, Ethyl ether, Hexane, Methanol and Tetrahydrofuran.

Reagents: 2-(aminomethyl)pyridine, 2-chloroethylmethylsulfide, 2-formylthiophene, 2-methylpyridylamine, 2-methylthioaniline, 2-pyridinecarboxyaldehyde, bromopentacarbonylmanganese(I), ferrocene, iodomethane, molecular sieves 4Å, *o*-aminothiophenol, palladium 10% on carbon, potassium bromide, sodium borohydride, sodium hydroxide, sodium sulphate and sulfuric acid (95-98%).

1.3.2 INSTRUMENTATION AND METHODS

The analyses were carried out on equipments located in the Laboratório de Bioinorgânica e Cristalografia (LABINC) and in the Central de Análises, both belonging to the Departamento de Química da Universidade Federal de Santa Catarina, unless otherwise stated.

All analysis from the photosensitive compounds were carried out under inert atmosphere and dim light conditions. All glassware was protected from light wrapped on aluminum foil or thick dark paper.

1.3.2.1 Elemental analysis (CHN)

Elemental analysis was performed on a CHNS/O Analyser equipment, PerkinElmer brand, model 2400 series II using helium carrier gas.

1.3.2.2 Infrared spectroscopy (FTIR)

The spectra in the infrared region were obtained on a Perkin Elmer spectrophotometer, in the 4000 to 450 cm^{-1} regions. Before placing the samples in the equipment, an air (blank) spectrum was taken to correct for noise in the background. The solid samples were analyzed using the Total Attenuated Reflectance accessory, with a ZnSe crystal (45°) and a triglycine sulfate detector, Triglycine sulfate (TGS). For solubilized samples, in acetonitrile or dichloromethane, a drop of sample was added into mortar and macerated together with the KBr salt support until dried, then placed under pressures of to generate the analysis pellet.

1.3.2.3 Nuclear magnetic resonance (NMR)

1.3.2.3.1 Solution

The preliminary ^{1}H NMR and ^{13}C NMR spectra of the ligands were obtained on a Bruker - AC 200 spectrophotometer at 200 MHz and the spectra of the carbonyl coordination compounds were carried out on Varian Mercury Plus AS equipment at 400 MHz, with the tubes protected from light. The chemical shift (δ) of hydrogen recorded in ppm were obtained using tetramethylsilane (TMS) as an internal reference (δ = 0.00 ppm) and the analyses were carried out in deuterated solvents. For the MCCs NMR spectra were acquired and elucidated by Prof. Dr. Juan Manuel Lázaro-Martínez, using a Bruker Avance-III HD spectrometer equipped with a 14.1 T narrow bore magnet (600 MHz), located at Departamento de Ciências Químicas from Universidad de Buenos Aires.

1.3.2.3.2 Solid State

Solid-state NMR data were acquired with a spectrometer equipped with a 14.1 T narrow bore magnet operating at Larmor frequencies of 600.09 MHz and 150.91 MHz for ^{1}H and ^{13}C, respectively, located at Servicios Centrales de Apoyo a la Investigación (SCAI) from Universidad de Málaga (UMA). Powdered samples were packed into 3.2 mm ZrO_2 rotors and rotated at room temperature at different magic angle spinning (MAS) rates (8-15 kHz). Glycine was used as an external reference for the ^{13}C spectra and to set the Hartmann−Hahn matching condition in the cross-polarization experiments in ^{13}C spectra [71]. The recycling time was set at five seconds with a contact time during CP of two milliseconds for ^{13}C spectra. The SPINAL64 sequence (small phase incremental alternation with 64 steps) [72] was used for heteronuclear decoupling during acquisition. The ^{13}C natural abundance direct polarization experiments with proton decoupling (SPINAL64) during acquisition were conducted for the different solid samples at different MAS rates (8-12 kHz), using an excitation pulse of 4.0 seconds and a recycling time of 10 seconds were used. ^{13}C spectral editing with the pulse sequence for cross-polarization with polarization inversion (CPPI) was used for ^{13}C resonance signal assignments [73].

1.3.2.4 X-ray diffraction (XRD)

1.3.2.4.1 Crystal XRD

The single crystals obtained from the organometallic compounds were analyzed by single-crystal X-ray diffraction. The data was collected on a Bruker APEX II DUO diffractometer using radiation generated by a molybdenum tube (MoKα = 0.71073 Å) and a graphite monochromator, at a temperature of 190.01 K. The crystal structures were solved using direct methods and partially refined by the least squares method with a complete matrix, using the programs SIR97 and SHELXL 97 [74], respectively. Both the collection structures were carried out by Prof. Dr. Adailton João Bortoluzzi.

1.3.2.4.2 Powder XRD

Powder XRD measurements were performed using a PANalytical X'Pert PRO equipped with a Ge(111) monochromator using CuKα1 monochromatic radiation or a

PANalytical Empyrean with CuKα1,2 radiation between 2θ=10-100º with a step of 0.01º, both located at SCAI at the Universidad de Málaga.

1.3.2.5 Ultraviolet-visible spectroscopy (UV-VIS)

The electronic spectra in the UV-Vis region were obtained on a Varian Cary 50 BIO UV-vis spectrophotometer, Varian Cary 50 BIO. The samples were dissolved in spectroscopic solvents in a concentration of 1 x 10^{-3} mol L^{-1} and diluted if necessary. Analyses were conducted in quartz cuvettes with a capacity of 1.0 mL and an optical path of 1.0 cm at 25 °C.

1.3.2.6 Cyclic voltammetry (CV)

The redox behavior of the complexes was investigated by cyclic voltammetry in a BAS potentiostat-galvanostat (Bioanalytical Systems, Inc.) model Epsilon. The solutions were made in spectroscopic solvents at concentrations of 1 x 10^{-3} mol L^{-1} and under an inert atmosphere. A suitable electrolyte with a concentration of 0.1 mol L^{-1} was used. The electrodes used in the electrochemical cell were a glassy carbon electrode (working electrode), a platinum wire (auxiliary electrode) and an Ag/AgCl or platinum electrode (reference electrode). The potential correction was made with the ferrocene/ferrocinium pair as an internal reference [75]

1.3.2.7 Electrospray ionization mass spectrometry (ESI-MS)

Samples of the ligands and complexes were dissolved in spectroscopic grade acetonitrile to obtain a solution with a concentration of approximately 500 ppb and a solvent flow rate of 180 µL min^{-1}. The temperature of the capillary was kept between 180 and 200°C and the voltage between -400 and -500 V. The electrospray ionization mass spectrometry (ESI-MS) analyses was carried out in an Amazon-Ions Trap MS equipment, at the Centro de Biologia Molecular Estrutural (LABIME) at UFSC. The simulated spectra were calculated using the mMass software [76].

1.3.2.8 Solution stability

The stability of the organometallic compounds obtained were monitored over time, observing the changes in the charge transfer bands, using the material and equipment mentioned in section 1.3.2.5 coupled to a Visomes Plus thermostatic bath

at 25 °C. In order to standardize the results, the spectra were collected every 30 min for 24 h at a scan rate of 6000 nm min^{-1}.

1.3.2.9 CO releasing kinetic studies

To analyze the rate at which the CO molecule is released from the coordination sphere of the organometallic, dilute solutions of the compounds were prepared to avoid precipitation of by-products and setting the absorbance of the MLCT between 0.15 and 0.20, in order to observe intraligand bands. All the analyses were carried out in tri or quadruplicates. The irradiation system was created and developed by the LABINC research group itself (**Figure 24**).

The irradiation system consists of two modules: a support for the LED plate and the cuvettes, fixed at a distance of 3.5 cm between them, with irradiation perpendicular to the cuvette. The LEDs were arranged in series with four rows of four LEDs with the desired wavelength, **Figure 24**. LEDs are controlled by an Arduino UNO R3 board in the second module. At the start of irradiation, a button attached to the box is pressed and the exposure time is controlled by the Arduino module and a timer on a display shows the remaining time of exposure.

Figure 24: Irradiation chamber used at CO release assays.

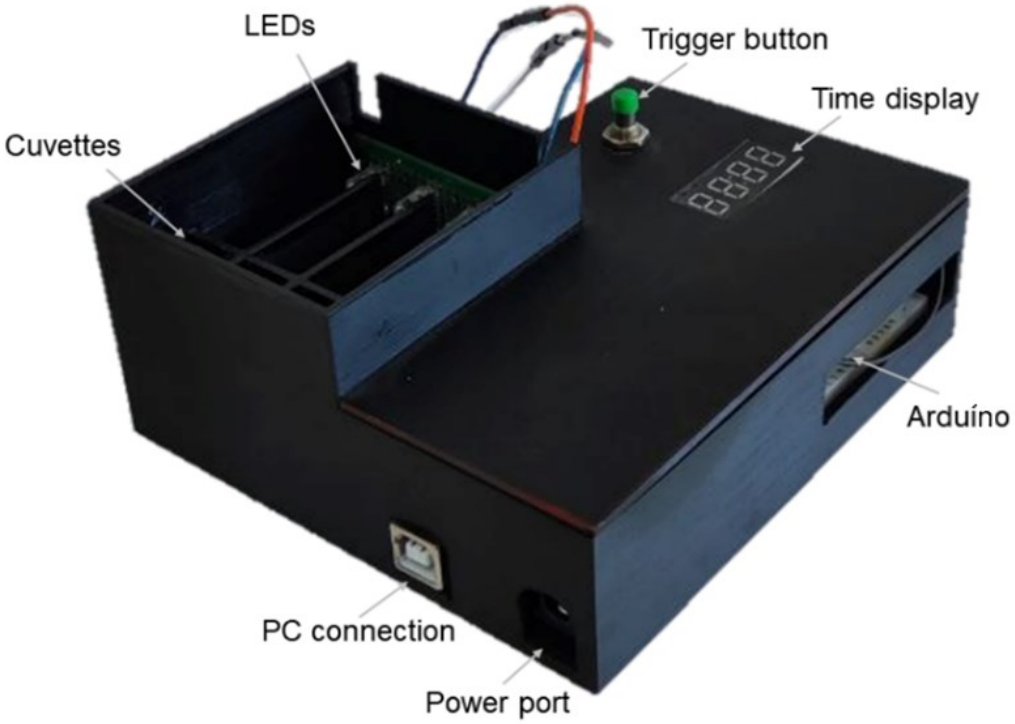

The absorbance of the band in question was normalized by **Equation 1**, in which A_t is the absorbance at the time analyzed, A_i is the absorbance before exposure to light irradiation and A_∞ is the absorbance at the time of zero decay, when there is no further decrease in the band.

$$A = \frac{(A_t - A_i)}{(A_i - A_\infty)} \qquad \textbf{(Eq 1)}$$

To calculate the CO release rate, the decomposition rate of the compounds is calculated using **Equation 2**, in which A_1 and A_0 are correction parameters. With the information on t_1, **Equation 3** can then be used to obtain the CO release rate (k_{CO}) of the compounds per second of exposure.

$$A = A_1 - e^{\left(-\frac{t}{A_1}\right)} + A_o \qquad \textbf{(Eq 2)}$$

$$k_{CO} = -\left(\frac{1}{t_1}\right) \qquad \textbf{(Eq 3)}$$

1.3.2.10 Actinometry and quantum yield

To determine the quantum yield (**φ**), it is first necessary to know the photon flux (**Φ**) released by the source through actinometry. The methodology proposed by Bischof et. al., with some modifications [77], was used and three stock solutions denoted as A, B and C were prepared.

For solution A, in a 50 mL volumetric flask, where 147.5 mg of potassium tris(oxalate)ferrate(III) trihydrate was dissolved in 40 mL of deionized water, 5 mL of 0.05 mol L^{-1} sulfuric acid and, finally, deionized water is added until the volume is complete.

Solution B consists of 50 mg of anhydrous 1,10-phenanthroline (phen) dissolved in 50 mL of deionized water. Finally, for solution C, 3.4 g of sodium acetate trihydrate was dissolved in 25 mL of deionized water. From this solution a 15 mL aliquot is taken and 9 mL of 0.5 mol L^{-1} sulfuric acid was added, thus completing until obtaining 25 mL with deionized water.

For the analysis of **φ**, two equal solutions were prepared, one used as a control, not to irradiated, and the other to irradiate. The irradiated solution contains 3 mL of solution A in a quartz cuvette with a 1 cm optical path and a total volume of 3 mL. The sample was irradiated with the same irradiation module described in section 1.3.2.9 used in the CO photorelease tests. Then, 1 mL of the irradiated solution was transferred to a 10 mL volumetric flask and 1 mL of solution B and 0.5 mL of solution C are added and the remaining volume topped up with deionized water. The solution is then left to rest for two hours in the absence of light. The absorption spectra is measured at 510 nm, corresponding to the formation of the complex ion $[Fe(phen)_3]^{2+}$ with **ε** =11,100 L mol^{-1} cm^{-1} [78].

The concentration of the iron(II) compound was calculated using the Lambert-Beer equation, **Equation 4**. The same procedure was carried out for the control solution without the irradiation part. This process was repeated five more times with different irradiation times.

$$\varepsilon = c * l * A \qquad \textbf{(Eq 4)}$$

Equation 5 was used to calculate the number of moles (n) of the Fe^{2+} ion formed, in which V_1 is the volume of the irradiated ferrioxalate solution, V_2 is the volume of the aliquot for the determination of the Fe^{2+} ion and V_3 is the total volume after reaction with phenanthroline. ΔA_{510} is the difference between the absorbance of the irradiated solution and the control solution, "l" is the optical comminution of the cuvette and ε_{510} is the absorption coefficient of the complex ion $[Fe(phen)3]^{2+}$.

$$n = \frac{V_1 * V_3 * \Delta A_{510}}{10^3 * l * V_2 * \varepsilon_{510}} \qquad \textbf{(Eq 5)}$$

To calculate the amount of carbon dioxide released, we used the chemical equations that occurred in the photoinduction process and used the stoichiometric ratios, as shown in **Equations 6** and **7**.

$$[Fe(C_2O_4)_n]^{3-2n} + hv \rightarrow Fe^{2+} + (n-1)(C_2O_4)^{2-} + (C_2O_4)^{-} \qquad \textbf{(Eq 6)}$$

$$[Fe(C_2O_4)_n]^{3-2n} + hv \rightarrow Fe^{2+} + (n-1)(C_2O_4)^{2-} + (C_2O_4)^{-} + 2CO_2 \qquad \textbf{(Eq 7)}$$

The flux of photons passing through the cuvette was quantified using **Equation 8**. Where we have the relationship between the number of moles of the ion Fe^{2+} (n) with the irradiation time (t) and the quantum yield **φ** [79].

$$\phi = \frac{n}{t} * \varphi \qquad \textbf{(Eq 8)}$$

1.3.2.11 Myoglobin assay

As a complementary way of detecting the carbon monoxide released and quantifying the CO equivalents released during photoinduction, the interaction test between the released carbon monoxide and myoglobin (Mb) was carried out. The test used is similar to that used in the literature for deoxymyoglobin (deoxy-Mb) [80], [81]. By monitoring the change in Q band absorbance from Mb spectra, CO absorption by MB can be determined by UV-Vis spectroscopic analysis. For this study, it was decided to use a concentration of myoglobin in the cuvette at least three times greater than the concentration of the complexes, in order to provide an equal amount of myoglobin for each CO potentially released per complex.

A stock solution of myoglobin with a concentration of 1.80 x 10^{-4} mol L^{-1} (9.22 mg, 3 mL) was prepared by dissolving the protein in a 0.1 mol L^{-1} solution of phosphate-buffered saline (PBS) (pH 7.4). The organometallic compounds were dissolved in DCM, resulting in concentrations of 3 x 10^{-3} mol L^{-1}. Measurements were carried out by diluting the MCC solution in a myoglobin solution and adding an excess of sodium dithionite to the oxidized myoglobin, converting the myoglobin into deoxy-Mb. The final concentrations in the cuvette were calculated so that the concentration of carbonyl compound was approximately three times lower than the concentration of myoglobin. The cuvettes were tightly sealed with a Teflon cap to assure that all CO released came from the MCC and prevented them to escape quickly from moiety. The samples were irradiated in the same way as the CO release test previously reported in section 1.3.2.9. To detect the influence of sodium dithionite on the carbon monoxide release, the samples were also analyzed without light incidence.

The amount of CO released was measured spectrophotometrically using the absorbance of the Q band referred to the carboxy-Myoglobin (MbCO) species at 540 nm using **Equation 9** [77], in which C_0 is the initial concentration of myoglobin, l the

optical path, A_0 the absorption at time zero and ε_{540} the coefficient of absorption coefficient of myoglobin at 540 nm, from the literature ε_{540} = 15,400 L mol^{-1} cm^{-1} [82].

$$c(MbCO) = \frac{\left(\frac{A_t}{l} - \frac{A_0}{l}\right)}{\varepsilon_{540} - \left(\frac{A_t}{c_0 * l}\right)} \qquad \textbf{(Eq 9)}$$

1.3.4 SYNTHESIS

1.3.4.1 Ligands

1.3.4.1.1 2-pyridyl-N-(2'-methylthiophenyl)-methyleneimine (L1)

The first step is the methylation of *o*-aminothiophenol and was obtained through the method already described in the literature [83]. A solution containing *o*-aminothiophenol (20 mmol) was stirred in 50 mL of methanol, and then 15 mL of an aqueous solution of NaOH (24 mmol) was slowly added. The mixture was stirred at room temperature (rt) for 10 min and then iodomethane (MeI) (24 mmol) was added, and the solution stirred for 3 h. After time, the solvent was removed at low pressure to then 20 mL of CH_2Cl_2 and 20 mL of deionized water were then added for a liquid extraction (3 x 30 mL CH_2Cl_2). The organic phases were combined, dried with Na_2SO_4 and filtered. The remaining solvent was removed by evaporation under reduced pressure, resulting in a purple liquid, used for the next step without prior purification.

Figure 25. Synthetic route for L1.

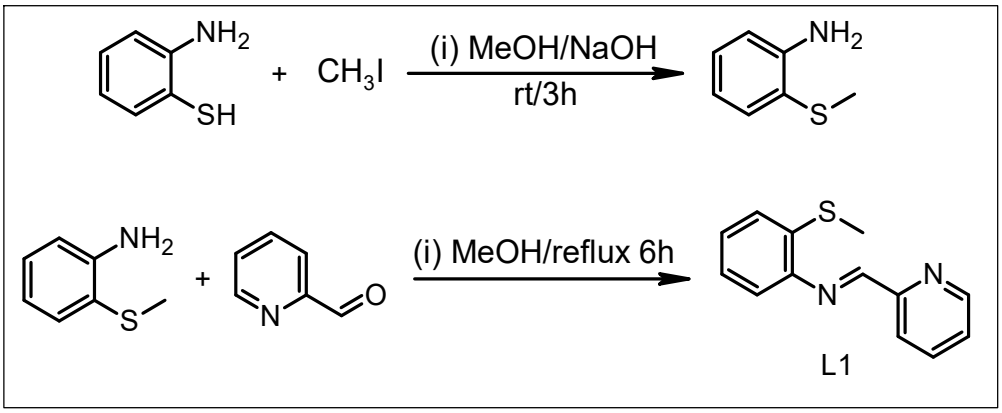

The imine (L1) was obtained using the method described in the literature [84], **Figure 25**. A methanolic solution (5 mL) of 2-pyridinecarboxyaldehyde (10 mmol) was added to a methanolic solution (10 mL) containing the 2-methylthioaniline (10 mmol)

and stirred at room temperature for 5 h. Afterwards, the solvent was removed, resulting in a yellow oil which was dissolved in CH_2Cl_2 and washed three times with 30 mL of H_2O. The organic phase is dried with Na_2SO_4, and the solvent is removed. The resulting oil was kept in the freezer overnight, resulting in a yellow solid, which was recrystallized from ethyl ether, obtaining yellow crystals that were washed with ice-cold ethyl ether. Yield: 88 %. **Figures 26** and **27**, show the NMR spectra of the purified compound that was indeed obtained.

Figure 26. ^{1}H NMR ($CDCl_3$, 200 MHz) δ (ppm), spectra of L1: δ 2.46 (s, 3H); 7.08-7.24 (m, 4H); 7.41 (dd, *J*= 5.2 and 6.2 Hz, 1H); 7.86 (dd, *J*= 7.6 and 7.7 Hz, 1H); 8.34 (d, *J*= 7.7 Hz, 1H); 8.64 (s, 1H) and 8.70 (d, *J*= 3.2 Hz, 1H,).

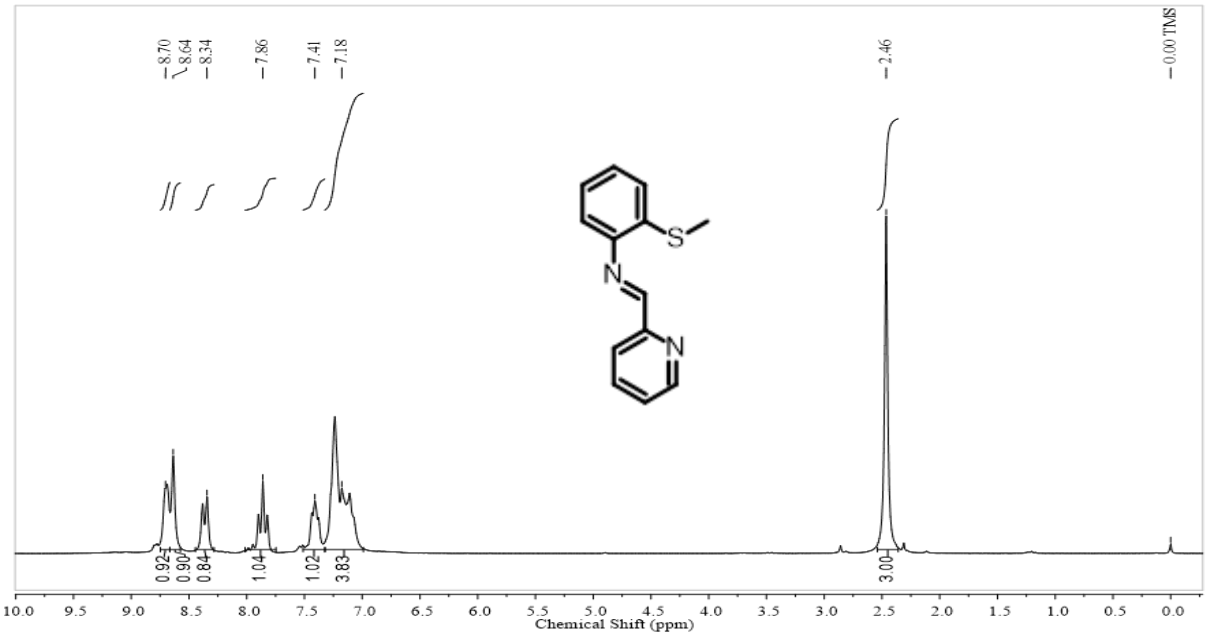

Figure 27. ^{13}C NMR ($CDCl_3$, 50 MHz) δ (ppm), spectra of L1: δ 14.9; 117.5; 122.2; 124.8; 125.5; 127.5; 135.0; 137.4; 147.7; 148.9; 150.3; 154.3; 159.2.

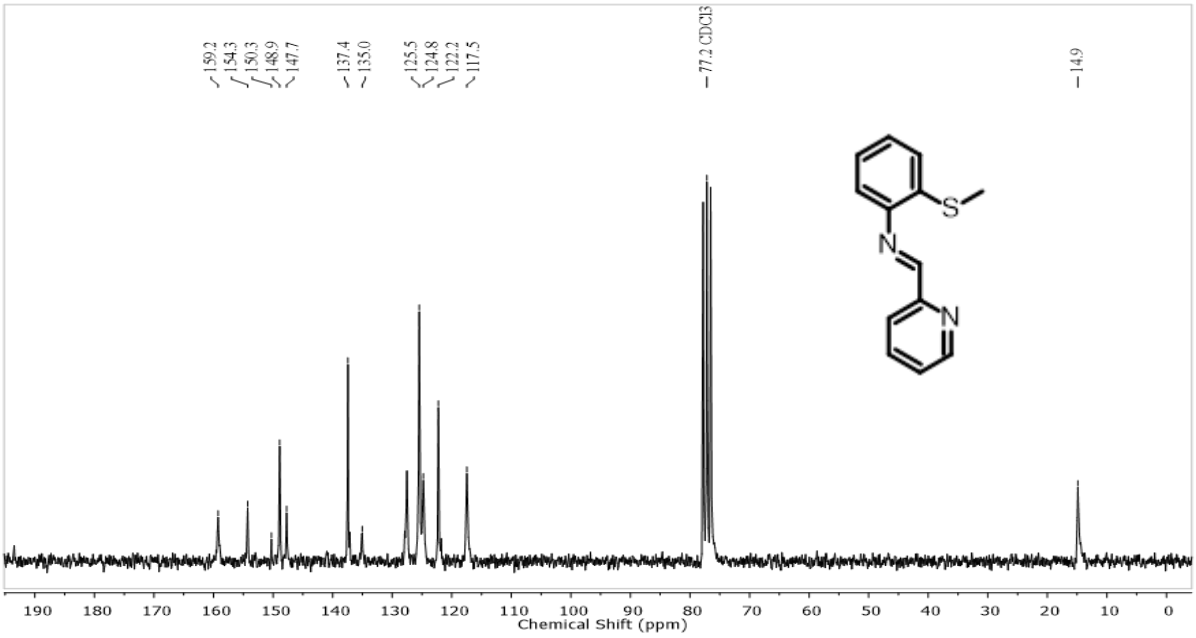

1.3.4.1.2 2-pyridyl-N-(2'-methylthiophenyl)-methyleneamine (L2)

The amine (L2) was obtained by reducing the imine (L1) above using catalytic hydrogenation (Pd/C 10%) at a pressure of 50 psi overnight, as summarized in **Figure 28**. Solution was filtered obtaining a yellow oil with a 70% yield. **Figures 29** and **30**, show the NMR spectra of the purified compound that was certainly obtained.

Figure 28. Synthetic route for L2.

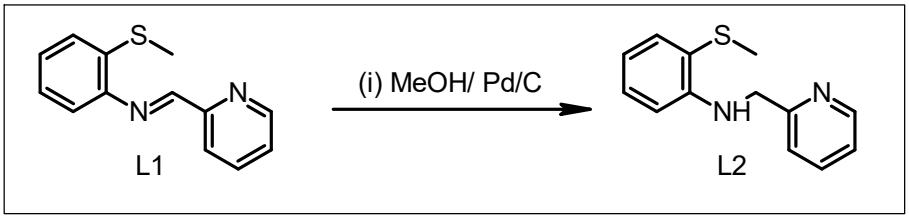

Figure 29. ^{1}H NMR ($CDCl_3$, 200 MHz) δ (ppm) spectra of L2: 2.36 (s, 3H); 4.54 (s, 2H); 5.67 (s, 1H); 6.55 (d, *J*= 8.0 Hz, 1H); 6.65 (dd, *J*= 6.9, 7.4 Hz, 1H); 7.07-7.18 (m, 2H); 7.32 (d, *J*= 7.8 Hz, 1H); 7.42 (d, *J*= 8.0 Hz, 1H); 7.61 (dd, *J*= 7.2 and 7.5 Hz, 1H) and 8.58 (d, *J*= 4.3 Hz, 1H).

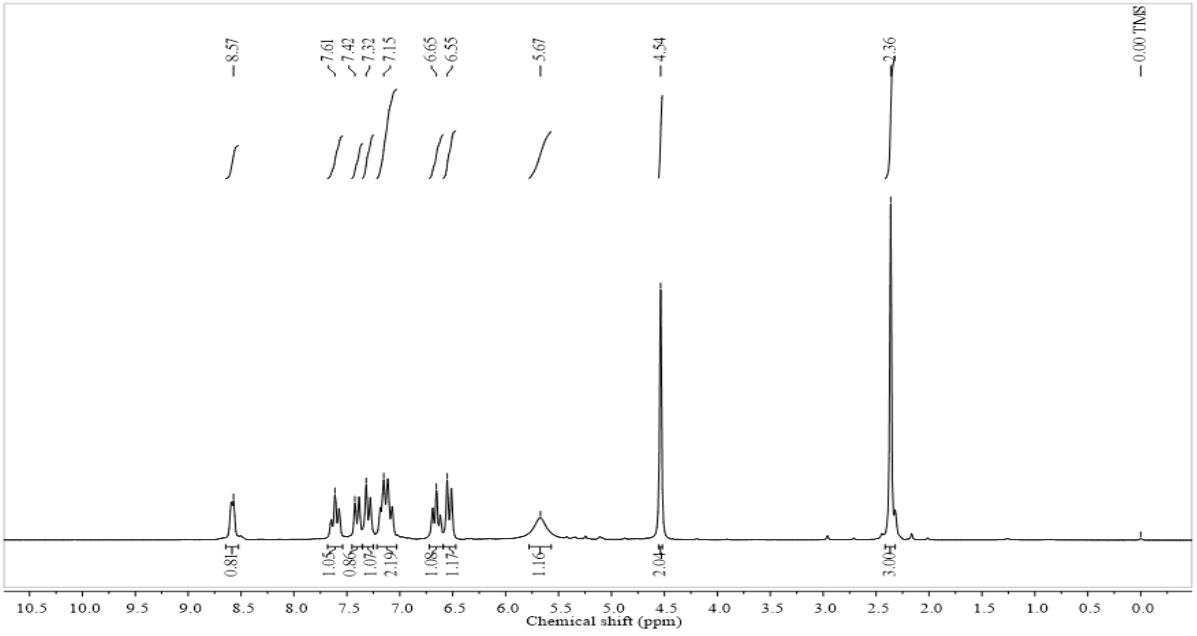

Figure 30. ^{13}C NMR ($CDCl_3$, 50 MHz) δ (ppm), spectra of L2: 18.2; 49.2; 110.5; 117.4; 120.4; 121.3; 122.1; 129.3; 133.9; 139.9; 147.8; 149.0 and 158.6.

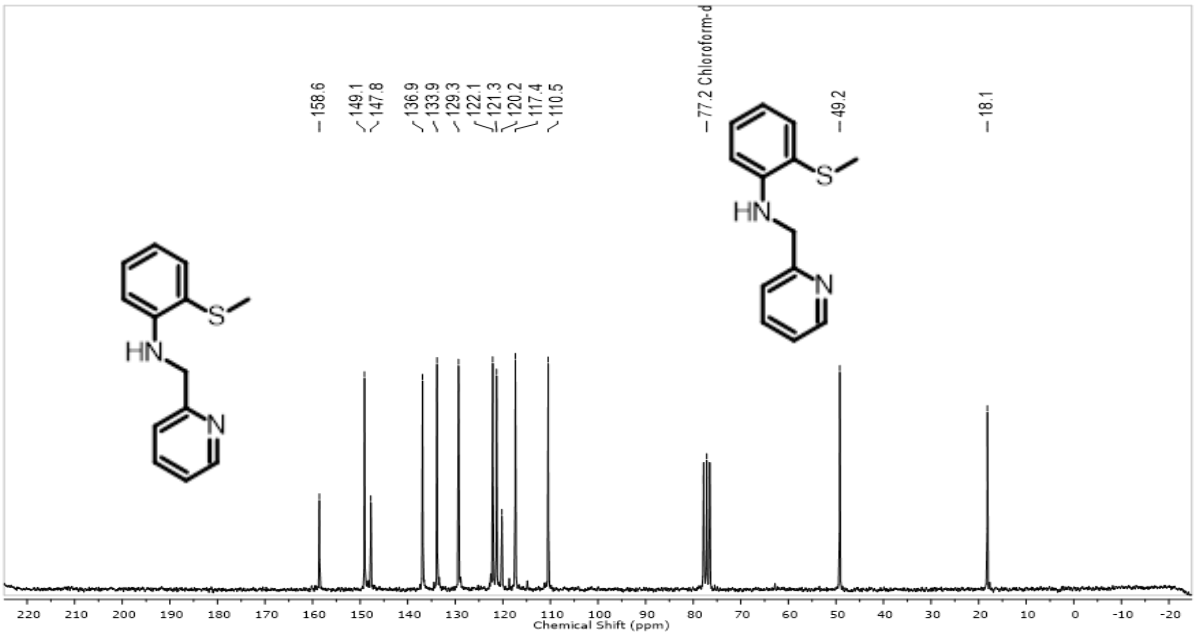

1.3.4.1.3 2-pyridyl-N-(2-(methylthio)ethyl)amine (L3)

Figure 31. Synthetic route for L3.

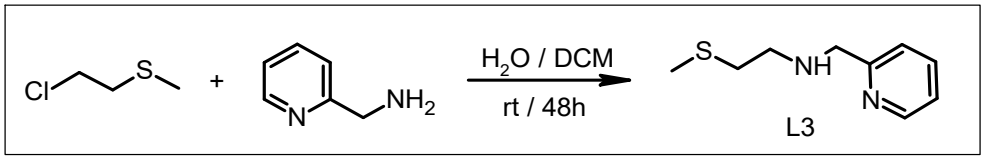

Ligand L3 was synthesized according to the procedure described in the literature, with a few modifications [85], **Figure 31**. In a flask, a solution of 2-chloroethylmethylsulfide (24 mmol) in 20 mL of H_2O was cooled in an ice bath. To this solution was slowly added a solution of 2-(aminomethyl)pyridine (20 mmol) in 35 mL of CH_2Cl_2. This mixture was stirred for 48 h at room temperature. After this period, 12 mL of a 2 mol L^{-1} NaOH solution were added under stirring. The mixture was washed with 40 mL of a 4 mol L^{-1} NaOH solution, the organic phase was dried with Na_2SO_4, and the solvent removed in the rotary evaporator, resulting in a yellow oil. The product was purified by liquid column chromatography eluting with a hexane/ethyl acetate mixture. Yellow oil, 27.5% yield, 5.5 mmol. **Figure 32** and **33** presents the NRM spectra of the obtained ligands.

Figure 32. ^1H NMR ($CDCl_3$, 200 MHz) δ (ppm), spectra of L3: 2.09 (s, 3H); 2.39 (s, 1H); 2.70 (t, *J*= 6.2 Hz, 2H); 2.87 (t, *J*= 6.1 Hz, 2H); 3.94 (s, 2H); 7.14-7.20 (m, 1H); 7.36 (d, *J*= 7.8 Hz; 1H); 7.66 (ddd, *J*= 1.6, 6.0 and 7.6 Hz, 1H) and 8.57 (d, *J*= 4.2 Hz, 1H).

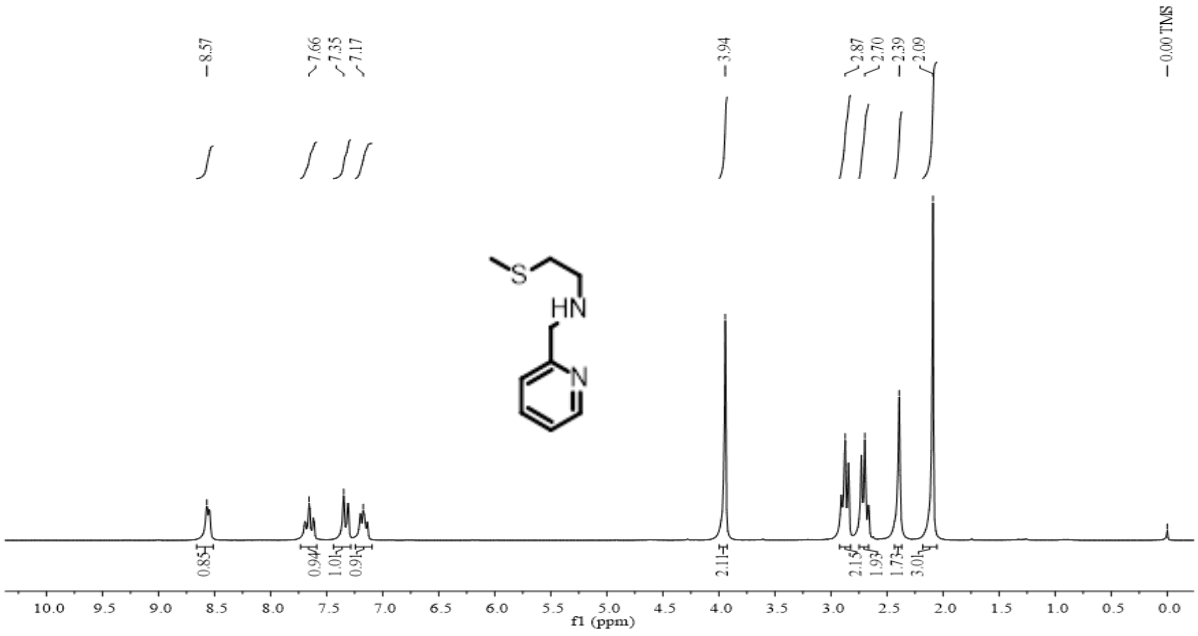

Figure 33. ^{13}C NMR ($CDCl_3$, 50 MHz) δ (ppm), spectra of L3: δ 115.3; 34.5; 47.7; 54.9; 122.0; 122.3; 136.6; 149.4 and 159.7.

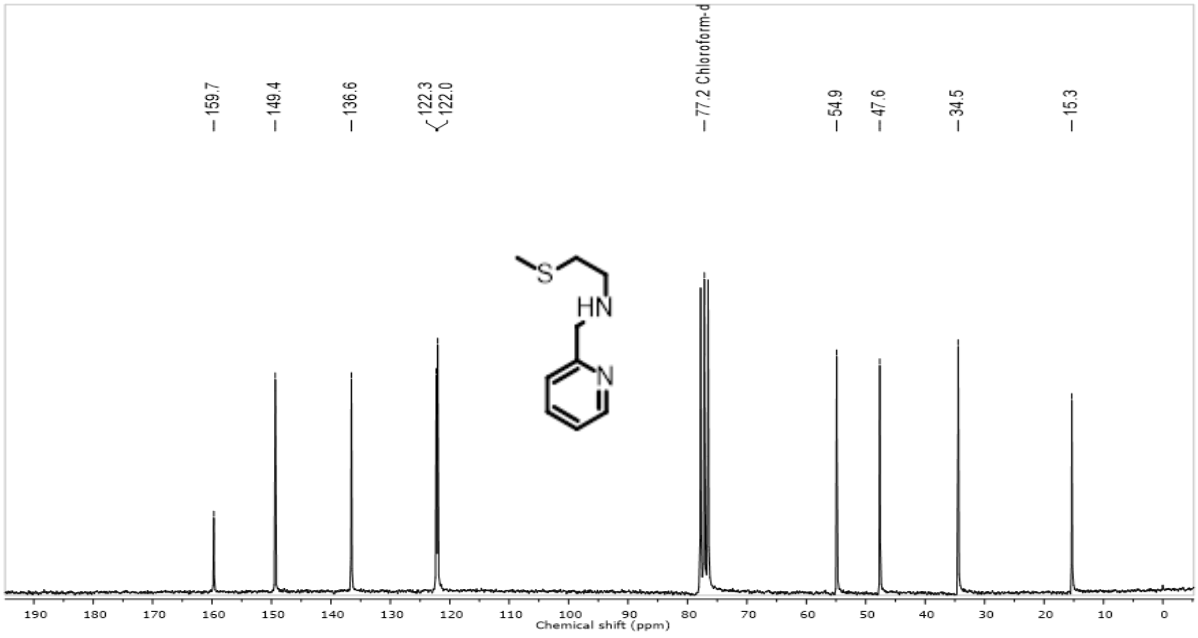

1.3.4.1.4 2-pyridyl-N-(2-thiophenylmethyl)amine (L4)

The synthesis of the amine (2-picolyl)(2-thiophenyl)amine (L4) was carried out according to the literature [86], as resumed on **Figure 34**. A methanolic solution (10 mL) of 2-methylpyridylamine (10 mmol) was slowly added into a methanolic solution (10 mL) of 2-formylthiophene (10 mmol) while stirring at room temperature, this solution was stirred overnight. After this period, $NaBH_4$ (20 mmol) was added in small portions, the solvent was then removed in the rotary evaporator, resulting in a brown oil, this was dissolved in CH_2Cl_2 and extracted with H_2O (3 times), then the organic phase was dried with Na_2SO_4, resulting in a dark yellow/ brownish oil. The product was purified by liquid column chromatography eluting with a hexane/ethyl acetate mixture. Yellow oil, 77% yield, 7.7 mmol. Caution: Compound L4 is photo sensitive and after synthesized it must be stored in the dark at low temperatures. **Figure 35** and **36** shows their NMR spectra.

Figure 34. Synthetic route for L4.

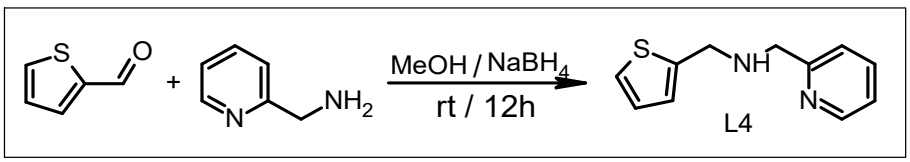

Figure 35. ^{1}H NMR ($CDCl_3$, 200 MHz), δ (ppm), spectra of L4: 2.41 (s, 1H); 3.85 (s, 2H); 3.93 (s, 2H); 6.85 (d, *J*= 2.3 Hz, 1H); 7.12 - 7.02 (m, 2H); 7.21 (d, *J*= 7.6 Hz, 1H); 7.53-7.57 (m, 1H) and 8.45 (d, *J*= 3.4 Hz, 1H).

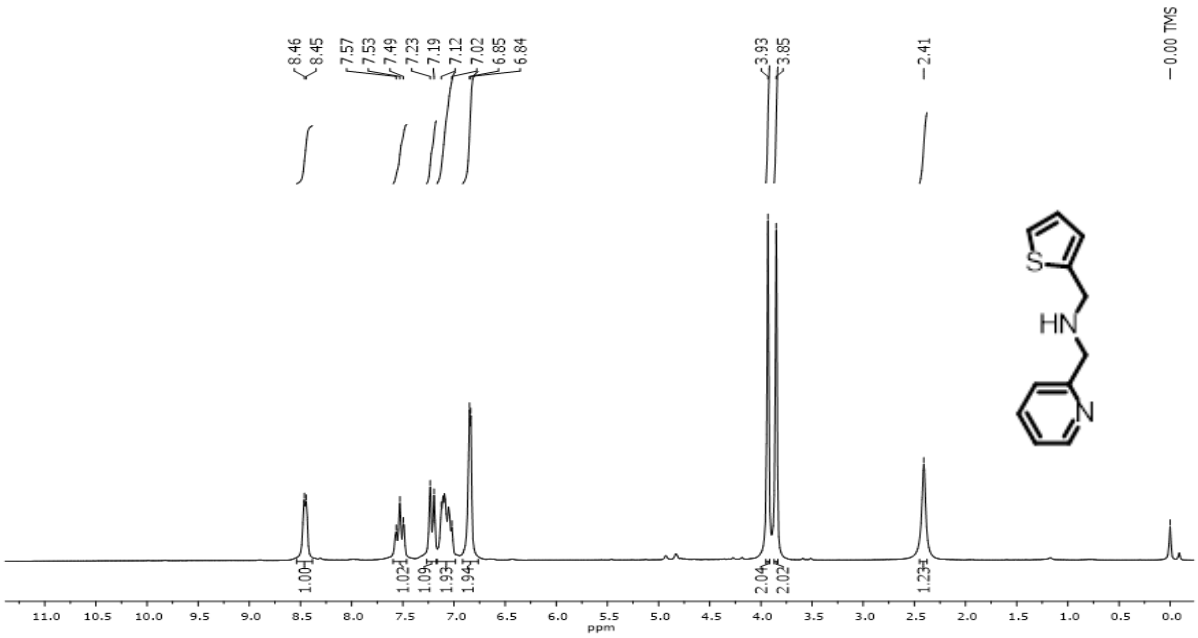

Figure 36. ^{13}C NMR ($CDCl_3$, 50 MHz) δ (ppm), spectra of L4: δ 47.9; 54.0; 122.0; 122.45; 124.5; 125.2; 126.7; 136.5; 143.8; 149.3 and 159.4.

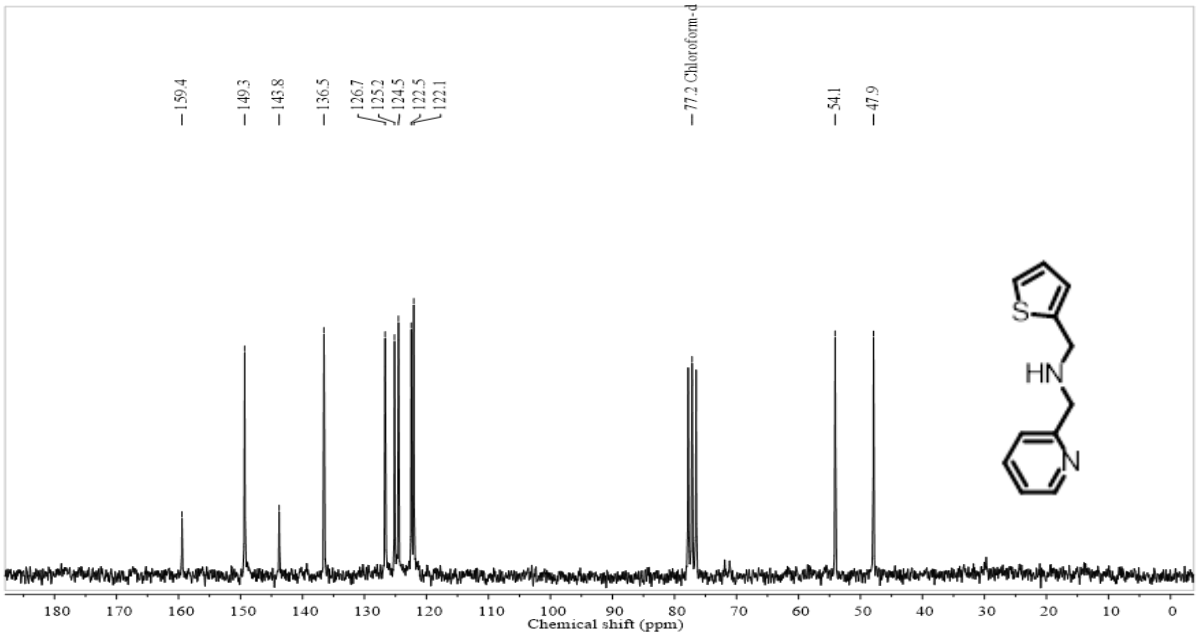

1.3.4.2 Coordination compounds

The Mn(I) compounds **1**-**4**, follow the same synthesis method seen in **Figure 37.**

Figure 37. General scheme for the coordination compounds synthesis.

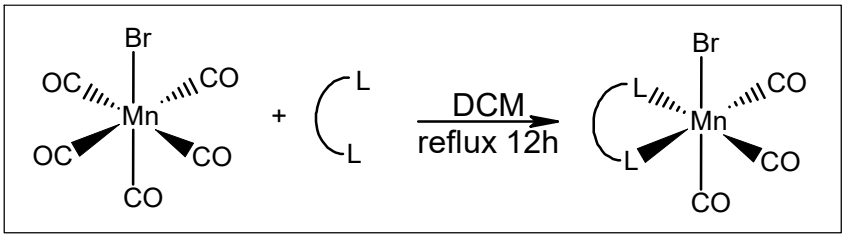

All compounds were prepared according to previous published work [69], [87], [88] , following the same procedure: a solution of the appropriate ligand (0.25 mmol) was dissolved in dry THF (5 mL) in a Schlenk tube. The resulting solution was degassed by applying four freeze-pump-thaw cycles. The manganese precursor [$MnBr(CO)_5$] (0.25 mmol) was added to the frozen solution of the ligand, thawed and degassed three more times, and then kept stirring until the mixture reached room temperature. The resulting solution was then heated at 60 °C for 12 h under inert atmosphere and dark conditions to give a brownish solution. Cold hexane (30 mL) was added to the cooled mixture, resulting in a precipitate. Further purification was performed, the pellets were washed three times with 30 mL of cold hexane, then dried under reduced pressure and kept under dark conditions. **Table 1** and **Figure38** summarize the synthetic results for all compounds.

Figure 38. Chemical structures for **1)** [$(L1)Mn(CO)_3Br$], **2)** [$(L2)Mn(CO)_3Br$]**, 3)** [$(L3)Mn(CO)_3Br$] and **4)** [$(L4)Mn(CO)_3Br$].

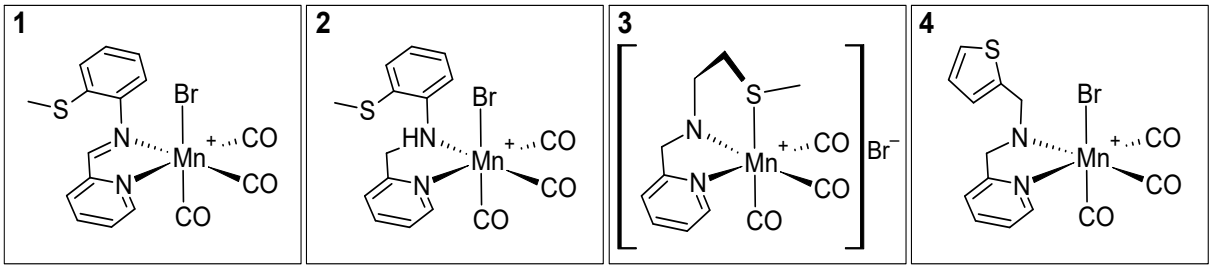

Table 1. General information for compounds synthesized in this work.

(L)Mn(CO)$_3$Br	Color	Yield (%)	Mass (mg)
L1	Dark red	83	57.0
L2	Dark orange	76	52.2
L3	Light yellowish	43	29.5
L4	Dark yellowish-	71	48.8

1.4 RESULTS AND DISCUSSIONS

1.4.1 MCCs SOLID STATE CHARACTERIZATION

1.4.1.1 X-Ray Diffractions

Compounds **1** and **4** have already been described in the literature by the Gonzalez and Jana groups, respectively [87], [88]. Suitable crystals for X-ray diffraction using the slow layer diffusion method were obtained from a 1:1 mixture of dichloromethane and hexane for the new MCC **3,** all the crystallographic parameters, bond lengths and angles are displayed in Appendix B. However, despite our efforts, no suitable crystals for compound **2** could be obtained.

The Oak Ridge Thermal-Ellipsoid Plot Program (ORTEP) view of compound **3** crystal, as shown in **Figure 63 (appendix A)**, demonstrates a level of complexity arising from its crystallization in a non-centrosymmetric space group, leading to the presence of four molecules of compound **3** within the asymmetric unit of the cell. These molecules are differentiated by their association with the Mn ion. Specifically, Mn1 exhibits isomerism with Mn2, while Mn1 and Mn4 possess identical properties, as do Mn2 and Mn3. Furthermore, the asymmetric part of the cell accommodates four molecules of the Mn complex, along with four bromide ions and a single molecule of CH_2Cl_2, left over from crystallization solvent.

Figure 39 illustrates the representative isolated structure of compound **3**, which adopts an orthorhombic crystal system with space group P 21 21 21.

Figure 39. Molecular structure of complex **3** with thermal ellipsoid at 40% probability. Hydrogen atoms were omitted for clarity. Selected bond lengths (Å) and angles (deg): Mn1-C1 = 1.810(5); Mn1-C2 = 1.803(5); Mn1-C3 = 1.806(4); Mn1-N1 = 2.071(3); Mn1-N2 = 2.048(3); Mn1-S1 = 2.3610(12); C1−Mn1−C2 = 89.6(2); C1−Mn1−C3 = 91.2(2); C1-Mn1-N1 = 93.21(17); C1-Mn1-N2 = 93.37(16); C1-Mn1-S1 = 91.98(14); C2-Mn1-S1 = 92.82(14); N(1)-Mn-S = 84.96(9).

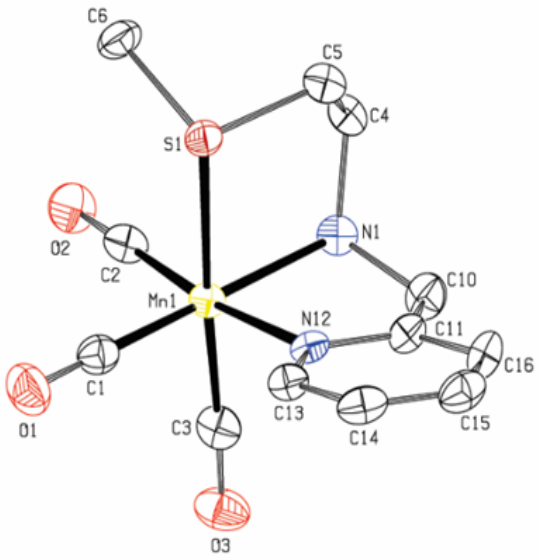

Compounds **1** and **4** are described in a distorted octahedral coordination mode, wherein the three CO ligands are arranged in a *fac*-coordination fashion. A bidentate N2-donor ligand binds, forming a five-membered ring, and the sulfur arm remains pendant. The displacement of the bromide, which is present in the starting material, was not favored for **1** and **4**, but can be attributed to the syntheses being conducted under mild conditions. Additionally, the low affinity of manganese(I) towards the soft chalcogenated portion of the ligand, contributes to the slightly harder bromide ligand to remain coordinated. The non-coordination of sulfur is also not favorable due to the lack of mobility from the pendant arm, in which chalcogenic is bond, whereas the chelate forces can't counterfeit Br ion due to rigidity, angles and torsions from the ligand presuming coordination [59].

On the other hand, for compound **3** there is the displacement of bromide ion from the coordination sphere where the coordination of sulfur occurs. The bond is most likely due to the high mobility and flexibility that ligand **L3** has over the other ligands in this series. The chelate effect proves to be strong enough to favor sulfur coordination

as this behavior is also observed in similar aliphatic sulfur ligands coordinated to other metal carbonyl manganese compounds.

Table 2. Selected bond lengths (Å) and angles (degrees) of **1** [87], **3** and **4** [88]**.**

	1	**3**	**4**
	Bond Length (Å)		
Mn-C(1)	1.815(2)	1.803(5)	1.801 (5)
Mn-C(2)	1.816(2)	1.806(4)	1.827(5)
Mn-C(3)	1.794(2)	1.810 (5)	1.783 (5)
Mn-N(1)	2.0533(18)	2.048(3)	2.061 (4)
Mn-N(2)	2.0506(16)	2.071(3)	2.104 (4)
Mn-Br	2.5320(4)	-	2.5373 (9)
Mn-S	-	2.3610(12)	-
	Bond Angles (°)		
N(1)-Mn-Br	88.15(5)	-	86.13 (11)
N(2)-Mn-Br	87.61(5)	-	88.69 (12)
N(1)-Mn-S	-	82.47(9)	-
N(2)-Mn-S	-	88.69 (12)	-
C(1)-Mn-Br	86.99(7)		91.56(16)
C(2)-Mn-Br	88.52(7)		84.33 (16)
C(1)-Mn-S		91.98(14)	
C(2)-Mn-S		92.82(14)	

Structurally, sulfur coordination does not seem to alter the geometry significantly. Bond length CO (C3) does not significantly alter, regardless of bromide or S pendant in trans position, indicating that the donor effect from both ligands is similar. However, the bond length of Mn-Br is longer than Mn-S, probably due to slightly bigger naturally bigger radii from bromide [89]. Besides, the steric effects from the coordinated sulfur pendant from **3** generate a bigger angle relative to the COs from xy plane from the MCC, meaning those not under trans effect influence. Selected bond angles and lengths are displayed in **Table 2**.

When compared to similar coordination compounds from literature, [Mn(NNHS**Pr**)$CO)_3^+$], (**pr**) [90] and [Mn(NNHS**Et**)$CO)_3^+$] (**Et**) [91], where 2-pyridyl-N-(2-(isopropylthio)ethyl)amine and 2-pyridyl-N-(2-(ethylthio)ethyl)amine are respectfuly NNHSPr and NNHSEt, with coordinated sulfur to the metal (**Table 3**) compound **3** presents little to non-deviation on its structure. The bond length Mn-S is longer when compared to Mn1-N1 and Mn1N12, typical nitrogen donors, due to their higher covalent radii. Electron donor aliphatic fraction bond to sulfur seems to not alter significantly bond lengths, but it does decrease stress angle when coordinating due to less steric hindrance from methyl than propyl and ethyl.

Table 3. Selected bond lengths (Å) and angles (degrees) of **3**, [Mn(NNHS**Pr**)$CO)_3^+$] [90], [Mn(NNHS**Et**)$CO)_3^+$] [91]**.**

	3	**pr**	**et**
	Bond Length (Å)		
Mn-C(1)	1.803(5)	1.807(3)	1.780(17)
Mn-C(2)	1.806(4)	1.807(3)	1.753(19)
Mn-C(3)	1.810 (5)	1.813(2)	1.782(19)
Mn-N(1)	2.048(3)	2.0592(18)	2.064(11)
Mn-N(2)	2.071(3)	2.0804(18)	2.091(12)
Mn-S	2.3610(12)	2.3745(6)	2.358(4)
	Bond Angles (°)		
C(1)-Mn-S	91.98(14)	96.65(7)	95.6(5)
C(2)-Mn-S	92.82(14)	90.94(8)	92.1(5)
C(3)-Mn-S	175.67(15)	175.24(7)	172.6(5)
N(1)-Mn-N(2)	80.44(13)	80.28(7)	80.8(5)
N(1)-Mn-S	82.47(9)	84.64(6)	83.9(4)
N(2)-Mn-S	88.69 (12)	83.77(5)	82.3(3)

Powder X-ray diffraction analysis was also performed, and the patterns for all compounds are presented in **Figure 40**. Crystallographic data from compound **1** were utilized for fitting and calibration. The diffraction patterns exhibit high crystallinity, as evidenced by the absence of background noise. Among the compounds, compound **3** displays the lowest degree of crystallinity, which can be attributed to its more complex unit cell structure, as discussed earlier. As per comparison on the series of the metal carbonyl compounds on their diffraction patterns, we might assume that **2** takes similar geometry as the others.

Figure 40. Powder X-ray diffraction comparisons for **1**-**4.**

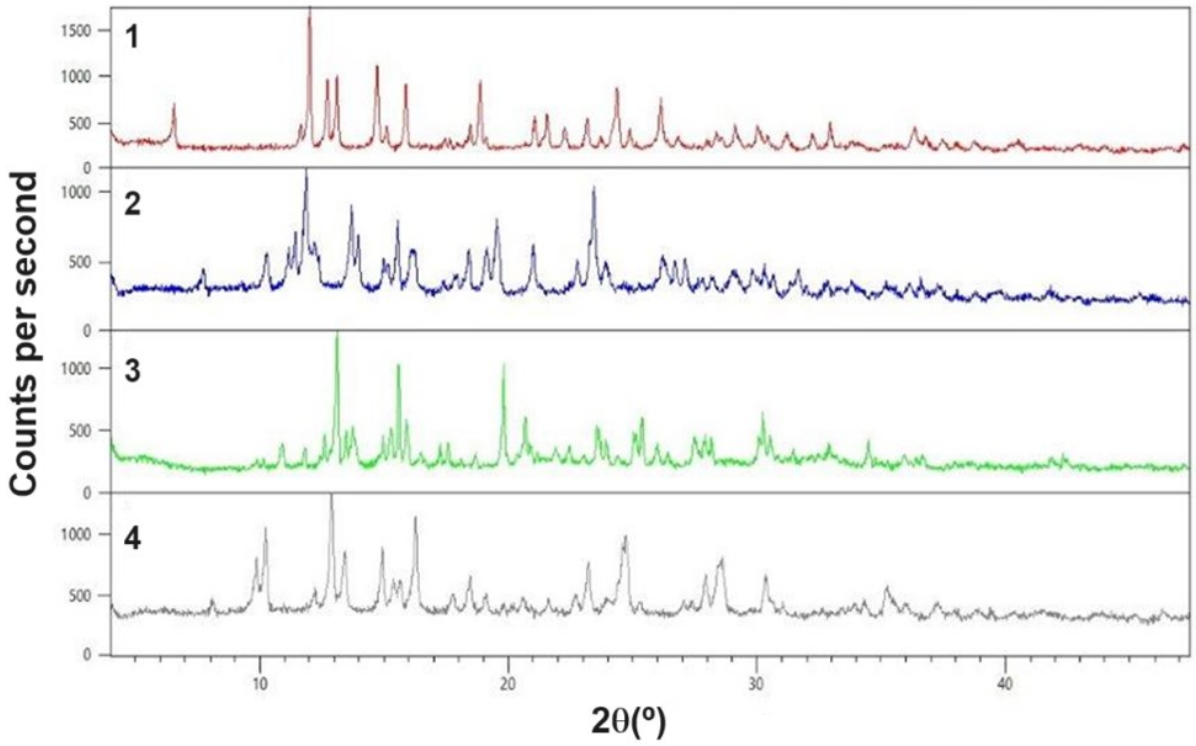

1.4.1.2 ^{213}C *solid-state* NMR

^{13}C *Solid-state* NMR spectra were investigated for compounds **1** to **4**, and selected ^{13}C chemical shifts are summarized in **Table 4**. It is noteworthy that compounds **1** and **4** have been previously published; however, their nuclear magnetic resonance properties in the solid state have not been extensively explored. Thus, this study provides a comprehensive analysis of their NMR characteristics providing complementary insights and enhancing our understanding of their structural attributes and geometric configurations.

The ^{13}C CPMAS spectrum, **Figure 88 (appendix B)**, for compound **1** displays a signal at 13.8 ppm, corresponding to the thioether moiety of the ligand. In compound **2**, this signal appears at 27.5 ppm, while in compound **3** it appears at 25.0 ppm. The resonance from ligand strongly influences the NMR shifts, upfielding in 13.7 ppm the carbon from the S-CH_3 moiety of **1** vs **2**, due to the naturally homogenous electron density caused by the resonance. However, when comparing coordinated sulfur (**3**) *vs* non coordinated one (**1**), but with resonance, the shifts indicate a weaker influence from the effect on chemical shifts, with 11.2 ppm upfield displacement. This might be due to **1** having the least shielded sulfur, despite **3** being directly coordinated to the

metal sulfur atom where the density of the dz^2 orbital from metal contributes to the increased density surrounding the chalcogenide moiety. Now, when comparing **3** vs **2**, it's noticeable that the coordination of sulfur shifts the electron density towards metal, upfielding the carbon signal by 2.5 ppm. This effect is also corroborated by X-rays analysis where the Mn-CO bond in the transposition of sulfur being smaller in **3**, where the extra density from sulfur strengthens the backdonation, tightening the bond in comparison with the non-bonded **1**.

Table 4. Compiled selected ^{13}C chemical shifts (δ) in ppm for compounds **1**-**4**, using CPMAS and CPPI experiments.

	S-$\underline{C}H_3$	$\underline{C}_2$(ph)	$\underline{C}_1$(ph)	$\underline{C}_2$(py)	$\underline{C}$H=N	Py-$\underline{C}H_2$-	$\underline{C}_2$(thio)	$\underline{C}$O
1	13.8	130.0	148.6	152.8	171.4	-	-	221.3
2	27.5	130.5	148.4	160.4	-	66.6	-	272.4
3	25.0	-	-	162.8	-	56.7	-	218.5
4	-	-	-	160.6	-	54.6	136.2	275.2

Using the CPPI experiment for the acquisition ^{13}C *solid-state* NMR spectra, **Figure 89 (appendix B)** shows compound **1** exhibiting a signal at 171.4 ppm for the Py-CH=N moiety, while in compound **2**, the same carbon signal appears at 66.6 ppm, corresponding to Py-CH_2-N due to a change of hybridization from sp^2 to sp^3 expected for a Schiff base reduction. In the presence of the thiophene moiety, this signal further shifts upfield to 60.2 ppm, indicating a stronger removal of density for such moiety. The C_2(py) also experiences a significant shift upon removal of the resonance effect from the ligand, appearing close to 160 ppm in compounds **2** and **3**, while in compound **1**, it appears upfield at 152.8 ppm.

Carbonyl carbons are observable using ^{13}C HPDec experiments (**Figure 90 appendix B)** with enlargement for the CO region seen in **Figure 41**, with signals appearing at 220.3, 272.4, 218.5, and 275.2 ppm for compounds **1** to **4**, respectively. This indicates a stronger donor influence from ligands **L4** and **L2** compared to the ligands **L3** and **L1**. The resonance effect also has its influence on the chemical shift of CO, whereas ligands without resonance could have their electron density more available to central metal ions than the resonance ligands, which have lower electron availability. It is important to mention that carbonyl signals were not observed using the

^{13}C CPMAS experiments due to the low polarization from the ^{1}H populations to the CO sites.

Figure 41. Solid-state ^{13}C High power proton decoupling experiments for the CO region for compounds **1** (black, MAS rate: 12 kHz), **2** (red, MAS rate: 8 kHz), **3** (green, MAS rate: 12 kHz), and **4** (blue, MAS rate: 8 kHz).

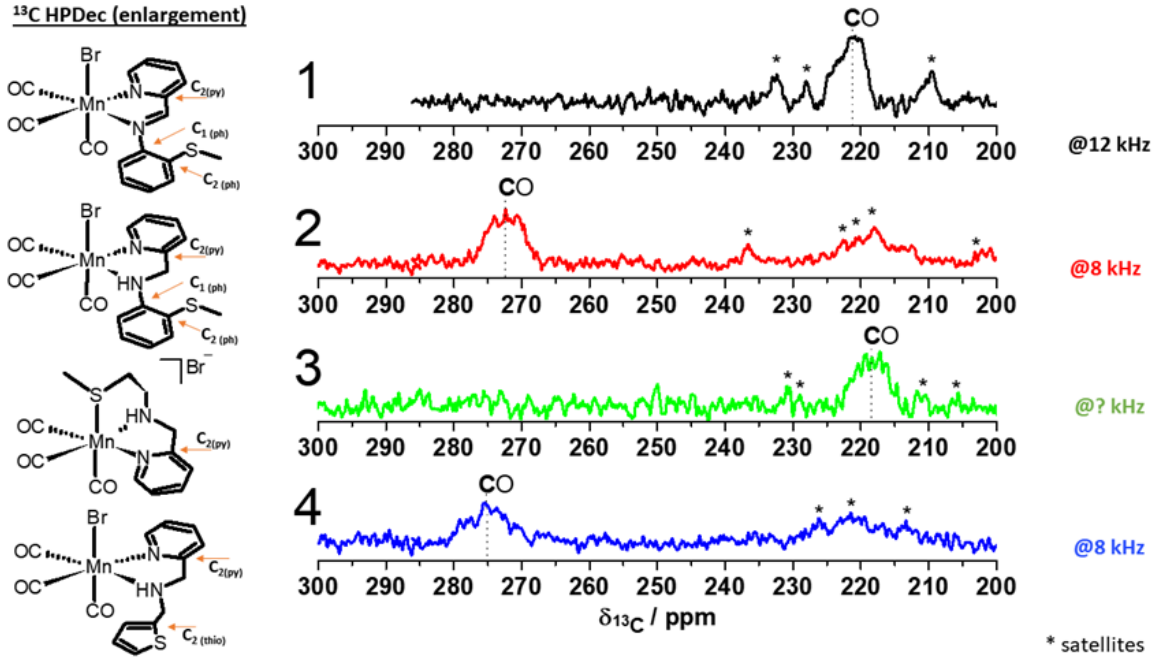

1.4.1.3 Infrared Spectroscopy

Owing to the inherent chemical properties of molecular bonds, Infrared analysis serves as a valuable tool for elucidating coordination patterns within the primary coordination sphere and its modifications. Vibrational modes arising from both the molecular bonds and compound symmetries manifest prominently in the FTIR spectra. Perturbations in chemical behavior resulting from alterations in molecular bonds induce shifts in energy, thereby leading to the displacement of spectral bands and alteration of overall spectral patterns.

In the context of MCC the carbonyl bands exhibit substantial intensity and sensitivity to any variations introduced by modifications in ligand structures and metal interaction. This heightened sensitivity can be attributed to the backdonation bond involving carbon monoxide and its changes can be monitored effectively.

The FTIR full spectra of compounds **1**-**4**, obtained in KBr, are seen in **Appendix D Figure 93.** The characteristic CO bands are highlighted in **Figure 42**, two distinct and noteworthy bands are seen around 2030 cm^{-1}, corresponding to symmetrical stretching within the A_1 symmetry, and 1930 cm^{-1}, assigned to the asymmetrical degenerated E symmetry. These vibration modes are attributed to the stretching vibrations of the carbonyl (CO) groups. The discerned spectral pattern is indicative of a facial geometry in the carbonyl groups, exhibiting a local C_{3v} symmetry. This observation aligns with previous findings in literature where *N,N'* coordinated ligands to Mn(I) compounds also exhibited a similar symmetry pattern [92].

Figure 42. FTIR spectra of CO stretching bands from **1**, **2**, **3** and **4** in KBr pellets.

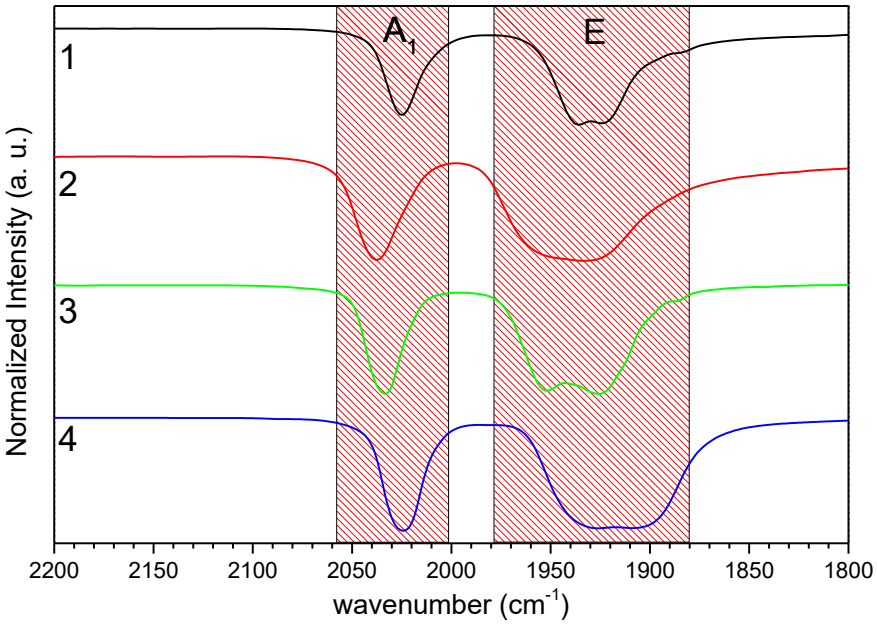

For the symmetrical CO stretching vibrations, higher energy frequencies are observed in 2025, 2038, 2034, and 2024 cm^{-1} for compounds **1**-**4**, respectively. Conversely, lower frequency energies centered around 1930, 1942, 1938, and 1918 cm^{-1} are associated with asymmetric splitting of the CO stretching band, for compounds **1**-**4**, respectively. Important stretched from FTIR analysis are shown in **Table 5**. The degenerate bands are most subject to changes due to the ligand symmetry and even though **3** has the displacement of the bromide ion by coordination, the local C_{3v} symmetry is maintained. The vCO values of compound **3** falls at higher wavenumbers than **1** and **4**, meanwhile having virtually the same band as **2**. This behavior indicates a weaker donor behavior when S atom on the ligand Br when coordinated on the metal. The crystal data of **3** corroborates with the FTIR findings,

where there is less electron density with respect to the metal and therefore the CO bond is not strengthened as much as the *N,N'* ligands and bromide, thus creating a longer M-C bond.

Table 5. Compiled selected FTIR bands for compounds **1-4**, in cm^{-1} and KBr pellets.

	S-C (cm^{-1})	C=N / C=C (cm^{-1})	CO(A_1) (cm^{-1})	CO(E) (cm^{-1})
1	629	1615-1468	2030	1944-1929
2	626	1608-1442	2043	1964-1938
3	628	1632-1403	2040	1959-1935
4	632	1620-1448	2029	1938-1912

In addition to the observed CO stretching bands, the FTIR spectra provided valuable information on other significant stretching vibrations. Notably, the spectra exhibited prominent stretching vibrations of C=N groups in the range of 1608-1632 cm^{-1} and stretching vibrations of C=C bonds within the aromatic rings were observed in the range of 1403-1468 cm^{-1}, confirming the aromatics structure of ligands intact in the compounds while they are coordinated.

The spectra also displayed stretching vibrations of the C-S bonds, observed in the range of 626-632 cm^{-1} for all compounds. Compound **4** exhibited an additional torsion vibration of the thiophene ring, observed at 715 cm^{-1}. This unique vibrational mode provides further insight into the structural characteristics of compound **4** [93].

1.4.2 MCCs GAS AND SOLUTION CHARACTERIZATION

1.4.2.1 ESI-Mass, ^{13}C and ^{1}H NMR

Electrospray mass spectrometry stands as a crucial analytical methodology wherein molecules from a given sample, undergo ionization within the gaseous phase. These ions are subjected to separation within the mass spectrometer based on their mass-to-charge ratio (*m/z*). The resulting mass spectrum graphically represents the relative abundance (intensity) of each ion, manifested as distinct peaks with well-defined *m/z* values.

Differently from solid state NMR, in solution a fast movement of the nuclei is possible, generating thinner peaks and giving better clarity from the chemical positions,

thus making possible the ^{1}H NMR analysis of the compounds. Comparing **1** and **2**, it's noticeable that the loss of resonance structure of the ligands causes huge changes in their electronic properties, making their spectra look distinct.

Table 6. Base peak values referring to the molecular and theorical ions of compounds **1**-**4** determined via ESI-MS in methanol.

	Experimental (m/z)	Calculated (m/z)	Representation
1	399.01 (100%)	399.02	$[L1Mn(CO)_3MeOH]^+$
	367.00 (80%)	366.99	$[L1Mn(CO)_3]^+$
2	369.04 (100%)	369.01	$[L2Mn(CO)_3]^+$
3	321.00 (100%)	321.01	$[L3Mn(CO)_3]^+$
4	342.98 (100%)	342.99	$[L4Mn(CO)_3]^+$

The mass spectra of the four MCCs reveal their stability, as evidenced by the absence of carbon monoxide release throughout the analysis duration. Given that these compounds feature manganese(I) as a metal center, all spectra exhibit a consistent isotopic distribution concerning the ligands. This uniformity is attributed to the nearly 100% abundance of the manganese isotope with a mass of 55 u.

The prominent molecular ions were identified as base peaks and detailed in **Table 6**. Only **1** presented a coordination of the solvent used in the analysis in the generated ion, leaving the second most prominent peak with 80% being the ion with five coordination modes as the other three MCCs. Comprehensive insights on the isotopic species profiles, along with corresponding simulations, for all four compounds are depicted in **Figure 43**.

Further structural analyses were performed using ^{13}C and ^{1}H NMR spectroscopy in solution, **Figures 64-87 (appendix B)**. As we know, such technique is an indispensable tool for the characterization of organic compounds, and it can be extended to the characterization of organometallic compounds. The magnetic field behavior of hydrogen and carbon atoms behave differently when they are free and coordinated, thus NMR can record the changes and discernible alterations caused by any symmetry and ligand differentiation. These alterations manifest themselves as displacements, appearances, or the disappearance of chemical shifts in the NMR spectra of organometallic compounds, facilitating their detailed characterization.

Figure 43. Experimental isotopic profile for the molecular ion peaks of MCCs and respective simulations of the isotopic species, where a) **1** and $[L1Mn(CO)_3MeOH]^+$ and $[L1Mn(CO)_3]^+$, b) **2** and $[L2Mn(CO)_3]^+$, c) **3** and $[L3Mn(CO)_3]^+$ and b) **4** and $[L4Mn(CO)_3]^+$.

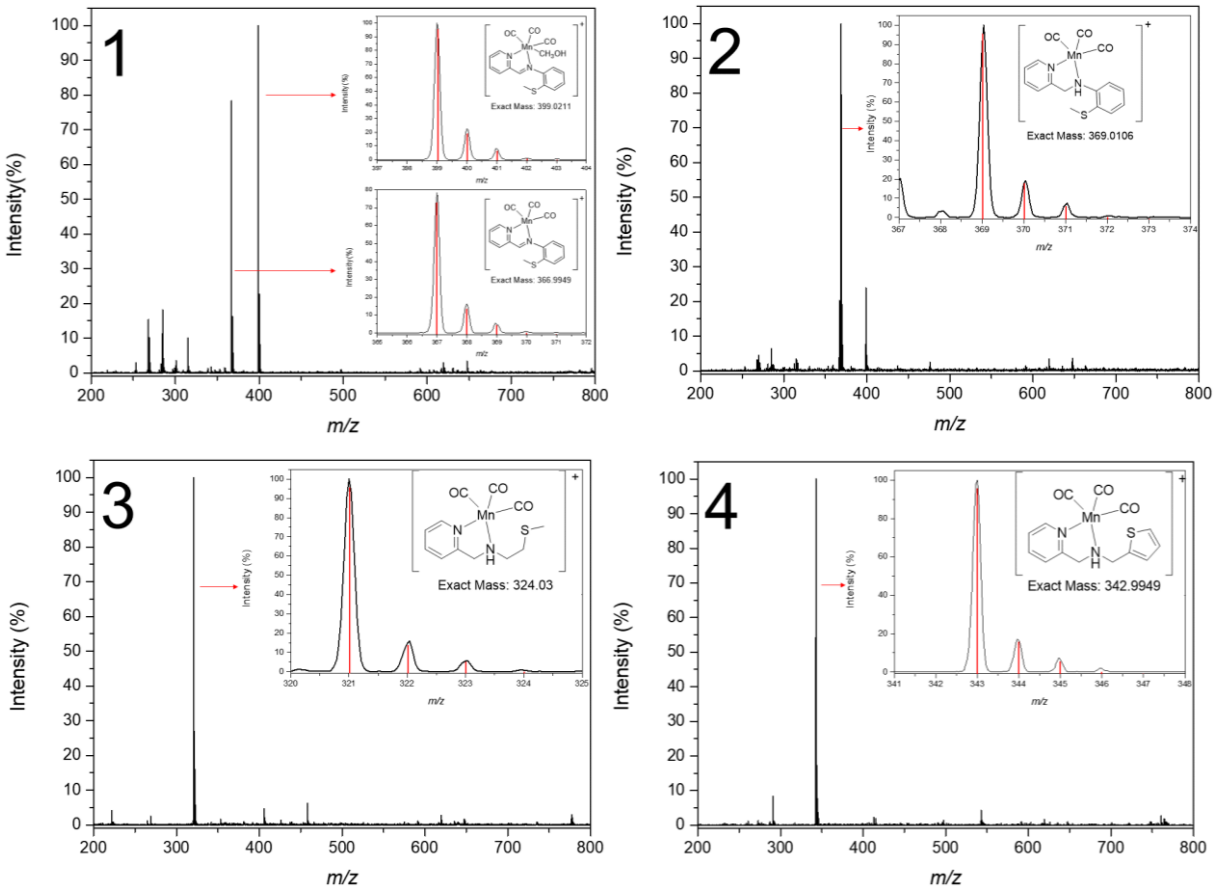

Compounds **1** and **4** have been previously published; however, compound **1** lacked NMR data for the carbon and nitrogen nuclei, while compound **4**, although published their ^{13}C and ^{1}H RNMs, was not thoroughly explored in all the techniques and details presented in this study. Therefore, this work serves to republish and complement their chemistry, providing a more comprehensive understanding of their properties and behavior. All selected chemical shift data for the ^{13}C and ^{1}H nuclei of compounds **1**-**4** are presented and organized on **Table 7** and **Table 8**, respectively.

Differently from solid state NMR, in solution a fast movement of the nuclei is possible, generating thinner peaks and giving better clarity of the chemical positions, which makes the analysis of compounds by ^{1}H NMR possible. Comparing **1** and **2**, it's noticeable that the loss of resonance structure of the ligands causes huge changes in their electronic properties, making their spectra look distinct.

Table 7. Compiled ^{1}H chemical shifts (δ) in ppm for compounds **1-4** in DMSO-d_6.

^{1}H(600 MHz)	-S-C**H**$_3$	-C**H**=N-	Py-C**H**$_2$-	-CH$_2$-N**H**-
1	2.47	8.86	-	-
2	2.95	-	4.95/4.57	-
3	2.54	-	4.60/4.28	1.67
4	-	-	4.35/4.05	6.38

Table 8. Compiled ^{13}C chemical shifts (δ) in ppm for compounds **1-4** in DMSO-d_6.

^{13}C(150 MHz)	S-C**H**$_3$	C$_2$(ph)	C$_1$(ph)	C$_2$(py)	C**H**=N	Py-C**H**$_2$-	C**O**
1	15.9	129.7	150.1	154.7	171.8	-	223.0
2	42.6	123.6	137.4	148.4	-	63.9	217.3
3	20.5	-	-	162.6	-	60.1	219.3
4	-	-	-	160.7	-	57.2	222.1

The methyl group bonded to the sulfur has a notable displacement to higher δ, meaning that in **2** the methyl hydrogens are in a poorer electron environment than **1**. The same ligands when free similarly δ are observed, being 2.46 ppm for **L1** and 2.36 ppm for **L2**, while when coordinated, the shift of those peaks is clear: 2.47 and 2.95 ppm for the same methyl groups. The reduction from imine to amine is proof of resonance break, where only one hydrogen (-C**H**=N-) is found at in 8.86 ppm is found for **1**; such higher δ is due to proximity to the highly electronegative N atom. While for the same fraction of molecule (-C**H**$_2$-N-) there are two hydrogens located at 4.95/4.57 ppm, δ much lower despite the same N as a neighbor. Collectively, these data imply a more pronounced donor characteristic for **L1** compared to **L2**, as also noticed by Maqsood et Al, studying the donor strength using theorical DFT calculation for N'N bidentate ligands from ligand phen derivatives, which increases with resonance and backdonation.[94]

For the ^{13}C NMR analysis, the same behaviors are noticed for the pair **1** and **2**, apart from the methyl carbon which goes the other way around, both in the free and coordinated states. For the S-**C**H$_3$ moiety, δ carbon is found to have a much poorer electron density at **1** than at **2**. Meaning that the resonance is strengthening the electronegativity of the sulfur, which pulls more density from the carbon. The carbon

atom peak of the CO fraction is also found at 223.0 ppm for **1** and 217.3 ppm for **2**. Since CO falls in a poorer electron density for **1** than for **2**, it's an indicator that **L1** weakens the backdonation bond, giving a O≡C-Mn characteristic to the moiety.

The same reasoning can be made when comparing the pairs **2**-**3** and **1**-**3**. The coordination of sulfur with the structure generates electronic effects similar to resonance, even though not as strong. Since a lower overall δ for hydrogen nuclei and a higher δ for carbon nuclei is observed for **3** in comparison with **2** but now as much as for **1**. MCC **4** has the richest electronic environment around the N atom bond to the metal center, even though if it is not in resonance. A very acidic hydrogen of the amine can be observed, compared to the other compounds in the group.

The observed modifications collectively suggest that the disruption of the resonance mechanisms impedes the direct interaction between the electron densities of the metal and the ligand. In the context of carbonyl release, these alterations render compound **2** less prone to CO liberation compared to compound **3**, followed by compounds **4** and **1**, with the latter exhibiting the highest predisposition to carbonyl release within this group.

1.4.2.2 Electronic properties

1.4.2.2.1 Voltammetry analysis

Cyclic voltammetry was employed to investigate the electrochemical behavior of the synthesized compounds, as depicted in **Figure 44**. Furthermore, a comprehensive summary of the pertinent parameters derived from these experiments are provided in **Table 9**.

Due to the low electron density surrounding the metal center by the π-acceptor character of the CO ligands, in this *quasi*-reversible voltammogram, a high oxidation value is expected for the MCCs, as observed in the experimental data of **1**-**4** [95]. The anodic peak of the first wave is related to the oxidation of the metal center from Mn^{I} to Mn^{II} and the second is attributed to a second oxidation of the redox pair $Mn^{II/III}$ [70]. The Mn oxidation process induces the release of CO molecules, thereby causing a permanent alteration in the structural configuration of the compounds, following the

same behaviors as other Mn(I) compounds in the literature [96]–[98]. This alteration significantly influences the reversibility of the process.

Figure 44. Cyclic voltammogram of **1**-**4** in CH_2Cl_2. Work electrode: Platinum; Reference electrode: Ag/Ag^+; Auxiliary electrode: Platinum; Support electrolyte: $TBAPF_6$ 1.00 × 10^{-1} mol L^{-1}, [MCC] = 1.00 × 10^{-3} mol L^{-1}. External reference Fc/Fc^+ was used.

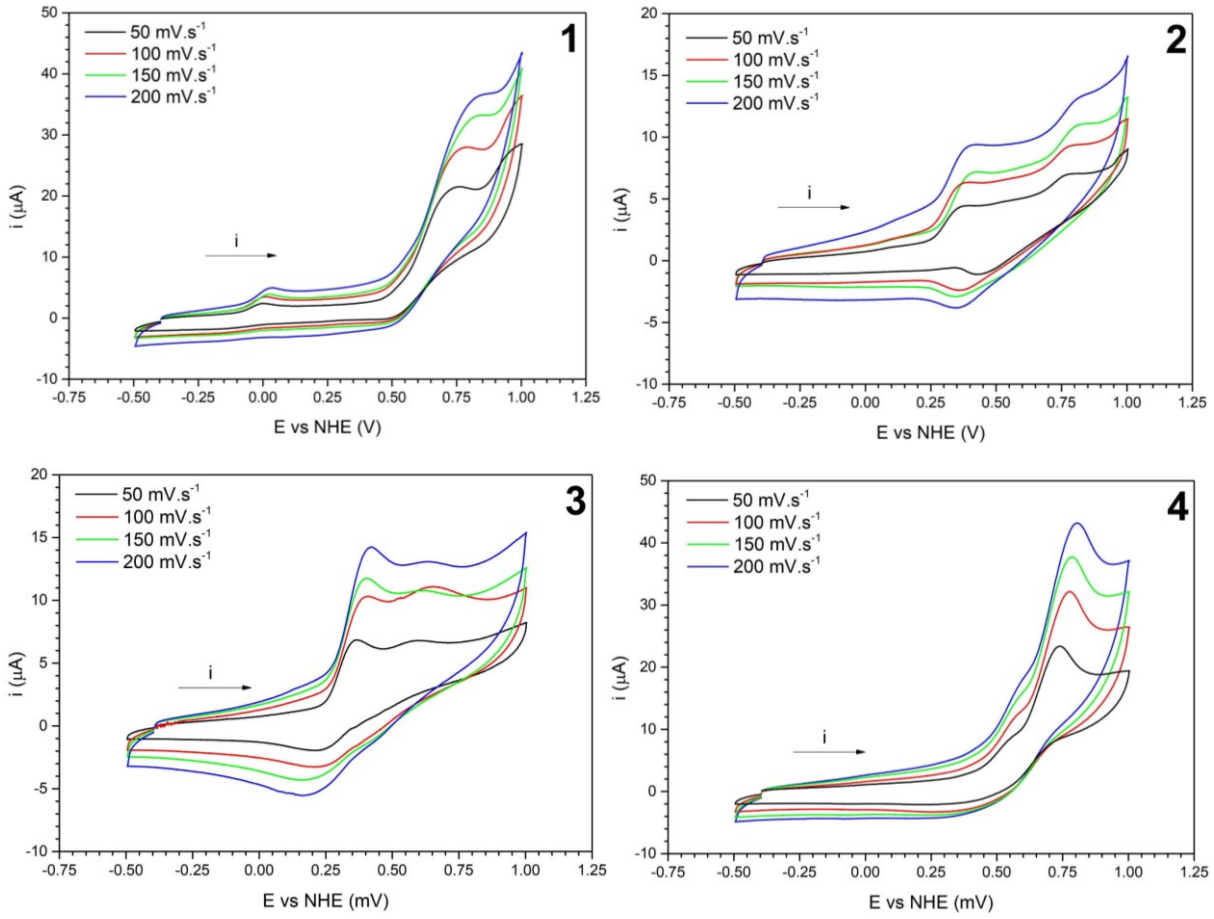

The electronic difference among ligands influences their oxidation potentials. Specifically, L1 possesses a stronger resonance, removing electron density from the metal center, resulting in oxidation peaks at higher values compared to other ligands. Simultaneously, the freedom of the sulfur ligand moiety contributes to the observed voltammogram variations. Compound **3**, characterized by a higher degree of freedom, shifts the oxidation potential to more cathodic values, whereas when the sulfur atom is constrained within a ring, the oxidation potential tends towards more anodic values.

The theoretical data aligns consistently with experimental observations. Amorim *et al.*, employing analogous ligands with pendant sulfur groups, such as bis(2-

(thiophenyl)ethyl)amine (phS) and bis(2-(selanylphenyl)ethyl)amine (phSe), demonstrated that the presence of heavy atoms it slightly diminishes the energy gap between HOMO and the LUMO of all MCC energies [69].

From **Table 9**, MCC **1** has the highest HOMO energy within the studied groups in this study, a phenomenon predominantly attributed to the resonant character of the ligand **L1**. The resonance effect stabilizes the electron density, thereby contributing significantly to the observed elevation in oxidation potential. The ligand **L2**, that is, the reduction of **L1**, was corroborated with the resonance influence. Upon loss of this effect, the manganese ion experiences facilitated oxidation to Mn^{II}, rendering compound **2** necessitating only half the voltage compared to compound **1**. For MCC **4**, the same behavior is noticed in NMR, even though the HOMO energy is slightly lower than **2**, this is due to **L4** having a higher electron acceptor characteristic which helps to stabilize **4** by increasing the oxidation energy of MCC **2**.

Table 9. Oxidation potentials *vs* Fc/Fc^{+} and HOMO energy for **1-4.**

Compounds	E_{pa} Mn $^{I/II}$(V)	E_{pa} Mn $^{II/III}$ (V)	HOMO energy (eV)
1	0.82	0.99	-5.70
2	0.41	0.81	-5.83
3	0.40	0.65	-
4	0.58	0.78	-5.89
phS	0.71	-	-4.85
phSe	0.77	-	-5.92

1.4.3 CO PHOTODISSOCIATION STUDIES

1.4.3.1 UV-Vis and FTIR analysis

The CO release activity of all synthesized compounds was tested in CH_2Cl_2 solutions, using an excitation wavelength on 450 ± 15 nm for **1** and **2** and 395 ± 5 nm for **3** and **4**, and the changes are monitored in V-Vis, and FTIR spectra solutions.

First, the stability of **1-4** in CH_2Cl_2 solution was offered by periodically recording its absorption spectrum over a period of 24 h, **Figure 45**. In dark conditions, no

significant decay was observed apart from **2** that had a significant decrease. To avoid discrepancies on their CO releases, all MCC solutions were freshly prepared prior analysis. When exposed to light, all MCC solutions exhibit systematic changes in electronic absorption spectra upon exposure to low power blue and violet light, with 450 nm; 4.47 mW cm^{-2} and 395 nm; 3.44 mW cm^{-2}, respectively, due to the photo excitation of the MCC triggering the release of the CO.

Figure 45. Compounds **1-4** stability based on maximum absorption value, 1.00 x 10^{-4} mol L^{-1} in dichloromethane.

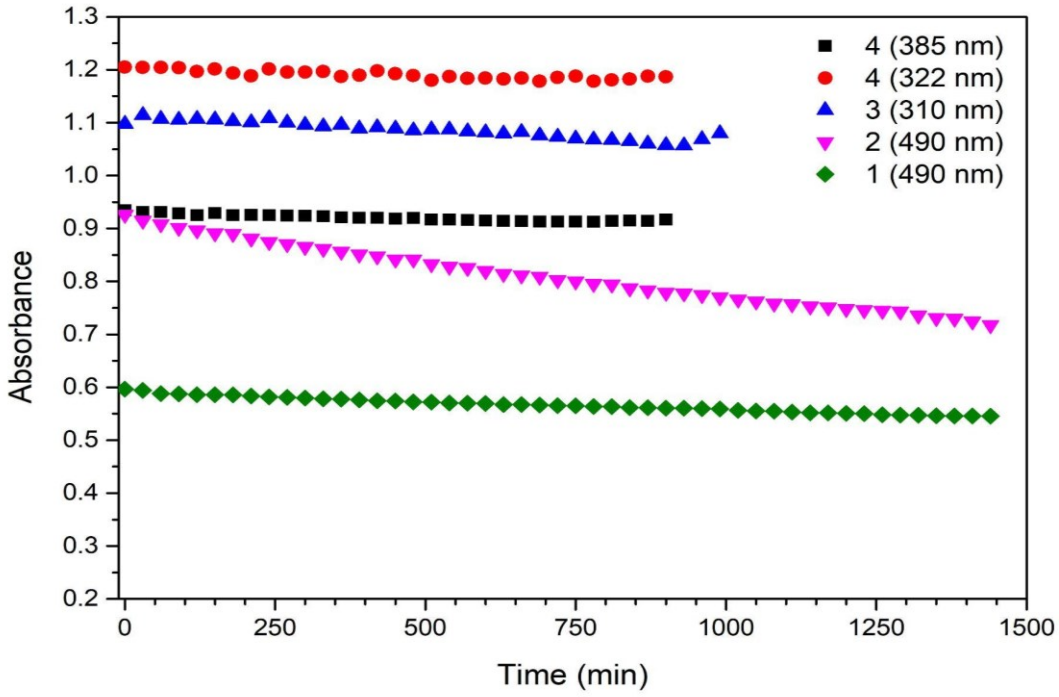

All photoCORMs show a constant decrease of their MLCT bands as more irradiation time is applied, **Figure 46**. Compounds **1** and **2** had, as their bands at 490 nm are extinguished, another band formed around 605 nm and 615 nm. Alongside with the process of release, the formation of an isosbestic point was also observed during the photodegradation process, indicating an equilibrium with the intermediates, for example biscarbonyl compound, in agreement with what is seen in the literature [99].

This pattern is due to the release of the CO molecules from coordination sphere for MCC with the C_{3v} symmetry that loses its form to form another photogenerated species with one less CO in its coordination, shifting the MCLT band to higher energy thus creating the new band at 605 nm and 615 nm. The same behavior is seen in **3**

and **4**, both without extra bands formed, showing only the decay of their MLCT band in 310 nm and 385/322 nm, respectively.

The increase in the baseline due to the formation of photoproducts as MnO is also noted for all compounds, with more attenuation for MCC **2**, that is insoluble and scatters light. Such behavior also is also noticed on other Mn(I) photoCORMs based and indicate a total degradation of MCC and the release of the CO molecules to the media [100].

Figure 46. Variation of MLCT in CH_2Cl_2 over the period of irradiation with 450±15 nm (blue light) for compounds **1** and **2** and 395±5 nm (violet light) for compounds **3** and **4**. The insert shows release kinetics for each compound.

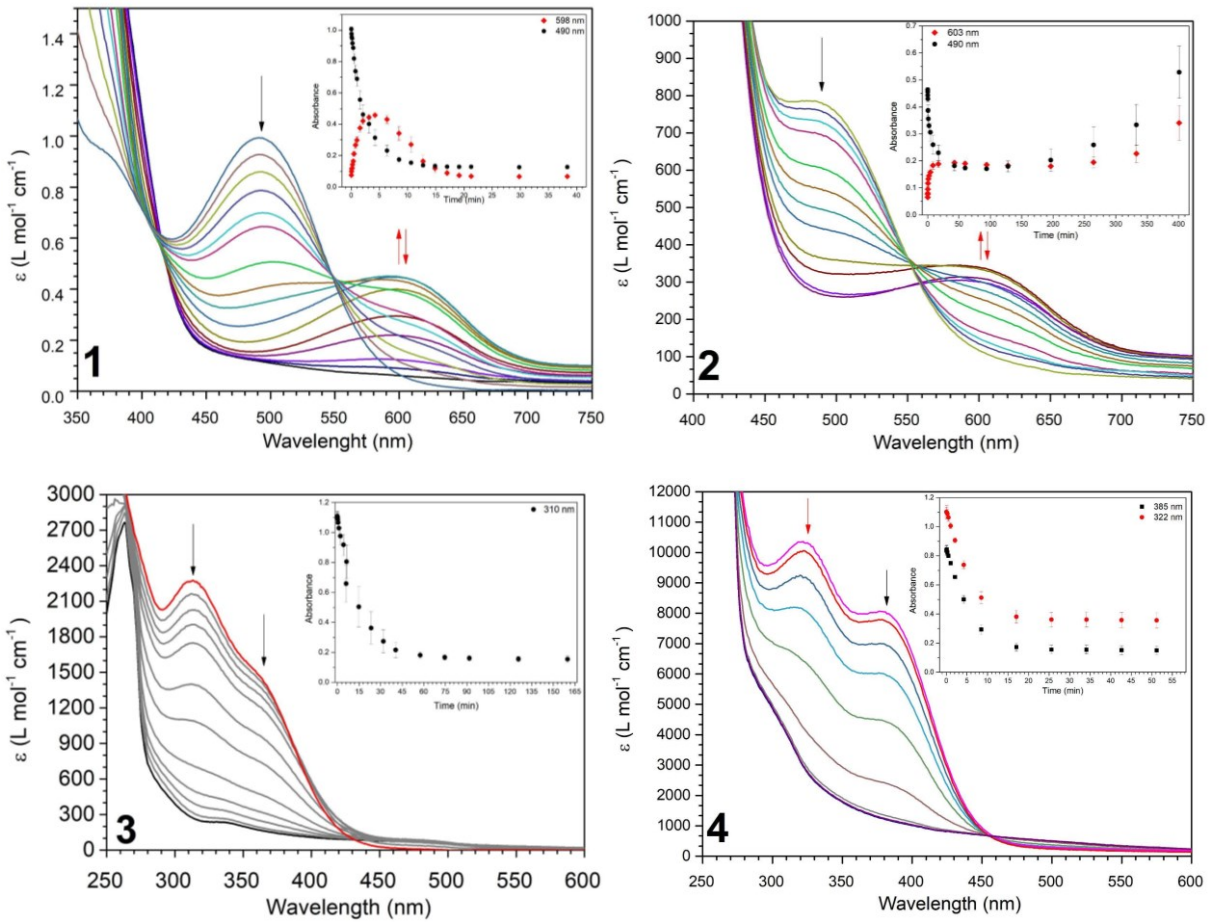

It has been reported that the quantum yield for the exchange of the first CO ligand (φ_{CO}) from Mn(I) photoCORMs generally increase with increasing the π-acidity of the *N*,*N*' ligand. The rate of CO-release (k_{CO}) from **1**-**4** was calculated from the changes in electronic absorption spectra upon exposure to light at regular time

intervals. The quantum yield (**φ**) values, **Table 10**, decreases when the resonance effect was removed from the structure, as expected, and found in the literature [101]. The values show a 10 times decrease from **1** to the other three compounds, which is consistent with the literature with similar MCCs with *N,N*' bonding ligands [92].

Structures **2-4** show a small variation in their quantum yield values, indicating the low influence of the chalcogen part of the ligand, independent of the way the sulfur is connected, in front of the resonance influence. The CO release process is directed proportionally to the excitation region, hence **3** and **4,** when irradiated with the blue led (395 ± 5 nm), fall too far from their absorption maxima, showing an insignificant CO release, resulting in low quantum yield and for those a suitable LED was used.

Table 10. Constants and quantum yield for the CO photodissociation process. Excitations were made at their absorption maxima being **1** and **2** with LED λ_{max} in 515±15 nm and **3** and **4** with LED λ_{max} in 395 ± 5 nm.

MCC	φ (10^{-3})	k_{CO} (10^{-3} s^{-1})
1	49.50 ± 0.20	7.13 ± 0.16
2	8.98 ± 0.28	3.59 ± 0.02
3	4.20 ± 0.05	1.16 ± 0.02
4	2.35 ± 0.14	2.79 ± 0.07

The changes in **1** to **4** IR spectra were monitored in solution and the behavior in the extinction of its three major CO stretching bands was followed during the photoirradiation process, providing important information about the photochemical reaction intermediates, **Figure 47**. Photoproducts are seen around the region of 1855 cm^{-1} for MCC **1** to **3**. According to the literature [102], this intermediate is likely to be a biscarbonyl complex, due to frequency of CO stretching matches with an antisymmetric movement, meaning that a CO and Br^- are replaced by solvent in this scenario. Compound **4** has not shown any new band appearing concomitant with the diminishment of the main CO stretching, indicating that MCC **4** does not form biscarbonyl as an intermediate and degrades at once while releasing CO. In all spectra a band forms as the photo irradiation progresses on 2135 cm^{-1} being related to free CO, another indication of the release of the gaseous molecule to the media.

Figure 47. Variation of FITR spectra in CH_2Cl_2 over the period of irradiation with blue light (450±15 nm) for compounds **1** and **2** and violet light (395±5 nm) for compounds **3** and **4.**

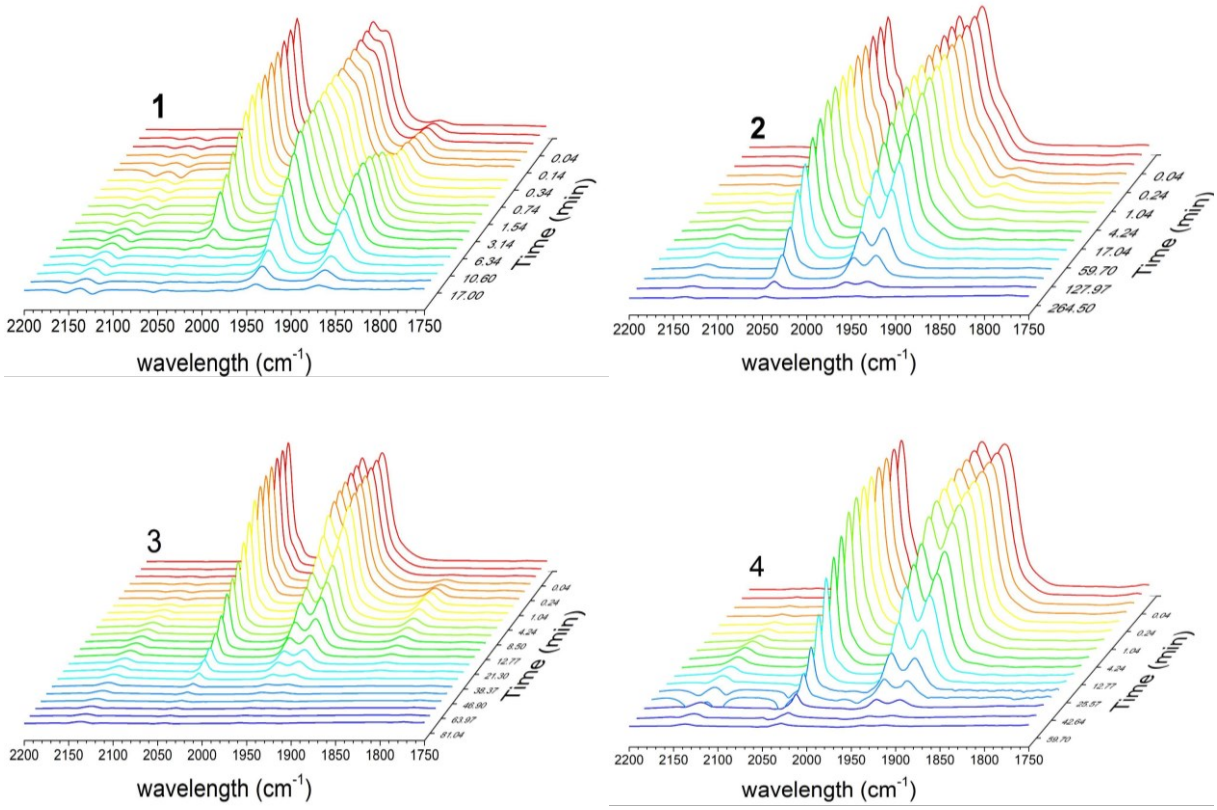

1.4.3.2 Myoglobin intake assay

Evaluation of CO release from photoCORMs under physiological conditions is typically performed by studying myoglobin carboxylation. Myoglobin (Mb) exhibits a characteristic absorption spectrum in the absence of any gas molecule (deoxy-Mb), with a maximum around 560 nm corresponding to its Q-band [82]. Upon coordination with CO gas, myoglobin forms carboxy-Mb (MbCO). The binding of CO gas to myoglobin leads to spectral changes, transitioning from a single absorption band to two absorption bands around 540 and 580 nm [81]. This spectrophotometric methodology utilizing myoglobin carboxylation serves as a standard approach for analyzing CO release from photoCORMs.

To ensure the capture of the three potentially labile CO molecules released from the photoCORMs, the concentration of myoglobin in the assay was maintained at least

three times higher than that of the photoCORMs. This ensures an adequate supply of myoglobin for the efficient coordination and capture of CO gas species.

A buffer solution containing compounds **1-4** was prepared, and their spectral changes were monitored using a modified myoglobin assay, as described by Weiss et al. [98]. The release of CO was tracked until no further visual changes were observed in the UV-Vis spectra, as shown in **Figure 48**. The release occurred approximately at 240 minutes of irradiation, and compounds **1** and **2** exhibiting LED λ_{max} at 515±15 nm and compounds **3** and **4** displaying LED λ_{max} at 395±5 nm. These results indicate the stabilization of MbCO, signifying that no further release of CO(g) from **1-4** occurs.

Figure 48. UV-Vis spectrum variation of deoxy-Mb in presence of CO(g) release to the media by **1-4** (1.00×10^{-5} mol L^{-1}) in PBS (0.1 mol L^{-1}) during UV light excitation (λ = 395 ± 5 nm).

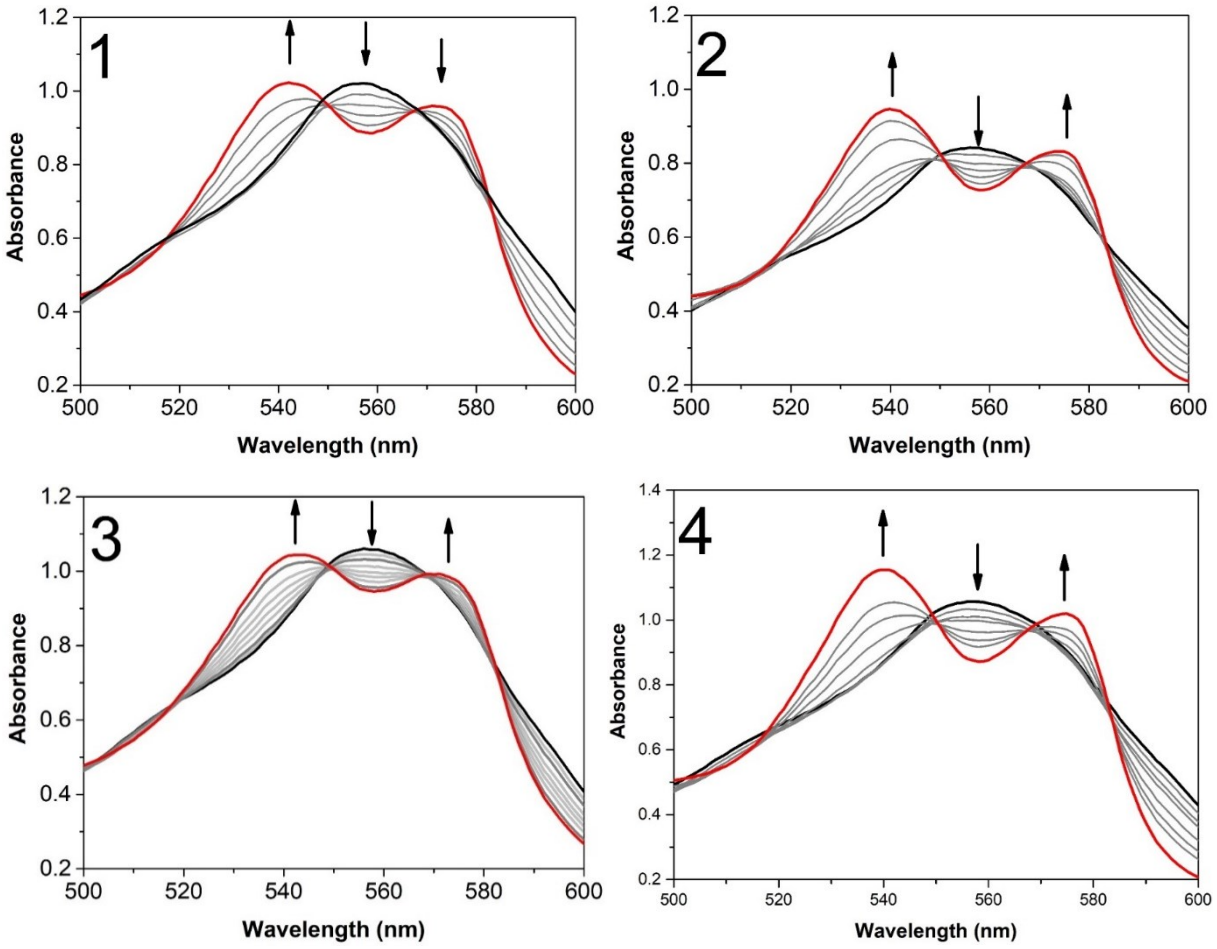

The findings derived from the myoglobin assay have been meticulously collated and systematically presented in **Table 11** for comprehensive analysis. The data elucidates the capture of approximately 2 moles of carbon monoxide gas per mole of

Mb. This observation underscores that the protein sequesters the released CO emanating from the compounds, affirming their role as CORMs.

The half-life times of CO release ($t_{½}$), which range from 50 to 155 minutes upon exposure, provide insights on the kinetics of this process. Notably, the observed half-life time in the myoglobin environment surpasses that determined by UV-Vis and FTIR measurements. This intriguing disparity likely derives from the unique intrinsic chromophoric characteristics of myoglobin and the nuances of the buffered protein solution. Furthermore, the presence of various ions and chemicals within the protein solution can lead to considerable variability in the data, making the analysis more intricate and challenging.[81].

Likewise, it is imperative to acknowledge the multifaceted nature of the mechanisms and parameters at play within the myoglobin milieu, as widely documented in the scientific literature [77]. This recognition underscores the need for a holistic understanding of the intricate interplay between biomolecular entities and their surrounding environments, serving as a cornerstone for elucidating complex physiological phenomena.

Table 11. Quantity of CO photo dissociated captured by Mb and half lifetime for MCC **1-4.**

MCCs	Nº Mol eq	$t_{½}$ (min)
1	2.5 ± 0.05	70.7 ± 2.4
2	2.6 ± 0.05	20.9 ± 4.1
3	2.2 ± 0.33	154.2 ± 14.5
4	2.5 ± 0.24	49.5± 9.0

1.5 CONCLUSIONS

The utilization of carbonyl compounds in the development of photoCORMs represents an advance in phototherapeutic interventions, offering applications in antitumor, vasoregulatory, and pulmonary therapies with minimal or negligible side effects.

In this investigation, we explored four well-established ligands from existing literature for the synthesis of three new manganese(I) based compounds for potential photoCORMs application. Using combined IR, UV- vis and NMR measurements, and electrochemistry research, we were able to confirm that all compounds release of CO upon exposed to visible blue and violet light (λ_{450}; λ_{395}).

The introduction of a sulfur atom into the ligand framework manifests only a marginal deviation in their quantum yield values, suggesting minimal influence of the chalcogen moiety of the ligand, irrespective of its connectivity. This observation emphasizes the predominant resonance effects observed in compound **1**.

Moreover, all synthesized compounds exhibited the ability to release CO in physiological media, subsequently sequestered by myoglobin. Among the novel photoCORMs investigated in this study, three displayed extended half-lives, indicative a slower CO release and subsequent capture by the myoglobin protein, with the order of longevity observed as **3** > **1** > **4** > **2**.

Overall, mechanistic insights into the photodissociation of these compounds offer valuable perspectives for enhancing control over carbonyl photorelease. Furthermore, scaling up these compounds for enhanced therapeutic applicability necessitates considerations such as solubility in aqueous media, π-acceptor character to facilitate bathochromic shifts, and aggregating such compounds to nanocarriers.

CHAPTER 2

TRANSFORMING LIGNOCELLULOSIC BIOMASS: A Sustainable Path to High-Performance Photo- and Electrocatalyst Carbon Dots

2.1 LITERATURE REVIEW

2.1.1 NANOMATERIALS

Materials ranging from 1 to 100 nanometers are called nanomaterials. From the sci-fi movies we get a close idea of how so-called quantum effects take place at scale, disclosing unique properties from their macroscopic counterparts [103]. The quantum confinement effect (QCF) and high surface-to-volume ratio are among the distinctive features establishing nanomaterials as an independent field of study. The Intrinsic material properties, such as optical, magnetic and electronic, are bond to their size making such materials highly versatile for applications [104].

The nanomaterials' dimensionality is the basis for their classification, properties and applications. They can be zero-dimensional (0D), one-dimensional (1D), two-dimensional (2D) or three-dimensional (3D) nanostructures. Some examples for each dimension are quantum dots (QDs), nanotubes, graphene and aerogels, respectively for 0D to 3D [105].

Humans have already used and dealt with nanoparticles since an early age, more than 4500 years ago, reinforcing ceramics with nanofibers of asbestos [106] or the Egyptians, 4000 years ago, with their hair dyes of PbS nanoparticles (NPs) [107]. The first scientific report on NPs production came from Michael Faraday back in 1857, where he revealed optical Au NPs properties, glazing at the quantum size effects vs their bulk counterparts [108]. A century later, in 1959, Richard Feynman said in a lecture, "There's Plenty of Room at the Bottom" [109] he envisioned and introduced the concept of nanotechnology, where he predicted manipulations of small machines down to the molecular level. The term itself was only formally defined by Drº Norio Taniguchi, a Japanese scientist in 1974.

Along with the ideas of nanotechnology, the need for new equipment capable of measuring and “seeing” such small particles. The development of scanning tunneling microscopy (STM) [110] arose soon after in 1981 by Gerd Binnig and Heinrich Rohrer, which besides granting the ability to not only to visualize atoms but also manipulate them. Soon after in 1989, milestone in the application of nanotechnology came when Don Eigler and Erhard Schweizer, researchers at IBM's

Almaden Research Center, manipulated 35 individual xenon atoms to spell the IBM logo, showing in their article the precision achievable in atom manipulation [111].

Back in 1981, a Russian scientist Alexei Ekimov discovered nanocrystalline, semiconducting quantum dots in a glass matrix and conducted pioneering studies of their electronic and optical properties, but due to several political issues, those findings were only revisited worldwide a few years later [112] [113].

Then came the discovery of a new allotropic form of carbon – the buckminsterfullerene (C_{60}) in 1985 by researchers Robert F. Curl, Harold W. Kroto, and Richard E. Fullerenes are carbon nanoballs with 60 atoms of carbon capable of enclosing metals with all quantum world properties, opening a new chemistry field based on carbon nanostructures, and granting the trio the Nobel Prize in Chemistry in 1996 [114].

In 1991, The first reports on carbon nanotubes by Sumio Iijima's, added another layer to the carbon-based nanomaterials field. These cylindrical carbon structures exhibited extraordinary mechanical, electrical, and thermal properties, laying the groundwork for numerous applications in modern industry.

In 2004 two other carbon allotropes forms of carbon came to light. One is graphene, a single layer of graphite isolated by Novoselov et al [115]. One atom thick sheet of sp^2 carbon possesses remarkable properties, including outstanding electrical conductivity, expansive surface area, excellent mechanical strength, high thermal conductivity, optical transparency, and elasticity. Since then, graphene has garnered recognition as a fundamental building block for other carbon materials and allotropes. Graphene still holds the role as the thinners and stronger material ever and with a widespread application in the industry and technology [116].

The other carbon allotrope accidentally discovered by Xu et al during the purification of carbon nanotubes are carbon dots (CDs), the newest to join the family of carbonaceous material. Their photoluminescence properties rapidly made CDs a rising star of nanocarbon materials due to their low relativity toxicity, high solubility, good thermal and chemical resistance, abundant in sources and cost-effective nature [117].

2.1.2 CARBON DOTS

Since their accidental discovery, carbon dots have been extensively investigated by several groups around the world, having more than 10 thousand publications in the first 2 months of 2024. Such interest from the scientific community is due to their strong and tunable fluorescence emission properties, high stability and solubility with and ease functionalization [118]. Since CDs are basically carbon, their intrinsic non-toxicity also calls attention to their biological and medicinal applications, especially on bioimaging [119]. Their surfaces also allow easy functionalization with different functional groups such as amino, carboxyl, hydroxyl and sulfonic groups. Therefore, implying the property of a more controllable particle.

The fundamentals of CDs fluorescence are not yet set in stone[120]. As some authors describe the traditional concept of any nanoparticles, their fluorescence being size-dependable. Meaning that their electronic transitions come from within the CDs core layers, which are influenced by quantum confinement [121], [122]. This theory is the most accepted by the scientific community, but other authors also report their fluorescence arises from surface-trapped charges recombination [123]–[125] or a mixture of both phenomena [126], [127] plus some yet question the solvent influence on their optoelectronic properties [128]. The fact is that the materials are yet a mystery to be unveiled in their nanoworld but they have interesting properties applications in the macroworld.

2.1.2.1 Properties

2.1.2.1.1 Physical and chemical

As already stated, carbon dots are extremely small particles, whereas several quantum effects come to have major influences. CDs, as generic term, classifies different nano structures upon their morphologies, constituting the polymers dots, graphene dots and carbon dots groups [129]. Polymer dots (PDs) are considered those formed by aggregation or a conjoin of several polymers like fibers. PDs have a complex core and an undefined overall shape with their photoluminescent (PL) effect mostly coming from the high density molecular surface [130] . For graphene dots (GDs), their structure is based on graphene sheets (maximum of 5 layers) with functionalities at the edges of the materials, granting them an overall anisotropic shape. The GDs PL

properties usually arise from the π-conjugations and their functional groups [131], whereas the increase of defects by oxidation is reported to increase the PL effect [132]. Carbon dots are always (semi)-spherical, and their core consists of several layers of graphene, being crystalline or not. CDs with an amorphous core structure tend not to present quantum confinement effect (QCE) like those with a crystalline lattice in their core, therefore the PL are only given by the molecular and surface states and not by the quantum confinement effect [133], [134].

CDs present a high thermal resistance, since their synthesis occurring at high temperatures (over 1000ºC) [135]. They also present better photostability over metallic quantum dots, granting them longer and greener applications and usability [136].

In addition to their already good solubility, CDs present a PL response to their media. Such changes are due to the fact that their functional groups changed their charges as the pH and temperature are altered [137]. The Chang groups produced CDs from green tea leaves where PL decreases while the pH becomes more basic [138]. Even though their structure changed, they kept their core and structure, showing only surface changes. CDs show a remarkable resistance and can be stored over a year without major degradation [139].

2.1.2.1.2 Optical and electronic

One of the most attractive properties is that CDs exhibit PL due to their quantum-limited structure, optical stability, and high fluorescent quantum yield (QY). The diverse synthesis methods, condition and start materials grants CDs emissions from ultraviolet to red, and even white [140]. The mechanisms of PL are still under investigation and dependent on their physical characteristics, such as size and surface groups, in which they directly affect their band gap [136], [140]. A widely accepted theory on the PL of carbon dots suggests that this strong effect arises predominantly from electronic transitions within the sp^2 domains of their core structure. This property exhibits an inverse relationship with size, implying that smaller CDs possess larger band gaps. Additionally, the nature of the carbon source used in the synthesis process, and even the synthesis process itself, dictate core size, crystallinity and composition, thus playing a crucial role in determining the optical properties of the CDs.[141].

Since the core structure determines the band gap of CDs and exerts a noteworthy influence on their PL, the usage of a doping strategy with electron-rich heteroatoms, such as nitrogen or sulfur, might alter their optical and electronic properties. Moreover, the literature also points out that the presence of oxygen groups on their surface also takes part in the electron transfers from CDs, contributing to their PL effect [142]. Since CDs are considered semiconductors, when their structures are doped with an electron donor atom such as nitrogen, the heteroatom acts as a bridge shortening the energies between highest valence and the lowest condition bands [143]. Therefore, carefully studying and planning their synthesis is essential for modulating the physical and optical properties of CDs. This includes selecting appropriate source materials, optimizing synthesis processes and applying various treatments. Such considerations enable CDs to exhibit versatility and offer a wide range of potential applications.

2.1.2.2 Synthesis methods

There are two most common approaches for the synthesis of CDs, Top-down and bottom-up methods. Top-down synthesis generates more well-defined carbon dots structures and allows an up-scale for industrial fabrications. On the other hand, bottom-up produces a more diverse CDs, allowing an easy surface modification, allows doping and possesses greener synthesis [144].

2.1.2.2.1 Top-down methods

In the top-down approach, the carbon dots are synthesized by breaking down larger carbon structures into smaller nanoparticles [145]. Techniques such as laser abolition, arc discharges and ultrasonic synthesis are a few examples for cutting down initial material into the carbon dots. Most commonly uses cleavage and exfoliation of other carbon structures such as graphite, carbon fiber, carbon nanotubes and coal. Since it comes from already known carbon structures, this approach generates a more uniform, precise size and composition of carbon dots [146].

A drawback of these methods is the difficulty of generating doped CDs, as doping can better define properties and applications. Therefore, graphene-oxide is widely used for CDs generation over other sources since the graphene sheet is abundant in reactive hydroxyl, carboxyl and epoxy groups [116]. Another limitation is

the need for advanced machinery to acquire such nanostructures, which produces waste and requires more energy, leaving the scope of greener chemistry.

2.1.2.2.1.1 laser ablation

Laser ablation consists of using a high-energy laser to irradiate material and rapidly increase sample temperature and removing carbon from material. As a result, carbon vapor crystallizes forming CDs structures. Laser ablation produces almost zero contamination and laser power, distance and irradiated area can control particle sizes [147].

It was first used by Sun et al. when they used graphite as source to be ablated with laser at 900ºC and 75 kPa pressure, using argon as carrier gas [148]. The product was further refluxed for 12 h on HNO_3 in the presence of polymers such as PEG1500N and PPE-EI to passivate the surface. The CDs obtained by them presented QY up to 10% and 5 nm wide.

Szymanski group used graphite and rGO as carbon sources in a two-step laser ablation, 1st at 1064 nm and 2nd on 355 nm in the presence of PEG200 polymer. Obtaining CDs with average size of 2 nm within 90 min of irradiation for graphite and 15 nm for rGO [149].

2.1.2.2.1.2 arc discharge

Arc discharge usually happens in a closed chamber with an inert gas and low pressures. The electrodes can be constituted of pure graphite or a metal with the cathode being the source of carbon. The applied electric current generates plasma that evaporates carbon and crystallizes on the cathode.

This method was proposed by Xu et al. that was used in the purification step of carbon nanotubes, producing the by-product that was later named and gave origin to CDs novel [117]. Unfortunately, this method offers mediocre quality CDs, with small yield. It was later discovered that the distance between the electrodes and the appliance of a magnetic field boot size control and quality of CDs generated [150].

2.1.2.2.1.3 ultrasonic synthesis

This method uses ultrasonic energy that creates pressure zones within the liquid media generating vacuum bubbles. This unique energy source can drive chemical reactions to occur, especially when trying to break down particles while keeping solute dispersed avoiding their aggregation. It is one of the few techniques from top-down that can use materials other than carbon allotropes.

First used by Park et al. in a greener synthesis process using various food wastes as source for CDs. They used an alcoholic medium and 40k Hz ultrasound on dispersed food waste to mass produce CDs of around 4 nm wide with strong PL at ~435 nm [148] . Zhu et al used GO as a source and $KMnO_4$ as an oxidizing agent for a relatively short time of 4h; managed to generate graphene CDs of 3 nm wide and PL at 475 nm [151].

2.1.2.2.2 Bottom-up methods

In the context of bottom-up synthetic methodologies, CDs are systematically formed from small precursor molecules, predominantly of organic origin. Techniques such as microwave, pyrolysis and hydrothermal treatments can produce sp^2 carbon domains of nanometric sizes [152]. Bottom-up approaches are usually preferable due to their easy set up and diverse source materials of CDs, that usually involve using biomass waste. There are several reports from CDs being produced from Human Hair [153], acerola [154], olive pits [155], a number of fruits [156] and industrial waste [157].

Coupled with the low cost, greener synthesis and easy setups, such methods allow easy size control, doping and photoluminescence. Nonetheless a few challenges from this approach needs to be addressed such as the low yield, especially when it comes from organic waste materials, that need of purification steps and present difficulties on scaling up [158].

2.1.2.2.2.1 microwave synthesis

Microwave synthesis is a well-established method for chemical reactions. It produces fast and homogenous thermal zones from within the system. Such energies from microwave breakdown bind and excite molecules, being advantageous on conversions of matter, especially from biomass and small molecules [159].

Algarra et al. produced CDs by microwaving 15 min lactose in HCl at 160ºC. These products had high quality fluorescence and averaged 6 nm of size [160]. CDs were also obtained using crab shells by Yaw et al., where they added metal salts into the media. They obtained metal doped CDs of around 4 nm width after microwaving the grounded material 10 min with $GdCl_3$, $MnCl_2$, and $EuCl_3$, at 220 ºC [161].

2.1.2.2.2.2 thermal decomposition

Thermal decomposition or pyrolysis is a straightforward technique involving carbonizing organic matter into photoluminescence CDs at high temperatures. Hu et al., produced CDs of 4 nm from ammonium citrate through a one-pot pyrolysis method. Ma et al., prepared blue emitting CDs with high fluorescence QY and sizes of 5 nm using citric acid monohydrate and ethylenediamine [162]. Nitrogen doped CDs of 5 nm and 38% QY were also obtained from black soy beans by Shuang team [163].

2.1.2.2.2.3 hydrothermal treatments

Being one of the most used techniques, hydrothermal synthesis is based on pyrolysis of organic matter giving rise CDs in aqueous solution and high pressures. The use of water brings benefits when it comes to purifications, reaction conditions, environmentally friendly and doping [164].

Firstly being reported by Wang group, when they used glucose in the presence of monopotassium phosphate (KH_2PO_4) in an autoclave to generate blue (2 nm size) and green (4 nm size) emitting CDs [165]. Sulfur and nitrogen doped CDs were obtained from citric acid and L-Cysteine after 3h at 200 ºC by Amjadi et al.[166] .

Due to the easy synthesis this method is widely used to obtain CDs from biomass sources. Zue et al. used peanut shells and produced CDs of less than 10 nm wide. Pomelo peels were used by Sun group to obtain CDs of 3 nm and 6% QY [167] and bamboo leaves were used by Liu et al. obtaining 3 nm CDs with 7% QY.

2.1.2.3 Applications

Due to their physicochemical properties and diverse synthesis manner CDs have been used in a broad range of applications such as, bioimaging and drug for

medical used delivery, sensing diverse ions and catalyzing pollutant molecules, used on technological equipment and energy generation, storage and conversion.

2.1.2.3.2 Bioimaging

Bioimaging must be sensitive and precise to provide a high-resolution diagnostic. The exceptional optical properties of carbon dots, including tunable fluorescence and low cytotoxicity, make them ideal candidates for this application. Zhu et al. produced suitable red-emitting CDs which were used for bioimaging in mice and for lung lesions [168]. Han et al. synthesized CDs capable of binding with DNA and RNA that emit fluorescence making them suitable for real-time image tracking [169]. Haupt and Wegener team obtained, using the hydrothermal method, N-CDs coupled with molecularly imprinted polymers as cancer biomarkers probes [170]. Several other groups also reported imaging capacity for glioma [171], breast cancer cells [172], stem cells [173], neural cells [174] and mitochondria [175]. CDs doped with manganese have also been reported as contrast agents for magnetic resonance imaging [176].

2.1.2.3.3 Drug Delivery

Carbon dots, with their biocompatibility and ability to encapsulate therapeutic agents, are explored for drug delivery applications [177]. Their nanoscale size facilitates efficient cellular uptake, and their surface can be modified for targeted drug delivery, potentially revolutionizing drug delivery systems[178].

Koduru's team were able to develop CDs made from carrots to successfully deliver mitomycin by hydrogen bonding the drug to MCF-7 and bacteria cells [179]. Gu et al. synthesized CDs from milk, there were capable of delivering doxorubicin, a chemotherapeutic drug, to cancerous cells [180]. The Zhao group fabricated CDs as carriers of *cis*platin(IV) into tumorous cells, increasing its uptake and reducing cytotoxicity. Other drugs already used for cancer treatments, such as lisinopril and vancomycin, have also been reported as being transported, monitored and delivered by CDs [181].

2.1.2.3.4 Sensing

Due to their surface being covered by diverse chemical functions, carbon dots are extremely sensitive to changes in their environment, making them excellent

candidates for chemical and biological sensing. They can be engineered to detect specific analytes, contributing to the development of highly selective and responsive sensors [182].

CDs fluorescence quenching is exploited to selectively sense metal ions, changes in pH, and small inorganic and organic molecules. Nag *et al* developed CDs functionalized with chitosan that were able to detect water in organic solvents [183]. Meanwhile, Wang's team modified the surface of CDs, made from citric acid, with PEI. PEI-CDs were able to detect CO_2 in organic solvent [184] and SO_2 were quantitatively measured using CD engineered cyanine dye by Wang et al. [185]. Variations on pH of living cells were also able to be monitored using N-CDs synthesized by Jiao et al.[186]. CDs were also able to sense several biological analytes as enzymes, DNA and metal ions [187].

2.1.2.3.5 Catalysis

CDs exhibit photocatalytic activity under light irradiation, hence enhancing the efficiency of titanium dioxide (TiO_2) and other compounds. They can be employed for pollutant degradation, water purification, and removal of contaminants due to their ability to generate reactive oxygen species (ROS) [188]. Qu et al. used GO as a source of CDs to modify the TiO_2 surface and improve the degradation of methyl orange. Haitao et al. synthesizes a novel of multi-colored size dependable CDs using graphite rods via arc discharge method. They used their CDs to enrich TiO_2 and SiO_2 based photocatalysis to degrade methylene blue [136]. Several medical contaminants as antibiotics were able to be degraded by a photocatalytic process assisted by CDs [189].

2.1.2.3.6 Optronics

Since CDs are best known for their PL, obvious applications in electronic devices and optoelectronics are expected. They can be incorporated into sensors, light-emitting diodes (LEDs), and photodetectors, benefiting from their conductivity and luminescent properties [190].

Zhang et al. were able to produce blue emitting CDs, functionalized with polymers, increasing in 12% the power conversion of solar cells, by just coating with a layer of nanostructures into the cover glass [191]. Wang et al. developed a white

emitting CD from citric acid as an alternative to phosphorus compounds for LED [192]. Guo et al. were also able to fabricate blue, orange and white LED devices by pyrolyzing colloidal polymer crystal at different temperatures to obtain the different emitting CDs [193].

2.1.2.3.7 Energy generation

Carbon dots demonstrate captivating photophysical properties characterized by robust light absorption and tunable photoluminescence. These distinctive features render them well-suited for integration into photovoltaic devices where CDs can augment light absorption, facilitate charge separation, and potentially enhance the overall efficiency of solar energy conversion [194]

Since the CDs surface can act as an electron trap, thus stabilizing an electrode, Tong et al. used a hydrothermal method to produce CDs from sucrose to coat VO_2 nanowires, enhancing the chemical properties of the material but also the storage performance of Li^+ and Na^+ ions [195]. Briscoe et al. designed a biomass derived CDs to improve the ZnO nanorods light absorption, making them optimal to solid-state solar cell [196].

Moreover, the inherent photocatalytic activity of CDs, driven by their capability to generate reactive oxygen species under light irradiation, positions them as promising contenders for photocatalytic water splitting. This process, geared at the hydrogen production via Hydrogen Evolution Reaction (HER), presents a viable path for sustainable and clean energy sources [197].

Yeh et al. were able to fabricate nitrogen CDs with band gaps of 2.2 eV, active for H_2 and O_2 evolution reactions under visible light, mimicking biological pathways [198]. Kang's group proposed a diverse CDs surface modification with phosphorus, via electrochemical graphite etching, and amidogens, via hydrothermal, that had electrocatalytic activity close to the Pt/C catalyst under visible light [199]. Song et al. used theoretical predictions to design defective N-doped CDs to create a molybdenum phosphate nanocomposite, using different concentrations of N to optimize the HER. They found out that N doping promoted the adsorption of HER intermediates by changing their electronic arrangement of composite [200].

2.2 AIMS AND OBJECTIVES

2.2.2 AIMS

This research endeavors to design a facile and environmentally sustainable synthetic pathway for producing a novel of carbon dots nanomaterials. This entails utilizing biomass as a precursor, aiming to establish a green synthesis approach. The ensuing nanomaterials will undergo meticulous characterization, unraveling their intrinsic properties through systematic investigation. Furthermore, the investigation will explore and assess the prospective utility of these carbon dots as photocatalysts, as hydrogen generator and their influences on the photoCORMs properties (discussed on chapter 1), thereby contributing to a broader understanding and advancement of the sustainable nanomaterial applications.

2.2.3 OBJECTIVES

- Elaborate a green and easy bottom-up synthetic route for carbon dots using biomass;
- Synthesize carbon dots doped with nitrogen and sulfur;
- Characterize them using standard techniques: XPS, HR-TEM, TGA and other spectroscopies;
- Submit and studies the CDs in applications such as:
  - Hydrogen evolution reactions;
  - Photocatalyst performance front the PNP pollutant;
  - As support in activating photoCORMs.

2.3 METHODOLOGY AND EXPERIMENTAL DATA

2.3.2 MATERIALS AND REAGENTS

The precursor material for producing carbon dots nanoparticles consisted of dry paper residues obtained from a paper manufacturer located in Aveiro, northern Portugal. These residues were initially shredded and milled using a 1 mm circular blade until obtaining a fine powder, which served as starting material for the subsequent hydrothermal treatment to synthesize the carbon nanoparticles. Chemicals utilized in the nanoparticle synthesis included sulfuric acid (95-98%), L-Cysteine, and urea (powder), all purchased from Sigma-Aldrich (Barcelona, Spain). These chemicals were

used as received, without requiring further purification unless specifically mentioned. Additionally, 4-nitrophenol (4-NP), sourced from Thermo Scientific, was employed in the catalytic tests. Ultrapure water, characterized by a conductivity of less than 1 μS/cm, was utilized in all experiments for the preparation of aqueous solutions.

2.3.3 INSTRUMENTATION AND METHODS

2.3.3.2 Elemental analysis (CHN)

Elemental analysis was performed on a CHNS/OAnalyser equipment, PerkinElmer brand, model 2400 series II using helium carrier gas.

2.3.3.3 High Resolution-Transmission Electron Microscopy (HR-TEM)

The morphology analysis to obtain particle size was obtained by HR-TEM with a FEI Talos F200X equipped with an FEG 200kV electron gun, four STEM detectors, and four FEG detectors in conventional TEM mode, 80 kV power.

2.3.3.4 X-Ray Photoelectron Spectroscopy (XPS)

The surface analysis was recorded on a Physical Electronic spectrometer (PHI Versa Probe II) using monochromatic AlK_{α} radiation (15 kV, 1486.6 eV), a dual beam charge neutralizer for analyzing the core-level signals of the elements of interest, and a hemispherical multichannel detector. The sample spectra were recorded with a constant pass energy value of 29.35 eV, and a beam diameter of 100 or 200 μm. The energy scale was calibrated using Cu $2p_{3/2}$, Ag $3d_{5/2}$, and Au $4f_{7/2}$ photoelectron lines at 932.7, 368.2, and 83.95 eV, respectively. The spectra obtained were processed using MultiPak v 9.3. All values were referenced to adventitious carbon (C 1*s* at 284.8 eV).

2.3.3.5 Fourier transform infrared (FTIR)

The FTIR spectra were acquired using the FTIR spectrometer model 6800FV manufactured by Jasco Analytica. The measurements were conducted on dry potassium bromide pellets. Each spectrum was collected 64 times and subsequently corrected for background noise to ensure accuracy and reliability of the data.

2.3.3.6 Thermogravimetric analysis (TGA)

Thermogravimetric analysis was conducted using a DTG-60 thermogravimetric analyzer manufactured by Shimadzu, Japan. Approximately 5 mg of sample were utilized, and a heating rate of 10 °C/min was applied under a nitrogen atmosphere. Elemental chemical analyses were performed employing a CHNS/O analyzer from PerkinElmer, specifically the model 2400 series II.

2.3.3.7 Quantum yield (ϕ)

The quantum yield calculation was based on **Equation 10**, following IUPAC protocol [201].

$$\Phi=\Phi_{qs}*I/I_{qs}*A_{qs}/A*\eta^2/(\eta_{qs})^2 \quad \textbf{(Eq 10)}$$

Where Φ_{qs} represents the quantum yield of the standard quinine sulphate solution, I denote the integrated area under the emission peak, A is the absorbance of the solution at the excitation wavelength, and η indicates the average refractive index of the solution. The subscripts QS pertain to the standard quinine sulphate solution.

2.3.3.8 Optic Band Gap

The diffuse reflectance spectra (DRS) of the powder samples against a background of MgO were obtained using a Cary 5000 UV-Vis-NIR spectrophotometer (Varian). Samples were diluted in 1:10 ratio and band gap were measured from obtained spectra and extracted by Tauc plot of the Kubelka–Munk (F(R)) function, **Equation 11**. Where *K* and *S* are the K-M absorption and scattering coefficients, respectively and R is the diffuse reflectance value of que pallets.

$$F(R)=\frac{K}{S}=\frac{(1-R)^2}{2R} \quad \textbf{(Eq 11)}$$

2.3.3.9 Acute toxicity test

Acute toxicity tests consist in a suspension of 1 $mg{\cdot}cm^{-3}$ of each carbon dot variant in distilled water, followed by bioluminescence measurements of *Aliivibrio fischeri* bacteria using Microtox® equipment (BIOLUX, Brazil) following the ISO 11348-3 procedure [202]. Duplicate measurements were taken after 30 minutes of contact.

The resulting data were then inputted into Microtox® OMNI 4.0 software to calculate the EC_{50} values with a 95% confidence level.

2.3.3.10 Cyclic (CV) and Linear sweep (LSV) voltammetry's

CV measurements were conducted over a non-Faradaic potential range, employing scan rates ranging from 10 to 200 mV s^{-1}. The slope of the CV curves facilitated the calculation of the electrocatalysts' double-layer capacitance (C_{dl}). The active surface area (ECSA) was then computed using the equation expressing C_{dl} in terms of current density, **Equation 12** and **13**:

$$J_{dl} = \upsilon\, C_{dl} \qquad \textbf{(Eq 12)}$$

$$\mathrm{ECSA} = \frac{C_{dl}}{C_S} \qquad \textbf{(Eq 13)}$$

Here, C_s represents the specific capacitance of the glassy carbon electrode (GCE) in a 0.5 mol L^{-1} H_2SO_4 solution [203], [204].

Linear sweep voltammetry (LSV) curves were recorded with a scan rate of 0.02 V s^{-1}. Dispersions of each electrocatalyst were prepared by mixing 3 mg of each material with 375 µL of ultrapure water, 125 µL of ethanol, and 5 µL of Nafion solution (5 wt%). Following sonication, 2 µL of the resulting homogeneous dispersion of CDs or N-CDs were deposited onto a pre-polished GCE and dried at 40 °C for five minutes. All experiments were conducted under an inert atmosphere by purging N_2 for 7 minutes before each electrochemical measurement.

2.3.3.11 Hydrogen Evolution Reaction

The electrochemical experiments were conducted using a portable potentiostat, PalmSens 4, interfaced with a microcomputer, and data analysis was performed using PSTrace software (version 5.8). A three-electrode cell setup was utilized, consisting of a bare glassy carbon electrode (GCE) or CDs/GCE or N-CDs/GCE as the working electrodes (diameter: 3 mm), an Ag/AgCl (KCl saturated) electrode as the reference electrode, and a platinum wire as the counter electrode. A supporting electrolyte of 0.5 mol L^{-1} H_2SO_4 was employed. All potentials were referenced to the reversible hydrogen electrode (RHE), with the converted potential calculated as $E_{RHE} = E_{Ag/AgCl} + 0.059 \times$

pH + $E°_{Ag/AgCl}$, where $E°_{Ag/AgCl}$ = 0.1976 at 25 °C, and $E_{Ag/AgCl}$ represents the experimentally measured potential against the Ag/AgCl reference electrode.

2.3.3.12 Electrochemical Impedance Spectroscopy (EIS)

EIS measurements were performed in $[Fe(CN)_6]^{4-/3-}$ (5.0 mmol L^{-1} in KCl 0.1 mol L^{-1}) probe. The results were obtained in the frequency range between 50 kHz and 0.1 Hz applying 10 mV of sinusoidal voltage. The equivalent circuit was obtained with PSTrace software (version 5.8) for fitting the data of $-Z_{imag}$ *vs*. Z_{real} plot.

2.3.3.13 Photocatalysis studies

The photocatalytic activity of the carbon dots under UV light was assessed through the conversion of 4-nitrophenol (4-NP) in an aqueous solution. To compare the photocatalytic efficiencies of the CDs, a mixed aqueous solution containing 10 mg/dm^3 of 4-NP and CDs (1 mg cm^{-3}) was subjected to irradiation using a LED lamp with a power output of 560 mW and a peak wavelength of 365 nm. The irradiation process was conducted in magnetically stirred quartz cells, with the pH of the solution adjusted to 3.0 by adding 1 mol L^{-1} nitric acid solution. Absorbance measurements were performed at the wavelength corresponding to the maximum absorbance of 4-NP (310 nm) using a Jasco V-730 UV-visible spectrometer. The concentration of 4-NP was determined by applying Lamber Beer's law to a calibration curve of 4-NP concentration versus absorbance.

2.3.3.14 N-CD interaction with the PhotoCORMs

Nitrogen-doped carbon dots nanoparticles were synthesized via a simplified hydrothermal method reported in this work. In this process, 2.5 g of shredded paper and 0.25 g of urea were set in a 150 cm^3 Teflon lined stainless-steel reactor along with 50 cm^3 of H_2SO_4 (2.5% v/v solution). The resulting mixture was heated to 200 °C for 5.5 hours. Upon completion, the mixture was cooled to room temperature, centrifuged to remove any graphitic residue, and then filtered using 0.45 µm filters (Durapore). Subsequently, purification was carried out using dialysis bags with a molecular weight cutoff of 500 Da for three days, with the water being changed daily. The resulting solution was then dried by lyophilization to obtain fine powders.

For the interaction studies, 2 mg of N-CDs were dissolved in 1 cm^3 of acetone and transferred to a 10 cm^3 volumetric flask, which was then filled to volume with a solution of 0.1 mmol L^{-1} of the photoCORMs from chapter 1. The resulting solution underwent systematic exposure to light with wavelengths of 515 ± 15 nm for compounds **1** and **2**, and 395 ± 5 nm for compounds **1-4**. Spectral changes were monitored using the FTIR solution technique.

2.3.4 SYNTHESIS OF CARBON DOTS

To obtain non-doped and nitrogen-doped-carbon dots nanoparticles (CDs, N-CDs and S-CDs), 2.5 g of the biomass were transferred into a 150 cm^3 Teflon lined stainless-steel reactor with 50 cm^3 of H_2SO_4 (2.5% v/v solution). The resulting mixture was heated at 200 °C for 5.5 h. For the doped-carbon dots, urea was used as N source to synthesize N-CDs by adding a 10:1 ratio of biomass/doping agent in the synthesis (w/w) and L-Cysteine in same conditions to generate S-CDs. After the hydrothermal reaction (**Figure 49**), the mixture was cooled to room temperature and centrifuged to remove any graphitic residue following a filtration with 0.45 µm filters (Durapore). For further purification, the solution underwent dialysis in 500 Da bags for three days, changing the water daily. The resulting solution was dried by lyophilization, obtaining fine powders.

Figure 49: Schematic representation to obtain the CDs, N-CDs and S-CDs.

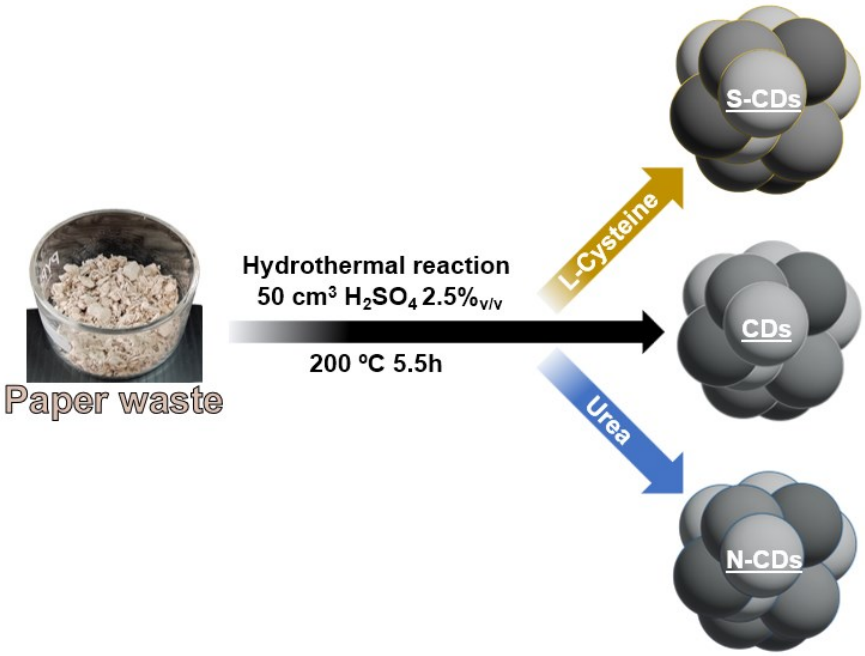

2.4 RESULTS AND DISCUSSION

The CDs and N-CDs were fully characterized and evaluated in various applications. However, the low yield of S-CDs has hindered its fully characterization and application test, more material is being synthesized for future characterization and application investigations. S-CDs results will be shared along the text for analysis it has done up to the time of the writing.

2.4.2 CDs CHARACTERIZATION

CDs nanoparticles were obtained by top-down approach from the paper industry sludge, lignocellulosic biomass containing 12.8% C, 0.4% H, and 0.03% N. The hydrothermal reaction performed to obtain the carbon nanoparticles is depicted in **Figure 50**. In the first step, the carbon sources are obtained through an acidic reaction, with the main components based in xylose, glucose, and furfural which were analyzed and confirmed by HPLC analysis on 1.5 h and after synthesis completion (See **Figure 91 and 92 from appendix C)**.

Table 12 presents the elemental analysis results of both the starting material and the synthesized carbon dots. Particularly, the CDs exhibit a lower carbon percentage compared to the crude biomass. This discrepancy can be attributed to residual lignin fibers that did not fully disintegrate during the conversion process. The lower carbon content suggests that while cellulose likely decomposed into the sugar sources utilized for nanomaterial production, certain lignin components remained largely intact.

Table 12: Elemental chemical analysis of the materials (wt.%).

Sample	C	H	N
Biomass	12.80	0.43	0.03
CDs	5.60	2.81	0.00
N-CDs	4.69	3.92	4.49
S-CDs	10.22	3.33	2.03

The elevated nitrogen percentage detected in the N-CDs is of particular significance, as it strongly suggests the successful integration of nitrogen heteroatoms into the carbon nanostructure matrix. The S-CDs presented the highest carbon

percentage, and it can be reasoning due to the sulphonic groups being formed, fixing carbon into the CDs structure.

Thermal degradation analysis was conducted in biomass, CDs, and N-CDs, using TGA (**Figure 50** and **Table 13**). The biomass exhibited four stages of mass loss, totaling approximately 64 wt. %. Both types of carbon dots displayed higher thermal stability, with losses occurring gradually over five stages, accounting for 36 wt.% for CDs, **Figure 50B** and 59 wt.% for N-CDs, **Figure 50C**. All samples exhibited a first stage of mass loss at around 110 or 135 ºC, attributable to the removal of adsorbed water from the surface. Additionally, the carbon dot samples exhibited a second stage at 200 ºC, characterized by the release of hydroxyl groups from the surface. Above 200 ºC, significant differences were observed in the pyrolysis behavior of the three samples, indicating variations in their composition.

Figure 50: TGA and derivative thermogravimetry (DTG) curves of the **c**) biomass; **b**) CDs; and **c**) N-CDs samples under nitrogen atmosphere at the rate of 10 °C/min.

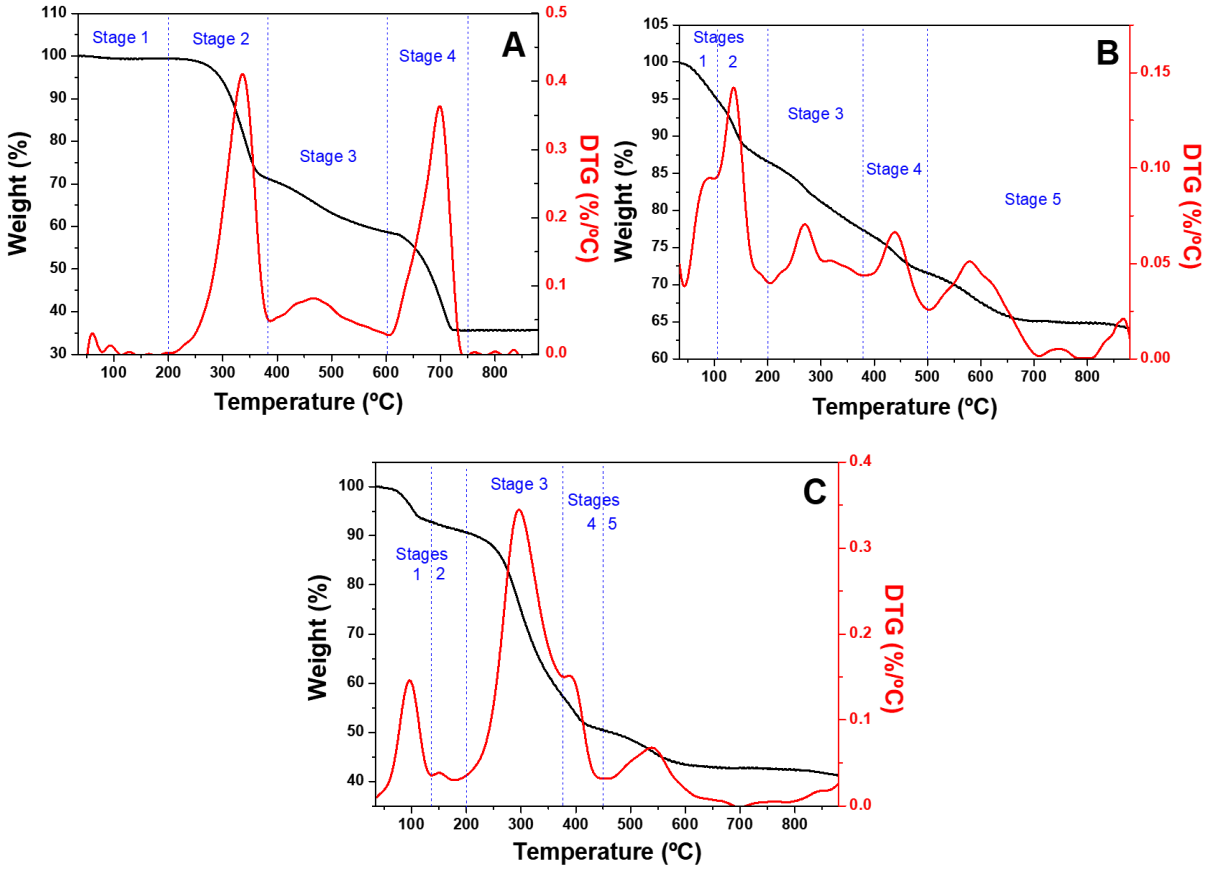

Lignocellulosic materials are made up of substances that decompose at different temperature ranges, such as cellulose (310-400 ºC), hemicellulose (200-300

ºC), and lignin (200-900 ºC) [204], [205]. In the case of biomass (**Figure 50A**), the second stage (200-380 ºC) corresponds to a notable mass reduction (~28%), primarily attributed to the decomposition of hemicellulose, cellulose, and partially lignin. The peak of the maximum derivative thermogravimetric analysis is centered at 332.2 ºC, indicating a higher cellulose content within the structure. During the third stage (380-610ºC), a weight loss of 12.65 wt.% is associated with lignin decomposition. A distinct DTG peak at 699.3 ºC is observed in the fourth stage (610-750 ºC), accompanied by a weight loss of 23.07%, potentially indicative of lignin carbonization. [203], [206].

Table 13:. TGA and DTG data of biomass, CDs, and N-CDs.

Sample	Stage	Temperature range (ºC)	DTG peak (ºC)	Weight loss (%)
Biomass	1	35-200	-	0.63
	2	200-380	337.2	28.01
	3	380-610	466.5	12.65
	4	610-750	699.3	23.07
				Total = 64.36%
CDs	1	0-110	88.1	5.52
	2	110-200	136.1	7.82
	3	200-380	271.3	9.39
	4	380-500	439.0	5.74
	5	500-880	579.6	7.78
				Total = 35.95%
N-CDs	1	0-135	96.7	7.12
	2	135-200	150.5	2.20
	3	200-380	296.0	33.94
	4	380-450	388.0	6.27
	5	450-880	539.5	9.37
				Total = 58.90%

During the third stage of thermal decomposition for both carbon dots CDs (9.39 wt.%) and N-CDs (33.94 wt.%) as shown in **Figure 50B-C**, it's notable that this occurs within the same temperature range as observed in the biomass (200-380 ºC). However, the maximum DTG peaks are observed at lower temperatures: 271.3 ºC (CDs) and 296.0 ºC (N-CDs). This suggests that the composition of carbon dots contains higher fractions of hemicellulose and lignin. The substantial weight loss observed in the N-CDs sample at this stage (33.94%) is attributed to the decomposition of hemicellulose and residual cellulose, as well as the decomposition of amide groups. This is followed by a peak in the temperature range of 380 to 450°C (stage 4), which can be attributed to the decomposition of carbonyl and amine groups observed in the N-CDs structure, resulting in a mass loss of 6.27%.

The fourth stage of decomposition for the CDs sample (380-500 ºC) shows a mass variation of 5.74% and a maximum DTG peak at 439.0 ºC. This behavior is similar to that observed in coke samples obtained from glucose in an acid medium [207], potentially associated with the decomposition of furfural and HMF structures. The final stage for both carbon dots samples is linked to lignin decomposition, with mass losses totaling approximately 7.5% for CDs and 9.39% for N-CDs. The displacement of the main maximum DTG peaks observed in this region may be attributed to interactions between the different constituents of the biomass.

2.4.2.2 Morphology of CDs

The morphology of the carbon dots was examined using high-resolution transmission electron microscopy (HR-TEM). The images depict the quasi-spherical shape of the raw CDs, with an average size of 4.4 nm (**Figure 51A**). Additionally, the inset in **Figure 51A** reveals an interplanar gap of 0.2 nm between the graphitic planes, a characteristic value corresponding to the standard interplanar distance [208].

In contrast, the N-CDs and S-CDs exhibited larger diameters, measuring 6.8 nm and 5.2 nm, respectively (**Figure 52B-C**). This disparity in size can be attributed to the presence of the doping agent, which alters the nature of the surface groups and consequently influences on the interactions between the nanoparticles [209]. The electronegative nature of nitrogen, being higher than sulfur, might be the interpretation of the bigger particle, since it can create hydrogen bonds within the structure and media

solvent, increasing the graphene core layers distance. In addition to it, the polarizability of sulfur atoms might create compact structures [210].

Figure 51:. TEM images for **A**) CDs, inset the graphitic lattice obtained by hydrothermal treatment, **B**) N-CDs and **C**) S-CDs. The distribution of CDs sizes was included.

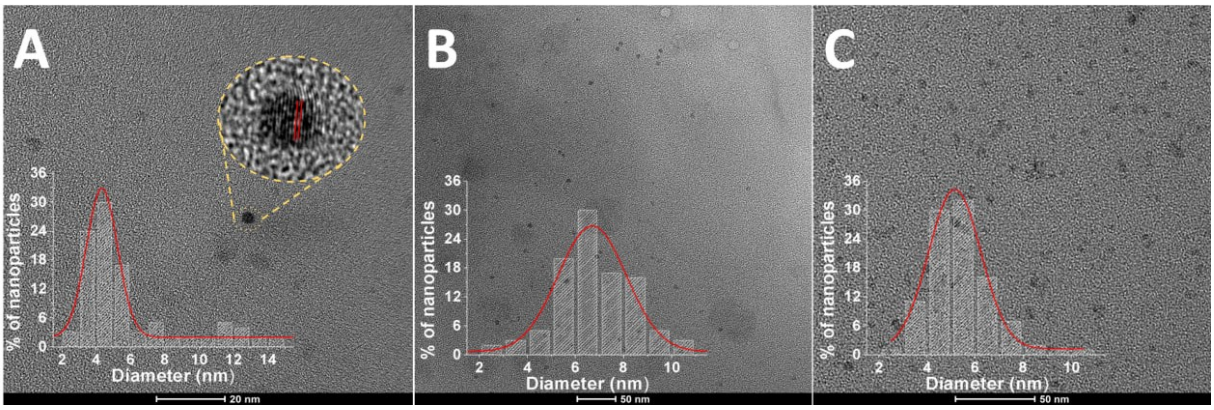

2.4.2.3 Surface analysis

The functional groups of CDs, N-CDs and S-CDs were characterized by the combination of FTIR, TGA, and XPS.

2.4.2.3.2 FTIR analysis

FTIR analysis revealed that the surface functional groups composition of the CDs is nearly identical (**Figure 52**). The presence of sulfonic groups in all CDs can be attributed to the synthesis medium, sulfuric acid. Sulfonic groups ($-SO_3H$) are known to confer water solubility to carbon-based materials and can participate in various chemical reactions, potentially enhancing the dispersibility and stability of the nanoparticles in aqueous solutions. These functional groups may also contribute to the catalytic activity of CDs in certain reactions due to their acidic nature [211].

The stretching frequencies observed at 875 cm^{-1} for S-O bonds, 1165 cm^{-1} for C-O-C bonds, and 1400 cm^{-1} for C=N bonds are indicative of various chemical functionalities present on the surface of the CDs. S-O bonds are characteristic of sulfonic acid groups, while C-O-C bonds are often associated with ether or ester linkages, which could originate from surface passivation or functionalization during synthesis. The presence of C=N bonds suggests the possible incorporation of nitrogen-

containing moieties into the carbon dot structure, which is consistent with the doping process in N-CDs and S-CDs.

Furthermore, the bands observed around 1630 and 1675 cm^{-1} correspond to C=S and N=O vibrations, respectively, providing evidence of additional chemical functionalities. C=S bonds are typically associated with thiocarbonyl groups, while N=O bonds indicate the presence of nitro groups [212]. These functional groups may arise from precursor doping molecules during the synthesis process, contributing to the overall chemical diversity of the CDs.

Figure 52:. FTIR spectra for the biomass and the obtained CDs, N-CDs and S-CDs.

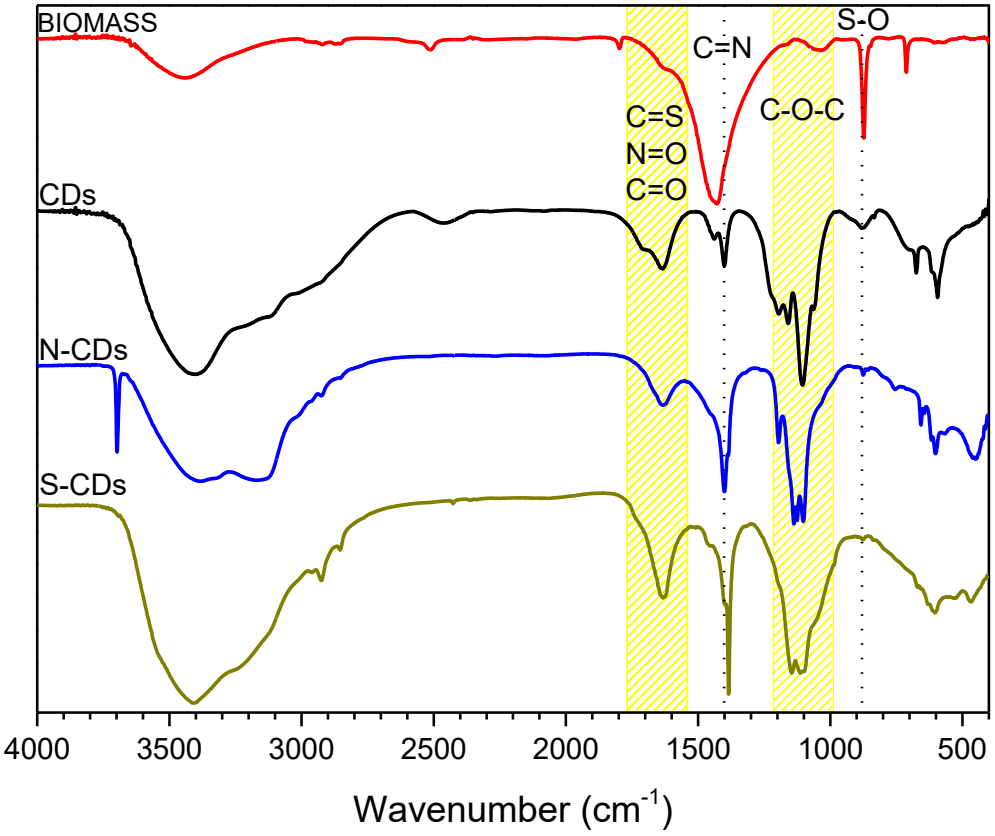

The vibrations observed at 3150 cm^{-1} (N-H) and between 3410 and 3430 cm^{-1} (O-H) are characteristic of amino and hydroxyl groups, respectively. These functional groups can impart enhanced water solubility to the CDs and promote interactions with biomolecules or other surfaces. The strong presence of carbonyl surface groups (C=O) at 1700 cm^{-1} is indicative of carbonyl-containing species, which could originate from oxidative processes during synthesis or surface functionalization [213]. Additionally,

they may play a role in surface passivation, stabilization, or functionalization, thereby influencing the physicochemical properties of the nanoparticles.

Lastly, the detection of traces of S-H localized at 2500 cm^{-1} suggests the presence of thiol groups, which may arise from sulfur-containing precursors or chemical reactions involving sulfur species during synthesis. Thiol groups are known for their ability to undergo various chemical reactions, including thiol-disulfide exchange and metal coordination, which could impart unique properties or functionalities to the CDs, N-CDs, and S-CDs.

2.4.2.3.3 XPS analysis

Figure 53:. XPS core level spectra C 1*s* (**A, A'** and **A''**), N 1s (**B, B'** and **B''**), S 2*p* (**C, C'** and **C''**), and O 1*s* (**D, D'** and **D''**) of CDs, N-CDs and S-CDs, respectfully.

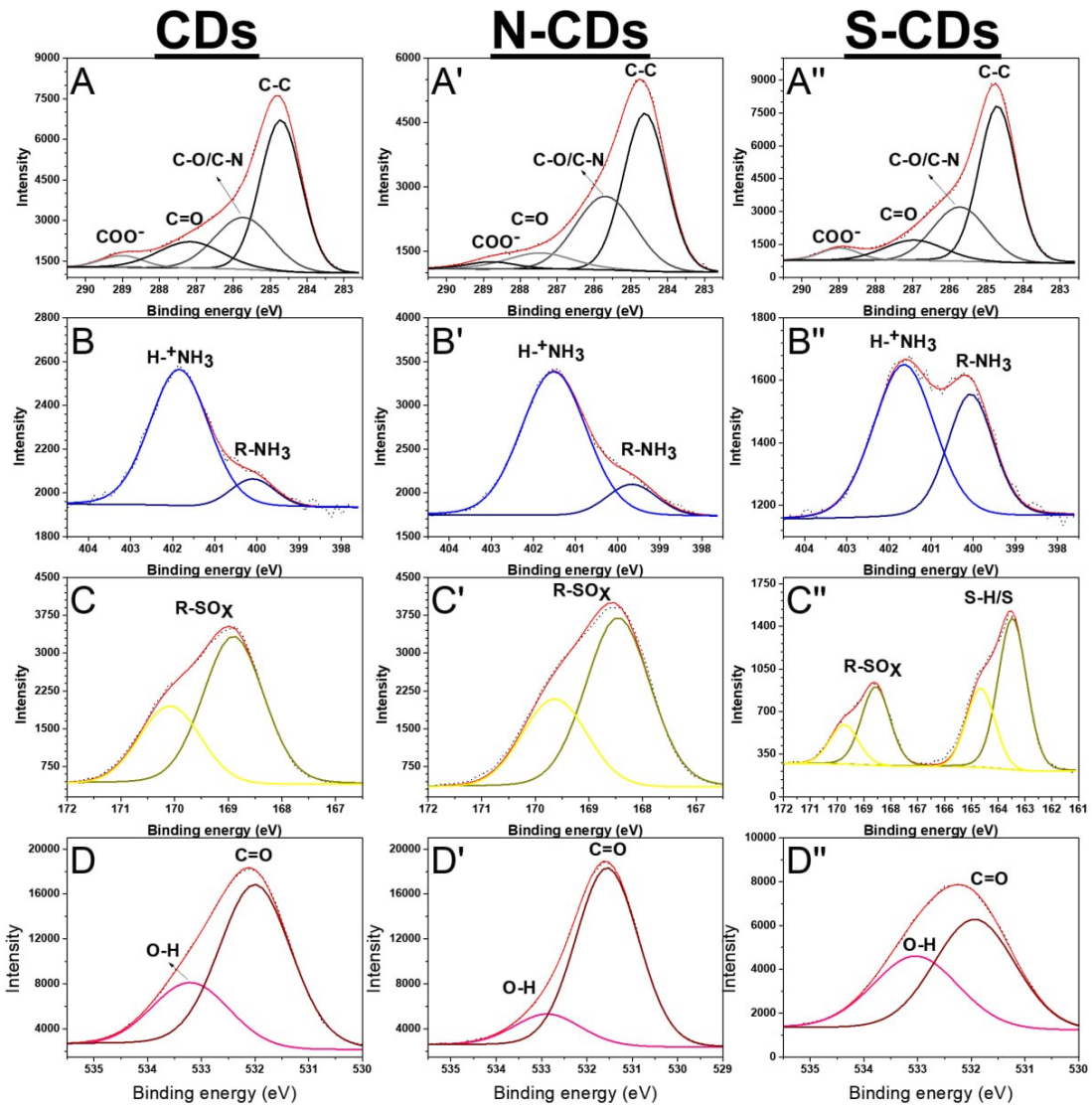

The high-resolution X-ray photoelectron spectra of all carbon dots displayed distinctive binding energy peaks corresponding to core energy levels, including C 1*s*, O 1*s*, N 1*s*, and S 2*p* (**Figure 53)**.

A summary of these peaks, along with the presence of impurities from other elements such as Ca, Si, Na and Al in CDs, probably from salts present in the biomass, is provided in **Table 14**.

Table 14:. Content of elements on the surface in atomic concentration % (from XPS HRS analysis) and the deconvolution for C 1*s*, O 1*s*, N 1*s*, and S 2*p* core energy levels.

		Biomass	CDs	N-CDs	S-CDs
Composition, %	**C**	54.4	47	51.4	43.0
	O	42.1	41	30.3	30.6
	S	0.0	5.6	3.9	21.8
	N	0	2.7	13.6	4.6
	Na	0	0	0.7	-
	Ca	2.3	0.6	0	-
	Si	1	2	0	-
	Al	0.2	1	0	0.2
		Bond assignment	**CDs**	**N-CDs**	**S-CDs**
Binding energy (eV)	**C 1s**	C-C	284.7(67%)	284.8(59%)	284.8(61%)
		C-O, C-H, C-N (phenolic, alcoholic, etheric)	286.1(18%)	286.2(29%)	286.2(23%)
		C=O (carbonyl or ester)	287.3(9%)	288.3(12%)	287.3(6%)
		-COO- (carboxylic acids)	288.9(7%)		288.9(10%)
	O 1s	C=O in carbonyl/sulfonic/sulfates	532.2(75%)	531.5(78%)	531.6(54%)
		O-H alcoholic/sulfonic/water (silicates)	533.4(25%)	532.8(22%)	532.8(46%)
	N 2p	NH amides, C–NH_2	400.6(11%)	399.7(57%)	399.9(28%)
		C–H_3N^+ (ammonium)	401.9(89%)	401.5(43%)	401.5(72%)
	S 2p	Elemental S / S-H	-	-	163.4(60%)
		R-SO_x (sulfates / sulfonics)	169.0(100%)	168.2(100%)	169.6(40%)

The nitrogen doping levels varied among the samples, with the doped material showing a higher nitrogen content than CDs (14% N in N-CDs vs. 3% in CDs),

exhibiting a successful insertion of the heteroatom originating from urea among the CDs matrices. Furthermore, the successful incorporation of nitrogen within the graphitic layers is further substantiated by evidence for the lower C/N ratio observed at the surface compared to the bulk, indicating that nitrogen doping primarily occurs within the carbon core matrix. Nitrogen within the core matrix aligns with the larger particle sizes observed in the HR-TEM images. Incorporation of nitrogen atoms within the carbon lattice can lead to structural modifications, resulting in larger particle sizes.

The same reasoning can be applied for doping with sulfur, whereas the high presence of S atoms causes the slight lower % of C and the S content being higher four-fold in S-CDs in comparison with CDs and N-CDs, hence indicating a successful doping method. HR-TEM images corroborate with the S incorporated presenting bigger structures in comparison with bare CDs. Comparing the elemental analysis results, the carbon structure's graphitic core contains a sizable amount of the carbon structure.

Analysis of the deconvolution XPS curves, **Figure 53A-A''** for C 1*s* core level revealed that all CDs exhibited a prominent peak at approximately 284.8 eV, corresponding to graphitic carbon. In addition, the C-N/C-OH and -COO- species were also identified at around 286.1 eV and 288.9 eV, respectively. Remarkably, doped CDs exhibited elevated concentrations of such groups attributed to the broader spectrum of potential functional groups introduced by nitrogen and sulfur dopants. This observation suggests a high density of such functional groups, turning the surface highly functionalized.

Upon analyzing the N 1s core level spectra for N-containing groups, a discernible influence of the high levels of amine/amides groups is evident. Particularly noteworthy is the prominence of amide/amines groups on the surface of N-CDs, with the highest percentage (57%) centered around 400 eV, as illustrated in **Figure 53B-B''**, over its pears. CDs exhibited a significantly lower proportion, with only 11% of such groups detected, whereas S-CDs presented 28% [214]. This variation can be attributed to the broader array of potential functional groups introduced by nitrogen and sulfur dopants. It is noteworthy that due to the acidic nature of synthesis and the electronegativity of nitrogen, the predominant form of nitrogen on the particle surfaces is ammonium for both CDs and S-CDs, while less prominent in N-CDs.

The presence of S-containing groups in all samples was expected (**Figure 53C-C''**), given the use of sulfuric acid as the solvent. However, the prevalence of such groups is notably more significant in S-CDs. Analysis of the S 2*p* core level unveiled the presence of sulfates and sulfonic groups at approximately 168-169 eV across all samples. Interestingly, peaks corresponding to S-H /S were exclusively observed on S-CDs, indicating a broad functionalization of sulfur species fixating them onto the surface. This observation suggests a robust method for surface passivation. These findings hold significant importance, particularly in the context of utilizing sulfur-doped materials in batteries and various coupling reactions [215]. Moreover, these results are consistent with the findings obtained from Fourier-transform infrared spectroscopy, thereby providing comprehensive insights into the surface composition and functional groups of the carbon dots [216].

Regarding the O 1*s* core level spectra, as illustrated in **Figure 53D-D''**, the predominant species for all CDs were primarily associated with carbonyl and sulfate groups, observed at approximately 532 eV. The substantial oxygen content observed in all samples can be attributed to the presence of CO_x, NO_x, and SO_x species on the particle surface, with the SO_x species likely originating from the acidic synthesis media employed for CDs and N-CDs. In which both exhibited over 75% contribution from carbonyl and sulfate groups, indicating a significant presence of these functional groups on their surfaces. In contrast, S-CDs represented approximately 54% of O-containing functional groups, suggesting a slightly lower proportion compared to CDs and N-CDs. Notably, the concentration of OH groups, indicative of alcohols as well as of sulfonic groups, was notably higher on S-CDs, covering 46% of the surface. In contrast, CDs and N-CDs exhibited 25% and 22% of OH groups, respectively. This difference suggests a substantial increase of 20% in the proportion of sulfonic groups when sulfur is utilized as the doping agent.

2.4.1.3 TOXICITY ANALYSIS

Given their carbon-based nature, carbon dots are inherently and widely categorized as non-toxic compounds, especially when comparing with their metal-based peers [217], [218]. However, few concerns are raised regarding their lack of toxicity assessments [219], [220]. In order to validate our greener and low-toxicity synthesis methodology for CDs and doped-CDs, samples of produced nanostructures

underwent toxicity testing. This assessment was conducted through the determination of the half-maximum effective concentration (EC_{50}), which evaluates the toxic effects by considering a 50% reduction in the growth rate of the bacteria. A lower EC_{50} value indicates higher toxicity.

The results revealed EC_{50} values of 308.8% for CDs and 160.5% for N-CDs suggesting no acute toxic effects on *Aliivibro fischeri* bacteria [221]. These findings offer promising preliminary insights into the potential toxicity profile of the synthesized nanoparticles. However, it is imperative to conduct further investigations to assess both acute and chronic ecotoxicity across various trophic levels [222].

Considering the potential environmental implications, the synthesis of CDs and N-CDs from paper residues emerges as a favorable alternative for valorizing paper waste. The utilization of primarily H_2SO_4 as a reactant raises concerns regarding potential toxicity to ecosystems, but the requirement for small quantities of this reactant, coupled with its ease of treatment and potential for recycling within the system, mitigates such concerns.

Furthermore, given that the paper industry generates a significant amount of residue, with up to 50% of paper production constituting waste, addressing this issue is vital [223]. Carbon dot synthesis from paper waste presents itself as a viable solution to both environmental and economic challenges faced by the paper industry. Moreover, the versatility of carbon dots allows for their application in environmentally friendly processes such as photocatalysis and hydrogen generation, further enhancing their potential as a sustainable solution.

2.4.2.4 PHOTOPHYSICAL PROPERTIES

The intrinsic photoluminescence (PL) of carbon nanoparticles serves as a fundamental indicator of their size, structure, and surface functionalization, dictating their overall properties, especially optical characteristics. To explore this phenomena, UV-Vis and fluorescence spectra were meticulously acquired. In **Figure 54A**, discernible absorption peaks around 300 nm are evident, attributed to π -π* transitions stemming from C=C bonds within the graphitic core, alongside n-π* transitions originating from C-N/O bonds on the surface [224], [225].

Upon examining the fluorescence spectra of CDs, N-CDs, and S-CDs under excitation at 475 nm (**Figure 54B**), distinct emission spectra emerge at 560 nm, 550 nm, and 600 nm, respectively. Remarkably, a subtle red shift in the emission peak of N-CDs suggests the potential presence of a distribution of surface energy traps. This observation may stem from variances in the abundance of amine and carboxyl groups, elucidated through XPS analysis, as well as differences in particle sizes between doped and non-doped CDs.

Figure 54:: A) The UV-vis absorption spectra of CDs and doped-CDs. B) The fluorescence spectra of CDs and doped-CDs, in aqueous solution.

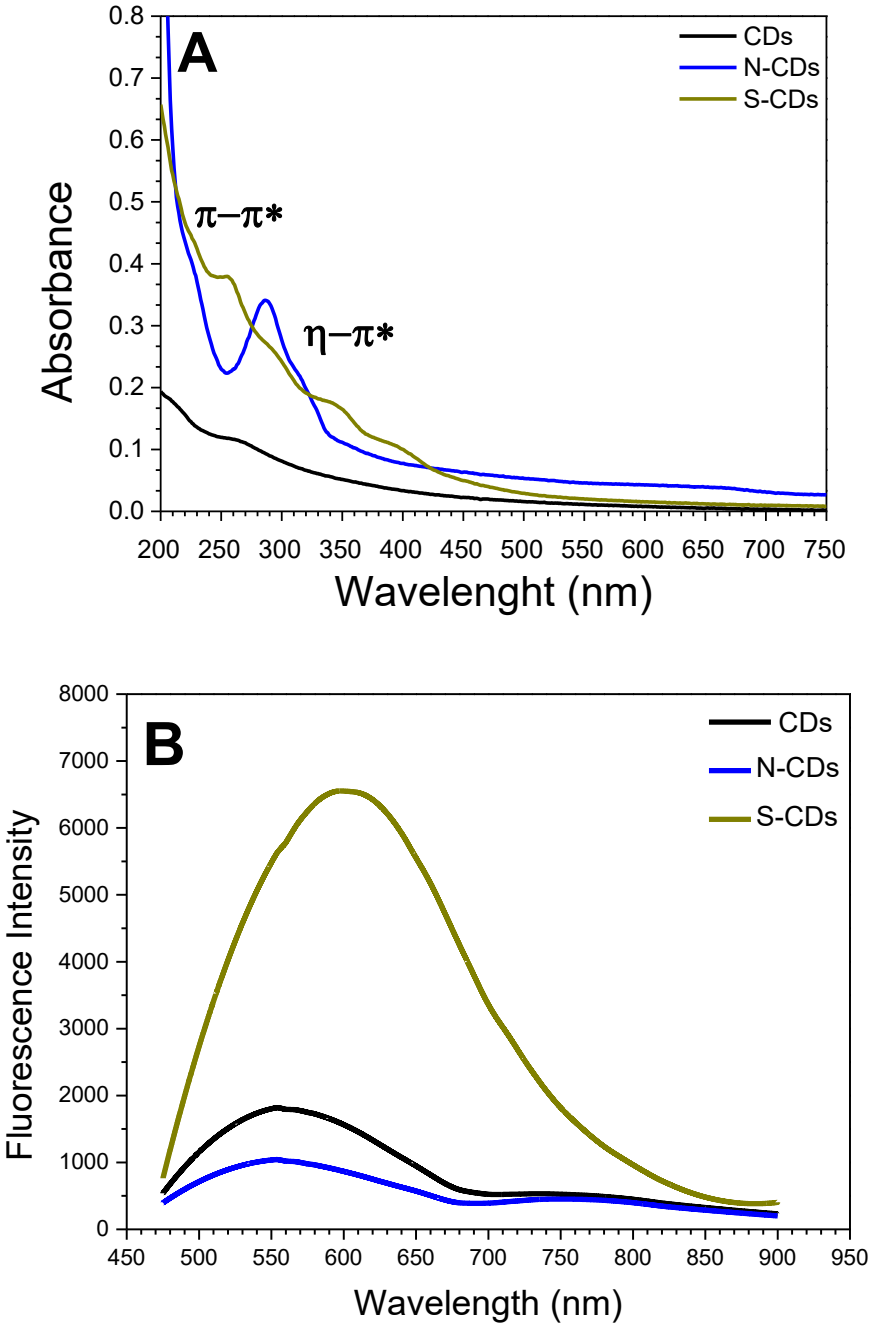

On the contrary, the phenomena observed in S-CDs suggest a diminished dependence on size for photoluminescence properties, with a greater emphasis on surface functionalization [226]. The elevated density of functional groups such as sulfonic groups (SO_x) and sulfur-hydrogen groups (S-H) are likely significant contributors to fluorescence [153]. This implies that the higher fluorescence is intricately linked to the dense sulfur content on the surface, as corroborated by XPS analysis. The abundance of sulfur functional groups facilitates the formation of additional emission centers and emissions traps, thereby augmenting the overall fluorescence intensity.

2.4.1.3.1 Quantum yields (QY)

The quantum yield of carbon dots is known to be influenced by various parameters, including the precursor composition, time and temperature used in the synthesis, as well as the presence of doping elements. Literature reports a wide range of QY values obtained from different methods and biomass sources materials, typically falling within the range of 1.0 to 7.6% [227], [228]. The quantum yield of carbon dots and doped-CDs was determined using standard quinine sulfate (QY_{qs}) in 0.1 mol L^{-1} H_2SO_4 as a reference (**Table 15**). Notably, the quantum yield for N-doped CDs was found to be double that of the non-doped CDs, exhibiting an increase from 3% to 6%. Conversely, S-CDs exhibited QY of 14%, which is considered notably high for its class [229], [230].

Table 15:. The fluorescence quantum yield of CDs and N-CDs in aqueous solution.

	Integrated FL intensity (I)	**Absorbance intensity (*A*)**	**Quantum yield (%)**
CDs	466.69	0.057	3
N-CDs	1300.48	0.038	6
S-CDs	1691.74	0.066	14
Quinine sulfate	1368.98	0.33	55

This disparity in quantum yield values underscores the significant impact of heteroatom doping on the photoluminescence efficiency of carbon dots. The

introduction of nitrogen and sulfur dopants not only modifies the electronic structure but also enhances the light-emitting properties of the nanomaterials. Additionally, the substantially higher quantum yield observed in S-CDs suggests the potential superiority of sulfur-doped carbon dots in terms of their luminescent performance. Such insights shed light on the doped carbon dot synthetic route and strategies from our work for applications requiring efficient light emission, such as bioimaging and optoelectronic devices [231].

2.4.1.3.2 Band Gap

Carbon dots are commonly classified as *n*-type semiconductors due to their distinctive electronic properties [232]. In the case of the synthesized CDs, a band gap of 3.64 eV was observed, as depicted in **Figure 55A**. This band gap value signifies their potential for efficient charge transport and electron conduction. However, upon nitrogen doping, the band gap of the carbon dots decreased to 2.33 eV, as illustrated in **Figure 55B**. Furthermore, sulfur-doped carbon dots, as shown in **Figure 55C**, exhibited an even smaller band gap of 2.28 eV.

The discernible variation in band gap values between pristine CDs and doped CDs can be attributed to the incorporation of heteroatoms into the graphitic layer's matrix [233]. This incorporation alters the electronic structure and introduces additional energy levels within the band gap, consequently affecting the band gap size [234]. Specifically, nitrogen and sulfur dopants introduce new energy levels within the band gap, leading to a reduction in the band gap energy. This reduction facilitates enhanced charge carrier mobility and conductivity in the doped carbon dots, rendering them potentially more suitable for applications requiring efficient charge transport, such as photocatalysis and energy storage devices[235].

Figure 55:. The optical band gap of A) CDs and derived B) N-CDs and C)S-CDs was determined using a Kubelka Munk Function.

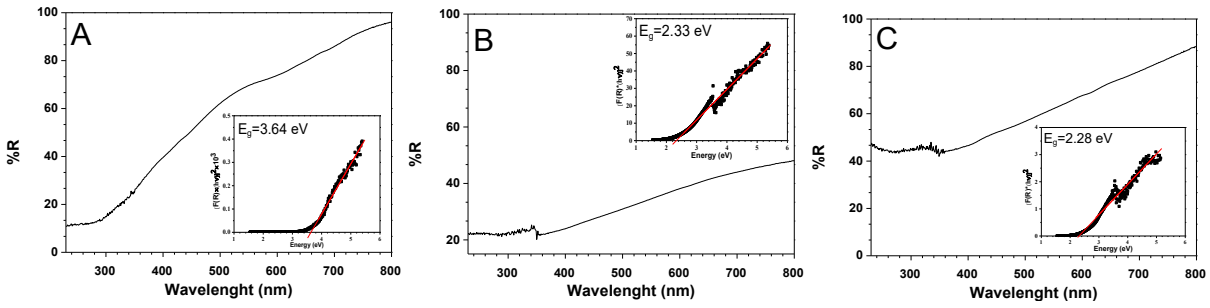

Park et al. synthesized carbon dots, yielding band gap values of 3.51 and 3.44 eV for CDs and N-CDs, respectively. These synthesized materials were subsequently employed as light harvesters for photovoltaic cells. Their investigation revealed that the reduced band gap facilitated electronic transfer into the TiO_2 layer, thereby enhancing the photovoltaic performance of solar-powered devices [236]. In a separate study, the group led by Peng-Gang Ren utilized N-CDs generated from spent coffee grounds biomass as a doping agent to lower the band gap of their composite to 2.90 eV. This modification resulted in a remarkable 2.25 times increase in the photodegradation velocity of the pollutant methylene blue, achieving an efficiency of 86% after four cycles, surpassing the performance of the non-doped counterpart [237].

Goswami's group successfully synthesized non-toxic S-CDs with a wider band gap of 4.43 eV, which rendered them suitable for bioimaging, DNA interaction, and synergistic interaction with gold nanoparticles. They also anticipate that such a wide band gap could be advantageous for the fabrication of solar cells, owing to the findings of its reasonably higher open circuit voltage and high fill factor [238].

In comparison to the findings in the literature, the narrower band gap observed in CDs generated from this work derived from biomass indicates enhanced electronic mobility. This characteristic enables them to absorb and emit light at longer wavelengths more effectively, positioning them as promising candidates for various applications, particularly in photocatalysis.

2.4.1.4 ELECTROCHEMICAL STUDIES

In the evaluation of electrocatalyst performance, the determination of the active surface area holds paramount importance [239]. A critical parameter in this assessment is the electrochemical double-layer capacitance (C_{dl}). For the samples CDs and N-CDs it has been observed that an increase in scan rates correlates with a proportional escalation in both positive and negative peak currents (**Figure 56A-B**).

These findings suggest that the mass transfer processes occurring at the interface of the solution on N-CD modified glassy carbon electrode predominantly adhere to a diffusion-controlled mechanism. The quantification of C_{dl} is typically achieved through cyclic voltammetry, as detailed in section 3.2.8. The CV curves,

plotted in a non-faradaic region (+0.4 to +0.75 V), were examined as a function of various scan rates (**Figure 56C-D**).

Subsequently, the double-layer capacitance (C_{dl}) was assessed from the slope of the linear regression between the differences in current density ($\Delta J \cdot 2^{-1} = (Ja - Jc) \cdot 2^{-1}$ in the middle of the potential window of CV curves and the studied scan rates (**Figure 58**). For the calculation of the electrochemical surface area (ECSA), a reported C_s value of 0.02 mF cm^{-2} for carbon electrode materials was utilized. Consequently, the C_{dl} value for N-CD/GCE was measured to be 18.8 $mF \cdot cm^{-2}$, significantly surpassing that of CD/GCE (7.17 mF cm^{-2}). Consequently, the ECSA for N-CD/GCE was determined to be 939 cm^{-2}, while for CD/GCE it was 388 cm^{-2}.

Figure 56:. A) Cyclic voltammograms in the potential range without redox current peaks of CD/GCE in 0.5 M H_2SO_4; (B) plot of $\Delta J \cdot 2^{-1}$ *vs.* scan rate for CD/GCE, (C) Non-Faradaic region CVs for N-CD/GCE in 0.5 M H_2SO_4 and (D) plot of $\Delta J \cdot 2^{-1}$ *vs.* scan rate for N-CD/GCE.

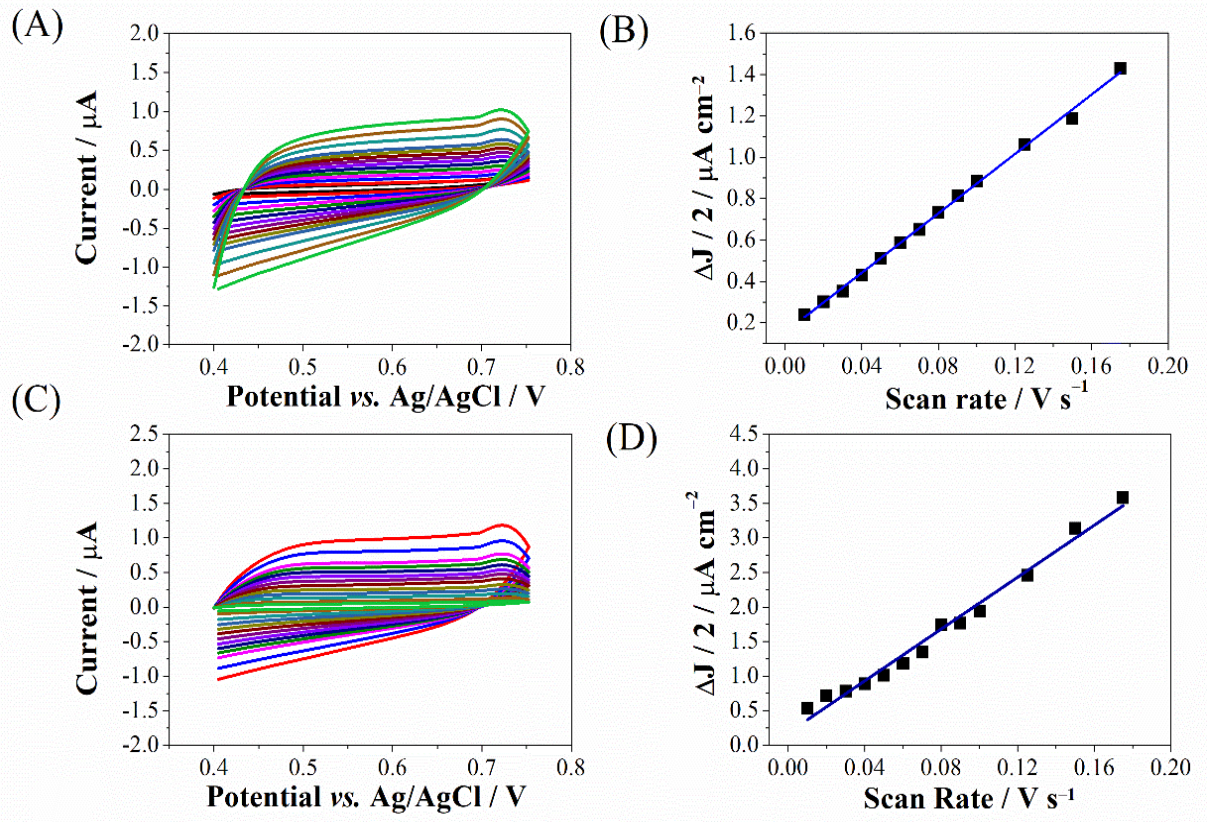

These outcomes underscore the substantial active surface area provided by N-CD/GCE, which secures an increased number of active sites, which are essential for applications on energy generations such as on Hydrogen Evolution Reactions.

2.4.3 HYDROGEN EVOLUTION REACTION

Efficient hydrogen evolution during water electrolysis necessitates rapid electrical transmission, which can be facilitated by a conductive substrate. CDs are known to enhance electron transport within a catalyst and at its interface with the electrolyte due to their superior conductivity and hydrophilicity. Incorporating heteroatoms such as nitrogen (N), boron (B), phosphorus (P), and sulfur (S) into the carbon matrix can further enhance the reactivity of electrocatalysts by modifying their electronic structure [240].

Among the heteroatom-modified CDs, nitrogen-doped CDs are widely utilized due to nitrogen's atomic size and its five valence electrons, which closely resemble those of carbon. **Figure 57A** depicts the linear sweep voltammetry (LSV) curves of CDs and N-CDs catalysts evaluated for hydrogen evolution reaction (HER) catalytic activity. The overpotential (η_{10}) of N-CDs was measured at 451 mV, while that of CDs was 581 mV at -10 mA cm^{-2}. Although these values exceed the overpotential (η_{10} = 78 mV) of commercial Pt catalysts under similar conditions, they demonstrate that non-metallic electrocatalysts exhibit promising HER catalytic activity at a relatively lower cost compared to Pt-based counterparts. Notably, doped N-CDs exhibited higher suitability for high current density applications than non-doped CDs, highlighting their potential in eco-friendly water electrolyzers

Figure 57:. Polarization curves of (a) CDs, (b) N-CDs and (c) Pt/C electrocatalysts in 0.5 mol L^{-1} H_2SO_4 solution (A) and corresponding Tafel plots for each electrocatalyst (B).

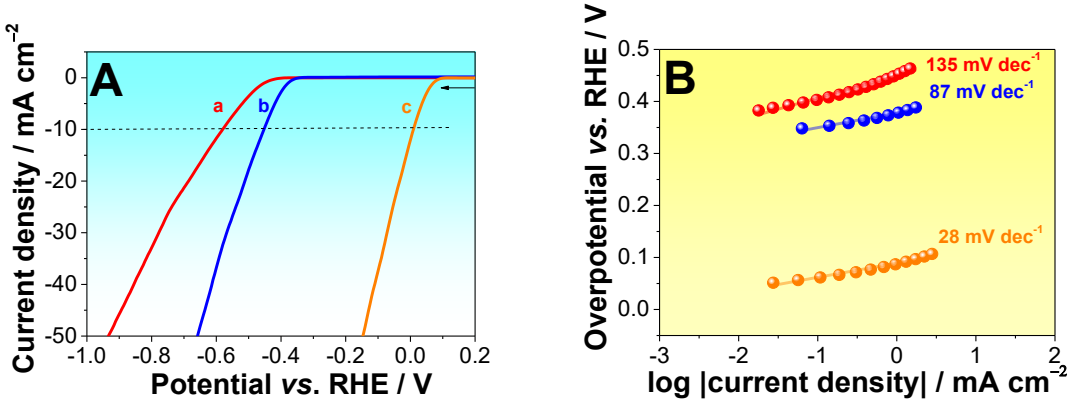

Similarly, Prabu and co-workers found that the graphene-like hierarchical porous nanosheets obtained from palm waste biomass exhibited also a high HER

performance (η_{10}= 330 mV, Tafel slope = 63 mV dec^{-1}) [241]. This indicates that electrocatalysts designed with eco-friendly strategies hold promise for hydrogen evolution reaction applications.

The Tafel slopes of N-CDs, CDs, and Pt/C are presented in **Figure 57B**. Commercial Pt/C, N-CDs, and CDs exhibit Tafel slopes of 28 mV dec^{-1}, 87 mV dec^{-1}, and 135 mV dec^{-1}, respectively. This indicates that doped N-CDs possess superior HER kinetics compared to non-doped CDs, attributed to the modulation of electronic characteristics within neighboring carbon atoms through nitrogen doping, facilitating intramolecular charge transfer and amplifying the electrocatalytic efficacy of the HER [242].

Electrochemical impedance spectroscopy (EIS) measurements were conducted to assess the charge transfer resistance (R_{ct}) values. The typical Nyquist plots of CDs and N-CDs are depicted in **Figure 58**, from which R_{ct} values were determined by fitting the data to Randle's equivalent circuit, as shown in the inset of **Figure 58**. It was observed that the electron transfer kinetics are significantly enhanced in the N-CDs, as evidenced by lower R_{ct} values for the doped N-CDs (approximately 1504 Ω) compared to non-doped CDs (approximately 2103 Ω).

Figure 58:. Nyquist plots of different catalysts: (a) CDs and (b) N-CDs in 5 mmol L^{-1} $[Fe(CN)_6]^{3-/4-}$ containing 0.1 mol L^{-1} KCl. Frequency range: 50 kHz to 0.1 Hz; OCP value: 0.225 V. The Inset shows the Randle equivalent circuit applied to fit the data and the equivalent circuit.

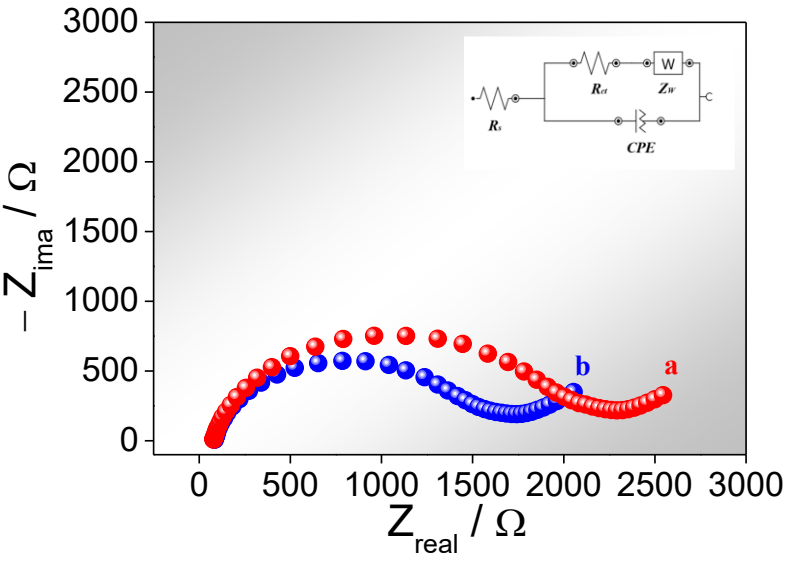

Additional parameters evaluated in the EIS spectra include the solution resistance (R_s) and a constant phase element (CPE), indicating the double-layer nature of the system. Accordingly, the N-CDs catalyst demonstrates promising characteristics for promoting the hydrogen evolution reaction compared to non-doped CDs. These characteristics hold a reduced Tafel slope and higher current density at a lower onset potential. These findings are corroborated by the analysis of band gap energies, collectively suggesting the catalyst's significant potential for facilitating an effective hydrogen evolution reaction.

2.4.4 PHOTOCATALYST PERFORMANCE

Due to their noticeable PL and electronic properties CDs are often tested as photocatalyst. CDs produced from several carbon sources, as individual material has been used in detection of organic pollutants, especially on 4-NP by quenching of the carbons dots PL [239], [243]–[246]. Despite their impressive photophysical properties, CDs are frequently incorporated into various matrices to enhance the catalytic properties of metallic materials (**Table 16**). For instance, the addition of CDs to materials like cerium oxide has shown to improve the reduction of the 4-NP by 4%. Similarly, in the case of gold nanoparticles (AuNPs), where CDs only presented photocatalytic properties when incorporated in the AuNPs.

Moreover, many studies involves the reduction or degradation of 4-NP to 4-aminophenol (4-AP) in the presence of a strong reduction agent such as $NaBH_4$ [247], [248]. While sodium borohydride is widely used throughout several applications and being relatively eco-friendly, it still poses high risk to human health [249].

As evidenced by the examples provided in **Table 16**, there are few instances of composites utilizing CDs as a support to enhance their photophysical chemistry for elimination of 4-NP pollutant from water was and there are even less on utilizing bare carbon dots for such photocatalytic processes. There are, however, more examples for methyl orange and rhodamine B, that are known organic dyes pollutants as well [250]. It is clear a need in literature for research specifically focused on employing employing bare CDs for elimination of the highly toxic pollutant 4-NP. Thus, advancing in a greener chemistry through simplified and metal-free methodologies

Table 16:. Comparison of 4-NP photodegradation performance to previous published data using different types of carbon dots.

(continue)

Catalyst	CD source	Catalyst load (mg/L)	Initial 4-NP concentration (mg/L)	pH	Light source	Reaction time (min)	4-NP removal (%)	Method	Reference
GQDs	citric acid	1000	10	-	-	20	<10	Reduction of 4-NP	[251]
N-GQDs	4-NP	2000	10	-	NIR (1 W)	8	99.5	Reduction of 4-NP	[252]
CDs	Glucose	2000	10	-	Vis (1.5 W)	30	>55	Reduction of 4-NP	[253]
AuNPs@NGQDs	citric acid and dicyandiamide	400	10	-	Vis	5	>90	Reduction of 4-NP	[254]
CDs/CuO/mHA	citric acid	500	15	-	Vis (300 W)	120	>99	Reduction of 4-NP	[255]
AuNPs@CDLs	Triolein	-	10	8	-	12	>92	Reduction of 4-NP	[256]
AgNPs/NCDs	ripen blue black berries of Lantana camara	3200	10	-	-	2.5	~100	Reduction of 4-NP	[257]
AuNPs/CDs	Acetyl pyridinium chloride monohydrate	0.5	-	-	-	16	~100	Reduction of 4-NP	[258]
N,S-CD-Au NC	Citric acid	-	27.8	-	Vis	12	82	Reduction of 4-NP	[259]

(Conclusion)

Catalyst	CD source	Catalyst load (mg/L)	Initial 4-NP concentration (mg/L)	pH	Light source	Reaction time (min)	4-NP removal (%)	Method	Reference
CD-embedded nanodroplets	Citric acid	1	10	10	-	100	~100	Reduction of 4-NP	[260]
Bi2O3/Bi2S3/CD	Aspartic acid	600	500	-	Vis (300 W)	8	~100	Reduction of 4-NP	[261]
CQDs@CeO2	Citric acid	1000	14	9	UV (125 W)	120	~100	Reduction of 4-NP	[247]
SN-CD/g-C3N4	p-amino benzenesulfonic acid	2000	20	-	Vis (300 W)	5	89	Reduction of 4-NP	[262]
CDs	citric acid and 1,2-phenylenediamine	750	20	7.5-9.5	Vis (310 W)	150	70	Degradation of 4-NP	[263]
N-CDs/CN-catalyzed PMS	Citric acid and urea	1250	10	-	Vis (300 W)	10	95.9	Degradation of 4-NP	[264]
FeOOH@SQDs	sodium citrate and urea	400	-	-	UV (500 W)	5	88	Degradation of 4-NP	[265]
CDs	**Industrial paper waste**	**1000**	**10**	**3**	**UV (560mW)**	**90**	**62**	**Degradation of 4-NP**	**This work**
N-CDs	**Industrial paper waste**	**1000**	**10**	**3**	**UV (560mW)**	**90**	**71**	**Degradation of 4-NP**	**This work**

Therefore, we evaluated CDs and N-CDs as catalysts for the photodegradation of 4-NP under the conditions summarized in the Experimental Section. Various experiments were conducted to distinguish the possible effects occurring in the process: i) photolysis (action of UV light in the absence of catalyst), ii) adsorption (action of the CDs in the absence of UV light), and iii) photocatalysis (action of UV light in the presence of CDs). The curves showing the removal of the contaminant under these experimental conditions are presented in **Figure 59**.

Figure 59:. Comparison of the evolution with an irradiation time of the concentration of 4-nitrophenol concerning the initial concentration (10 mg/dm^3; UV radiation = 560 mW, 365 nm; pH = 3.0).

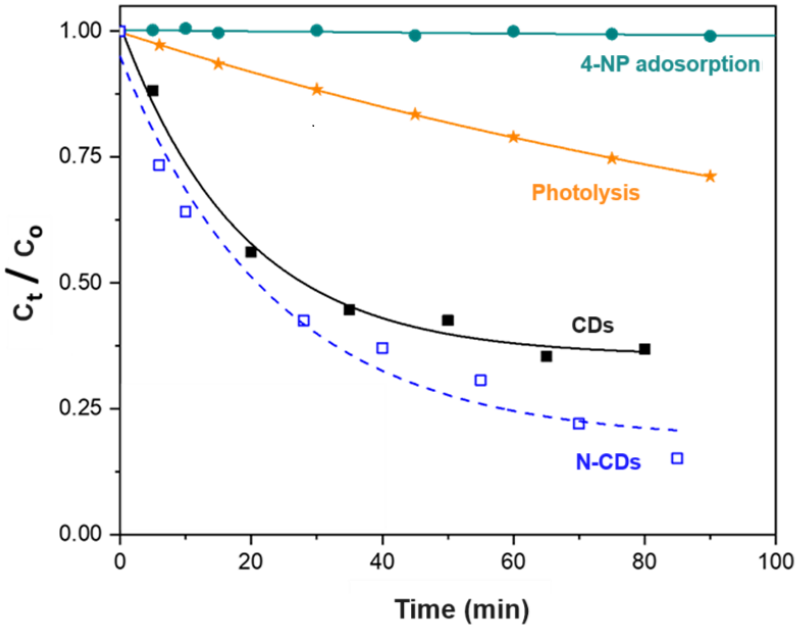

Figure 59 shows the absence of 4-nitrophenol adsorption on the surface of the carbon dots, with the photolysis process revealing that 71% of the contaminant remains in the solution after 90 minutes of reaction. Consequently, the presence of CDs leads to a more significant disappearance of 4-NP, suggesting catalytic action in the removal of the contaminant from the solution. This observation features the exceptional photocatalytic properties of bare carbon-based with metal-free nanoparticles support or help produced via this method from waste lignocellulosic material.

Previous investigations conducted in our laboratories have demonstrated the photocatalytic degradation of 4-NP, resulting in the progressive disappearance of the

molecule. However, it has been established that several intermediates are generated during this process, as the mineralization of the initial molecule occurs gradually. While existing literature predominantly advocates for the conversion of 4-NP to 4-aminophenol (4-AP) as a means of eliminating this pollutant, such an approach has proven to be inadequate [266]. Hence the need of exploration for new materials and methodologies that are less detrimental to the environment. Consequently, the CDs developed in this study have exhibited superior efficiency and represent a more environmentally friendly approach to the elimination of toxic water pollutants like 4-NP. A proposed degradation pathway, incorporating previously identified compounds [267], is depicted in **Figure 60**.

Figure 60:. Possible initial steps in deleting 4-nitrophenol, aqueous solution, pH 3.0, and irradiation at 365 nm.

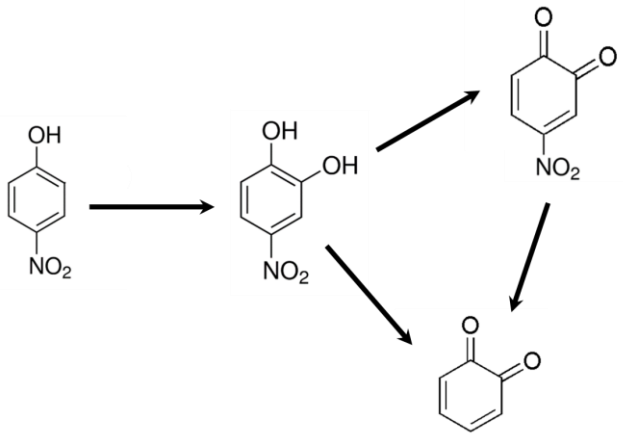

As mentioned above (**Table 16**), published studies present high 4-NP removal rates were achieved (≥ 82%), representing a degradation up to 29% higher than that observed with the N-doped carbon dots synthesized in this work. However, it is imperative to underline three critical aspects regarding the synthesized materials:

i) The photocatalysts were derived from paper waste biomass, whereas the majority of studies utilize high-purity materials for CD synthesis;

ii) The synthesized materials employed a less expensive dopant compared to the majority of works, particularly when juxtaposed with metal additives, underscoring the potential of metal-free catalysts; and

iii) Many investigations still rely on the addition of $NaBH_4$ to enhance the reduction rate of 4-NP during photocatalytic reactions [259]–[261], a step omitted in this study.

Thus, the materials developed in this study not only exhibit noteworthy clean, and without external reducing agent, photocatalytic performance (62% to 71% 4-NP removal) but also signify the potential for cost-effective production and the valorization of industrial waste. However, it is essential to emphasize the necessity for further studies to optimize their synthesis processes to attain competitive materials, particularly concerning catalytic activity.

2.4.5 N-CDs INTERACTIONS WITH PHOTOCORMS

By now we are very aware of the multi facet application of CDs solidifying their place as a new high-end class of carbon-based materials in several research areas due to their distinctive optical, spectroscopic, and electronic properties. Such properties make CDs highly attractive for various technological fields, such as sensors, biomedicine, optoelectronics, energy devices, and photocatalysis due to their versatility [268]. Doping carbon dots with hetero atoms such as Nitrogen has been reported to enhance their electronic properties by diminishing their band gap energy and improving their photoluminescence (PL) properties [269].

Thus, N-CDs were synthesized in this work and used in symbiosis with the photoCORMs also from this work (chapter 1 section 3.3.2), as a support to gather photons emitted from light sources in a wider wavelength transferring them to use as trigger CO release from the MCC. Such tests works as a proof of concept, since it has never been done or mentioned so far. As upper mentioned (chapter 2 section 4.1.3) fluorescence spectra from N-CDs shown an absorption around 300 nm due to the π-π transition from graphitic core and an emission band from 470 nm to around 700 nm, **Figure 61**, which overlaps with the absorption band from photoCORMs, thus triggering the CO release.

Following the addition of N-CDs into solutions of **1** to **4**, their infrared spectra in the liquid phase were meticulously tracked during exposure to light (λ_{max}=515±15 nm for **1** and **2**; and λ_{max}=395 ± 5 nm for **1- 4**), **Figure 62**. The distinct stretching bands associated with CO exhibited a pattern of behavior wherein they diminished in intensity as the duration of photoirradiation increased. In general, the presence of N-CDs in the solution expedited the rate of decay of CO bands, except for **1**, which displayed a relatively slower decay. The delayed decay observed in **1** may be attributed to its

resonance characteristics, effectively impeding the efficient transfer of energy from the N-CDs to the molecule via either direct photon transfer or fluorescence. Conversely, photoCORMs **2** to **4** lack such resonant electronic configurations, facilitating a more facile release of CO triggered by an increase in electronic density at N,N' moiety and further weakened by the trans effect on the M-CO bond.

Figure 61:. Emission spectra for N-CDs disperse in water.

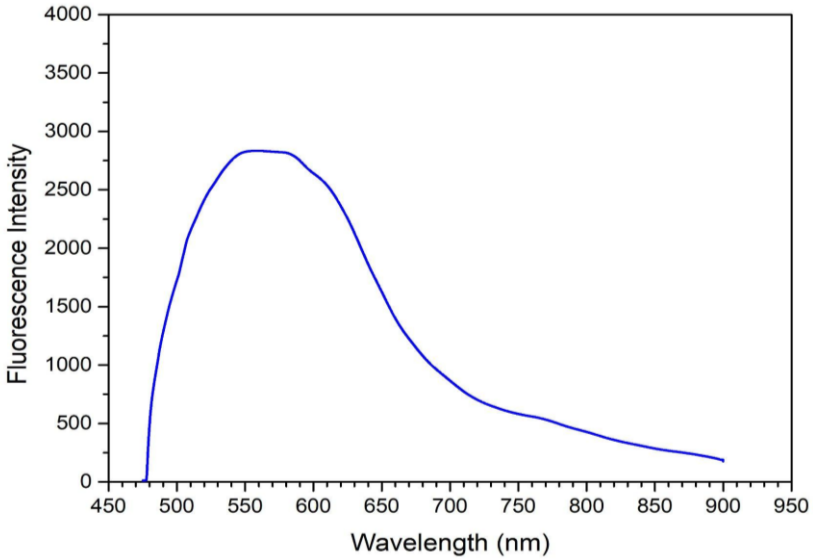

The fact **1** and **2** were both irradiated in λ_{max}=515±15 nm and λ_{max}=395 ± 5 nm, is due to N-CDs being optimally exited on lower wavelengths, while photoCORMs are optimal on higher wavelengths. Thus, studying if N-CDs influences on CO triggering method through electron/energy transfer in and out of optimal exciting light. As shown on **Figure 62-1'/2'** N-CDs were able to trigger CO release in their optimal wavelength *vs* non-optimal for photoCORMs.

Kinects influences and constants were also evaluated to better quantify such synergy. Thus, values of Φ_{CO} from Mn^{I} photoCORMs and rate of CO-release (k_{CO}) from **1**-**4** calculated and organized at **Table 17**. It's possible to see the same behavior for **1** and **2** while the photo is irradiated with 515 nm light, with a decrease of a 10x in their Φ_{CO}. While the same is not observed when under 395nm exposure, where **1** to **3** exhibits a small decreasing yield difference and **4** presents half of **3**. The k_{CO} were also higher for **1**, followed by **4**,**3** and **2**, which can also indicate the resonance effect having a bigger influence on than the chalcogenic moiety.

Figure 62:. Variation of FTIR spectra in CH_2Cl_2 over the period of irradiation for MMCs with N-CDs systema, being **1'** and **2'** with LED λ_{max} in 515±15 nm and **1- 4** with LED λ_{max} in 395 ± 5 nm.

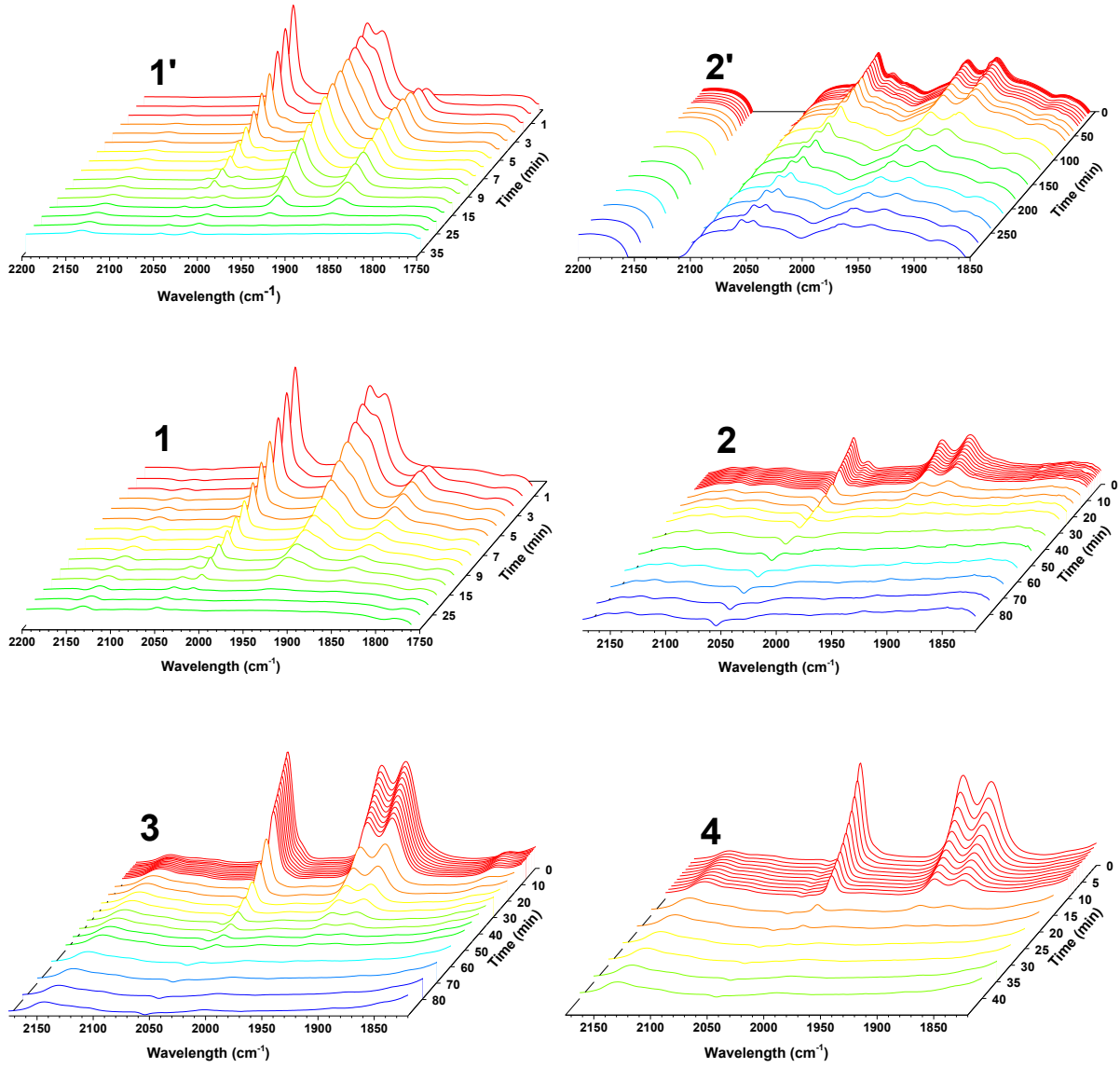

Notably, when subjected to photoirradiation at 515 nm, compounds **1** and **2** exhibited a reduction of Φ_{CO} by a factor of 10, following the same behavior without the presence of N-CDs. This characteristic behavior was conspicuously absent during exposure to 395 nm light where the doped carbon dots have a stronger absorption. Under the latter conditions, compounds **1** to **3** demonstrated a marginal decrease in yield, whereas compound **4** displayed a yield approximately half of that of **3**. Additionally, the k_{CO} values were found to be sequentially higher for **1**, followed by **4**, **3**, and **2**. This trend suggests that the resonance effect likely exerts a more significant

influence than the chalcogenic moiety on the observed variations in their release rate, even under the nanoparticles presence.

Table 17:. Photodissociation constants and quantum yield for the CO photodissociation process. Excitations were made at their absorption maxima being **1'** and **2'** with LED λ_{max} in 515±15 nm and **1- 4** with LED λ_{max} in 395 ± 5 nm.

System (MCC+N-CDs)	Φ(10^{-3})	k_{CO} (10^{-3} s^{-1})	k (10^{-3} s^{-1})
1'	10.15 ± 0.25	5.43 ± 0.83	7.39 ± 0.24
2'	1.31 ± 0.04	0.13 ± 0.01	1.68 ± 0.01
1	5.81 ± 0.10	4.23 ± 0.79	3.87 ± 0.03
2	5.48 ± 0.18	1.22 ± 0.07	1.72 ± 0.01
3	4.04 ± 0.01	1.24 ± 0.08	1.52 ± 0.03
4	2.05 ± 0.14	3.11 ± 0.48	2.78 ± 0.05

2.5 CONCLUSIONS

The top-down hydrothermal approach employed in this study to fabricate non-doped and doped carbon dots has proven to be a straightforward, efficient, and sustainable method for producing high-quality customizable nanoparticles from biomass sources like paper waste. The presence of nitrogen doping in these materials was confirmed through chemical analysis, FTIR, and XPS techniques. Morphological examination using HR-TEM revealed the presence of quasi-spherical nanoparticles exhibiting sizes between 4.4 - 6.8 nm.

When the catalytic activity of CDs and N- CDs in the photodegradation of 4-nitrophenol was evaluated, these biomass-derived materials demonstrated favorable performance compared to similar composites. Notably, being metal-free, self-catalyzing, and sourced of environmentally sustainable origins, they present a greener alternative for such applications. Moreover, at low overpotentials and Tafel slopes, these materials were further investigated as electrocatalysts for hydrogen evolution reactions (HER), showcasing promise for HER applications.

Thus, this study introduces a viable way for the development of modified multifaceted CDs, contributing to a new generation of heterogeneous catalysts. These catalysts have shown effectiveness in the degradation of highly toxic organic contaminants and hold potential for extending their application to other dye pollutants. Additionally, they offer a pathway towards the production of cleaner energy through HER, both in doped and non-doped forms. The straightforward doping process, facilitated by the inclusion of nitrogen in the carbon dots, has led to improved catalytic performance.

The synthesized N-CDs were tested together with photoactivated carbon monoxide releasing molecules (photoCORMs) to capture and transfer photons, thereby influencing the CO release. Serving as a proof of concept, the study demonstrates the significant potential of N-CDs as an effective support for photoCORMs, presenting a novel strategy for CO release and expanding the scope of CDs in sustainable technologies.

Future investigations shall explore deeper into exploring the utilization of different raw materials for synthesizing CDs nanoparticles, thereby broadening our

understanding, and expanding the scope of potential applications. Overall, this thesis presents promising results for the utilization of CDs and N-CDs across various domains, including the photodegradation of 4-NP, HER and support for activations of photoCORMs. Subsequent studies will continue to explore the utilization of alternative materials for these and other applications, driving forward advancements in sustainable and environmentally friendly technologies.

FUTURE DEVELOPMENTS

Moving forward, we aim to complete the comprehensive characterization of sulfur-doped carbon dots (S-CDs) and explore their potential applications, similar to those demonstrated for CDs and N-CDs. Additionally, the synthetic route proposed in this study was evaluated for its capacity to generate CDs from alternative biomass sources. Specifically, CDs were successfully synthesized from two types of dried distillers' grains with soluble (DDGS), a waste biomass from the ethanol production industry.

Our methodology proved effective in synthesizing CDs from DDGS samples. Initial characterization indicates that these materials exhibit fluorescence capabilities. HR-TEM revealed that the CDs derived from high-fat DDGS have an average size of 21.3 nm, while those from low-fat DDGS have an average size of 5.4 nm. Additionally, nitrogen doping was achieved through this synthetic route, with initial XPS analysis showing promising results, particularly a five-fold increase in N-H groups on the surface of DDGS-derived N-CDs. Sulfur doping is also planned. Further characterization is required to fully understand the surface properties and potential application possibilities of these newly synthesized CDs.

All CDs synthesized in this work are also planned to be tested as support agents for other biomimetic metal coordination compounds developed by our group. This will further solidify their multifaceted use and application, enhancing the value of human waste and diminishing the environmental impact of human activities. By repurposing waste biomass into valuable materials, this research contributes to sustainable technology development and environmental conservation.

REFERENCES

[1] F. Zobi, “CO and CO-releasing molecules in medicinal chemistry,” *Future Med. Chem.*, vol. 5, no. 2, pp. 175–188, 2013, doi: 10.4155/fmc.12.196.

[2] F. Winau, O. Westphal, and R. Winau, “Paul Ehrlich - In search of the magic bullet,” *Microbes Infect.*, vol. 6, no. 8, pp. 786–789, 2004, doi: 10.1016/j.micinf.2004.04.003.

[3] S. Riethmiller, “From atoxyl to salvarsan: Searching for the magic bullet,” *Chemotherapy*, vol. 51, no. 5, pp. 234–242, 2005, doi: 10.1159/000087453.

[4] J. E. T. & V. H. M. BARNETT ROSENBERG, LORETTA VANCAMP, “Platinum Compounds: a New Class of Potent Antitumour Agents,” *Nature*, vol. 222, pp. 385–386, 1969.

[5] G. B. Kauffman, R. Pentimalli, S. Doldi, and M. D. Hall, “Michele Peyrone (1813-1883), discoverer of Cisplatin,” *Platin. Met. Rev.*, vol. 54, no. 4, pp. 250–256, 2010, doi: 10.1595/147106710X534326.

[6] B. Rosenberg, *Cisplatin: Its History and Possible Mechanisms of Action*. ACADEMIC PRESS, INC., 1980. doi: 10.1016/b978-0-12-565050-2.50006-1.

[7] S. Dasari and P. Bernard Tchounwou, “Cisplatin in cancer therapy: Molecular mechanisms of action,” *Eur. J. Pharmacol.*, vol. 740, pp. 364–378, 2014, doi: 10.1016/j.ejphar.2014.07.025.

[8] J. B. Sumner, “Enzyme Urease,” *J. Biol. Chem.*, vol. 69, pp. 435–441, 1926, [Online]. Available: http://www.jbc.org/content/69/2/435.full.pdf+html

[9] D. C. Hodgkin, J. Pickworth, J. H. Robertson, K. N. Trueblood, R. J. Prosen, and J. G. White, “Structure of vitamin B12:The crystal structure of the hexacarboxylic acid derived from B12 and the molecular structure of the vitamin,” *Nature*, vol. 176, no. 4477, pp. 325–328, 1955, doi: 10.1038/176325a0.

[10] A. C. T. PERUTZ, M. F., ROSSMANN, M. G., CULLIS, A. F., MUIRHEAD, H., WILL, G., & NORTH, “Structure of Hæmoglobin: A Three-Dimensional Fourier Synthesis at 5.5-Å. Resolution, Obtained by X-Ray Analysis,” *Nature*, vol. 185, pp. 416–422, 1960.

[11] C. J. Miller and L. A. Davidson, “The interplay between cell signalling and mechanics in developmental processes,” *Nat. Rev. Genet.*, vol. 14, no. 10, pp. 733–744, 2013, doi: 10.1038/nrg3513.

[12] R. A. Bradshaw and E. A. Dennis, *Cell signaling. yesterday, today, and*

tomorrow, Second Edi., vol. 1. Elsevier Inc., 2010. doi: 10.1016/B978-0-12-374145-5.00001-2.

[13] J. Feher, “Cell Signaling,” *Quant. Hum. Physiol.*, pp. 205–217, 2017, doi: 10.1016/b978-0-12-800883-6.00019-7.

[14] L. S. Argetsinger and C. Carter-Su, “Mechanism of signaling by growth hormone receptor,” *Physiol. Rev.*, vol. 76, no. 4, pp. 1089–1107, 1996, doi: 10.1152/physrev.1996.76.4.1089.

[15] G. Burnstock, “NEUROTRANSMITTERS AND TROPHICFACTORS IN THE AUTONOMIC NERVOUS SYSTEM,” vol. 313, pp. 1–35, 1981.

[16] R. Sapolsky, “Biology and Human Behavior: The Neurological Origins of Individuality, 2nd Edition,” *Biol. Hum. Behav. Neurol. Orig. Individ.*, p. 124, 2005.

[17] R. M. M. de Almeida, J. C. C. Cabral, and R. Narvaes, “Behavioural, hormonal and neurobiological mechanisms of aggressive behaviour in human and nonhuman primates,” *Physiol. Behav.*, vol. 143, pp. 121–135, 2015, doi: 10.1016/j.physbeh.2015.02.053.

[18] B. S. Meldrum, “Glutamate and Glutamine in the Brain Glutamate as a Neurotransmitter in the Brain : Review of Physiology and Pathology 1,” no. May, pp. 1007–1015, 2018.

[19] L. Moses, “Serotonin : a review,” no. 1957, pp. 187–199, 2008, doi: 10.1111/j.1365-2885.2008.00944.x.REVIEW.

[20] F. Sánchez-Jiménez, M. V. Ruiz-Pérez, J. L. Urdiales, and M. A. Medina, “Pharmacological potential of biogenic amine-polyamine interactions beyond neurotransmission,” *Br. J. Pharmacol.*, vol. 170, no. 1, pp. 4–16, 2013, doi: 10.1111/bph.12109.

[21] T. Kadowaki and T. Yamauchi, “Adiponectin and adiponectin receptors,” *Endocr. Rev.*, vol. 26, no. 3, pp. 439–451, 2005, doi: 10.1210/er.2005-0005.

[22] M. E. Hasselmo, “Neuromodulation and cortical function: modeling the physiological basis of behavior,” *Behav. Brain Res.*, vol. 67, no. 1, pp. 1–27, 1995, doi: 10.1016/0166-4328(94)00113-T.

[23] L. Wang, X. Xie, B. Ke, W. Huang, X. Jiang, and G. He, “Recent advances on endogenous gasotransmitters in inflammatory dermatological disorders,” *J. Adv. Res.*, vol. 38, pp. 261–274, 2022, doi: 10.1016/j.jare.2021.08.012.

[24] J. Li, G. Zhang, S. Cai, and A. N. Redington, “Effect of inhaled hydrogen sulfide on metabolic responses in anesthetized, paralyzed, and mechanically ventilated

piglets," *Pediatr. Crit. Care Med.*, vol. 9, no. 1, pp. 110–112, 2008, doi: 10.1097/01.PCC.0000298639.08519.0C.

[25] D. Liu, H. Jin, C. Tang, and J. Du, "Sulfur Dioxide: a Novel Gaseous Signal in the Regulation of Cardiovascular Functions," *Mini-Reviews Med. Chem.*, vol. 10, no. 11, pp. 1039–1045, 2012, doi: 10.2174/1389557511009011039.

[26] A. K. Mustafa, M. M. Gadalla, and S. H. Snyder, "Signaling by gasotransmitters," *Sci. Signal.*, vol. 2, no. 68, 2009, doi: 10.1126/scisignal.268re2.

[27] H. M. Schipper, H. Chertkow, K. Mehindate, D. Frankel, C. Melmed, and H. Bergman, "Evaluation of heme oxygenase-1 as a systemic biological marker of sporadic AD," *Neurology*, vol. 54, no. 6, pp. 1297–1304, 2000, doi: 10.1212/WNL.54.6.1297.

[28] M. Westphal, T. P. Weber, S. Von Kegler, H. Van Aken, and M. Booke, "Oxygen Fractions," vol. 295, pp. 975–977, 2002.

[29] J. B. Leikin, R. M. Goldenberg, D. Edwards, and M. Zell-Kantor, "Carbon monoxide poisoning," *Vet. Hum. Toxicol.*, vol. 30, no. 1, pp. 40–42, 1988.

[30] W. Durante, "Role of carbon monoxide in cardiovascular function," *J. Cell. Mol. Med.*, vol. 10, no. 3, 2006, doi: 10.2755/jcmm010.003.11.

[31] T. Sjöstrand, "Endogenous formation of carbon monoxide in man," *Nature*, vol. 164, no. 4170. pp. 580–581, 1949. doi: 10.1038/164580a0.

[32] A. Verma, D. J. Hirsch, C. E. Glatt, G. V. Ronnett, and S. H. Snyder, "Carbon monoxide: A putative neural messenger," *Science (80-.).*, vol. 259, no. 5093, pp. 381–384, 1993, doi: 10.1126/science.7678352.

[33] G. P. Roberts, H. Youn, and R. L. Kerby, "CO-Sensing Mechanisms," vol. 68, no. 3, pp. 453–473, 2004, doi: 10.1128/MMBR.68.3.453.

[34] S. W. Ryter, J. Alam, and A. M. K. Choi, "Heme oxygenase-1/carbon monoxide: From basic science to therapeutic applications," *Physiol. Rev.*, vol. 86, no. 2, pp. 583–650, 2006, doi: 10.1152/physrev.00011.2005.

[35] I. Andreadou, E. K. Iliodromitis, T. Rassaf, R. Schulz, A. Papapetropoulos, and P. Ferdinandy, "The role of gasotransmitters NO, H2S and CO in myocardial ischaemia/reperfusion injury and cardioprotection by preconditioning, postconditioning and remote conditioning," *Br. J. Pharmacol.*, vol. 172, no. 6, pp. 1587–1606, 2015, doi: 10.1111/bph.12811.

[36] L. Dong, H. Wang, K. Chen, and Y. Li, "Roles of hydroxyeicosatetraenoic acids in diabetes (HETEs and diabetes)," *Biomed. Pharmacother.*, vol. 156, no.

August, p. 113981, 2022, doi: 10.1016/j.biopha.2022.113981.

[37] B. Brune and V. Ullrich, “Inhibition of platelet aggregation by carbon monoxide is mediated by activation of guanylate cyclase,” *Mol. Pharmacol.*, vol. 32, no. 4, pp. 497–504, 1987.

[38] T. L. Poulos, “Soluble guanylate cyclase,” *Curr. Opin. Struct. Biol.*, vol. 16, no. 6, pp. 736–743, 2006, doi: 10.1016/j.sbi.2006.09.006.

[39] I. Bauer and B. H. J. Pannen, “Bench-to-bedside review: Carbon monoxide--from mitochondrial poisoning to therapeutic use.,” *Crit. Care*, vol. 13, no. 4, p. 220, 2009, doi: 10.1186/cc7887.

[40] L. M. Chu, S. Shaefi, J. D. Byrne, R. W. Alves de Souza, and L. E. Otterbein, “Carbon monoxide and a change of heart,” *Redox Biol.*, vol. 48, no. November, p. 102183, 2021, doi: 10.1016/j.redox.2021.102183.

[41] A. M. K. Choi *et al.*, “Carbon monoxide has anti-inflammatory effects involving the mitogen-activated protein kinase pathway,” *Nat. Med.*, vol. 6, no. 4, pp. 422–428, 2000, [Online]. Available: http://www.nature.com/doifinder/10.1038/74680%5Cnpapers2://publication/doi/10.1038/74680

[42] W. W. Hancock, R. Buelow, M. H. Sayegh, and L. A. Turka, “Antibody-induced transplant arteriosclerosis is prevented by graft expression of anti-oxidant and anti-apoptotic genes,” *Nat. Med.*, vol. 4, no. 12, pp. 1392–1396, 1998, doi: 10.1038/3982.

[43] S. W. Ryter, D. Morse, and A. M. K. Choi, “Carbon monoxide: to boldly go where NO has gone before.,” *Sci. STKE*, vol. 2004, no. 230, pp. 1–11, 2004, doi: 10.1126/stke.2302004re6.

[44] M. Knauert, S. Vangala, M. Haslip, and P. J. Lee, “Therapeutic applications of carbon monoxide,” *Oxid. Med. Cell. Longev.*, vol. 2013, 2013, doi: 10.1155/2013/360815.

[45] S. W. Ryter and A. M. K. Choi, “Carbon monoxide: Present and future indications for a medical gas,” *Korean J. Intern. Med.*, vol. 28, no. 2, pp. 123–140, 2013, doi: 10.3904/kjim.2013.28.2.123.

[46] T. R. Johnson, B. E. Mann, J. E. Clark, R. Foresti, C. J. Green, and R. Motterlini, “Metal carbonyls: A new class of pharmaceuticals?,” *Angew. Chemie - Int. Ed.*, vol. 42, no. 32, pp. 3722–3729, 2003, doi: 10.1002/anie.200301634.

[47] S. D. Friis, R. H. Taaning, A. T. Lindhardt, and T. Skrydstrup, “Silacarboxylic

acids as efficient carbon monoxide releasing molecules: Synthesis and application in palladium-catalyzed carbonylation reactions," *J. Am. Chem. Soc.*, vol. 133, no. 45, pp. 18114–18117, 2011, doi: 10.1021/ja208652n.

[48] T. Slanina and P. Šebej, "Visible-light-activated photoCORMs: Rational design of CO-releasing organic molecules absorbing in the tissue-transparent window," *Photochem. Photobiol. Sci.*, vol. 17, no. 6, pp. 692–710, 2018, doi: 10.1039/c8pp00096d.

[49] R. Alberto and R. Motterlini, "Chemistry and biological activities of CO-releasing molecules (CORMs) and transition metal complexes," *Dalt. Trans.*, no. 17, pp. 1651–1660, 2007, doi: 10.1039/b701992k.

[50] Brian W. Pfennig, *PRINCIPLES OF INORGANIC CHEMISTRY*. 2015.

[51] C. C. Romão, W. A. Blättler, J. D. Seixas, and G. J. L. Bernardes, "Developing drug molecules for therapy with carbon monoxide," *Chem. Soc. Rev.*, vol. 41, no. 9, pp. 3571–3583, 2012, doi: 10.1039/c2cs15317c.

[52] A. L. Amorim, "Liberação fotoinduzida de monóxido de carbono: Novas perspectivas no design de compostos carbonílicos metálicos," *Tese*, p. 216, 2020, [Online]. Available: https://repositorio.ufsc.br/handle/123456789/216460

[53] L. Hewison *et al.*, "New types of CO-releasing molecules (CO-RMs), based on iron dithiocarbamate complexes and [Fe(CO) 3I(S 2COEt)]," *Organometallics*, vol. 31, no. 16, pp. 5823–5834, 2012, doi: 10.1021/om3003637.

[54] X. He, "Thermostability of Biological Systems: Fundamentals, Challenges, and Quantification," *Open Biomed. Eng. J.*, vol. 5, no. 1, pp. 47–73, 2011, doi: 10.2174/1874120701105010047.

[55] F. Zobi, O. Blacque, R. A. Jacobs, M. C. Schaub, and A. Y. Bogdanova, "17 e - rhenium dicarbonyl CO-releasing molecules on a cobalamin scaffold for biological application," *Dalt. Trans.*, vol. 41, no. 2, pp. 370–378, 2012, doi: 10.1039/c1dt10649j.

[56] S. Romanski *et al.*, "Acyloxybutadiene tricarbonyl iron complexes as enzyme-triggered CO-releasing molecules (ET-CORMs): A structure-activity relationship study," *Dalt. Trans.*, vol. 41, no. 45, pp. 13862–13875, 2012, doi: 10.1039/c2dt30662j.

[57] E. Kottelat and F. Zobi, "Visible Light-Activated PhotoCORMs," *inorganics*, vol. 5, no. 24, 2017, doi: 10.3390/inorganics5020024.

[58] S. Bonnet, "Shifting the Light Activation of Metallodrugs to the Red and Near-

Infrared Region in Anticancer Phototherapy," *Comments Inorg. Chem.*, vol. 35, no. 4, pp. 179–213, 2015, doi: 10.1080/02603594.2014.979286.

[59] I. Chakraborty, S. J. Carrington, and P. K. Mascharak, "Design strategies to improve the sensitivity of photoactive metal carbonyl complexes (photoCORMs) to visible light and their potential as CO-donors to biological targets," *Acc. Chem. Res.*, vol. 47, no. 8, pp. 2603–2611, 2014, doi: 10.1021/ar500172f.

[60] A. E. Pierri *et al.*, "A photoCORM nanocarrier for CO release using NIR light," *Chem. Commun.*, vol. 51, no. 11, pp. 2072–2075, 2015, doi: 10.1039/c4cc06766e.

[61] Q. He *et al.*, "NIR-Responsive On-Demand Release of CO from Metal Carbonyl-Caged Graphene Oxide Nanomedicine," *Adv. Mater.*, vol. 27, no. 42, pp. 6741–6746, Nov. 2015, doi: 10.1002/adma.201502762.

[62] S. E. McGlynn, D. W. Mulder, E. M. Shepard, J. B. Broderick, and J. W. Peters, "Hydrogenase cluster biosynthesis: Organometallic chemistry nature's way," *Dalt. Trans.*, no. 22, pp. 4274–4285, 2009, doi: 10.1039/b821432h.

[63] R. L. Arrowsmith *et al.*, "Confocal and fluorescence lifetime imaging sheds light on the fate of a pyrene-tagged carbon monoxide-releasing Fischer carbene chromium complex," *Dalt. Trans.*, vol. 44, no. 11, pp. 4957–4962, 2015, doi: 10.1039/c4dt03312d.

[64] R. Long, I. Salouage, A. Berdeaux, R. Motterlini, and D. Morin, "CORM-3, a water soluble CO-releasing molecule, uncouples mitochondrial respiration via interaction with the phosphate carrier," *Biochim. Biophys. Acta - Bioenerg.*, vol. 1837, no. 1, pp. 201–209, 2014, doi: 10.1016/j.bbabio.2013.10.002.

[65] M. A. Gonzalez, N. L. Fry, R. Burt, R. Davda, A. Hobbs, and P. K. Mascharak, "Designed iron carbonyls as carbon monoxide (CO) releasing molecules: Rapid CO release and delivery to myoglobin in aqueous buffer, and vasorelaxation of mouse aorta," *Inorg. Chem.*, vol. 50, no. 7, pp. 3127–3134, 2011, doi: 10.1021/ic2000848.

[66] R. Kretschmer, G. Gessner, H. Görls, S. H. Heinemann, and M. Westerhausen, "Dicarbonyl-bis(cysteamine)iron(II): A light induced carbon monoxide releasing molecule based on iron (CORM-S1)," *J. Inorg. Biochem.*, vol. 105, no. 1, pp. 6–9, 2011, doi: 10.1016/j.jinorgbio.2010.10.006.

[67] L. A. Casson *et al.*, "N-Heterocyclic carbenes as π*-acceptors in luminescent Re(i) triscarbonyl complexes," *Dalt. Trans.*, vol. 40, no. 44, pp. 11960–11967,

2011, doi: 10.1039/c1dt11233c.

[68] S. J. Carrington, I. Chakraborty, and P. K. Mascharak, “Exceptionally rapid CO release from a manganese(i) tricarbonyl complex derived from bis(4-chloro-phenylimino)acenaphthene upon exposure to visible light,” *Dalt. Trans.*, vol. 44, no. 31, pp. 13828–13834, 2015, doi: 10.1039/c5dt01007a.

[69] A. L. Amorim *et al.*, “Synthesis, characterization and biological evaluation of new manganese metal carbonyl compounds that contain sulfur and selenium ligands as a promising new class of CORMs,” *Dalt. Trans.*, vol. 48, no. 17, pp. 5574–5584, 2019, doi: 10.1039/c9dt00616h.

[70] H. Berends and P. Kurz, “Investigation of light-triggered carbon monoxide release from two manganese photoCORMs by IR , UV – Vis and EPR spectroscopy,” *Inorganica Chim. Acta*, vol. 380, pp. 141–147, 2012, doi: 10.1016/j.ica.2011.10.047.

[71] S. R. Hartmann and E. L. Hahn, “Nuclear double resonance in the rotating frame,” *Phys. Rev.*, vol. 128, no. 5, pp. 2042–2053, 1962, doi: 10.1103/PhysRev.128.2042.

[72] B. M. Fung, A. K. Khitrin, and K. Ermolaev, “An Improved Broadband Decoupling Sequence for Liquid Crystals and Solids,” *J. Magn. Reson.*, vol. 142, no. 1, pp. 97–101, 2000, doi: 10.1006/jmre.1999.1896.

[73] X. Wu and K. W. Zilm, “Complete spectral editing in CPMAS NMR,” *Journal of Magnetic Resonance - Series A*, vol. 102, no. 2. pp. 205–213, 1993. doi: 10.1006/jmra.1993.1092.

[74] A. Altomare *et al.*, “SIR97: A new tool for crystal structure determination and refinement,” *J. Appl. Crystallogr.*, vol. 32, no. 1, pp. 115–119, 1999, doi: 10.1107/S0021889898007717.

[75] R. R. Gagne, C. A. Koval, and G. C. Lisensky, “Ferrocene as an Internal Standard for Electrochemical Measurements,” *Inorg. Chem.*, vol. 19, no. 9, pp. 2854–2855, 1980, doi: 10.1021/ic50211a080.

[76] M. Strohalm, D. Kavan, P. Novák, M. Volný, and V. Havlíček, “MMass 3: A cross-platform software environment for precise analysis of mass spectrometric data,” *Anal. Chem.*, vol. 82, no. 11, pp. 4648–4651, 2010, doi: 10.1021/ac100818g.

[77] C. Bischof, T. Joshi, A. Dimri, L. Spiccia, and U. Schatzschneider, “Synthesis, spectroscopic properties, and photoinduced CO-release studies of functionalized ruthenium(II) polypyridyl complexes: Versatile building blocks for

development of CORM-peptide nucleic acid bioconjugates," *Inorg. Chem.*, vol. 52, no. 16, pp. 9297–9308, Aug. 2013, doi: 10.1021/ic400746n.

[78] R. R. Sauers, S. D. Van Arnum, and A. A. Scimone, "Green chemistry analytical method development: A revisit on the use of potassium ferrioxalate as a chemical actinometer," *Green Chem.*, vol. 6, no. 11, pp. 578–582, 2004, doi: 10.1039/b410391b.

[79] H. J. Kuhn, S. E. Braslavsky, and R. Schmidt, "Chemical actinometry," *Pure Appl. Chem.*, vol. 76, no. 12, pp. 2105–2146, 2004, doi: 10.1351/pac198961020187.

[80] S. McLean, B. E. Mann, and R. K. Poole, "Sulfite species enhance carbon monoxide release from CO-releasing molecules: Implications for the deoxymyoglobin assay of activity," *Anal. Biochem.*, vol. 427, no. 1, pp. 36–40, 2012, doi: 10.1016/j.ab.2012.04.026.

[81] A. J. Atkin *et al.*, "Modification of the deoxy-myoglobin/carbonmonoxy-myoglobin UV-vis assay for reliable determination of CO-release rates from organometallic carbonyl complexes," *Dalt. Trans.*, vol. 40, no. 21, pp. 5755–5761, 2011, doi: 10.1039/c0dt01809k.

[82] A. Eraldo and M. Brunori, *Hemoglobin and myoglobin in their reactions with ligands*. Amsterdam : North-Holland, 1971., 1971. [Online]. Available: https://lib.ugent.be/catalog/rug01:001650991

[83] C. Bosset *et al.*, "Iron-Catalyzed Synthesis of Sulfur-Containing Heterocycles," *J. Org. Chem.*, vol. 82, no. 8, pp. 4020–4036, Apr. 2017, doi: 10.1021/acs.joc.6b01827.

[84] S. Roy, P. Mitra, and A. K. Patra, "Cu(II) complexes with square pyramidal (N2S)CuCl2 chromophore: Jahn-Teller distortion and subsequent effect on spectral and structural properties," *Inorganica Chim. Acta*, vol. 370, no. 1, pp. 247–253, May 2011, doi: 10.1016/j.ica.2011.01.068.

[85] D. C. Bebout, W. Lai, S. M. Stamps, S. M. Berry, and R. J. Butcher, "Zinc triad metal ion complexes of NN′S ligand N-(2-pyridylmethyl)-N-(2-(methylthio)ethyl)amine," *Main Gr. Chem.*, vol. 6, no. 3–4, pp. 155–168, Sep. 2007, doi: 10.1080/10241220802144552.

[86] I. A. Koval *et al.*, "Dinuclear CuII complexes with a new phenol-based ligand bearing pyridine and thiophene substituents: Synthesis, characterization and interaction with catechol substrates," *Eur. J. Inorg. Chem.*, no. 20, pp. 4036–4045, Oct. 2004, doi: 10.1002/ejic.200400092.

[87] M. A. Gonzalez, S. J. Carrington, N. L. Fry, J. L. Martinez, and P. K. Mascharak, “Syntheses, structures, and properties of new manganese carbonyls as photoactive co-releasing molecules: Design strategies that lead to co photolability in the visible region,” *Inorg. Chem.*, vol. 51, no. 21, pp. 11930–11940, Nov. 2012, doi: 10.1021/ic3018216.

[88] A. Jana, K. Das, A. Kundu, P. R. Thorve, D. Adhikari, and B. Maji, “A Phosphine-Free Manganese Catalyst Enables Stereoselective Synthesis of (1 + n)-Membered Cycloalkanes from Methyl Ketones and 1, n-Diols,” *ACS Catal.*, vol. 10, no. 4, pp. 2615–2626, 2020, doi: 10.1021/acscatal.9b05567.

[89] R. D. Shannon, “Revised effective ionic radii and systematic studies of interatomic distances in halides and chalcogenides. Acta Crystallographica,” *Pharm. Res. An Off. J. Am. Assoc. Pharm. Sci.*, vol. 32, no. 5, pp. 751–767, 1976, doi: 10.1107/s0567739476001551.

[90] A. Mondal, R. Sharma, B. Dutta, D. Pal, and D. Srimani, “Well-Defined NNS-Mn Complex Catalyzed Selective Synthesis of C-3 Alkylated Indoles and Bisindolylmethanes Using Alcohols,” *J. Org. Chem.*, vol. 87, no. 6, pp. 3989–4000, 2022, doi: 10.1021/acs.joc.1c02702.

[91] K. Das, A. Mondal, and D. Srimani, “Selective Synthesis of 2-Substituted and 1,2-Disubstituted Benzimidazoles Directly from Aromatic Diamines and Alcohols Catalyzed by Molecularly Defined Nonphosphine Manganese(I) Complex,” *J. Org. Chem.*, vol. 83, no. 16, pp. 9553–9560, 2018, doi: 10.1021/acs.joc.8b01316.

[92] A. L. Amorim *et al.*, “Synthesis, characterization and photoinduced CO-release by manganese(i) complexes,” *New J. Chem.*, vol. 44, no. 26, pp. 10892–10901, Jul. 2020, doi: 10.1039/d0nj02260h.

[93] G. A. Crowder, “The C-S stretching frequency in thiols acids and esters,” vol. 26, no. 4, pp. 486–487, 1972, doi: 10.1366/000370272774351912.

[94] S. R. Maqsood, N. Islam, S. Bashir, B. Khan, and A. H. Pandith, “Sigma donor and pi acceptor characteristics of certain NN-bidentate ligands: A DFT study,” *J. Coord. Chem.*, vol. 66, no. 13, pp. 2308–2315, 2013, doi: 10.1080/00958972.2013.800866.

[95] A. M. Bond, R. Colton, and M. E. McDONALD, “Chemical and Electrochemical Studies of Tricarbonyl Derivatives of Manganese and Rhenium,” *Inorg. Chem.*, vol. 17, no. 10, pp. 2842–2847, 1978, doi: 10.1021/ic50188a032.

[96] R. Maria, I. Ap, B. S. Lima, and M. G. Neumann, “Spectroscopic and electrochemical properties of [Mn (phen)(CO) 3 (imidazole)](SO 3 CF 3) complexes,” *Inorganica Chim. Acta*, vol. 299, pp. 231–237, 2000.

[97] S. Pordel and J. K. White, “Impact of Mn(I) photoCORM ligand set on photochemical intermediate formation during visible light-activated CO release,” *Inorganica Chim. Acta*, vol. 500, p. 119206, Jan. 2020.

[98] V. C. Weiss *et al.*, “Luminescent PhotoCORMs: Enabling/Disabling CO Delivery upon Blue Light Irradiation,” *Inorg. Chem.*, vol. 59, no. 18, pp. 13078–13090, Sep. 2020, doi: 10.1021/acs.inorgchem.0c00638.

[99] S. Pordel and J. K. White, “Impact of Mn(I) photoCORM ligand set on photochemical intermediate formation during visible light-activated CO release,” *Inorganica Chim. Acta*, vol. 500, p. 119206, Jan. 2020, doi: 10.1016/j.ica.2019.119206.

[100] U. Sachs, G. Schaper, D. Winkler, D. Kratzert, and P. Kurz, “Light- or oxidation-triggered CO release from [MnI(CO)3(κ3-L)] complexes: Reaction intermediates and a new synthetic route to [MnIII/IV2 (μ-O)2(L)2] compounds,” *Dalt. Trans.*, vol. 45, no. 43, pp. 17464–17473, 2016, doi: 10.1039/c6dt02020h.

[101] U. Schatzschneider, “PhotoCORMs: Light-triggered release of carbon monoxide from the coordination sphere of transition metal complexes for biological applications,” *Inorganica Chim. Acta*, vol. 374, no. 1, pp. 19–23, 2011, doi: 10.1016/j.ica.2011.02.068.

[102] R. N. Pickens, B. J. Neyhouse, D. T. Reed, S. T. Ashton, and J. K. White, “Visible Light-Activated CO Release and 1O2 Photosensitizer Formation with Ru(II),Mn(I) Complexes,” *Inorg. Chem.*, vol. 57, no. 18, pp. 11616–11625, 2018, doi: 10.1021/acs.inorgchem.8b01759.

[103] D. Sumanth Kumar, B. Jai Kumar, and H. M. Mahesh, *Quantum Nanostructures (QDs): An Overview*. Elsevier Ltd., 2018. doi: 10.1016/B978-0-08-101975-7.00003-8.

[104] A. B. Asha and R. Narain, *Nanomaterials properties*. Elsevier Inc., 2020. doi: 10.1016/B978-0-12-816806-6.00015-7.

[105] B. Mekuye and B. Abera, “Nanomaterials: An overview of synthesis, classification, characterization, and applications,” *Nano Sel.*, vol. 4, no. 8, pp. 486–501, 2023, doi: 10.1002/nano.202300038.

[106] F. J. Heiligtag and M. Niederberger, “The fascinating world of nanoparticle

research," *Mater. Today*, vol. 16, no. 7–8, pp. 262–271, 2013, doi: 10.1016/j.mattod.2013.07.004.

[107] P. Walter *et al.*, "Early use of PbS nanotechnology for an ancient hair dyeing formula," *Nano Lett.*, vol. 6, no. 10, pp. 2215–2219, 2006, doi: 10.1021/nl061493u.

[108] M. T. Rahman and E. V. Rebrov, "Microreactors for gold nanoparticles synthesis: From faraday to flow," *Processes*, vol. 2, no. 2, pp. 466–493, 2014, doi: 10.3390/pr2020466.

[109] R. P. Feynman, "There's plenty of room at the bottom," *Resonance*, vol. 16, no. 9, pp. 890–905, 2011, doi: 10.1007/s12045-011-0109-x.

[110] G. Binnig and H. Rohrer, "Scanning Tunneling Microscopy.," *IBM J. Res. Dev.*, vol. 30, no. 4, pp. 355–369, 1986, doi: 10.2320/materia1962.25.821.

[111] D. Eigler, M and E. Scweizer, K, "Positioning single atoms with a scanning tunnelling microscope," *Nature*, vol. 344. pp. 524–526, 1990.

[112] A. L. Efros and L. E. Brus, "Nanocrystal Quantum Dots: From Discovery to Modern Development," *ACS Nano*, vol. 15, no. 4, pp. 6192–6210, 2021, doi: 10.1021/acsnano.1c01399.

[113] R. Rossetti and L. Brus, "Electron-hole recombination emission as a probe of surface chemistry in aqueous CdS colloids," *J. Phys. Chem.*, vol. 86, no. 23, pp. 4470–4472, 1982, doi: 10.1021/j100220a003.

[114] R. E. Kroto, H. W., Heath, J. R., O'Brien, S. C., Curl, R. F., & Smalley, "C60: Buckminsterfullerene," *Nature*, vol. 318, no. 6042, pp. 162–163, 1985, doi: 10.1038/318162a0.

[115] K. S. Novoselov et al, "Electric Field Effect in Atomically Thin Carbon Films," vol. 306, no. 5696, pp. 666–669, 2016.

[116] W. Yu, L. Sisi, Y. Haiyan, and L. Jie, "Progress in the functional modification of graphene/graphene oxide: A review," *RSC Adv.*, vol. 10, no. 26, pp. 15328–15345, 2020, doi: 10.1039/d0ra01068e.

[117] X. Xu *et al.*, "Electrophoretic analysis and purification of fluorescent single-walled carbon nanotube fragments," *J. Am. Chem. Soc.*, vol. 126, no. 40, pp. 12736–12737, Oct. 2004, doi: 10.1021/JA040082H.

[118] S. H. Choi, "Unique properties of graphene quantum dots and their applications in photonic/electronic devices," *J. Phys. D. Appl. Phys.*, vol. 50, no. 10, 2017, doi: 10.1088/1361-6463/aa5244.

[119] Y. Wang *et al.*, “Carbon dots of different composition and surface functionalization: Cytotoxicity issues relevant to fluorescence cell imaging,” *Exp. Biol. Med.*, vol. 236, no. 11, pp. 1231–1238, 2011, doi: 10.1258/ebm.2011.011132.

[120] S. K. Das, Y. Liu, S. Yeom, D. Y. Kim, and C. I. Richards, “Single-particle fluorescence intensity fluctuations of carbon nanodots,” *Nano Lett.*, vol. 14, no. 2, pp. 620–625, 2014, doi: 10.1021/nl403820m.

[121] H. Ali, S. Ghosh, and N. R. Jana, “Fluorescent carbon dots as intracellular imaging probes,” *Wiley Interdiscip. Rev. Nanomedicine Nanobiotechnology*, vol. 12, no. 4, pp. 1–15, 2020, doi: 10.1002/wnan.1617.

[122] A. Xu *et al.*, “Carbon-Based Quantum Dots with Solid-State Photoluminescent: Mechanism, Implementation, and Application,” *Small*, vol. 16, no. 48, pp. 1–31, 2020, doi: 10.1002/smll.202004621.

[123] N. Ngafwan *et al.*, “Study on novel fluorescent carbon nanomaterials in food analysis,” vol. 2061, pp. 1–6, 2022.

[124] Z. Liang, M. Kang, G. F. Payne, X. Wang, and R. Sun, “Probing Energy and Electron Transfer Mechanisms in Fluorescence Quenching of Biomass Carbon Quantum Dots,” *ACS Appl. Mater. Interfaces*, vol. 8, no. 27, pp. 17478–17488, 2016, doi: 10.1021/acsami.6b04826.

[125] Y. Liu, C. yan Liu, and Z. ying Zhang, “Synthesis and surface photochemistry of graphitized carbon quantum dots,” *J. Colloid Interface Sci.*, vol. 356, no. 2, pp. 416–421, 2011, doi: 10.1016/j.jcis.2011.01.065.

[126] H. Ding, X. H. Li, X. B. Chen, J. S. Wei, X. B. Li, and H. M. Xiong, “Surface states of carbon dots and their influences on luminescence,” *J. Appl. Phys.*, vol. 127, no. 23, 2020, doi: 10.1063/1.5143819.

[127] B. Li *et al.*, “Insight into excitation-related luminescence properties of carbon dots: synergistic effect from photoluminescence centers in the carbon core and on the surface,” *RSC Adv.*, vol. 6, no. 109, pp. 107263–107269, 2016, doi: 10.1039/c6ra20562c.

[128] R. Sato, Y. Iso, and T. Isobe, “Fluorescence Solvatochromism of Carbon Dot Dispersions Prepared from Phenylenediamine and Optimization of Red Emission,” *Langmuir*, 2019, doi: 10.1021/acs.langmuir.9b02739.

[129] S. Zhu, Y. Song, X. Zhao, J. Shao, J. Zhang, and B. Yang, “The photoluminescence mechanism in carbon dots (graphene quantum dots, carbon

nanodots, and polymer dots): current state and future perspective," *Nano Res.*, vol. 8, no. 2, pp. 355–381, Feb. 2015, doi: 10.1007/S12274-014-0644-3.

[130] C. Xia, S. Zhu, T. Feng, M. Yang, and B. Yang, "Evolution and Synthesis of Carbon Dots: From Carbon Dots to Carbonized Polymer Dots," *Adv. Sci.*, vol. 6, no. 23, 2019, doi: 10.1002/advs.201901316.

[131] M. A. Sk, A. Ananthanarayanan, L. Huang, K. H. Lim, and P. Chen, "Revealing the tunable photoluminescence properties of graphene quantum dots," *J. Mater. Chem. C*, vol. 2, no. 34, pp. 6954–6960, 2014, doi: 10.1039/c4tc01191k.

[132] C. F. Chen *et al.*, "Controlling inelastic light scattering quantum pathways in graphene," *Nature*, vol. 471, no. 7340, pp. 617–620, 2011, doi: 10.1038/nature09866.

[133] A. A. Kokorina, A. V. Ermakov, A. M. Abramova, I. Y. Goryacheva, and G. B. Sukhorukov, "Carbon nanoparticles and materials on their basis," *Colloids and Interfaces*, vol. 4, no. 4, pp. 1–13, 2020, doi: 10.3390/colloids4040042.

[134] F. Zhang, X. Feng, Y. Zhang, L. Yan, Y. Yang, and X. Liu, "Photoluminescent carbon quantum dots as a directly film-forming phosphor towards white LEDs," *Nanoscale*, vol. 8, no. 16, pp. 8618–8632, 2016, doi: 10.1039/c5nr08838k.

[135] L. J. Mohammed and K. M. Omer, "Carbon Dots as New Generation Materials for Nanothermometer: Review," *Nanoscale Res. Lett.*, vol. 15, no. 1, 2020, doi: 10.1186/s11671-020-03413-x.

[136] H. Li *et al.*, "Water-Soluble Fluorescent Carbon Quantum Dots and Photocatalyst Design," *Angew. Chemie*, vol. 122, no. 26, pp. 4532–4536, Jun. 2010, doi: 10.1002/ANGE.200906154.

[137] F. Meierhofer *et al.*, "Citric Acid Based Carbon Dots with Amine Type Stabilizers: PH-Specific Luminescence and Quantum Yield Characteristics," *J. Phys. Chem. C*, vol. 124, no. 16, pp. 8894–8904, 2020, doi: 10.1021/acs.jpcc.9b11732.

[138] P. C. Hsu, P. C. Chen, C. M. Ou, H. Y. Chang, and H. T. Chang, "Extremely high inhibition activity of photoluminescent carbon nanodots toward cancer cells," *J. Mater. Chem. B*, vol. 1, no. 13, pp. 1774–1781, 2013, doi: 10.1039/c3tb00545c.

[139] X. C. Yang *et al.*, "One Stone, Two Birds: pH- and Temperature-Sensitive Nitrogen-Doped Carbon Dots for Multiple Anticounterfeiting and Multiple Cell Imaging," *ACS Appl. Mater. Interfaces*, vol. 12, no. 18, pp. 20849–20858, 2020, doi: 10.1021/acsami.0c02206.

[140] H. Ding, S. B. Yu, J. S. Wei, and H. M. Xiong, "Full-color light-emitting carbon

dots with a surface-state-controlled luminescence mechanism," *ACS Nano*, vol. 10, no. 1, pp. 484–491, 2016, doi: 10.1021/acsnano.5b05406.

[141] E. O. Chukwuocha, M. C. Onyeaju, and T. S. T. Harry, "Theoretical Studies on the Effect of Confinement on Quantum Dots Using the Brus Equation," *World J. Condens. Matter Phys.*, vol. 02, no. 02, pp. 96–100, 2012, doi: 10.4236/wjcmp.2012.22017.

[142] P. Dharmalingam, V. Ramanan, G. G. Karthikeyan, N. S. Palani, R. Ilangovan, and P. Ramamurthy, "A study on the electrochemical performance of nitrogen and oxygen co-doped carbon dots derived from a green precursor for supercapacitor applications," *J. Mater. Sci. Mater. Electron.*, vol. 28, no. 24, pp. 18489–18496, 2017, doi: 10.1007/s10854-017-7796-3.

[143] H. Tetsuka, A. Nagoya, T. Fukusumi, and T. Matsui, "Molecularly Designed, Nitrogen-Functionalized Graphene Quantum Dots for Optoelectronic Devices," *Adv. Mater.*, vol. 28, no. 23, pp. 4632–4638, 2016, doi: 10.1002/adma.201600058.

[144] N. Abid *et al.*, "Synthesis of nanomaterials using various top-down and bottom-up approaches, influencing factors, advantages, and disadvantages: A review," *Adv. Colloid Interface Sci.*, vol. 300, no. December 2021, p. 102597, 2022, doi: 10.1016/j.cis.2021.102597.

[145] F. Sun, H. Ghosh, Z. Tan, and S. Sivoththaman, "Top-down synthesis and enhancing device adaptability of graphene quantum dots," *Nanotechnology*, vol. 34, no. 18, 2023, doi: 10.1088/1361-6528/acb7fb.

[146] P. Roy, P. C. Chen, A. P. Periasamy, Y. N. Chen, and H. T. Chang, "Photoluminescent carbon nanodots: Synthesis, physicochemical properties and analytical applications," *Mater. Today*, vol. 18, no. 8, pp. 447–458, 2015, doi: 10.1016/j.mattod.2015.04.005.

[147] M. Kim, S. Osone, T. Kim, H. Higashi, and T. Seto, "Synthesis of nanoparticles by laser ablation: A review," *KONA Powder Part. J.*, vol. 2017, no. 34, pp. 80–90, 2017, doi: 10.14356/kona.2017009.

[148] Y. P. Sun *et al.*, "Quantum-sized carbon dots for bright and colorful photoluminescence," *J. Am. Chem. Soc.*, vol. 128, no. 24, pp. 7756–7757, 2006, doi: 10.1021/ja062677d.

[149] A. Małolepszy *et al.*, "Fluorescent carbon and graphene oxide nanoparticles synthesized by the laser ablation in liquid," *Appl. Phys. A Mater. Sci. Process.*,

vol. 124, no. 4, pp. 1–7, 2018, doi: 10.1007/s00339-018-1711-5.

[150] G. Raniszewski, M. Pyc, and Z. Kolacinski, “Optimization of magnetic field-assisted synthesis of carbon nanotubes for sensing applications,” *Sensors (Switzerland)*, vol. 14, no. 10, pp. 18474–18483, 2014, doi: 10.3390/s141018474.

[151] Y. Zhu, G. Wang, H. Jiang, L. Chen, and X. Zhang, “One-step ultrasonic synthesis of graphene quantum dots with high quantum yield and their application in sensing alkaline phosphatase,” *Chem. Commun.*, vol. 51, no. 5, pp. 948–951, 2015, doi: 10.1039/c4cc07449a.

[152] J. Liu, R. Li, and B. Yang, “Carbon Dots: A New Type of Carbon-Based Nanomaterial with Wide Applications,” *ACS Cent. Sci.*, vol. 6, no. 12, pp. 2179–2195, 2020, doi: 10.1021/acscentsci.0c01306.

[153] D. Sun, R. Ban, P. H. Zhang, G. H. Wu, J. R. Zhang, and J. J. Zhu, “Hair fiber as a precursor for synthesizing of sulfur- and nitrogen-co-doped carbon dots with tunable luminescence properties,” *Carbon N. Y.*, vol. 64, pp. 424–434, 2013, doi: 10.1016/j.carbon.2013.07.095.

[154] L. Spessato *et al.*, “Tuning photodegradation performance using carbon quantum dots and niobium pentoxide,” *J. Mater. Sci. Technol.*, 2024, doi: 10.1016/j.jmst.2023.12.039.

[155] M. Algarra *et al.*, “Sustainable Production of Carbon Nanoparticles from Olive Pit Biomass: Understanding Proton Transfer in the Excited State on Carbon Dots,” *ACS Sustain. Chem. Eng.*, vol. 7, no. 12, pp. 10493–10500, 2019, doi: 10.1021/acssuschemeng.9b00969.

[156] R. Das, R. Bandyopadhyay, and P. Pramanik, “Carbon quantum dots from natural resource: A review,” *Mater. Today Chem.*, vol. 8, pp. 96–109, 2018, doi: 10.1016/j.mtchem.2018.03.003.

[157] B. P. de Oliveira and F. O. M. da Silva Abreu, “Carbon quantum dots synthesis from waste and by-products: Perspectives and challenges,” *Mater. Lett.*, vol. 282, p. 128764, 2021, doi: 10.1016/j.matlet.2020.128764.

[158] A. M. El-Khawaga, A. Zidan, and A. I. A. A. El-Mageed, “Preparation methods of different nanomaterials for various potential applications: A review,” *J. Mol. Struct.*, vol. 1281, 2023, doi: 10.1016/j.molstruc.2023.135148.

[159] P. Priecel and J. A. Lopez-Sanchez, “Advantages and Limitations of Microwave Reactors: From Chemical Synthesis to the Catalytic Valorization of Biobased

Chemicals," *ACS Sustain. Chem. Eng.*, vol. 7, no. 1, pp. 3–21, 2019, doi: 10.1021/acssuschemeng.8b03286.

[160] C. López *et al.*, "Microwave-assisted synthesis of carbon dots and its potential as analysis of four heterocyclic aromatic amines," *Talanta*, vol. 132, pp. 845–850, 2015, doi: 10.1016/j.talanta.2014.10.008.

[161] Y. Y. Yao, G. Gedda, W. M. Girma, C. L. Yen, Y. C. Ling, and J. Y. Chang, "Magnetofluorescent Carbon Dots Derived from Crab Shell for Targeted Dual-Modality Bioimaging and Drug Delivery," *ACS Appl. Mater. Interfaces*, vol. 9, no. 16, pp. 13887–13899, 2017, doi: 10.1021/acsami.7b01599.

[162] C. Ma, C. Yin, Y. Fan, X. Yang, and X. Zhou, "Highly efficient synthesis of N-doped carbon dots with excellent stability through pyrolysis method," *J. Mater. Sci.*, vol. 54, no. 13, pp. 9372–9384, 2019, doi: 10.1007/s10853-019-03585-7.

[163] J. Jia *et al.*, "Highly luminescent N-doped carbon dots from black soya beans for free radical scavenging, Fe3+ sensing and cellular imaging," *Spectrochim. Acta - Part A Mol. Biomol. Spectrosc.*, vol. 211, pp. 363–372, 2019, doi: 10.1016/j.saa.2018.12.034.

[164] Q. Xu, H. Cai, W. Li, M. Wu, Y. Wu, and X. Gong, "Carbon dot/inorganic nanomaterial composites," *J. Mater. Chem. A*, vol. 10, no. 28, pp. 14709–14731, 2022, doi: 10.1039/d2ta02628g.

[165] Z. C. Yang *et al.*, "Intrinsically fluorescent carbon dots with tunable emission derived from hydrothermal treatment of glucose in the presence of monopotassium phosphate," *Chem. Commun.*, vol. 47, no. 42, pp. 11615–11617, 2011, doi: 10.1039/c1cc14860e.

[166] M. Amjadi, J. L. Manzoori, T. Hallaj, and N. Azizi, "Sulfur and nitrogen co-doped carbon quantum dots as the chemiluminescence probe for detection of Cu2+ ions," *J. Lumin.*, vol. 182, pp. 246–251, Feb. 2017, doi: 10.1016/J.JLUMIN.2016.10.021.

[167] W. Lu *et al.*, "Economical, green synthesis of fluorescent carbon nanoparticles and their use as probes for sensitive and selective detection of mercury(II) ions," *Anal. Chem.*, vol. 84, no. 12, pp. 5351–5357, 2012, doi: 10.1021/ac3007939.

[168] C. Liu *et al.*, "Red Emissive Carbon Dot Superoxide Dismutase Nanozyme for Bioimaging and Ameliorating Acute Lung Injury," *Adv. Funct. Mater.*, vol. 33, no. 19, pp. 1–12, 2023, doi: 10.1002/adfm.202213856.

[169] G. Han *et al.*, "Membrane-Penetrating Carbon Quantum Dots for Imaging

Nucleic Acid Structures in Live Organisms," *Angew. Chemie - Int. Ed.*, vol. 58, no. 21, pp. 7087–7091, 2019, doi: 10.1002/anie.201903005.

[170] B. Demir *et al.*, "Tracking Hyaluronan: Molecularly Imprinted Polymer Coated Carbon Dots for Cancer Cell Targeting and Imaging," *ACS Appl. Mater. Interfaces*, vol. 10, no. 4, pp. 3305–3313, 2018, doi: 10.1021/acsami.7b16225.

[171] S. Ruan *et al.*, "Fluorescent carbonaceous nanodots for noninvasive glioma imaging after angiopep-2 decoration," *Bioconjug. Chem.*, vol. 25, no. 12, pp. 2252–2259, 2014, doi: 10.1021/bc500474p.

[172] H. Li, X. Yan, S. Qiao, G. Lu, and X. Su, "Yellow-Emissive Carbon Dot-Based Optical Sensing Platforms: Cell Imaging and Analytical Applications for Biocatalytic Reactions," *ACS Appl. Mater. Interfaces*, vol. 10, no. 9, pp. 7737–7744, 2018, doi: 10.1021/acsami.7b17619.

[173] J. H. Liu *et al.*, "Carbon 'Quantum' Dots for Fluorescence Labeling of Cells," *ACS Appl. Mater. Interfaces*, vol. 7, no. 34, pp. 19439–19445, 2015, doi: 10.1021/acsami.5b05665.

[174] N. Zhou *et al.*, "A novel fluorescent retrograde neural tracer: cholera toxin B conjugated carbon dots," *Nanoscale*, vol. 7, no. 38, pp. 15635–15642, 2015, doi: 10.1039/c5nr04361a.

[175] X. W. Hua, Y. W. Bao, Z. Chen, and F. G. Wu, "Carbon quantum dots with intrinsic mitochondrial targeting ability for mitochondria-based theranostics," *Nanoscale*, vol. 9, no. 30, pp. 10948–10960, 2017, doi: 10.1039/c7nr03658b.

[176] S. Sun *et al.*, "Manganese-Doped Carbon Dots with Redshifted Orange Emission for Enhanced Fluorescence and Magnetic Resonance Imaging," *ACS Appl. Bio Mater.*, vol. 4, no. 2, pp. 1969–1975, 2021, doi: 10.1021/acsabm.0c01597.

[177] G. Calabrese *et al.*, "Carbon dots: An innovative tool for drug delivery in brain tumors," *Int. J. Mol. Sci.*, vol. 22, no. 21, 2021, doi: 10.3390/ijms222111783.

[178] A. Nair, J. T. Haponiuk, S. Thomas, and S. Gopi, "Natural carbon-based quantum dots and their applications in drug delivery: A review," *Biomed. Pharmacother.*, vol. 132, p. 110834, 2020, doi: 10.1016/j.biopha.2020.110834.

[179] S. L. D'souza, S. S. Chettiar, J. R. Koduru, and S. K. Kailasa, "Synthesis of fluorescent carbon dots using Daucus carota subsp. sativus roots for mitomycin drug delivery," *Optik (Stuttg).*, vol. 158, pp. 893–900, 2018, doi: 10.1016/j.ijleo.2017.12.200.

[180] Y. Yuan *et al.*, "Doxorubicin-loaded environmentally friendly carbon dots as a

novel drug delivery system for nucleus targeted cancer therapy," *Colloids Surfaces B Biointerfaces*, vol. 159, pp. 349–359, 2017, doi: 10.1016/j.colsurfb.2017.07.030.

[181] N. Sarkar, G. Sahoo, R. Das, G. Prusty, and S. K. Swain, "Carbon quantum dot tailored calcium alginate hydrogel for pH responsive controlled delivery of vancomycin," *Eur. J. Pharm. Sci.*, vol. 109, pp. 359–371, 2017, doi: 10.1016/j.ejps.2017.08.015.

[182] D. Xu, Q. Lin, and H. T. Chang, "Recent Advances and Sensing Applications of Carbon Dots," *Small Methods*, vol. 4, no. 4, pp. 1–17, 2020, doi: 10.1002/smtd.201900387.

[183] S. Pawar, U. K. Togiti, A. Bhattacharya, and A. Nag, "Functionalized Chitosan-Carbon Dots: A Fluorescent Probe for Detecting Trace Amount of Water in Organic Solvents," *ACS Omega*, vol. 4, no. 6, pp. 11301–11311, 2019, doi: 10.1021/acsomega.9b01208.

[184] X. Pei, D. Xiong, J. Fan, Z. Li, H. Wang, and J. Wang, "Highly efficient fluorescence switching of carbon nanodots by CO2," *Carbon N. Y.*, vol. 117, pp. 147–153, 2017, doi: 10.1016/j.carbon.2017.02.090.

[185] M. Sun *et al.*, "Determination of gaseous sulfur dioxide and its derivatives via fluorescence enhancement based on cyanine dye functionalized carbon nanodots," *Anal. Chem.*, vol. 86, no. 19, pp. 9381–9385, 2014, doi: 10.1021/ac503214v.

[186] C. Wang, J. Xu, R. Zhang, and W. Zhao, "Facile and low-energy-consumption synthesis of dual-functional carbon dots from Cornus walteri leaves for detection of p-nitrophenol and photocatalytic degradation of dyes," *Colloids Surfaces A Physicochem. Eng. Asp.*, vol. 640, no. December 2021, p. 128351, 2022, doi: 10.1016/j.colsurfa.2022.128351.

[187] B. K. Walther *et al.*, "Nanobiosensing with graphene and carbon quantum dots: Recent advances," *Mater. Today*, vol. 39, no. October, pp. 23–46, 2020, doi: 10.1016/j.mattod.2020.04.008.

[188] M. Sun, X. Ma, X. Chen, Y. Sun, X. Cui, and Y. Lin, "A nanocomposite of carbon quantum dots and TiO2 nanotube arrays: Enhancing photoelectrochemical and photocatalytic properties," *RSC Adv.*, vol. 4, no. 3, pp. 1120–1127, 2014, doi: 10.1039/c3ra45474f.

[189] I. Alkian, H. Sutanto, B. Aprimanti Utami, I. Rafika Duri, D. Q. A'Yuni, and H.

Hadiyanto, “A Review of Carbon dots (CDs) Application in Sensing and Removing Medical Waste,” *E3S Web Conf.*, vol. 202, pp. 1–11, 2020, doi: 10.1051/e3sconf/202020206004.

[190] E. A. Stepanidenko, E. V. Ushakova, A. V. Fedorov, and A. L. Rogach, “Applications of carbon dots in optoelectronics,” *Nanomaterials*, vol. 11, no. 2, pp. 1–20, 2021, doi: 10.3390/nano11020364.

[191] J. J. Huang, Z. F. Zhong, M. Z. Rong, X. Zhou, X. D. Chen, and M. Q. Zhang, “An easy approach of preparing strongly luminescent carbon dots and their polymer based composites for enhancing solar cell efficiency,” *Carbon N. Y.*, vol. 70, pp. 190–198, 2014, doi: 10.1016/j.carbon.2013.12.092.

[192] F. Wang, Y. H. Chen, C. Y. Liu, and D. G. Ma, “White light-emitting devices based on carbon dots’ electroluminescence,” *Chem. Commun.*, vol. 47, no. 12, pp. 3502–3504, 2011, doi: 10.1039/c0cc05391k.

[193] X. Guo, C. F. Wang, Z. Y. Yu, L. Chen, and S. Chen, “Facile access to versatile fluorescent carbon dots toward light-emitting diodes,” *Chem. Commun.*, vol. 48, no. 21, pp. 2692–2694, 2012, doi: 10.1039/c2cc17769b.

[194] Y. Liu, S. Roy, S. Sarkar, J. Xu, Y. Zhao, and J. Zhang, “A review of carbon dots and their composite materials for electrochemical energy technologies,” *Carbon Energy*, vol. 3, no. 5, pp. 795–826, 2021, doi: 10.1002/cey2.134.

[195] M. S. Balogun *et al.*, *Carbon Quantum Dot Surface-Engineered VO2 Interwoven Nanowires: A Flexible Cathode Material for Lithium and Sodium Ion Batteries*, vol. 8, no. 15. 2016. doi: 10.1021/acsami.6b01305.

[196] J. Briscoe, A. Marinovic, M. Sevilla, S. Dunn, and M. Titirici, “Biomass-Derived Carbon Quantum Dot Sensitizers for Solid-State Nanostructured Solar Cells,” *Angew. Chemie - Int. Ed.*, vol. 54, no. 15, pp. 4463–4468, 2015, doi: 10.1002/anie.201409290.

[197] N. Dhenadhayalan, K. C. Lin, and T. A. Saleh, “Recent Advances in Functionalized Carbon Dots toward the Design of Efficient Materials for Sensing and Catalysis Applications,” *Small*, vol. 16, no. 1, pp. 1–24, 2020, doi: 10.1002/smll.201905767.

[198] T. F. Yeh, C. Y. Teng, S. J. Chen, and H. Teng, “Nitrogen-doped graphene oxide quantum dots as photocatalysts for overall water-splitting under visible light illumination,” *Adv. Mater.*, vol. 26, no. 20, pp. 3297–3303, 2014, doi: 10.1002/adma.201305299.

[199] J. Liu *et al.*, “Carbon Nanodot Surface Modifications Initiate Highly Efficient, Stable Catalysts for Both Oxygen Evolution and Reduction Reactions,” *Adv. Energy Mater.*, vol. 6, no. 9, pp. 2–9, 2016, doi: 10.1002/aenm.201502039.

[200] H. Song, Y. Li, L. Shang, Z. Tang, T. Zhang, and S. Lu, “Designed controllable nitrogen-doped carbon-dots-loaded MoP nanoparticles for boosting hydrogen evolution reaction in alkaline medium,” *Nano Energy*, vol. 72, no. March, p. 104730, 2020, doi: 10.1016/j.nanoen.2020.104730.

[201] A. M. Brouwer, “Standards for photoluminescence quantum yield measurements in solution (IUPAC Technical Report)*,” vol. 83, no. 12, pp. 2213–2228, 2011, doi: 10.1351/PAC-REP-10-09-31.

[202] ISO (International Organization for Standardization), “Water quality- Determination of the inhibitory effect of water samples on te light emission of vibrio fischeri (Luminescent bacteria test)- Part 3: Method using freeze-dried bacteria,” *Iso 11348-32007*, vol. 2007, pp. 1–21, 2007.

[203] Y. M. Faleeva, V. A. Lavrenov, and V. M. Zaichenko, “Investigation of plant biomass two-stage pyrolysis based on three major components: cellulose, hemicellulose, and lignin,” *Biomass Convers. Biorefinery*, no. 0123456789, 2022, doi: 10.1007/s13399-022-03385-1.

[204] H. Yang, R. Yan, H. Chen, D. H. Lee, and C. Zheng, “Characteristics of hemicellulose, cellulose and lignin pyrolysis,” *Fuel*, vol. 86, no. 12–13, pp. 1781–1788, 2007, doi: 10.1016/j.fuel.2006.12.013.

[205] D. Rodríguez-Padrón *et al.*, “Catalyzed Microwave-Assisted Preparation of Carbon Quantum Dots from Lignocellulosic Residues,” *ACS Sustain. Chem. Eng.*, vol. 6, no. 6, pp. 7200–7205, 2018, doi: 10.1021/acssuschemeng.7b03848.

[206] H. Yang, R. Yan, T. Chin, D. T. Liang, H. Chen, and C. Zheng, “Thermogravimetric analysis - Fourier transform infrared analysis of palm oil waste pyrolysis,” *Energy and Fuels*, vol. 18, no. 6, pp. 1814–1821, 2004, doi: 10.1021/ef030193m.

[207] X. Huang, H. Yin, B. Zhang, N. Mei, and L. Mu, “Pyrolysis of lignin (De–alkaline) via TG/DSC–FTIR and TG–MS: pyrolysis characteristics, thermo-kinetics, and gas products,” *Biomass Convers. Biorefinery*, no. 0123456789, 2022, doi: 10.1007/s13399-022-02387-3.

[208] M. R. Pallavolu, S. Prabhu, R. R. Nallapureddy, A. S. Kumar, A. N. Banerjee,

and S. W. Joo, “Bio-derived graphitic carbon quantum dot encapsulated S- and N-doped graphene sheets with unusual battery-type behavior for high-performance supercapacitor,” *Carbon N. Y.*, vol. 202, no. P1, pp. 93–102, 2023, doi: 10.1016/j.carbon.2022.10.077.

[209] K. Sun *et al.*, “Investigation into Properties of Carbohydrate Polymers Formed from Acid-Catalyzed Conversion of Sugar Monomers/Oligomers over Brønsted Acid Catalysts,” *Energy Technol.*, vol. 8, no. 6, pp. 1–13, 2020, doi: 10.1002/ente.201901476.

[210] J. P. Paraknowitsch and A. Thomas, “Doping carbons beyond nitrogen: An overview of advanced heteroatom doped carbons with boron, sulphur and phosphorus for energy applications,” *Energy Environ. Sci.*, vol. 6, no. 10, pp. 2839–2855, 2013, doi: 10.1039/c3ee41444b.

[211] S. Thiangtham, J. Runt, and H. Manuspiya, “Sulfonation of dialdehyde cellulose extracted from sugarcane bagasse for synergistically enhanced water solubility,” *Carbohydr. Polym.*, vol. 208, no. December 2018, pp. 314–322, 2019, doi: 10.1016/j.carbpol.2018.12.080.

[212] J. Chen, J. Liu, J. Li, L. Xu, and Y. Qiao, “One-pot synthesis of nitrogen and sulfur co-doped carbon dots and its application for sensor and multicolor cellular imaging,” *J. Colloid Interface Sci.*, vol. 485, pp. 167–174, 2017, doi: 10.1016/j.jcis.2016.09.040.

[213] S. C. Nunes *et al.*, “Amino-functionalized Green Fluorescent Carbon Dots as Surface Energy Transfer Biosensors for Hyaluronidase,” pp. 1–8, 2015, doi: 10.1039/C5NR00070J.

[214] K. D. B. J.F. Moulder, W.F. Stickle, P.E. Sobol, “Handbook of X-ray electron spectroscopy,” *Perkin-Elmer Corporation*. p. 192, 1992.

[215] D. A. Boyd, “Sulfur and Its Role In Modern Materials Science,” *Angew. Chemie - Int. Ed.*, vol. 55, no. 50, pp. 15486–15502, 2016, doi: 10.1002/anie.201604615.

[216] D. R. da Silva Souza, L. D. Caminhas, J. P. de Mesquita, and F. V. Pereira, “Luminescent carbon dots obtained from cellulose,” *Mater. Chem. Phys.*, vol. 203, pp. 148–155, 2018, doi: 10.1016/j.matchemphys.2017.10.001.

[217] M. Havrdova *et al.*, “Toxicity of carbon dots-Effect of surface functionalization on the cell viability, reactive oxygen species generation and cell cycle,” *Carbon N. Y.*, vol. 99, pp. 238–248, 2016, doi: 10.1016/j.carbon.2015.12.027.

[218] K. Wang *et al.*, “Systematic safety evaluation on photoluminescent carbon dots,”

Nanoscale Res. Lett., vol. 8, no. 1, pp. 1–9, 2013, doi: 10.1186/1556-276X-8-122.

[219] Y. Yang *et al.*, “Toxicity and bio-distribution of carbon dots after single inhalation exposure in vivo,” *Chinese Chem. Lett.*, vol. 29, no. 6, pp. 895–898, 2018, doi: 10.1016/j.cclet.2018.04.018.

[220] P. Dubey, “An overview on animal/human biomass-derived carbon dots for optical sensing and bioimaging applications,” *RSC Adv.*, vol. 13, no. 50, pp. 35088–35126, 2023, doi: 10.1039/d3ra06976a.

[221] R. N. Coleman and A. A. Qureshi, “Microtox® and Spirillum volutans tests for assessing toxicity of environmental samples,” *Bull. Environ. Contam. Toxicol.*, vol. 35, no. 1, pp. 443–451, 1985, doi: 10.1007/BF01636536.

[222] F. Zhao, H. Meng, L. Yan, B. Wang, and Y. Zhao, “Nanosurface chemistry and dose govern the bioaccumulation and toxicity of carbon nanotubes, metal nanomaterials and quantum dots in vivo,” *Sci. Bull.*, vol. 60, no. 1, pp. 3–20, 2015, doi: 10.1007/s11434-014-0700-0.

[223] M. Sutcu and S. Akkurt, “The use of recycled paper processing residues in making porous brick with reduced thermal conductivity,” *Ceram. Int.*, vol. 35, no. 7, pp. 2625–2631, 2009, doi: 10.1016/j.ceramint.2009.02.027.

[224] H. L. Yang *et al.*, “Carbon quantum dots: Preparation, optical properties, and biomedical applications,” *Mater. Today Adv.*, vol. 18, p. 100376, 2023, doi: 10.1016/j.mtadv.2023.100376.

[225] B. De and N. Karak, “A green and facile approach for the synthesis of water soluble fluorescent carbon dots from banana juice,” *RSC Adv.*, vol. 3, no. 22, pp. 8286–8290, 2013, doi: 10.1039/c3ra00088e.

[226] L. Bao *et al.*, “Electrochemical tuning of luminescent carbon nanodots: From preparation to luminescence mechanism,” *Adv. Mater.*, vol. 23, no. 48, pp. 5801–5806, Dec. 2011, doi: 10.1002/ADMA.201102866.

[227] S. J. Park, J. Y. Park, J. W. Chung, H. K. Yang, B. K. Moon, and S. S. Yi, “Color tunable carbon quantum dots from wasted paper by different solvents for anti-counterfeiting and fluorescent flexible film,” *Chem. Eng. J.*, vol. 383, no. July 2019, 2020, doi: 10.1016/j.cej.2019.123200.

[228] T. Anitha, M. Mrinalini, D. Vani, S. Prasanthkumar, K. Rajender Reddy, and L. Giribabu, “Synthesis and Opto-electronic Properties of BODIPY o-OPhos Systems,” *Photochem. Photobiol.*, vol. 96, no. 6, pp. 1182–1190, 2020, doi:

10.1111/php.13306.

[229] N. A. S. Omar, Y. W. Fen, I. Ramli, H. S. Hashim, N. S. M. Ramdzan, and N. I. M. Fauzi, “A Review on Carbon Dots: Synthesis, Characterization and Its Application in Optical Sensor for Environmental Monitoring,” *Nanomaterials*, vol. 12, no. 14, 2022, doi: 10.3390/nano12142365.

[230] Y. Lou *et al.*, “Recent advances of biomass carbon dots on syntheses, characterization, luminescence mechanism, and sensing applications,” *Nano Sel.*, vol. 2, no. 6, pp. 1117–1145, 2021, doi: 10.1002/nano.202000232.

[231] T. C. Wareing, P. Gentile, and A. N. Phan, “Biomass-Based Carbon Dots: Current Development and Future Perspectives,” *ACS Nano*, vol. 15, no. 10, pp. 15471–15501, 2021, doi: 10.1021/acsnano.1c03886.

[232] M. J. Molaei, “A review on nanostructured carbon quantum dots and their applications in biotechnology, sensors, and chemiluminescence,” *Talanta*, vol. 196, no. December 2018, pp. 456–478, 2019, doi: 10.1016/j.talanta.2018.12.042.

[233] M. Ghashghaee, Z. Azizi, and M. Ghambarian, “Conductivity tuning of charged triazine and heptazine graphitic carbon nitride (g-C3N4) quantum dots via nonmetal (B, O, S, P) doping: DFT calculations,” *J. Phys. Chem. Solids*, vol. 141, no. February, p. 109422, 2020, doi: 10.1016/j.jpcs.2020.109422.

[234] A. Wibrianto, S. Q. Khairunisa, S. C. W. Sakti, Y. L. Ni’Mah, B. Purwanto, and M. Z. Fahmi, “Comparison of the effects of synthesis methods of B, N, S, and P-doped carbon dots with high photoluminescence properties on HeLa tumor cells,” *RSC Adv.*, vol. 11, no. 2, pp. 1098–1108, 2020, doi: 10.1039/d0ra09403j.

[235] R. Kumar *et al.*, “Heteroatom doped graphene engineering for energy storage and conversion,” *Mater. Today*, vol. 39, no. October, pp. 47–65, 2020, doi: 10.1016/j.mattod.2020.04.010.

[236] S. Riaz and S. J. Park, “Thioacetamide-derived nitrogen and sulfur co-doped carbon quantum dots for ‘green’ quantum dot solar cells,” *J. Ind. Eng. Chem.*, vol. 105, pp. 111–120, 2022, doi: 10.1016/j.jiec.2021.09.009.

[237] Y. Jin *et al.*, “Construction of biomass derived carbon quantum dots modified TiO2 photocatalysts with superior photocatalytic activity for methylene blue degradation,” *J. Alloys Compd.*, vol. 932, p. 167627, 2023, doi: 10.1016/j.jallcom.2022.167627.

[238] S. Chandra *et al.*, “Luminescent S-doped carbon dots: An emergent architecture

for multimodal applications," *J. Mater. Chem. B*, vol. 1, no. 18, pp. 2375–2382, 2013, doi: 10.1039/c3tb00583f.

[239] D. Das and R. K. Dutta, "N-Doped Carbon Dots Synthesized from Ethylene Glycol and β-Alanine for Detection of Cr(VI) and 4-Nitrophenol via Photoluminescence Quenching," *ACS Appl. Nano Mater.*, vol. 4, no. 4, pp. 3444–3454, 2021, doi: 10.1021/acsanm.0c03329.

[240] Z. Chen, W. Wei, H. Chen, and B. J. Ni, "Eco-designed electrocatalysts for water splitting: A path toward carbon neutrality," *Int. J. Hydrogen Energy*, vol. 48, no. 16, pp. 6288–6307, 2023, doi: 10.1016/j.ijhydene.2022.03.046.

[241] N. Prabu, R. S. A. Saravanan, T. Kesavan, G. Maduraiveeran, and M. Sasidharan, "An efficient palm waste derived hierarchical porous carbon towards electrocatalytic hydrogen evolution reaction," *Carbon N. Y.*, vol. 152, pp. 188–197, 2019, doi: 10.1016/j.carbon.2019.06.016.

[242] Z. Liu, B. Li, Y. Feng, D. Jia, C. Li, and Y. Zhou, "N-Doped sp 2 /sp 3 Carbon Derived from Carbon Dots to Boost the Performance of Ruthenium for Efficient Hydrogen Evolution Reaction," *Small Methods*, vol. 6, no. 10, Oct. 2022, doi: 10.1002/smtd.202200637.

[243] H. Yuan, J. Yu, S. Feng, and Y. Gong, "Highly photoluminescent pH-independent nitrogen-doped carbon dots for sensitive and selective sensing of p-nitrophenol," *RSC Adv.*, vol. 6, no. 18, pp. 15192–15200, 2016, doi: 10.1039/c5ra26870b.

[244] S. Liao *et al.*, "Fluorescent nitrogen-doped carbon dots for high selective detecting p-nitrophenol through FRET mechanism," *Spectrochim. Acta - Part A Mol. Biomol. Spectrosc.*, vol. 259, 2021, doi: 10.1016/j.saa.2021.119897.

[245] G. Ren, M. Tang, F. Chai, and H. Wu, "One-Pot Synthesis of Highly Fluorescent Carbon Dots from Spinach and Multipurpose Applications," *Eur. J. Inorg. Chem.*, vol. 2018, no. 2, pp. 153–158, 2018, doi: 10.1002/ejic.201701080.

[246] A. Faza, K. Lathifah, F. Rahayu, H. Rayanisaputri, and N. Taufiqu, "Materials Today : Proceedings Carbon dots based fluorescence sensor for P-nitrophenol," *Mater. Today Proc.*, no. January, 2024, doi: 10.1016/j.matpr.2024.03.015.

[247] K. Lakshmi, R. Jayashri, and K. Kadirvelu, "Photoreduction of 4-nitrophenol catalysed by carbon quantum dots embedded cerium oxide nanocomposite," *J. Mater. Sci. Mater. Electron.*, vol. 34, no. 32, pp. 1–13, 2023, doi: 10.1007/s10854-023-11568-3.

[248] S. Ghosh, S. S. Satapathy, K. Ghosh, S. Jauhari, S. K. Panda, and S. Si, "Carbon

Dots Assisted Synthesis of Gold Nanoparticles and Their Catalytic Activity in 4-Nitrophenol Reduction," *ChemistrySelect*, vol. 4, no. 12, pp. 3416–3422, 2019, doi: 10.1002/slct.201804040.

[249] T. Tyner and J. Francis, "Sodium Borohydride," *ACS Reag. Chem.*, no. 1907, pp. 1–14, 2017, doi: 10.1021/acsreagents.4334.20170301.

[250] A. Cruz-Cruz *et al.*, "Recent Advances in Carbon Dots Based Biocatalysts for Degrading Organic Pollutants," *Curr. Pollut. Reports*, vol. 8, no. 4, pp. 384–394, 2022, doi: 10.1007/s40726-022-00228-5.

[251] R. Sinha and P. Purkayastha, "Metal-free catalysis for efficient reduction of 4-nitrophenol by graphene quantum dots controlled by the surface trapped water molecules," *Mater. Lett.*, vol. 316, no. February, p. 132054, 2022, doi: 10.1016/j.matlet.2022.132054.

[252] H. Liu *et al.*, "Nitrogen-Doped Graphene Quantum Dots as Metal-Free Photocatalysts for Near-Infrared Enhanced Reduction of 4-Nitrophenol," *ACS Appl. Nano Mater.*, vol. 2, no. 11, pp. 7043–7050, 2019, doi: 10.1021/acsanm.9b01549.

[253] H. Wang, J. Zhuang, D. Velado, Z. Wei, H. Matsui, and S. Zhou, "Near-Infrared- and Visible-Light-Enhanced Metal-Free Catalytic Degradation of Organic Pollutants over Carbon-Dot-Based Carbocatalysts Synthesized from Biomass," *ACS Appl. Mater. Interfaces*, vol. 7, no. 50, pp. 27703–27712, 2015, doi: 10.1021/acsami.5b08443.

[254] W. Lv, Y. Ju, Y. Chen, and X. Chen, "In situ synthesis of gold nanoparticles on N-doped graphene quantum dots for highly efficient catalytic degradation of nitrophenol," *Int. J. Hydrogen Energy*, vol. 43, no. 22, pp. 10334–10340, 2018, doi: 10.1016/j.ijhydene.2018.04.109.

[255] Q. Chang *et al.*, "Dynamic restructuring of carbon dots/copper oxide supported on mesoporous hydroxyapatite brings exceptional catalytic activity in the reduction of 4-nitrophenol," *Appl. Catal. B Environ.*, vol. 263, no. October 2019, p. 118299, 2020, doi: 10.1016/j.apcatb.2019.118299.

[256] T. Y. Huang, Y. F. Lin, S. R. Hu, C. C. Huang, Y. F. Huang, and H. T. Chang, "Carbon-dot liposome–based synthesis of gold nanocatalysts for efficient reduction of 4-nitrophenol in wastewater," *Sustain. Mater. Technol.*, vol. 40, no. March, p. e00896, 2024, doi: 10.1016/j.susmat.2024.e00896.

[257] R. R. Bhagavanth *et al.*, "Microwave-assisted preparation of a silver

nanoparticles/N-doped carbon dots nanocomposite and its application for catalytic reduction of rhodamine B, methyl red and 4-nitrophenol dyes," *RSC Adv.*, vol. 11, no. 9, pp. 5139–5148, 2021, doi: 10.1039/d0ra10679h.

[258] Y. Zhu *et al.*, "The synthesis of highly active carbon dot-coated gold nanoparticlesviathe room-temperaturein situcarbonization of organic ligands for 4-nitrophenol reduction," *RSC Adv.*, vol. 10, no. 33, pp. 19419–19424, 2020, doi: 10.1039/d0ra02048f.

[259] M. K. Mahto, D. Samanta, S. Konar, H. Kalita, and A. Pathak, "N, S doped carbon dots - Plasmonic Au nanocomposites for visible-light photocatalytic reduction of nitroaromatics," *J. Mater. Res.*, vol. 33, no. 23, pp. 3906–3916, 2018, doi: 10.1557/jmr.2018.324.

[260] B. Saini, S. Singh, and T. K. Mukherjee, "Nanocatalysis under Nanoconfinement: A Metal-Free Hybrid Coacervate Nanodroplet as a Catalytic Nanoreactor for Efficient Redox and Photocatalytic Reactions," *ACS Appl. Mater. Interfaces*, vol. 13, no. 43, pp. 51117–51131, 2021, doi: 10.1021/acsami.1c17106.

[261] J. Jiang *et al.*, "Facile preparation of a multicomponent catalytic system Bi2O3/Bi2S3/CDs with an exceptional catalytic activity in the photocatalytic reduction of 4-nitrophenol," *Colloids Interface Sci. Commun.*, vol. 51, no. August, p. 100678, 2022, doi: 10.1016/j.colcom.2022.100678.

[262] Q. Chang *et al.*, "Loading sulfur and nitrogen co-doped carbon dots onto g-C3N4 nanosheets for an efficient photocatalytic reduction of 4-nitrophenol," *Dalt. Trans.*, vol. 47, no. 18, pp. 6435–6443, 2018, doi: 10.1039/c8dt00735g.

[263] Y. Zhou *et al.*, "Size-dependent photocatalytic activity of carbon dots with surface-state determined photoluminescence," *Appl. Catal. B Environ.*, vol. 248, no. December 2018, pp. 157–166, 2019, doi: 10.1016/j.apcatb.2019.02.019.

[264] P. Yang *et al.*, "Construction of carbon nitride-based heterojunction as photocatalyst for peroxymonosulfate activation: Important role of carbon dots in enhancing photocatalytic activity," *Chem. Eng. J.*, vol. 464, no. April, p. 142724, 2023, doi: 10.1016/j.cej.2023.142724.

[265] P. Zhao, B. Jin, Q. Zhang, and R. Peng, "Graphitic-C3N4 quantum dots modified FeOOH for photo-Fenton degradation of organic pollutants," *Appl. Surf. Sci.*, vol. 586, no. February, p. 152792, 2022, doi: 10.1016/j.apsusc.2022.152792.

[266] G. Tokazhanov, S. Han, and W. Lee, "Enhanced catalytic reduction of p-nitrophenol by nano zerovalent iron - supported metal catalysts," *Catal.*

Commun., vol. 158, p. 106337, 2021, doi: 10.1016/j.catcom.2021.106337.

[267] S. González–Morán *et al.*, “Application of birnessite–type solids prepared by sol–gel and oxidation methods in photocatalytic degradation of 4–nitrophenol,” *Environ. Technol. (United Kingdom)*, vol. 0, no. 0, pp. 1–16, 2020, doi: 10.1080/09593330.2020.1791968.

[268] B. Wang and S. Lu, “The light of carbon dots: From mechanism to applications,” *Matter*, vol. 5, no. 1, pp. 110–149, 2022, doi: 10.1016/j.matt.2021.10.016.

[269] S. Miao, K. Liang, J. Zhu, B. Yang, D. Zhao, and B. Kong, “Hetero-atom-doped carbon dots: Doping strategies, properties and applications,” *Nano Today*, vol. 33, Aug. 2020, doi: 10.1016/J.NANTOD.2020.100879.

APPENDIX A: CRYSTALOGRAHPY DATA

Compound **3**

Figure 63. Unit cell from crystal structure of complex **3** with thermal ellipsoid at 40% probability. Hydrogen atoms were omitted for clarity.

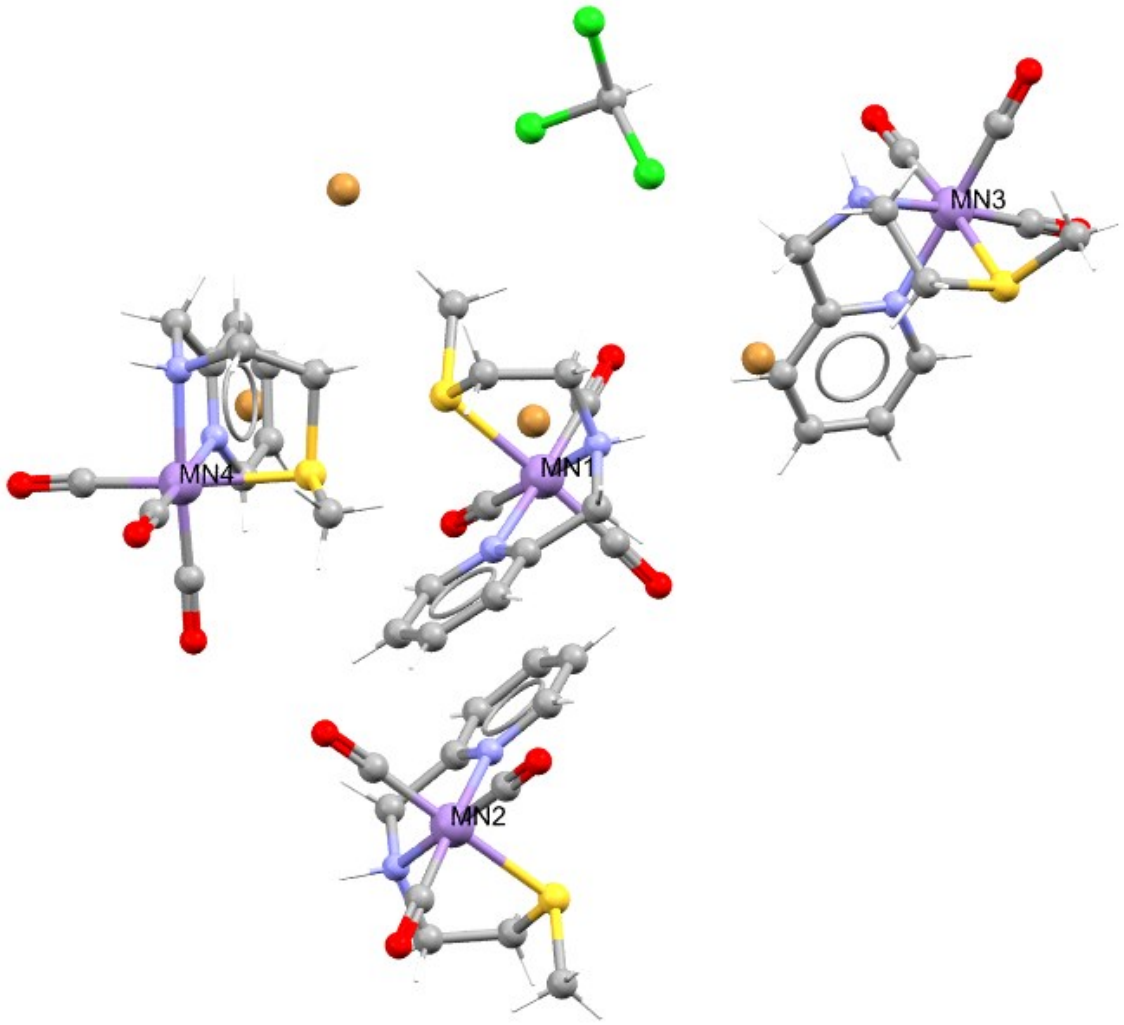

Details

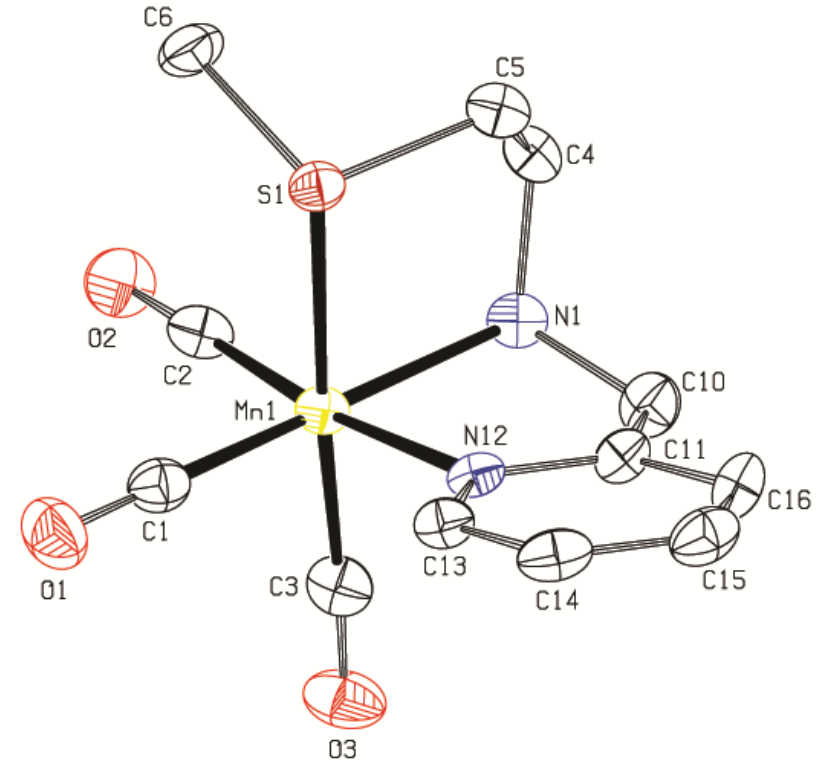
C6
C5
C4
S1
O2
C2
N1
C10
Mn1
N12
C11
C16
C1
C13
C15
O1
C3
C14
O3

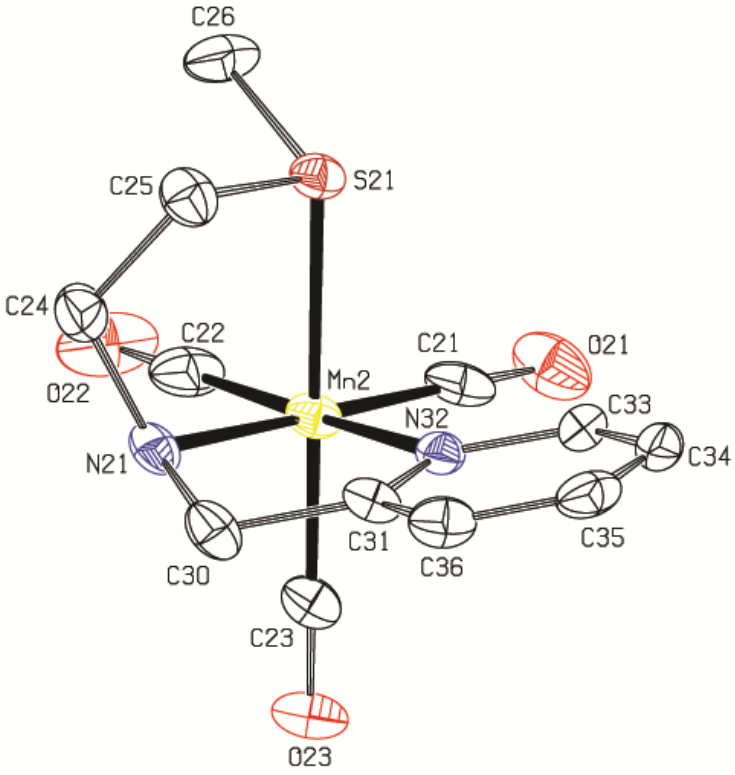
C26
S21
C25
C24
C22
C21
O21
O22
Mn2
C33
N32
C34
N21
C31
C35
C30
C36
C23
O23

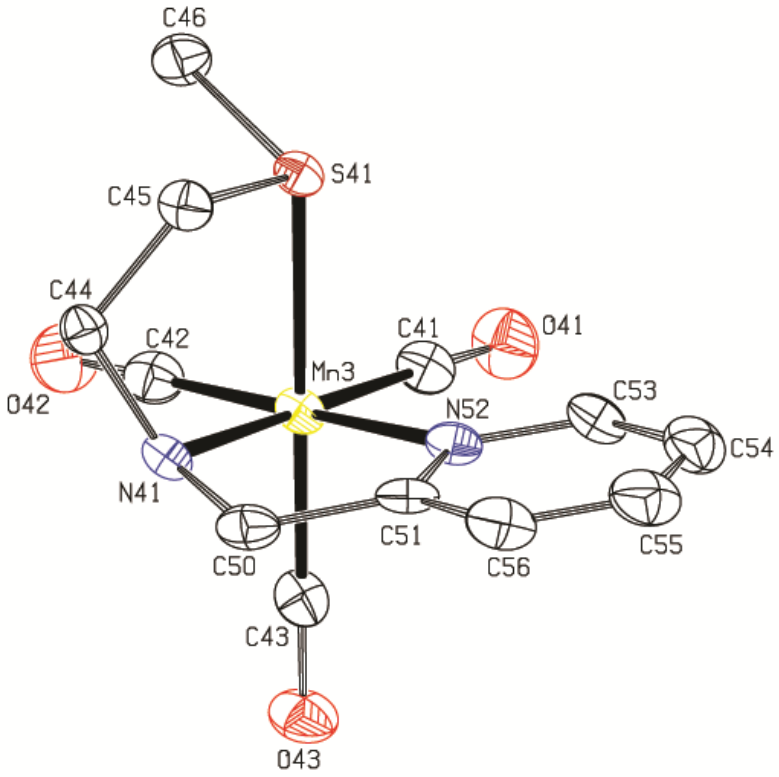
C46
S41
C45
C44
C42
C41
O41
O42
Mn3
N52
C53
C54
N41
C51
C55
C50
C56
C43
O43

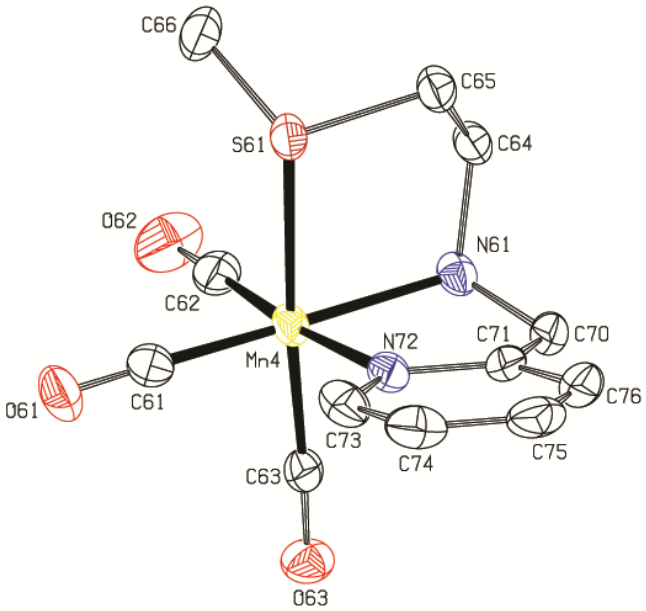
C66
C65
S61
C64
O62
N61
C62
C71
C70
N72
Mn4
O61
C61
C76
C73
C74
C75
C63
O63

Table 18. Crystal data and structure refinement for **3**·.

Identification code	shelx	
Empirical formula	C12.25 H14.25 Br Cl0.75 Mn N2 O3 S [+ solvent	
Formula weight	431.00	
Temperature	150(2) K	
Wavelength	0.71073 Å	
Crystal system	Orthorhombic	
Space group	P 21 21 21	
Unit cell dimensions	a = 16.3164(15) Å	a= 90°.
	b = 16.7861(16) Å	b= 90°.
	c = 25.314(2) Å	g = 90°.
Volume	6933.2(11) $Å^3$	
Z	16	
Density (calculated)	1.652 Mg/m^3	
Absorption coefficient	3.311 mm^{-1}	
F(000)	3432	
Crystal size	0.380 x 0.260 x 0.200 mm^3	
Theta range for data collection	1.741 to 30.188°.	
Index ranges	-23<=h<=22, -21<=k<=23, -35<=l<=35	
Reflections collected	82340	
Independent reflections	20494 [R(int) = 0.0413]	
Completeness to theta = 25.242°		100.0 %
Absorption correction	Semi-empirical from equivalents	
Max. and min. transmission	0.7460 and 0.6691	
Refinement method	Full-matrix least-squares on F^2	
Data / restraints / parameters	20494 / 0 / 762	
Goodness-of-fit on F^2	1.016	
Final R indices [I>2sigma(I)]	R1 = 0.0349, wR2 = 0.0618	
R indices (all data)	R1 = 0.0565, wR2 = 0.0673	
Absolute structure parameter	0.009(2)	
Extinction coefficient	n/a	
Largest diff. peak and hole	0.979 and -1.199 $e.Å^{-3}$	

Table 19. Selected bond lengths [Å] and angles [°] for 3.

Mn(1)-C(1) 1.803(5)	C(2)-Mn(1)-S(1)92.82(14)
Mn(1)-C(2) 1.806(4)	C(3)-Mn(1)-S(1)175.67(15)
Mn(1)-C(3) 1.810(5)	N(12)-Mn(1)-S(1)82.47(9)
Mn(1)-N(12) 2.048(3)	N(1)-Mn(1)-S(1)84.96(9)
Mn(1)-N(1) 2.071(3)	O(1)-C(1)-Mn(1)179.1(4)
Mn(1)-S(1) 2.3610(12)	O(2)-C(2)-Mn(1)178.2(4)
Mn(2)-C(21) 1.793(5)	O(3)-C(3)-Mn(1)176.7(4)
Mn(2)-C(22) 1.801(5)	C(21)-Mn(2)-C(22)90.2(2)
Mn(2)-C(23) 1.815(4)	C(21)-Mn(2)-C(23)88.70(19)
Mn(2)-N(32) 2.050(3)	C(22)-Mn(2)-C(23)89.38(19)
Mn(2)-N(21) 2.071(3)	C(21)-Mn(2)-N(32)95.86(17)
Mn(2)-S(21)2.3591(11)	C(22)-Mn(2)-N(32)172.50(19)
Mn(3)-C(41) 1.804(4)	C(23)-Mn(2)-N(32)95.16(16)
Mn(3)-C(43) 1.806(4)	C(21)-Mn(2)-N(21)175.97(17)
Mn(3)-C(42) 1.817(5)	C(22)-Mn(2)-N(21)93.32(19)
Mn(3)-N(52) 2.046(3)	C(23)-Mn(2)-N(21)93.28(16)
Mn(3)-N(41) 2.072(3)	N(32)-Mn(2)-N(21)80.49(13)
Mn(3)-S(41)2.3604(11)	C(21)-Mn(2)-S(21)92.62(13)
Mn(4)-C(61) 1.797(5)	C(22)-Mn(2)-S(21)92.16(14)
Mn(4)-C(62) 1.809(5)	C(23)-Mn(2)-S(21)177.97(14)
Mn(4)-C(63) 1.812(4)	N(32)-Mn(2)-S(21)83.17(9)
Mn(4)-N(72) 2.059(3)	N(21)-Mn(2)-S(21)85.30(10)
Mn(4)-N(61) 2.076(3)	O(21)-C(21)-Mn(2)177.8(4)
Mn(4)-S(61)2.3692(12)	O(22)-C(22)-Mn(2)179.1(5)
C(1)-Mn(1)-C(2)89.83(19)	O(23)-C(23)-Mn(2)174.6(4)
C(1)-Mn(1)-C(3)89.6(2)	C(41)-Mn(3)-C(43)90.56(18)
C(2)-Mn(1)-C(3)91.2(2)	C(41)-Mn(3)-C(42)88.64(19)
C(1)-Mn(1)-N(12)95.73(16)	C(43)-Mn(3)-C(42)89.60(18)
C(2)-Mn(1)-N(12)172.82(17)	C(41)-Mn(3)-N(52)95.36(16)
C(3)-Mn(1)-N(12)93.37(16)	C(43)-Mn(3)-N(52)92.63(16)
C(1)-Mn(1)-N(1)175.36(16)	C(42)-Mn(3)-N(52)175.40(16)
C(2)-Mn(1)-N(1)93.79(17)	C(41)-Mn(3)-N(41)175.91(16)
C(3)-Mn(1)-N(1)93.21(17)	C(43)-Mn(3)-N(41)91.11(16)
N(12)-Mn(1)-N(1)80.44(13)	C(42)-Mn(3)-N(41)95.10(16)
C(1)-Mn(1)-S(1)91.98(14)	N(52)-Mn(3)-N(41)80.84(13)

C(41)-Mn(3)-S(41)93.53(13)	C(63)-Mn(4)-N(72)93.18(16)
C(43)-Mn(3)-S(41)174.55(13)	C(61)-Mn(4)-N(61)175.10(17)
C(42)-Mn(3)-S(41)94.10(13)	C(62)-Mn(4)-N(61)93.57(18)
N(52)-Mn(3)-S(41)83.41(10)	C(63)-Mn(4)-N(61)92.57(16)
N(41)-Mn(3)-S(41)84.58(9)	N(72)-Mn(4)-N(61)80.95(14)
O(41)-C(41)-Mn(3)178.1(4)	C(61)-Mn(4)-S(61)92.41(14)
O(42)-C(42)-Mn(3)178.1(4)	C(62)-Mn(4)-S(61)94.13(14)
O(43)-C(43)-Mn(3)178.8(4)	C(63)-Mn(4)-S(61)175.57(13)
C(61)-Mn(4)-C(62)90.4(2)	N(72)-Mn(4)-S(61)83.18(10)
C(61)-Mn(4)-C(63)90.42(19)	N(61)-Mn(4)-S(61)84.38(10)
C(62)-Mn(4)-C(63)89.26(19)	O(62)-C(62)-Mn(4)178.5(4)
C(61)-Mn(4)-N(72)95.01(18)	O(63)-C(63)-Mn(4)177.5(4)
C(62)-Mn(4)-N(72)174.09(18)	O(61)-C(61)-Mn(4)178.6(4)

Symmetry transformations used to generate equivalent atoms:

Table 20:. Bond lengths [Å] and angles [°] for 3.

Mn(1)-C(1)	1.803(5)	C(5)-H(5B)	0.9900
Mn(1)-C(2)	1.806(4)	S(1)-C(6)	1.803(4)
Mn(1)-C(3)	1.810(5)	C(6)-H(6A)	0.9800
Mn(1)-N(12)	2.048(3)	C(6)-H(6B)	0.9800
Mn(1)-N(1)	2.071(3)	C(6)-H(6C)	0.9800
Mn(1)-S(1)	2.361(12)	N(1)-C(10)	1.480(5)
C(1)-O(1)	1.145(5)	N(1)-H(1)	0.8660
C(2)-O(2)	1.148(5)	C(10)-C(11)	1.493(6)
C(3)-O(3)	1.142(5)	C(10)-H(10A)	0.9900
C(4)-N(1)	1.489(5)	C(10)-H(10B)	0.9900
C(4)-C(5)	1.509(5)	C(11)-N(12)	1.349(5)
C(4)-H(4A)	0.9900	C(11)-C(16)	1.387(6)
C(4)-H(4B)	0.9900	N(12)-C(13)	1.346(5)
C(5)-S(1)	1.807(4)	C(13)-C(14)	1.375(6)
C(5)-H(5A)	0.9900	C(13)-H(13)	0.9500

C(14)-C(15) 1.378(7)
C(14)-H(14) 0.9500
C(15)-C(16) 1.373(6)
C(15)-H(15) 0.9500
C(16)-H(16) 0.9500
Mn(2)-C(21) 1.793(5)
Mn(2)-C(22) 1.801(5)
Mn(2)-C(23) 1.815(4)
Mn(2)-N(32) 2.050(3)
Mn(2)-N(21) 2.071(3)
Mn(2)-S(21) 2.3591(11)
C(21)-O(21) 1.155(6)
C(22)-O(22) 1.142(5)
C(23)-O(23) 1.139(5)
C(24)-N(21) 1.484(5)
C(24)-C(25) 1.503(6)
C(24)-H(24A) 0.9900
C(24)-H(24B) 0.9900
C(25)-S(21) 1.811(4)
C(25)-H(25A) 0.9900
C(25)-H(25B) 0.9900
S(21)-C(26) 1.804(4)
C(26)-H(26A) 0.9800
C(26)-H(26B) 0.9800
C(26)-H(26C) 0.9800
N(21)-C(30) 1.476(5)
N(21)-H(21) 1.0110
C(30)-C(31) 1.510(6)
C(30)-H(30A) 0.9900
C(30)-H(30B) 0.9900
C(31)-N(32) 1.347(5)
C(31)-C(36) 1.381(6)
N(32)-C(33) 1.346(5)
C(33)-C(34) 1.367(6)
C(33)-H(33) 0.9500
C(34)-C(35) 1.377(7)
C(34)-H(34) 0.9500
C(35)-C(36) 1.382(6)
C(35)-H(35) 0.9500
C(36)-H(36) 0.9500
Mn(3)-C(41) 1.804(4)
Mn(3)-C(43) 1.806(4)
Mn(3)-C(42) 1.817(5)
Mn(3)-N(52) 2.046(3)
Mn(3)-N(41) 2.072(3)
Mn(3)-S(41) 2.3604(11)
C(41)-O(41) 1.148(5)
C(42)-O(42) 1.135(5)
C(43)-O(43) 1.141(5)
C(44)-N(41) 1.484(5)
C(44)-C(45) 1.507(5)
C(44)-H(44A) 0.9900
C(44)-H(44B) 0.9900
C(45)-S(41) 1.810(4)
C(45)-H(45A) 0.9900
C(45)-H(45B) 0.9900
S(41)-C(46) 1.808(4)
C(46)-H(46A) 0.9800
C(46)-H(46B) 0.9800
C(46)-H(46C) 0.9800
N(41)-C(50) 1.477(5)
N(41)-H(41) 0.9077
C(50)-C(51) 1.506(6)
C(50)-H(50A) 0.9900
C(50)-H(50B) 0.9900
C(51)-N(52) 1.347(5)
C(51)-C(56) 1.388(6)
N(52)-C(53) 1.353(5)

C(53)-C(54)	1.369(6)
C(53)-H(53)	0.9500
C(54)-C(55)	1.381(7)
C(54)-H(54)	0.9500
C(55)-C(56)	1.368(7)
C(55)-H(55)	0.9500
C(56)-H(56)	0.9500
Mn(4)-C(61)	1.797(5)
Mn(4)-C(62)	1.809(5)
Mn(4)-C(63)	1.812(4)
Mn(4)-N(72)	2.059(3)
Mn(4)-N(61)	2.076(3)
Mn(4)-S(61)	2.3692(12)
O(63)-C(63)	1.134(5)
O(61)-C(61)	1.155(5)
C(62)-O(62)	1.142(5)
C(64)-N(61)	1.491(5)
C(64)-C(65)	1.505(6)
C(64)-H(64A)	0.9900
C(64)-H(64B)	0.9900
C(65)-S(61)	1.814(4)
C(65)-H(65A)	0.9900
C(65)-H(65B)	0.9900
S(61)-C(66)	1.805(5)
C(66)-H(66A)	0.9800
C(66)-H(66B)	0.9800
C(66)-H(66C)	0.9800
N(61)-C(70)	1.481(6)
N(61)-H(61)	0.9203
C(70)-C(71)	1.490(7)
C(70)-H(70A)	0.9900
C(70)-H(70B)	0.9900
C(71)-N(72)	1.339(5)
C(71)-C(76)	1.394(6)
N(72)-C(73)	1.349(6)
C(73)-C(74)	1.377(7)
C(73)-H(73)	0.9500
C(74)-C(75)	1.367(7)
C(74)-H(74)	0.9500
C(75)-C(76)	1.372(7)
C(75)-H(75)	0.9500
C(76)-H(76)	0.9500
C(1S)-Cl(1)	1.754(5)
C(1S)-Cl(2)	1.763(5)
C(1S)-Cl(3)	1.767(5)
C(1S)-H(1S)	1.0000
C(1)-Mn(1)-C(2)	89.83(19)
C(1)-Mn(1)-C(3)	89.6(2)
C(2)-Mn(1)-C(3)	91.2(2)
C(1)-Mn(1)-N(12)	95.73(16)
C(2)-Mn(1)-N(12)	172.82(17)
C(3)-Mn(1)-N(12)	93.37(16)
C(1)-Mn(1)-N(1)	175.36(16)
C(2)-Mn(1)-N(1)	93.79(17)
C(3)-Mn(1)-N(1)	93.21(17)
N(12)-Mn(1)-N(1)	80.44(13)
C(1)-Mn(1)-S(1)	91.98(14)
C(2)-Mn(1)-S(1)	92.82(14)
C(3)-Mn(1)-S(1)	175.67(15)
N(12)-Mn(1)-S(1)	82.47(9)
N(1)-Mn(1)-S(1)	84.96(9)
O(1)-C(1)-Mn(1)	179.1(4)
O(2)-C(2)-Mn(1)	178.2(4)
O(3)-C(3)-Mn(1)	176.7(4)
N(1)-C(4)-C(5)	110.7(3)
N(1)-C(4)-H(4A)	109.5
C(5)-C(4)-H(4A)	109.5
N(1)-C(4)-H(4B)	109.5

C(5)-C(4)-H(4B)	109.5	C(11)-N(12)-Mn(1)	115.1(3)
H(4A)-C(4)-H(4B)	108.1	N(12)-C(13)-C(14)	122.6(4)
C(4)-C(5)-S(1)	110.0(3)	N(12)-C(13)-H(13)	118.7
C(4)-C(5)-H(5A)	109.7	C(14)-C(13)-H(13)	118.7
S(1)-C(5)-H(5A)	109.7	C(13)-C(14)-C(15)	119.1(4)
C(4)-C(5)-H(5B)	109.7	C(13)-C(14)-H(14)	120.5
S(1)-C(5)-H(5B)	109.7	C(15)-C(14)-H(14)	120.5
H(5A)-C(5)-H(5B	108.2	C(16)-C(15)-C(14)	118.9(4)
C(6)-S(1)-C(5)	100.6(2)	C(16)-C(15)-H(15)	120.5
C(6)-S(1)-Mn(1)	110.34(16)	C(14)-C(15)-H(15)	120.5
C(5)-S(1)-Mn(1)	98.27(13)	C(15)-C(16)-C(11)	119.7(4)
S(1)-C(6)-H(6A)	109.5	C(15)-C(16)-H(16)	120.1
S(1)-C(6)-H(6B)	109.5	C(11)-C(16)-H(16)	120.1
H(6A)-C(6)-H(6B)	109.5	C(21)-Mn(2)-C(22)	90.2(2)
S(1)-C(6)-H(6C)	109.5	C(21)-Mn(2)-C(23)	88.70(19)
H(6A)-C(6)-H(6C)	109.5	C(22)-Mn(2)-C(23)	89.38(19)
H(6B)-C(6)-H(6C)	109.5	C(21)-Mn(2)-N(32)	95.86(17)
C(10)-N(1)-C(4)	112.7(3)	C(22)-Mn(2)-N(32)	172.50(19)
C(10)-N(1)-Mn(1)	109.1(2)	C(23)-Mn(2)-N(32)	95.16(16)
C(4)-N(1)-Mn(1)	113.8(2)	C(21)-Mn(2)-N(21)	175.97(17)
C(10)-N(1)-H(1)	111.4	C(22)-Mn(2)-N(21)	93.32(19)
C(4)-N(1)-H(1)	105.3	C(23)-Mn(2)-N(21)	93.28(16)
Mn(1)-N(1)-H(1)	104.2	N(32)-Mn(2)-N(21)	80.49(13)
N(1)-C(10)-C(11)	110.2(3)	C(21)-Mn(2)-S(21)	92.62(13)
N(1)-C(10)-H(10A)	109.6	C(22)-Mn(2)-S(21)	92.16(14)
C(11)-C(10)-H(10A)	109.6	C(23)-Mn(2)-S(21)	177.97(14)
N(1)-C(10)-H(10B)	109.6	N(32)-Mn(2)-S(21)	83.17(9)
C(11)-C(10)-H(10B)	109.6	N(21)-Mn(2)-S(21)	85.30(10)
H(10A)-C(10)-H(10B)	108.1	O(21)-C(21)-Mn(2)	177.8(4)
N(12)-C(11)-C(16)	121.3(4)	O(22)-C(22)-Mn(2)	179.1(5)
N(12)-C(11)-C(10)	115.7(4)	O(23)-C(23)-Mn(2)	174.6(4)
C(16)-C(11)-C(10)	123.0(4)	N(21)-C(24)-C(25)	111.0(3)
C(13)-N(12)-C(11)	118.4(3)	N(21)-C(24)-H(24A)	109.4
C(13)-N(12)-Mn(1)	126.4(3)	C(25)-C(24)-H(24A)	109.4

N(21)-C(24)-H(24B)109.4
C(25)-C(24)-H(24B)109.4
H(24A)-C(24)-H(24B)108.0
C(24)-C(25)-S(21) 110.4(3)
C(24)-C(25)-H(25A)109.6
S(21)-C(25)-H(25A)109.6
C(24)-C(25)-H(25B)109.6
S(21)-C(25)-H(25B)109.6
H(25A)-C(25)-H(25B)108.1
C(26)-S(21)-C(25) 101.6(2)
C(26)-S(21)-Mn(2) 110.72(15)
C(25)-S(21)-Mn(2) 98.03(14)
S(21)-C(26)-H(26A)109.5
S(21)-C(26)-H(26B)109.5
H(26A)-C(26)-H(26B)109.5
S(21)-C(26)-H(26C)109.5
H(26A)-C(26)-H(26C)109.5
H(26B)-C(26)-H(26C)109.5
C(30)-N(21)-C(24) 113.9(3)
C(30)-N(21)-Mn(2) 110.0(3)
C(24)-N(21)-Mn(2) 112.4(3)
C(30)-N(21)-H(21) 102.8
C(24)-N(21)-H(21) 107.1
Mn(2)-N(21)-H(21) 110.1
N(21)-C(30)-C(31) 111.2(3)
N(21)-C(30)-H(30A)109.4
C(31)-C(30)-H(30A)109.4
N(21)-C(30)-H(30B)109.4
C(31)-C(30)-H(30B)109.4
H(30A)-C(30)-H(30B)108.0
N(32)-C(31)-C(36) 122.6(4)
N(32)-C(31)-C(30) 114.7(3)C(36)-
C(31)-C(30) 122.7(4)
C(33)-N(32)-C(31) 117.4(3)
C(33)-N(32)-Mn(2) 126.2(3)
C(31)-N(32)-Mn(2) 116.3(3)
N(32)-C(33)-C(34) 123.3(4)
N(32)-C(33)-H(33) 118.4
C(34)-C(33)-H(33) 118.4
C(33)-C(34)-C(35) 118.8(4)
C(33)-C(34)-H(34) 120.6
C(35)-C(34)-H(34) 120.6
C(34)-C(35)-C(36) 119.2(4)
C(34)-C(35)-H(35) 120.4
C(36)-C(35)-H(35) 120.4
C(31)-C(36)-C(35) 118.7(4)
C(31)-C(36)-H(36) 120.7
C(35)-C(36)-H(36) 120.7
C(41)-Mn(3)-C(43) 90.56(18)
C(41)-Mn(3)-C(42) 88.64(19)
C(43)-Mn(3)-C(42) 89.60(18)
C(41)-Mn(3)-N(52) 95.36(16)
C(43)-Mn(3)-N(52) 92.63(16)
C(42)-Mn(3)-N(52) 175.40(16)
C(41)-Mn(3)-N(41) 175.91(16)
C(43)-Mn(3)-N(41) 91.11(16)
C(42)-Mn(3)-N(41) 95.10(16)
N(52)-Mn(3)-N(41) 80.84(13)
C(41)-Mn(3)-S(41) 93.53(13)
C(43)-Mn(3)-S(41) 174.55(13)
C(42)-Mn(3)-S(41) 94.10(13)
N(52)-Mn(3)-S(41) 83.41(10)
N(41)-Mn(3)-S(41) 84.58(9)
O(41)-C(41)-Mn(3) 178.1(4)
O(42)-C(42)-Mn(3) 178.1(4)
O(43)-C(43)-Mn(3) 178.8(4)
N(41)-C(44)-C(45) 109.4(3)
N(41)-C(44)-H(44A)109.8

C(45)-C(44)-H(44A)109.8
N(41)-C(44)-H(44B)109.8
C(45)-C(44)-H(44B)109.8
H(44A)-C(44)-H(44B)108.2
C(44)-C(45)-S(41) 111.0(3)
C(44)-C(45)-H(45A)109.4
S(41)-C(45)-H(45A)109.4
C(44)-C(45)-H(45B)109.4
S(41)-C(45)-H(45B)109.4
H(45A)-C(45)-H(45B)108.0
C(46)-S(41)-C(45) 100.5(2)
C(46)-S(41)-Mn(3) 110.50(15)
C(45)-S(41)-Mn(3) 98.32(13)
S(41)-C(46)-H(46A)109.5
S(41)-C(46)-H(46B)109.5
H(46A)-C(46)-H(46B)109.5
S(41)-C(46)-H(46C)109.5
H(46A)-C(46)-H(46C)109.5
H(46B)-C(46)-H(46C)109.5
C(50)-N(41)-C(44) 112.6(3)
C(50)-N(41)-Mn(3) 111.2(2)
C(44)-N(41)-Mn(3) 112.6(2)
C(50)-N(41)-H(41) 108.6
C(44)-N(41)-H(41) 99.6
Mn(3)-N(41)-H(41) 111.6
N(41)-C(50)-C(51) 111.8(3)
N(41)-C(50)-H(50A)109.3
C(51)-C(50)-H(50A)109.3
N(41)-C(50)-H(50B)109.3
C(51)-C(50)-H(50B)109.3
H(50A)-C(50)-H(50B)107.9
N(52)-C(51)-C(56) 121.9(4)
N(52)-C(51)-C(50) 115.9(3)
C(56)-C(51)-C(50) 122.2(4)
C(51)-N(52)-C(53) 117.7(4)
C(51)-N(52)-Mn(3) 116.2(3)
C(53)-N(52)-Mn(3) 126.1(3)
N(52)-C(53)-C(54) 123.0(4)
N(52)-C(53)-H(53) 118.5
C(54)-C(53)-H(53) 118.5
C(53)-C(54)-C(55) 118.9(5)
C(53)-C(54)-H(54) 120.6
C(55)-C(54)-H(54) 120.6
C(56)-C(55)-C(54) 119.2(4)
C(56)-C(55)-H(55) 120.4
C(54)-C(55)-H(55) 120.4
C(55)-C(56)-C(51) 119.4(4)
C(55)-C(56)-H(56) 120.3
C(51)-C(56)-H(56) 120.3
C(61)-Mn(4)-C(62) 90.4(2)
C(61)-Mn(4)-C(63) 90.42(19)
C(62)-Mn(4)-C(63) 89.26(19)
C(61)-Mn(4)-N(72) 95.01(18)
C(62)-Mn(4)-N(72) 174.09(18)
C(63)-Mn(4)-N(72) 93.18(16)
C(61)-Mn(4)-N(61) 175.10(17)
C(62)-Mn(4)-N(61) 93.57(18)
C(63)-Mn(4)-N(61) 92.57(16)
N(72)-Mn(4)-N(61) 80.95(14)
C(61)-Mn(4)-S(61) 92.41(14)
C(62)-Mn(4)-S(61) 94.13(14)
C(63)-Mn(4)-S(61) 175.57(13)
N(72)-Mn(4)-S(61) 83.18(10)
N(61)-Mn(4)-S(61) 84.38(10)
O(62)-C(62)-Mn(4) 178.5(4)
O(63)-C(63)-Mn(4) 177.5(4)
O(61)-C(61)-Mn(4) 178.6(4)
N(61)-C(64)-C(65) 110.1(4)

N(61)-C(64)-H(64A)109.6
C(65)-C(64)-H(64A)109.6
N(61)-C(64)-H(64B)109.6
C(65)-C(64)-H(64B)109.6
H(64A)-C(64)-H(64B)108.1
C(64)-C(65)-S(61) 110.1(3)
C(64)-C(65)-H(65A)109.6
S(61)-C(65)-H(65A)109.6
C(64)-C(65)-H(65B)109.6
S(61)-C(65)-H(65B)109.6
H(65A)-C(65)-H(65B)108.2
C(66)-S(61)-C(65) 100.7(2)
C(66)-S(61)-Mn(4) 110.45(16)
C(65)-S(61)-Mn(4) 98.62(14)
S(61)-C(66)-H(66A)109.5
S(61)-C(66)-H(66B)109.5
H(66A)-C(66)-H(66B)109.5
S(61)-C(66)-H(66C)109.5
H(66A)-C(66)-H(66C)109.5
H(66B)-C(66)-H(66C)109.5
C(70)-N(61)-C(64) 112.5(3)
C(70)-N(61)-Mn(4) 109.6(3)
C(64)-N(61)-Mn(4) 113.1(2)
C(70)-N(61)-H(61) 102.9
C(64)-N(61)-H(61) 111.8
Mn(4)-N(61)-H(61) 106.3
N(61)-C(70)-C(71) 111.9(3)
N(61)-C(70)-H(70A)109.2
C(71)-C(70)-H(70A)109.2
N(61)-C(70)-H(70B)109.2
C(71)-C(70)-H(70B)109.2
H(70A)-C(70)-H(70B)107.9
N(72)-C(71)-C(76) 120.8(4)
N(72)-C(71)-C(70) 116.1(4)
C(76)-C(71)-C(70) 123.2(4)
C(71)-N(72)-C(73) 118.6(4)
C(71)-N(72)-Mn(4) 115.3(3)
C(73)-N(72)-Mn(4) 125.9(3)
N(72)-C(73)-C(74) 122.5(5)
N(72)-C(73)-H(73) 118.8
C(74)-C(73)-H(73) 118.8
C(75)-C(74)-C(73) 119.3(5)
C(75)-C(74)-H(74) 120.4
C(73)-C(74)-H(74) 120.4
C(74)-C(75)-C(76) 118.6(4)
C(74)-C(75)-H(75) 120.7
C(76)-C(75)-H(75) 120.7
C(75)-C(76)-C(71) 120.3(4)
C(75)-C(76)-H(76) 119.9
C(71)-C(76)-H(76) 119.9
Cl(1)-C(1S)-Cl(2) 110.2(3)
Cl(1)-C(1S)-Cl(3) 109.3(3)
Cl(2)-C(1S)-Cl(3) 111.4(3)
Cl(1)-C(1S)-H(1S) 108.6
Cl(2)-C(1S)-H(1S) 108.6
Cl(3)-C(1S)-H(1S) 108.6

Symmetry transformations used to generate equivalent atoms:

Table 21. Torsion angles [°] for 3.

N(1)-C(4)-C(5)-S(1)	-52.7(4)	C(33)-C(34)-C(35)-C(36)	0.1(6)
C(4)-C(5)-S(1)-C(6)	-79.9(3)	N(32)-C(31)-C(36)-C(35)	0.0(6)
C(4)-C(5)-S(1)-Mn(1)	32.7(3)	C(30)-C(31)-C(36)-C(35)	178.8(4)
C(5)-C(4)-N(1)-C(10)	-78.4(4)	C(34)-C(35)-C(36)-C(31)	-0.2(6)
C(5)-C(4)-N(1)-Mn(1)	46.5(4)	N(41)-C(44)-C(45)-S(41)	52.3(4)
C(4)-N(1)-C(10)-C(11)	94.1(4)	C(44)-C(45)-S(41)-C(46)	85.0(3)
Mn(1)-N(1)-C(10)-C(11)	-33.3(4)	C(44)-C(45)-S(41)-Mn(3)	-27.8(3)
N(1)-C(10)-C(11)-N(12)	26.1(5)	C(45)-C(44)-N(41)-C(50)	74.7(4)
N(1)-C(10)-C(11)-C(16)	-155.4(4)	C(45)-C(44)-N(41)-Mn(3)	-52.1(3)
C(16)-C(11)-N(12)-C(13)	0.4(6)	C(44)-N(41)-C(50)-C(51)	-105.6(4)
C(10)-C(11)-N(12)-C(13)	179.0(4)	Mn(3)-N(41)-C(50)-C(51)	21.9(4)
C(16)-C(11)-N(12)-Mn(1)	176.0(3)	N(41)-C(50)-C(51)-N(52)	-15.8(5)
C(10)-C(11)-N(12)-Mn(1)	-5.4(5)	N(41)-C(50)-C(51)-C(56)	166.2(4)
C(11)-N(12)-C(13)-C(14)	-0.6(6)	C(56)-C(51)-N(52)-C(53)	0.1(6)
Mn(1)-N(12)-C(13)-C(14)	-175.7(3)	C(50)-C(51)-N(52)-C(53)	-177.9(3)
N(12)-C(13)-C(14)-C(15)	0.4(6)	C(56)-C(51)-N(52)-Mn(3)	179.6(3)
C(13)-C(14)-C(15)-C(16)	0.0(6)	C(50)-C(51)-N(52)-Mn(3)	1.6(4)
C(14)-C(15)-C(16)-C(11)	-0.2(7)	C(51)-N(52)-C(53)-C(54)	0.4(6)
N(12)-C(11)-C(16)-C(15)	0.0(7)	Mn(3)-N(52)-C(53)-C(54)	-179.0(3)
C(10)-C(11)-C(16)-C(15)	-178.5(4)	N(52)-C(53)-C(54)-C(55)	-0.8(7)
N(21)-C(24)-C(25)-S(21)	52.6(4)	C(53)-C(54)-C(55)-C(56)	0.6(7)
C(24)-C(25)-S(21)-C(26)	83.4(3)	C(54)-C(55)-C(56)-C(51)	-0.1(7)
C(24)-C(25)-S(21)-Mn(2)	-29.8(3)	N(52)-C(51)-C(56)-C(55)	-0.2(6)
C(25)-C(24)-N(21)-C(30)	76.6(5)	C(50)-C(51)-C(56)-C(55)	177.6(4)
C(25)-C(24)-N(21)-Mn(2)	-49.4(4)	N(61)-C(64)-C(65)-S(61)	-53.0(4)
C(24)-N(21)-C(30)-C(31)	-97.8(4)	C(64)-C(65)-S(61)-C(66)	-82.8(3)
Mn(2)-N(21)-C(30)-C(31)	29.5(4)	C(64)-C(65)-S(61)-Mn(4)	30.1(3)
N(21)-C(30)-C(31)-N(32)	-23.0(5)	C(65)-C(64)-N(61)-C(70)	-74.3(4)
N(21)-C(30)-C(31)-C(36)	158.1(4)	C(65)-C(64)-N(61)-Mn(4)	50.6(4)
C(36)-C(31)-N(32)-C(33)	0.4(6)	C(64)-N(61)-C(70)-C(71)	99.8(4)
C(30)-C(31)-N(32)-C(33)	-178.6(3)	Mn(4)-N(61)-C(70)-C(71)	-27.0(4)
C(36)-C(31)-N(32)-Mn(2)	-176.3(3)	N(61)-C(70)-C(71)-N(72)	22.6(5)
C(30)-C(31)-N(32)-Mn(2)	4.7(4)	N(61)-C(70)-C(71)-C(76)	-159.4(4)
C(31)-N(32)-C(33)-C(34)	-0.5(6)	C(76)-C(71)-N(72)-C(73)	-0.7(6)
Mn(2)-N(32)-C(33)-C(34)	175.9(3)	C(70)-C(71)-N(72)-C(73)	177.3(4)
N(32)-C(33)-C(34)-C(35)	0.2(6)	C(76)-C(71)-N(72)-Mn(4)	175.6(3)

C(70)-C(71)-N(72)-Mn(4)	-6.4(5)	C(73)-C(74)-C(75)-C(76)	-0.4(7)
C(71)-N(72)-C(73)-C(74)	0.0(6)	C(74)-C(75)-C(76)-C(71)	-0.3(7)
Mn(4)-N(72)-C(73)-C(74)	-175.9(3)	N(72)-C(71)-C(76)-C(75)	0.9(7)
N(72)-C(73)-C(74)-C(75)	0.6(7)	C(70)-C(71)-C(76)-C(75)	-177.0(4)

Symmetry transformations used to generate equivalent atoms:

APPENDIX B: ^{13}C AND ^{1}H NMR SPESTROSCOPY DATA

MCC **1** ^{13}C and ^{1}H NMR spectroscopies in solution

Figure 64. ^{1}H NMR (DMSO-d_6, 600 MHz): δ 2.47 (s, 3H); 7.31 (t, J= 7.3 Hz, 1H); 7,42 (t, J= 7.4 Hz, 1H); 7.50 (d, J= 7.5 Hz, 1H); 7.53 (d, J= 7.4 Hz, 1H); 7.81 (m, 1H); 8.24 (t, J= 7.1 Hz, 1H); 8.29 (d, J= 7.2 Hz, 1H); 8.86 (s, 1H); 9.23 (d, J= 4.7 Hz, 1H). ^{13}C NMR (DMSO-d_6, 150 MHz): δ 15.9; 123.1; 127.0; 129.0; 129.1; 129.7; 130.3; 139.9; 154.6; 154.7; 171.8; 223.0.

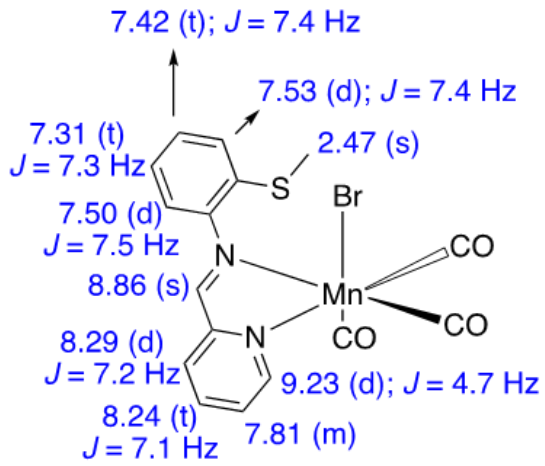

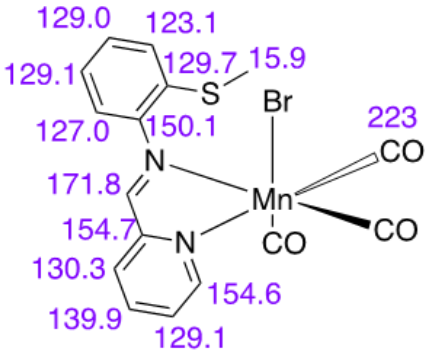

MnImPyS (1)

^{1}H

MnImPyS (1)

^{13}C

Figure 65:. ^{1}H NMR spectra for **1.**

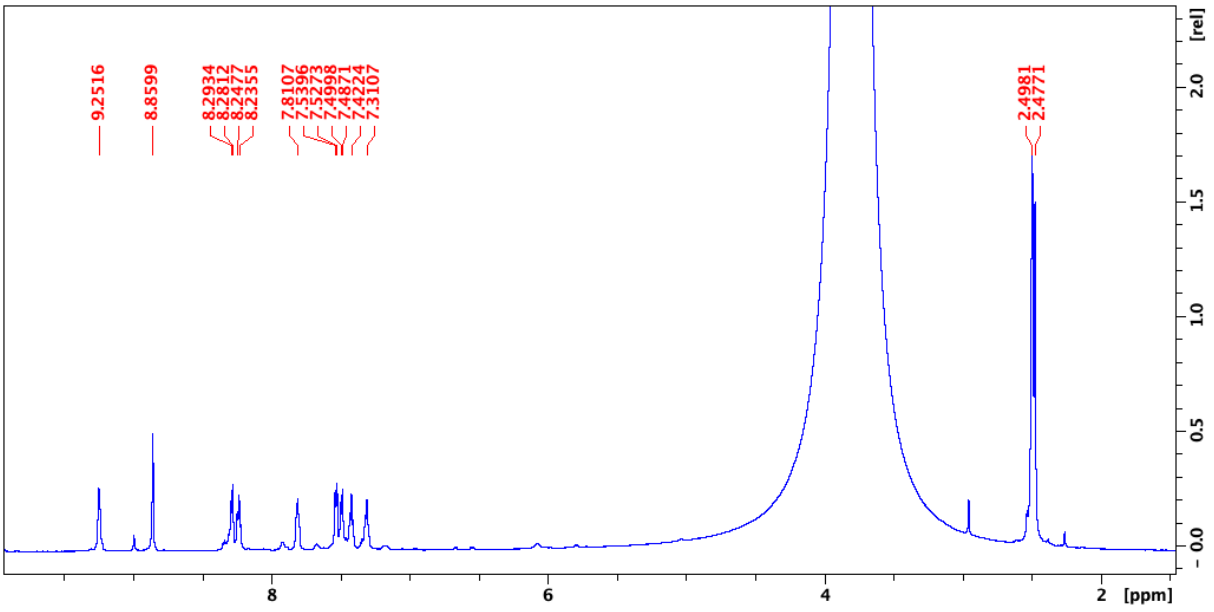

Figure 66:.^{1}H NMR spectra – Aromatic region expansion for **1**.

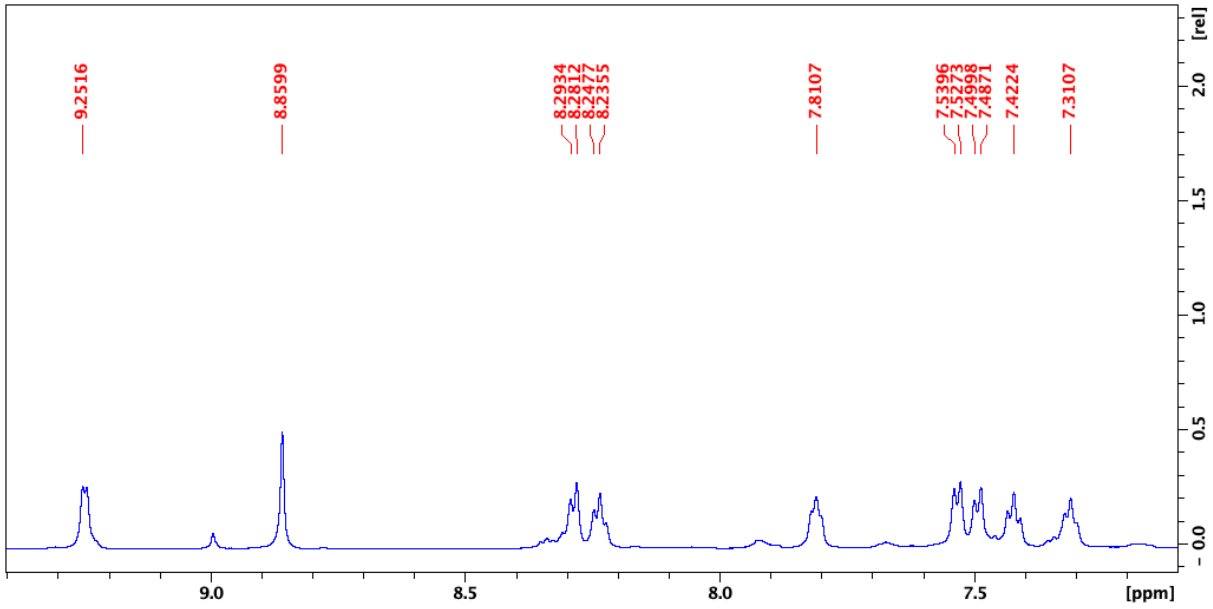

Figure 67:.^{13}C NMR spectra for **1.**

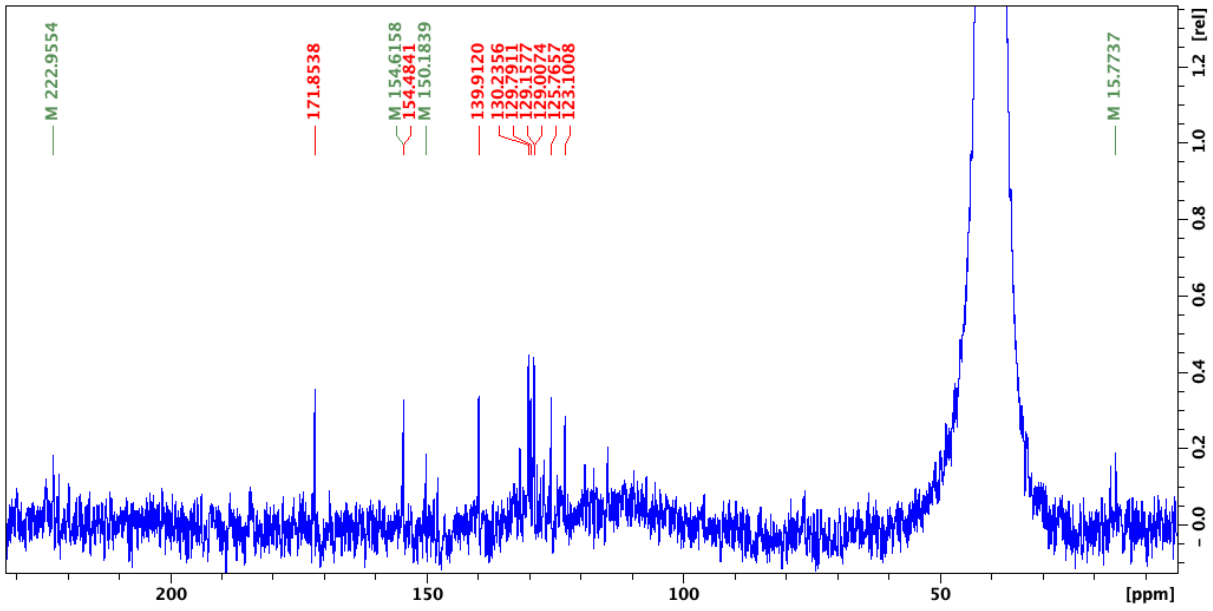

Figure 68:. HSQC spectra for **1.**

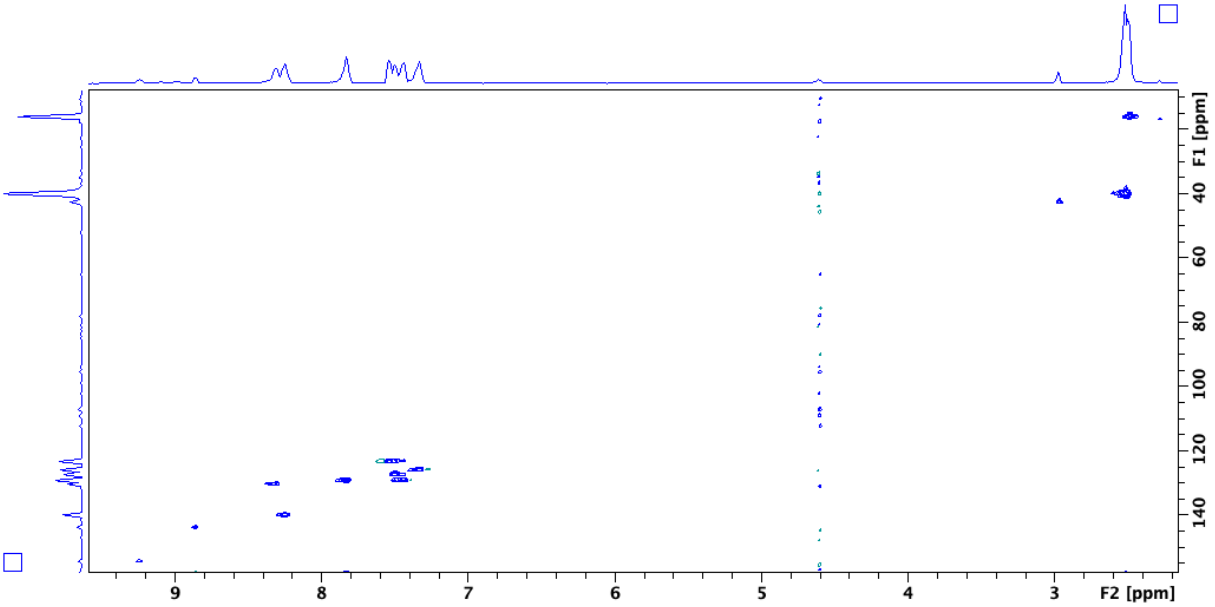

Figure 69:. HMBC spectra for **1.**

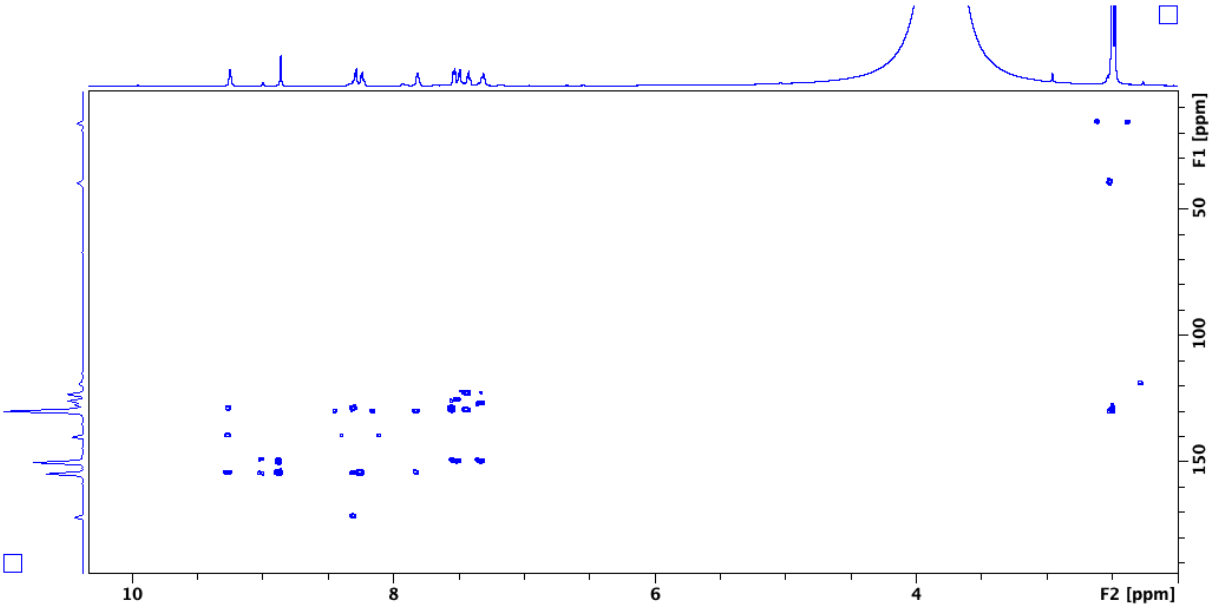

MCC **2** ^{13}C and ^{1}H NMR spectroscopy in solution

Figure 70. ^{1}H NMR (DMSO-d_6, 600 MHz): δ 2.95 (s, 3H); 4.57 (m, 1H); 4.95 (m, 1H); 7.47 (m, 1H); 7.52 (m, 1H); 7.59 (m, 1H); 7.61 (m, 1H); 7.77 (m, 1H); 7.82 (m, 1H); 7.96 (m, 1H); 8.92 (m, 1H).^{13}C NMR (DMSO-d_6, 150 MHz): δ 42.6; 63.9; 123.6; 126.3; 127.6; 130.1; 131.3; 131.6; 131.9; 137.4; 140.6; 148.4; 154.2; 217.3.

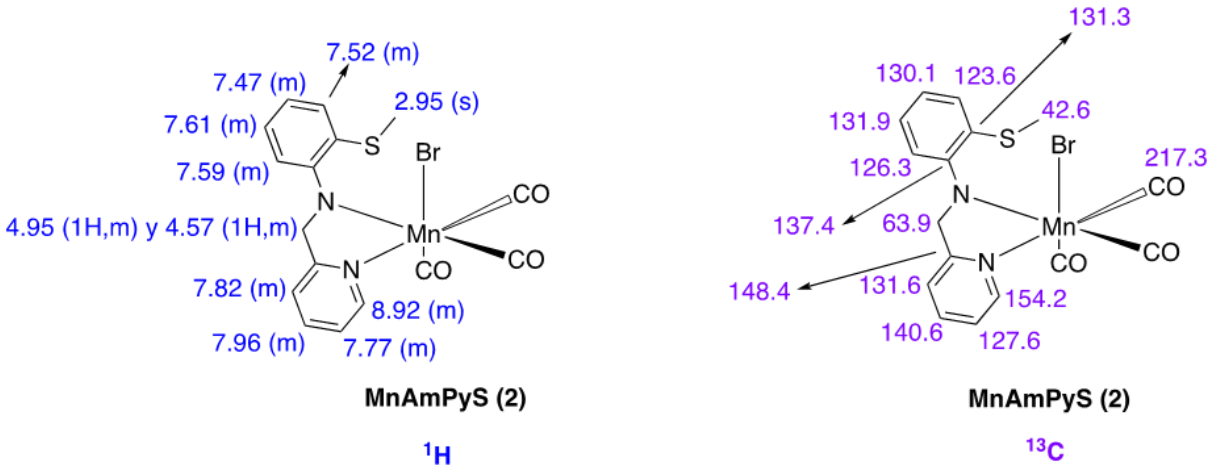

Figure 71:. ^{1}H NMR spectra for **2.**

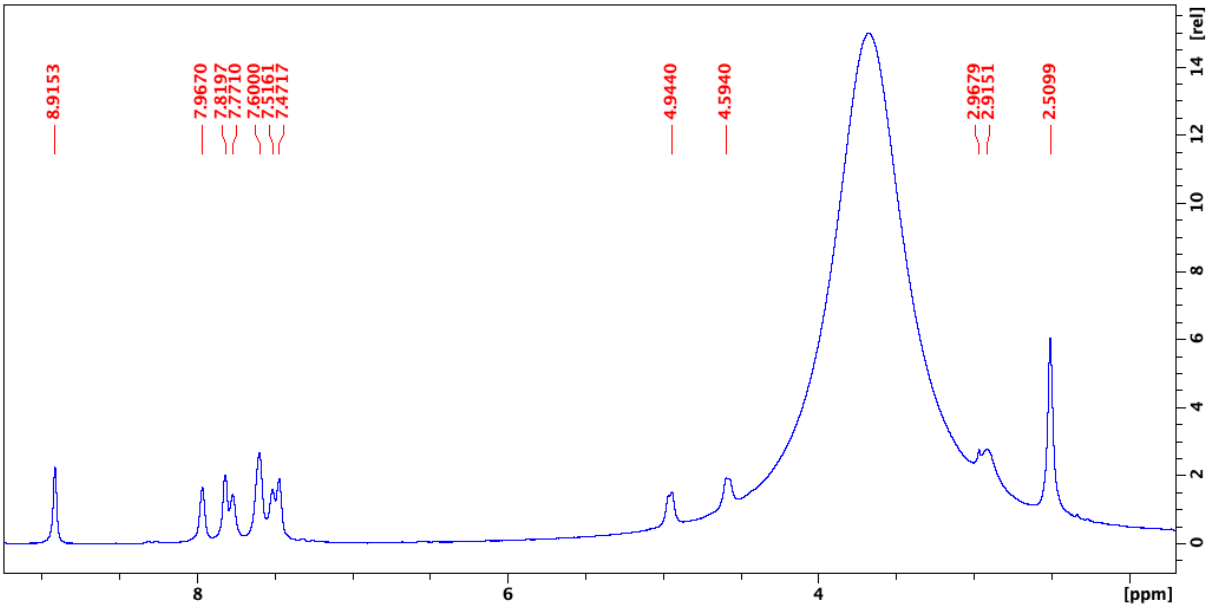

Figure 72:.^{13}C NMR spectra for **2.**

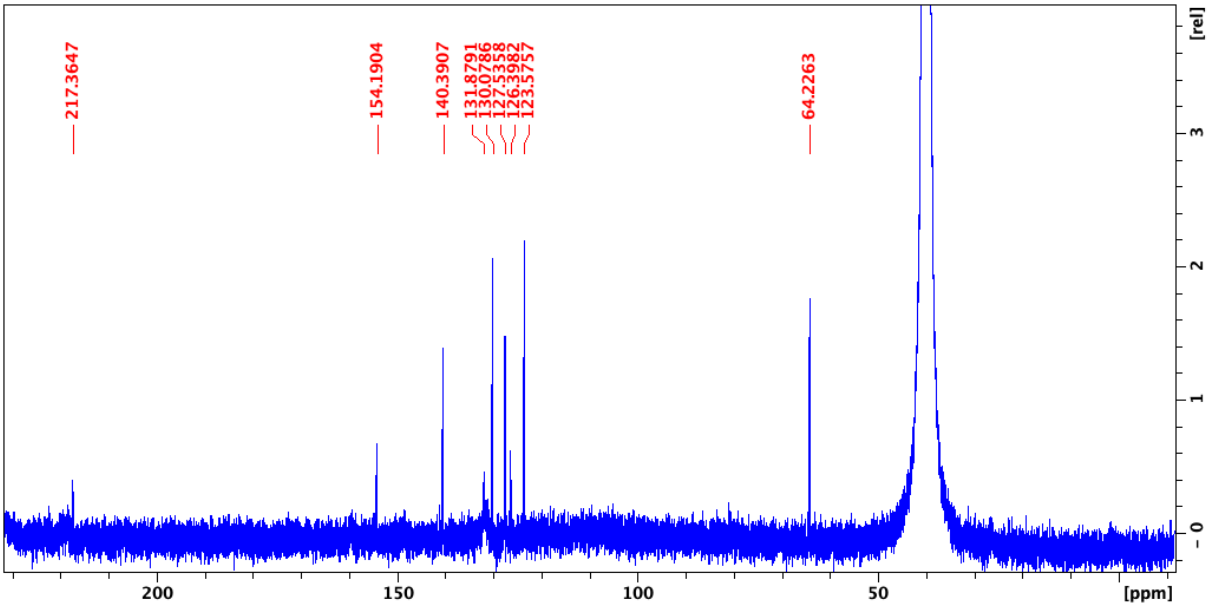

Figure 73:. HSQC spectra for **2.**

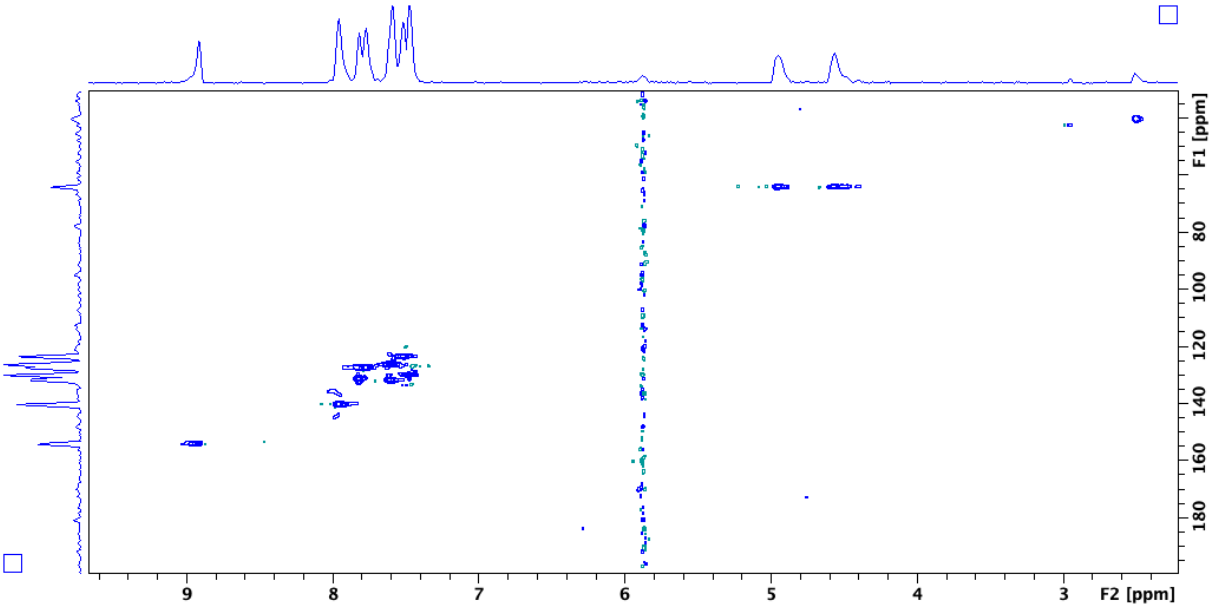

Figure 74:. HSQC spectra – aromatic expansion for **2.**

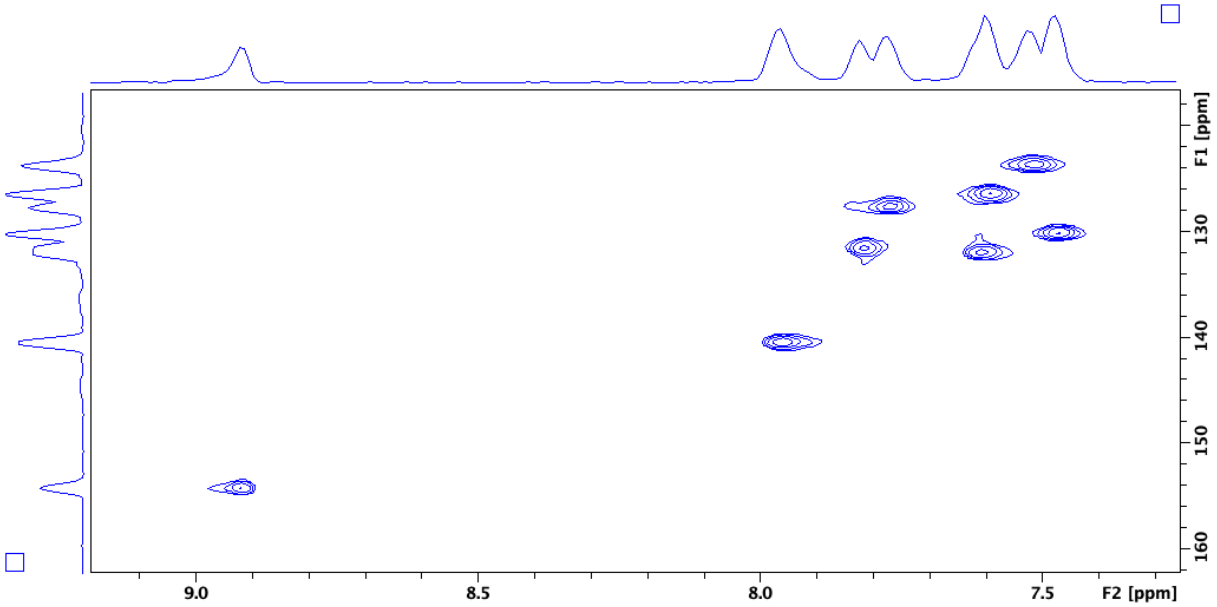

Figure 75:. HMBC spectra for **1.**

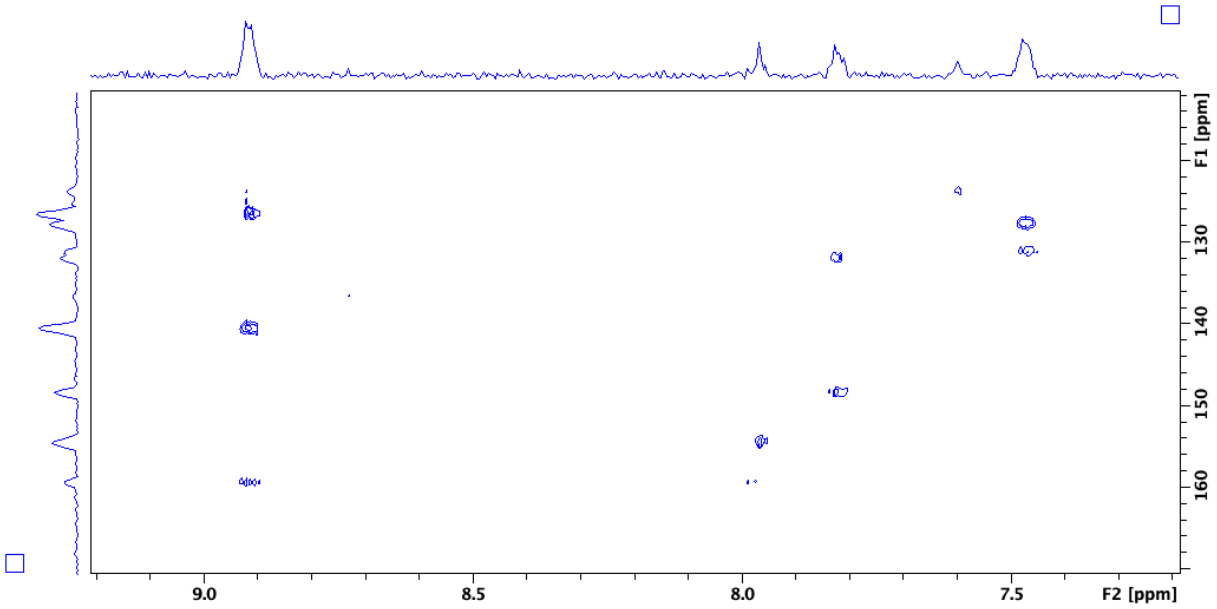

MCC **3** ^{13}C and ^{1}H NMR spectroscopy in solution

Figure 76. ^{1}H NMR (DMSO-d_6, 600 MHz): δ 1.67 (bs, 1H); 1.73 (m, 1H); 2.54 (s, 3H); 2.83 (m, 1H); 3.09 (m, 1H); 3.22 (m, 1H); 4.28 (d, J= 17.8 Hz, 1H); 4.60 (dd, J= 6.3 and 17.8 Hz, 1H); 7.57 (m, 1H); 7.58 (m, 1H); 8.04 (t, J= 7.4 Hz, 1H); 8.75 (t, J= 5.3 Hz, 1H). ^{13}C NMR (DMSO-d_6, 150 MHz): δ 20.5; 34.0; 53.8; 60.1; 122.6; 126.2; 140.4; 153.5; 162.6; 219.3.

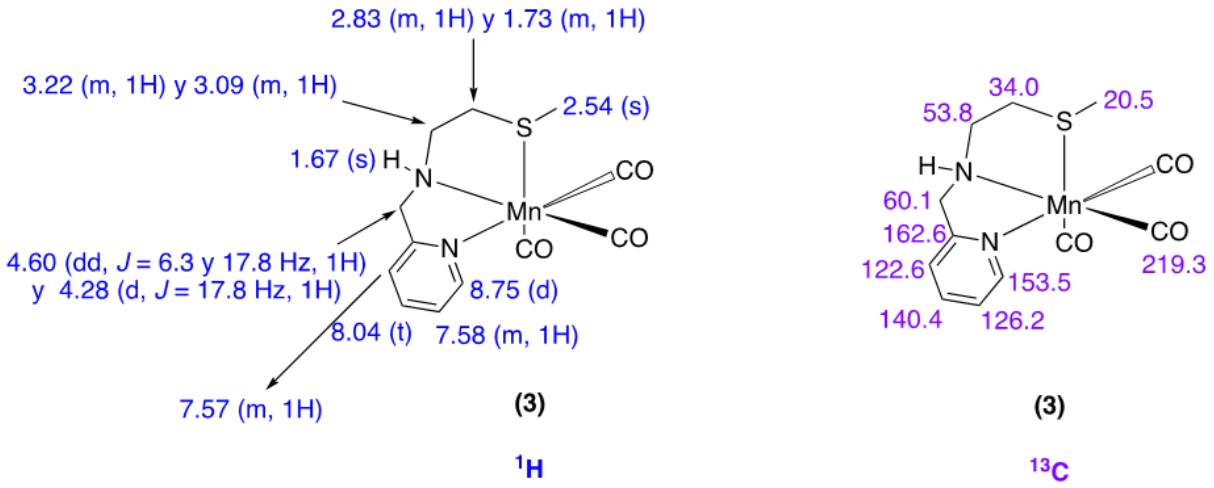

Figure 77:. ^{1}H NMR spectra for **3**

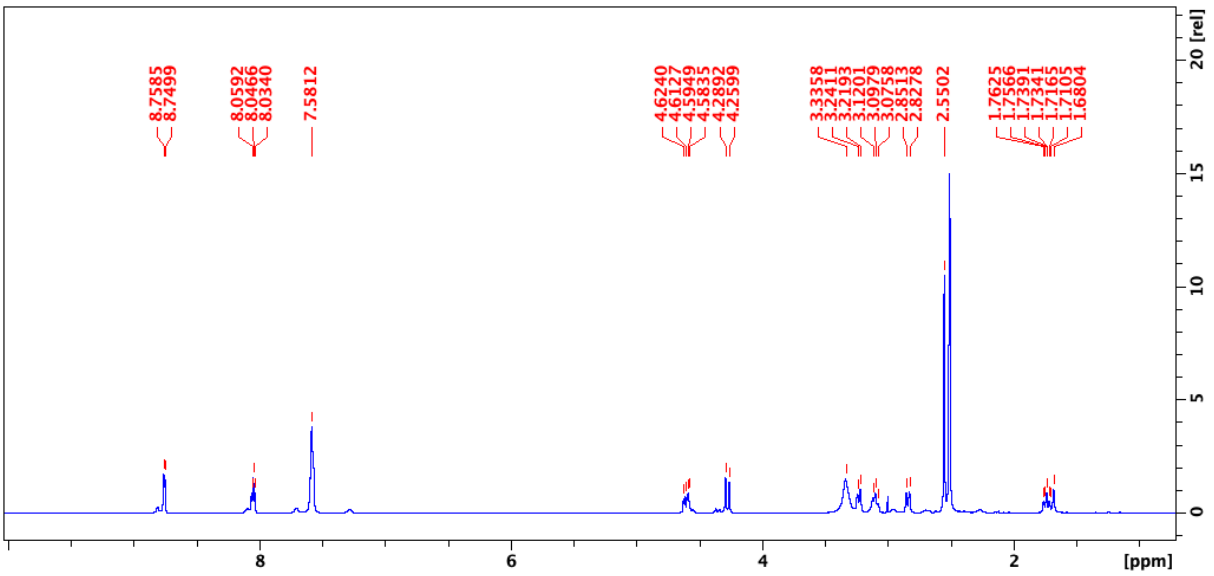

Figure 78:.^{1}H NMR– Aromatic region expansion for **3**.

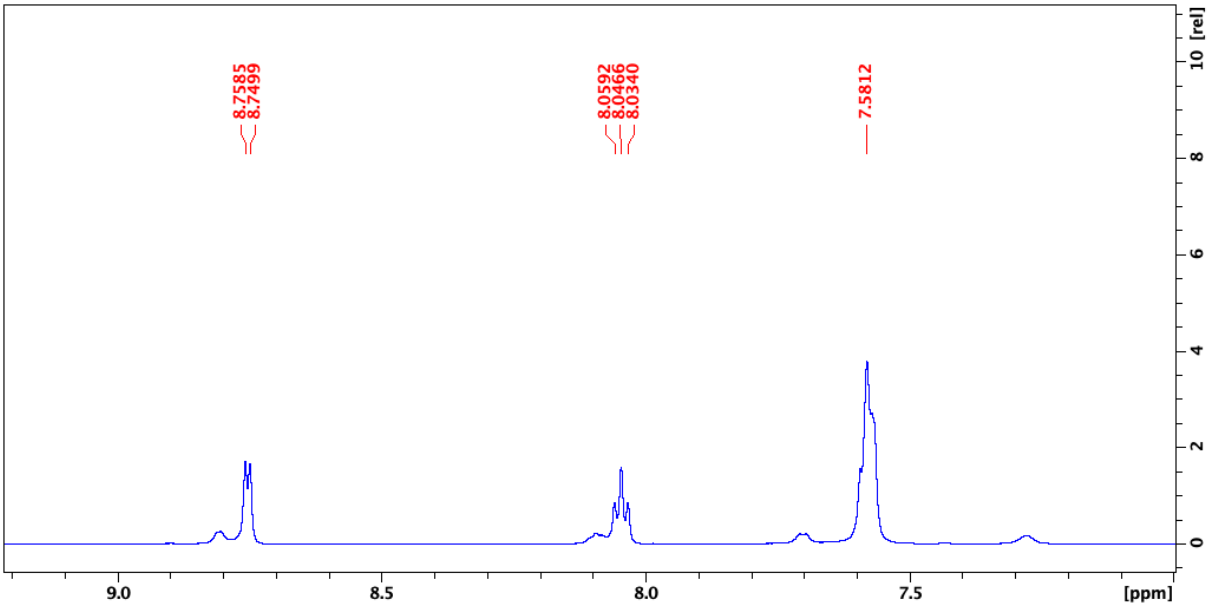

Figure 79:.^{1}H NMR– Aliphatic region expansion for **3**.

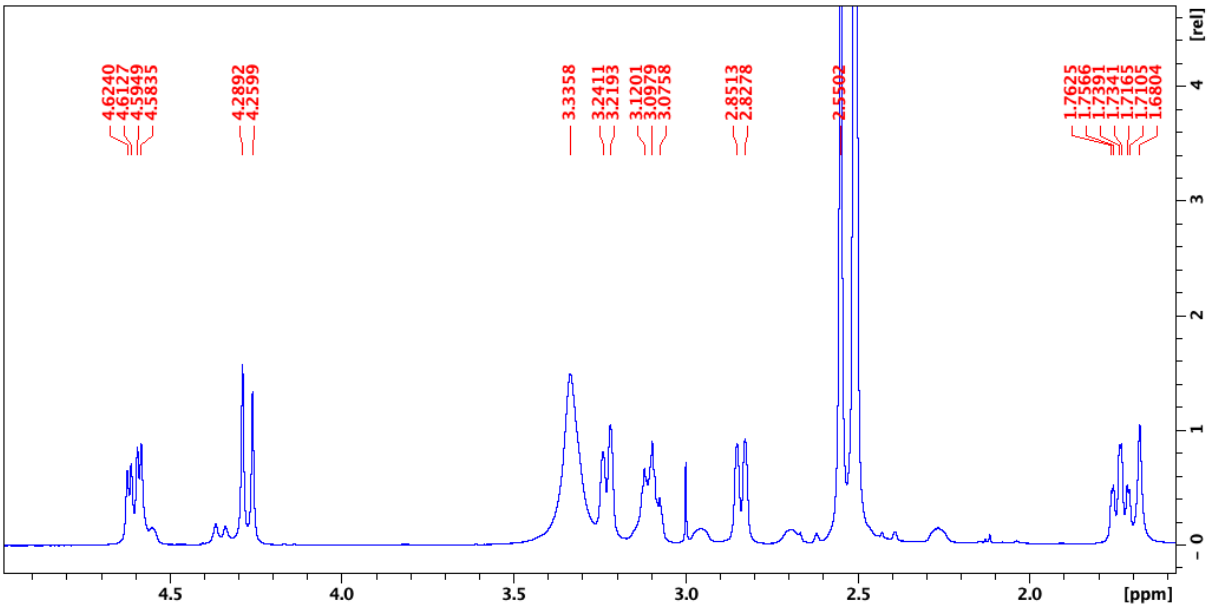

Figure 80:.^{13}C NMR spectra for 3**.**

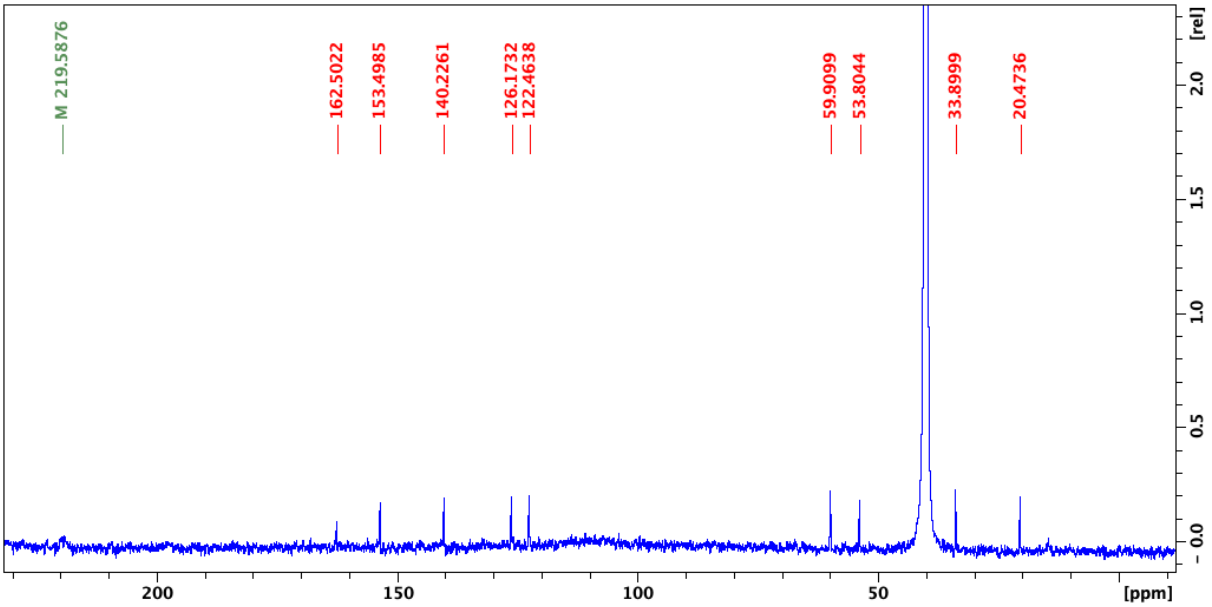

Figure 81:. HSQC spectra for **1.**

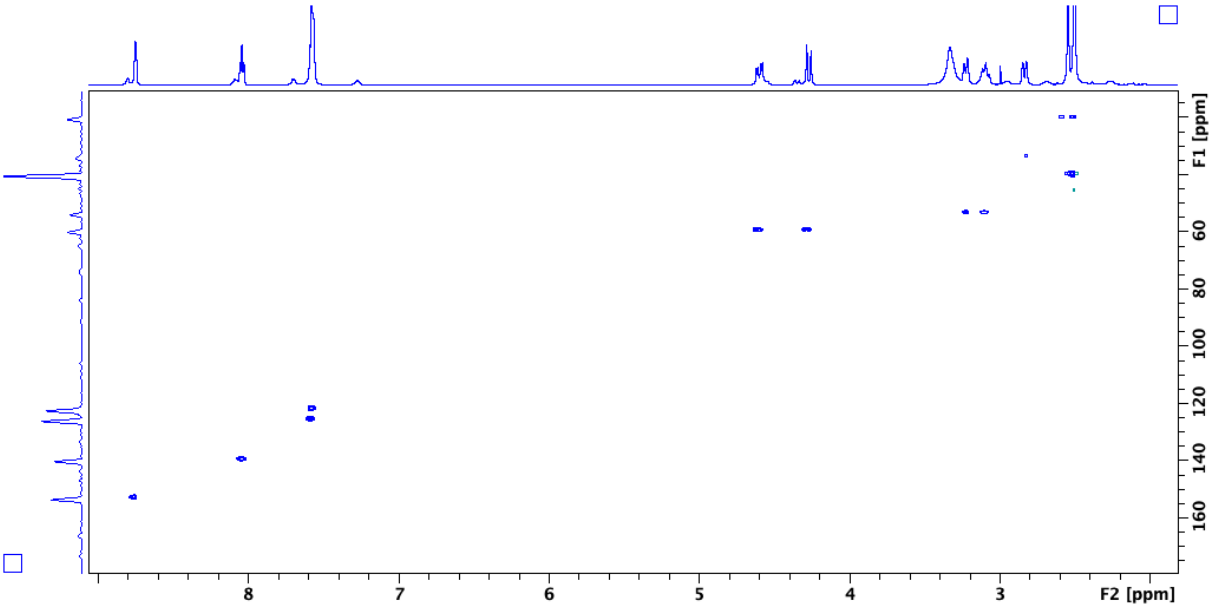

Figure 82:. HMBC spectra for **3.**

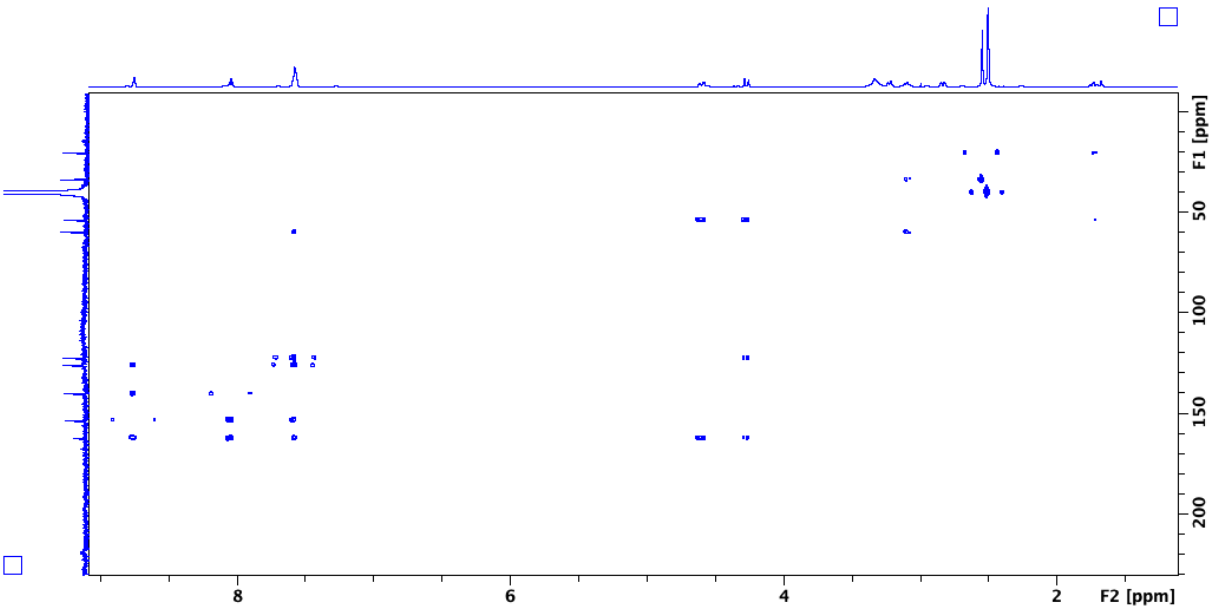

MCC **4** ^{13}C and ^{1}H NMR spectroscopy in solution

Figure 83. ^{1}H NMR (DMSO-d_6, 600 MHz): δ 4.05 (m, 1H); 4.28 (m, 1H); 4.35 (m, 1H); 4.42 (m, 1H); 6.38 (bs, 1H); 7.05 (m, 1H); 7.19 (m, 1H); 7.44 (m, 1H); 7.51 (m, 1H); 7.53 (m, 1H); 7.89 (m, 1H); 8.86 (m, 1H). ^{13}C NMR (DMSO-d_6, 150 MHz): δ 53.7; 57.2; 122.9; 125.0; 127.2; 127.9; 129.1; 138.3; 139.5; 153.1; 160.7; 222.1.

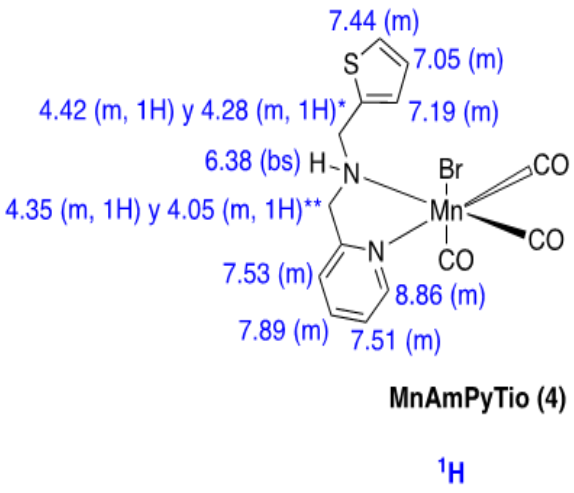

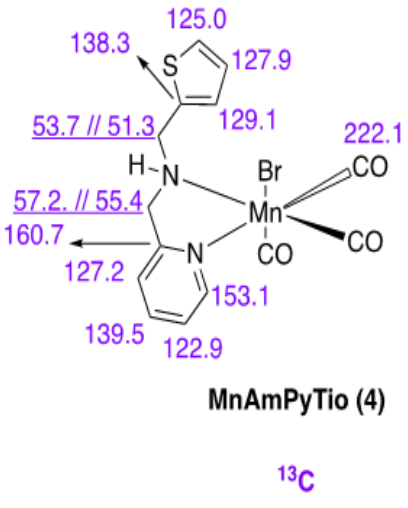

Figure 84:.^{1}H NMR spectra – Aromatic region expansion for **4**.

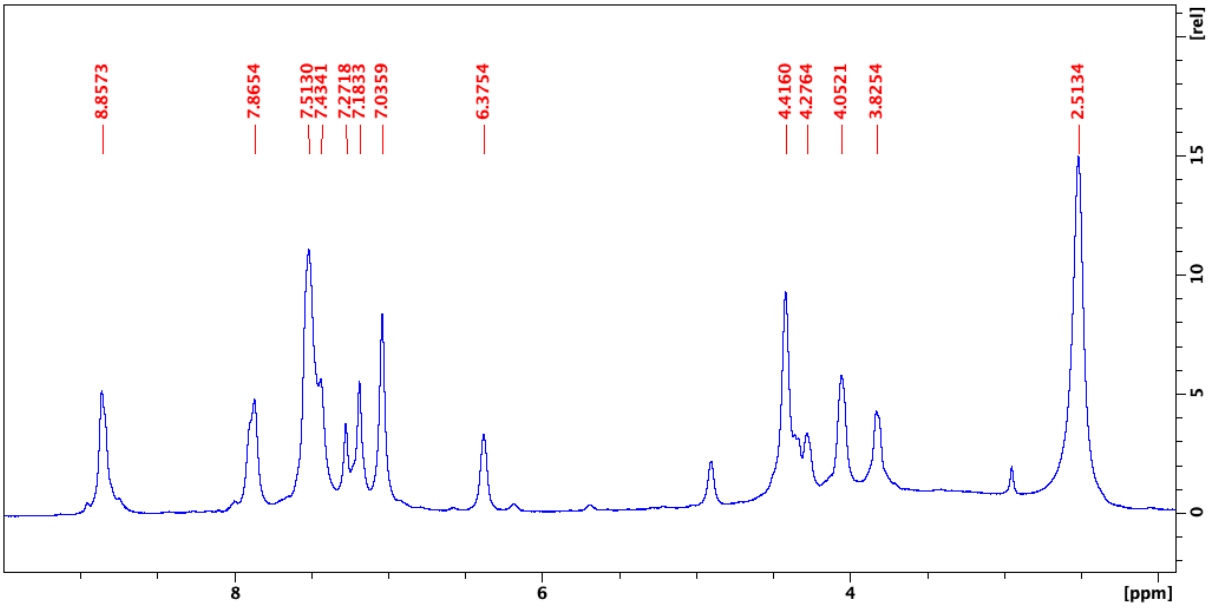

Figure 85:.^{13}C NMR spectra for **4.**

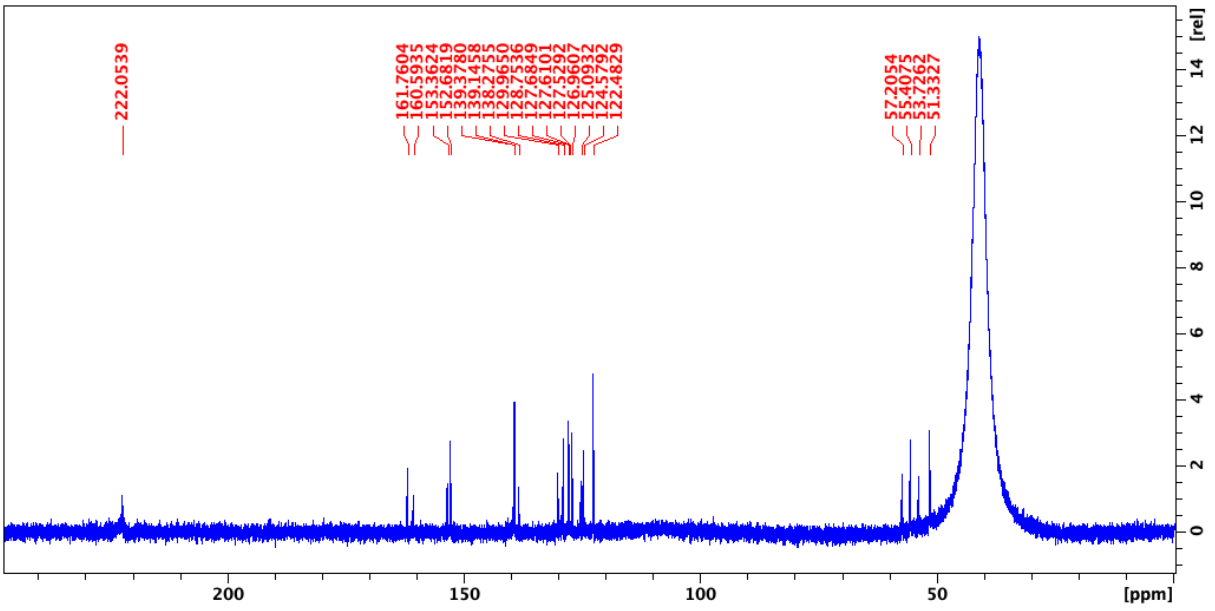

Figure 86:.^{13}C NMR spectra – Aromatic region expansion for **5.**

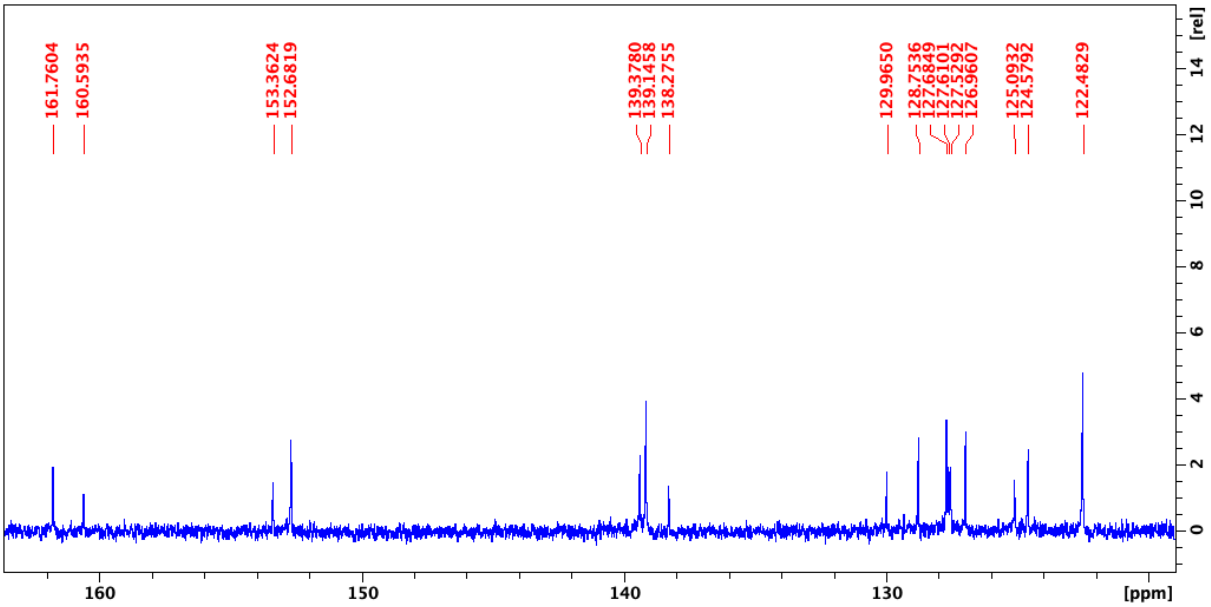

Figure 87:. HSQC spectra for **4.**

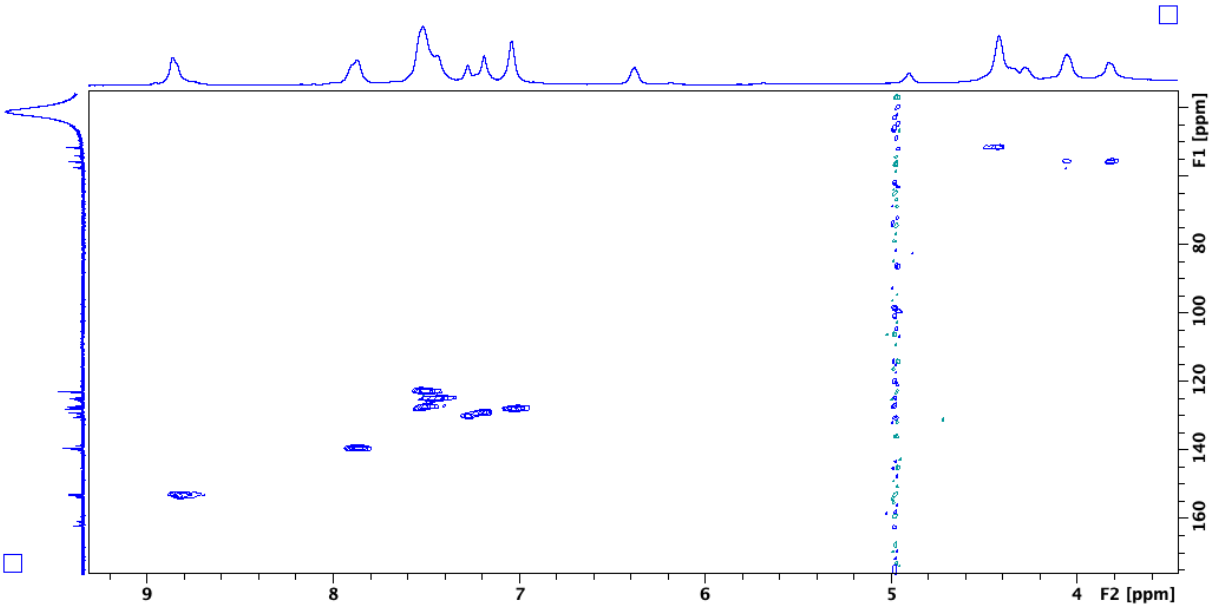

^{13}C *solid-state* NMR spectra in different modes for **1-4**

Figure 88. *Solid-state* ^{13}C Cross-Polarization Magic Angle Spinning experiments for compounds **1** (black) **2** (red), **3** (green), and **4** (blue) at MAS 15KHz.

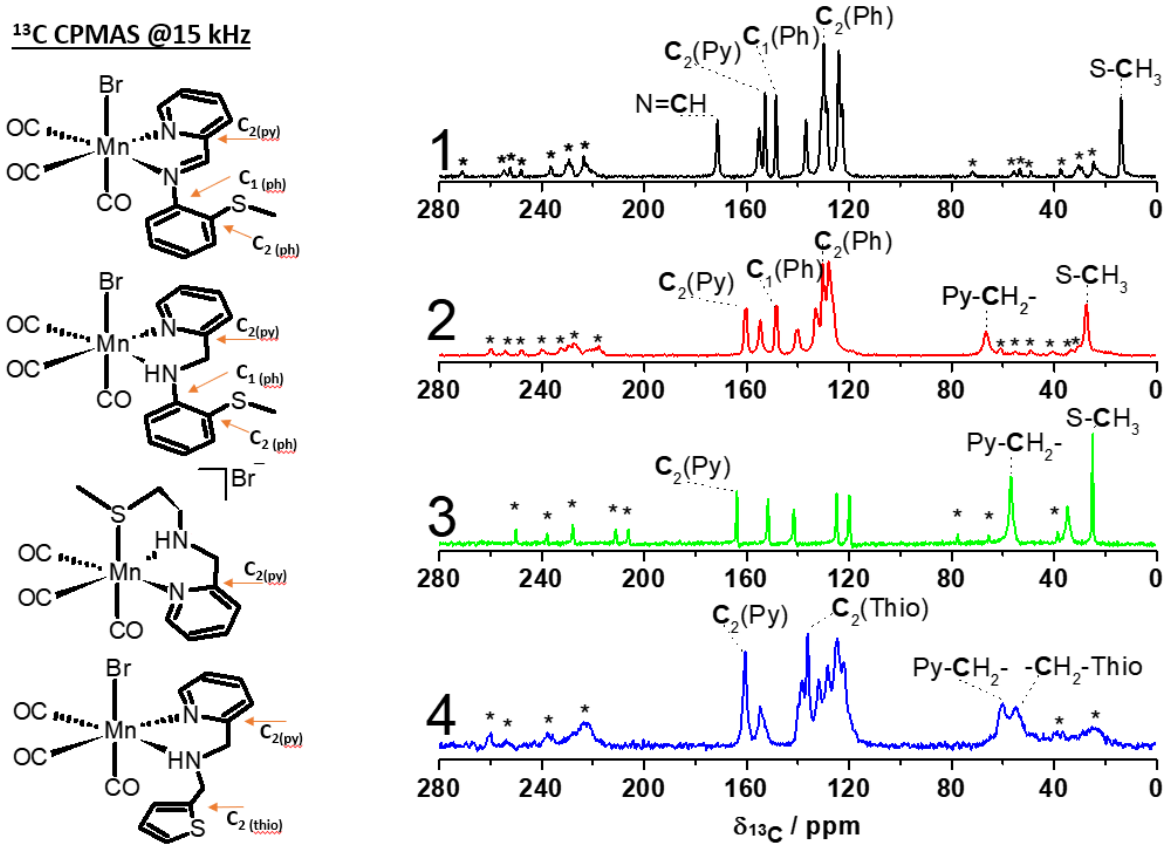

Figure 89. *Solid-state* ^{13}C Cross-polarization with polarization inversion experiments for compounds **1** (black) **2** (red) and **3** (green) at MAS 15KHz.

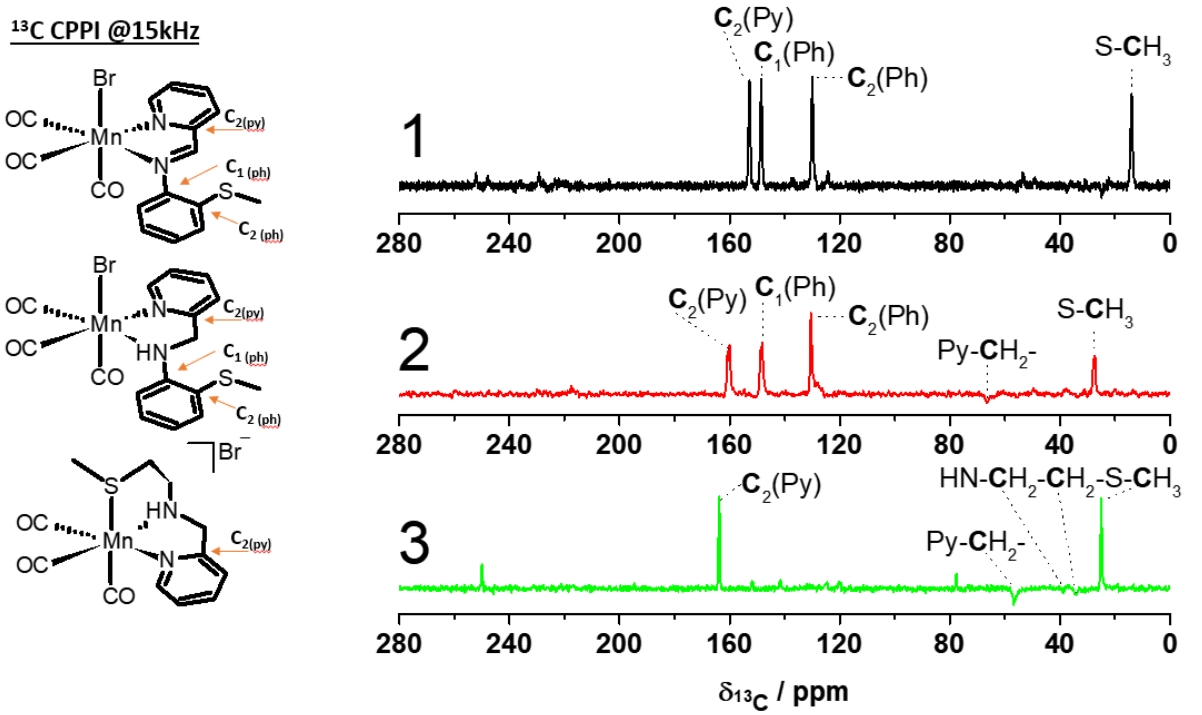

Figure 90. Full *solid-state* ^{13}C High power proton decoupling experiments for compounds **1** (black, MAS rate: 12 kHz), **2** (red, MAS rate: 8 kHz), **3** (green, MAS rate: 12 kHz), and **4** (blue, MAS rate: 8 kHz).

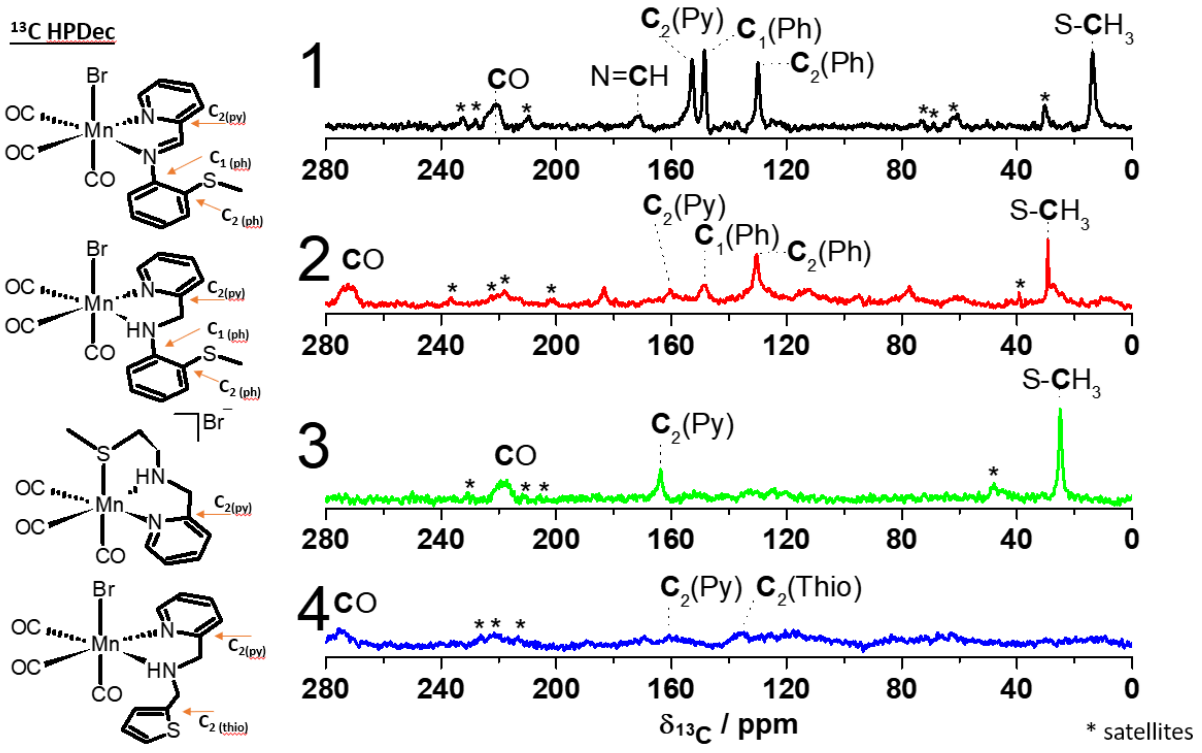

APPENDIX C: HPLC BIOMASS LIQUOR

Figure 91:. HPLC biomass sugar content breakdown after 1.5h synthesis.

PAPER BIOMASS

paper 90min [H⁺]	Retention time	Area
Glucose	17.75	15782.5
Xylose	18.933	4628.7
Levulinic Ac.	31.6	1326.8
Furfural	90.208	1931.4

Calibration curve 90min	
Glucose	y = 152588x + 226,61
Xylose	y = 124559x - 131,07
Furfural	y = 105586x + 113,11

Reaction time > 90min at 180 ºC ([H⁺] 2.5% v/v)

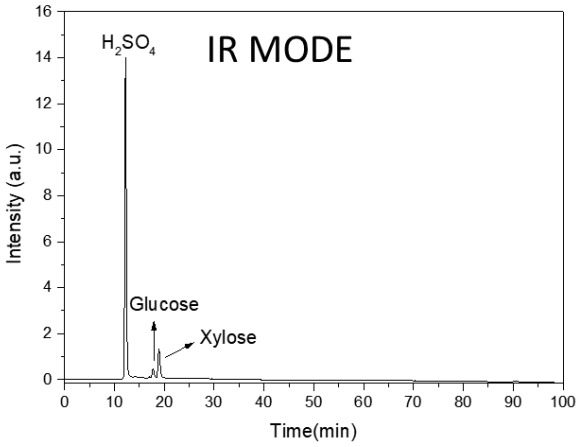

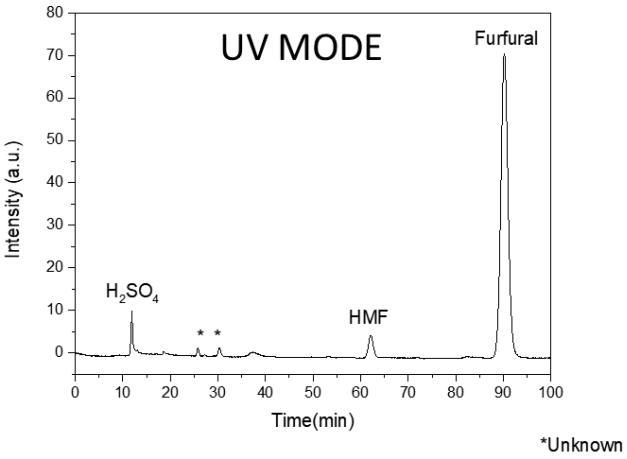

*Unknown

Figure 92:. HPLC biomass sugar content breakdown after 5.5h synthesis.

PAPER BIOMASS

Paper 360min [H]	Retention time	Area
Glucose	-	n/a
Xylose	-	n/a
Levulinic Ac.	31.492	228742
Furfural	89.88	352377

Calibration curve 360min	
Glucose	y = 2E10(08)x + 84279
Xylose	y = 247673176.85x - 13209.97
Furfural	y = 135712841645.70x - 185932.55

Reaction time > 3600min at 180 ºC ([H⁺] 2.5% v/v)

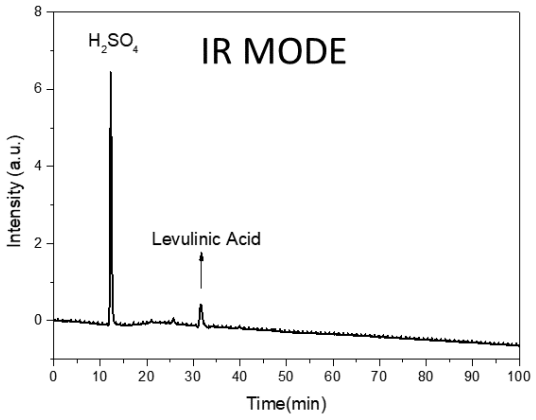

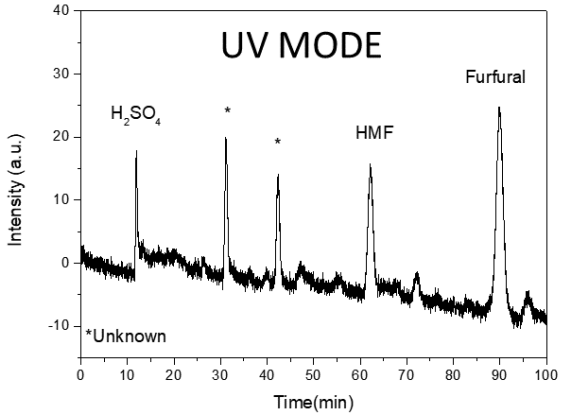

APPENDIX D: FTIR SPECTRA

Figure 93. FTIR spectra of CO stretching bands from **1**, **2**, **3** and **4** in KBr pellets.